CFD MODELING AND ANFIS DEVELOPMENT FOR THE HYDRODYNAMICS PREDICTION OF BUBBLE COLUMN REACTOR RING SPARGER

MOHAMMAD POURTOUSI

FACULTY OF ENGINEERING
UNIVERSITY OF MALAYA
KUALA LUMPUR

2016

CFD MODELING AND ANFIS DEVELOPMENT FOR THE HYDRODYNAMICS PREDICTION OF BUBBLE COLUMN REACTOR RING SPARGER

MOHAMMAD POURTOUSI

THESIS SUBMITTED IN FULFILMENT OF THE REQUIREMENTS FOR THE DEGREE OF DOCTOR OF PHILOSOPHY

FACULTY OF ENGINEERING
UNIVERSITY OF MALAYA
KUALA LUMPUR

2016

UNIVERSITY OF MALAYA
ORIGINAL LITERARY WORK DECLARATION

Name of Candidate: Mohammad Pourtousi
Matric No: KHA120013
Name of Degree: Doctor of Philosophy
Title of Thesis: CFD modeling and ANFIS development for the hydrodynamics prediction of bubble column reactor ring sparger

Field of Study: Mechanical engineering

I do solemnly and sincerely declare that:

(1) I am the sole author/writer of this Work;
(2) This Work is original;
(3) Any use of any work in which copyright exists was done by way of fair dealing and for permitted purposes and any excerpt or extract from, or reference to or reproduction of any copyright work has been disclosed expressly and sufficiently and the title of the Work and its authorship have been acknowledged in this Work;
(4) I do not have any actual knowledge nor do I ought reasonably to know that the making of this work constitutes an infringement of any copyright work;
(5) I hereby assign all and every rights in the copyright to this Work to the University of Malaya ("UM"), who henceforth shall be owner of the copyright in this Work and that any reproduction or use in any form or by any means whatsoever is prohibited without the written consent of UM having been first had and obtained;
(6) I am fully aware that if in the course of making this Work I have infringed any copyright whether intentionally or otherwise, I may be subject to legal action or any other action as may be determined by UM.

Candidate's Signature Date:

Subscribed and solemnly declared before,

Witness's Signature Date:

Name:

Designation:

ABSTRACT

A detailed understanding of the interactions between gas bubbles and the liquid phases in bubble column reactors (BCR), which enhance the heat and mass transfer and chemical reactions, will greatly assist in the design and optimization of the reactor. Despite of wide researches on industrial BCRs, there are still many design aspects of the reactor and sparger (e.g., sparger types, position and velocity, as well as orifice size of the sparger) that require further investigation. A proper selection of BCR and spargers for different industries would greatly improve BCR efficiency and productivity. In addition, an accurate prediction of BCR hydrodynamics with less computational efforts is a major concern in the design and optimization process.

In this study, the effect of ring sparger diameters, superficial gas velocities and number of sparger holes on the flow pattern and gas dynamics in BCR have been investigated. The two-phase Eulerian-Eulerian method embedded in the Commercial Computational Fluid Dynamic software, ANSYS CFX, V14 has been adopted to study the macroscopic hydrodynamics inside a cylindrical BCR. Relevant literature on experimental and numerical results and empirical correlations has been used for validation. Changing the ring sparger diameter and the superficial velocity has a significant effect on the results in comparison to that of the case of the different number of sparger holes.

The influence of microscopic parameters such as orifice size, inlet gas velocity, distance between orifices and number of orifices on a single bubble formation, rising, as well as bubble coalescence process are studied using the Volume of Fluid (VOF) method which is embedded in ANSYS FLUENT, V14. In addition, an experimental work has been carried out to validate some of the CFD cases investigated and also to study the effect of inlet flowrate and orifice size on bubble detachment from an orifice.

An increase in the number of orifices (more than two) resulted in faster bubble detachment from the orifices. This also lead to the production of large bubbles with non-uniform shapes. By determining the specific distance between orifices resulted in bubble formation without coalescence and a uniform size and shape of bubbles.

For the first time, the Adaptive Neuro Fuzzy Inference System (ANFIS) model has been developed to predict the microscopic and macroscopic parameters of BCR hydrodynamics. Some of the CFD results from the previous chapters have been used for the development, training, testing and validation of the ANFIS model. The developed ANFIS model is used to predict the liquid flow pattern and gas dynamics for different ring sparger diameters and BCR heights. ANFIS model is also developed for the prediction of the bubble formation from an orifice and to investigate the bubble rise characteristics. Some limitations are found in ANFIS model and this is discussed.

As a conclusion, ANFIS method can be employed to predict microscopic and macroscopic results for various operational conditions of BCRs. Unlike the CFD implementation process, ANFIS model has the capability to predict the required results fast and requires less computational effort in providing a non-discrete (continuous) result.

ABSTRAK

Pemahaman yang lebih terperinci berkenaan dengan interaksi diantara gelembung gas dan fasa cecair di dalam gelembung ruangan reaktor (BCR) yang menyebabkan peningkatan pemindahan haba, jisim dan kimia adalah tindak balas yang banyak membantu di dalam reka bentuk dan pengoptimuman reaktor. Walaupun kajian terkini berkenaan dengan gelembung ruangan reaktor (BCR), di dapati terdapat aspek-aspek reka bentuk reaktor yang masih banyak dan spargers (seperti contoh jenis penyembur, kedudukan dan halaju dan juga saiz orifis) yang memerlukan kajian selanjutnya. Pilihan yang betul bagi gelembung ruangan reaktor (BCR) dan spargers untuk industri yang berbeza dapat meningkatkan kecekapan BCR dan produktiviti. Selain itu, ketepatan di dalam usaha mengurangkan pengiraan bagi penggunaan hidrodinamik BCR amat menbimbangkan terutama bagi reka bentuk dan pengoptimum proses.

Didalam kajian ini, siasatan telah dibuat bagi membuktikan keberkesanan terhadap penggunaan diameter cincin semprot , halaju gas cetek dan beberapa lubang penyembur pada corak aliran dan dinamik gas bagi gelembung ruangan reaktor BCR. Kedua-dua fasa Eulerian – Kaedah Eulerian yang terdapat di dalam perisian "Commercial Computational Fluid Dynamic", ANSYS CFX, V14 diguna pakai bagi mengkaji hidrodinamik makroskopik di dalam sebuah silinder gelembung ruangan reaktor (BCR). Eksperimen terdahulu , keputusan dan korelasi empirikal berangka telah digunakan untuk bagi tujuan pengesahan kajian tersebut. Tindakan menukar diameter cincin penyembur dan halaju cetek telah memberi kesan yang besar kepada keputusan perbandingan di dalam kes perbezaan jumlah untuk lubang penyembur.

Pengaruh penggunaan parameter mikroskopik seperti saiz orifis , gas halaju masuk , jarak antara lubang dan beberapa lubang pada pembentukan gelembung tunggal

dan juga bagi meningkat ciri-ciri dan proses gelembung tautan yang sedang dikaji adalah dengan menggunakan kaedah Isipadu Cecair (VOF) iaitu kaedah yang terdapat di dalam ANSYS FLUENT , V14 . Di samping itu, kerja-kerja eksperimen juga telah dijalankan bagi mengesah beberapa kes CFD yang disiasat untuk mengkaji kesan kadar aliran masuk dan saiz orifis pada detasmen gelembung yang di dapati dari orifis. Peningkatan bilangan lubang orifis (lebih dari dua) memberi keputusan lebih cepat bagi gelembung detasmen dari lubang orifis dan juga pengeluaran buih besar dengan berbagai bentuk yang tidak seragam. Penentukan jarak tertentu adalah di antara keputusan lubang orifis di dalam pembentukan gelembung tanpa tautan (BCR) , seragam saiz dan bentuk buih.

Buat pertama kali, Sistem Kesimpulan kabur (ANFIS) iaitu model Adaptive Neuro telah digunakan bagi mengkaji parameter mikroskopik dan makroskopik BCR hidrodinamik. Beberapa keputusan CFD dari kajian-kajian terdahulu sebelum ini telah digunakan untuk pembangunan , latihan , pengujian dan pengesahan model ANFIS itu. Model ANFIS telah dicipta dan digunakan untuk mengkaji corak aliran cecair dan gas dinamik bagi diameter cincin semprotan yang berbeza dan juga untuk mengukur ketinggian gelembung tanpa tautan (BCR). Model ANFIS juga digunakan bagi kajian pembentukan gelembung dari orifis dan untuk menyiasat ciri-ciri peningkatan gelembung (iaitu, perubahan dalam saiz gelembung dan kedudukan). Namun terdapat beberapa kekangan di dalam model ANFIS ini yang akan dibincangkan.

Kesimpulannya , kaedah ANFIS boleh digunapakai bagi tujuan untuk mendapat keputusan bagi mikroskopik dan makroskopik di dalam pelbagai keadaan operasi BCRs . Tidak seperti proses pelaksanaan CFD , model ANFIS mempunyai keupayaan untuk meramalkan keputusan yang dikehendaki dengan pantas dan memerlukan usaha yang kurang bagi pengiraan di dalam menyediakan (berterusan) hasil yang bukan diskret.

ACKNOWLEDGEMENT

Foremost, I would like to express my sincere gratitude to my advisors namely Dr. Poo Balan Ganesan for the continuous support during my Ph.D study and research, for his patience, motivation, enthusiasm, and immense knowledge. His guidance helped me throughout the research and writing up this thesis. I could not have imagined having a better advisor and mentor for my Ph.D study. Besides my advisor, I would like to thank Prof. Jaya Narayanan Sahu and Dr. Ghufran Bin Redzwan for their encouragement and insightful comments. I would like to thank the Ministry of Higher Education High Impact Research (UM.C/HIR/MOHE/ENG/13) for the financial support of this research. Last but not least, I would like to thank my family and friends for supporting me spiritually throughout my life.

TABLE OF CONTENTS

LIST OF FIGURES

LIST OF TABLES

LIST OF SYMBOLS AND ABBREVIATIONS

AARE	Average absolute relative error
ANFIS	Adaptive neuro fuzzy inference system
ANN	Artificial Neural Network
BCR	Bubble column reactor
C_D	Drag force coefficient (dimensionless)
C_L	Lift force coefficient (dimensionless)
C_{TD}	Turbulent dispersion coefficient (dimensionless)
$C_{\varepsilon 1}$	Model parameter in turbulent dissipation energy equation (dimensionless)
$C_{\varepsilon 2}$	Model parameter in turbulent dissipation energy equation (dimensionless)
C_{μ}	Constant in *k*-ε model (dimensionless)
$C_{\mu BI}$	Constant in bubble induced turbulence model (dimensionless)
D	Diameter of the bubble column reactor (m)
d_b	Bubble diameter (m)
d_f	First bubble diameter (mm)
d_o	Sparger hole diameter (m)
d_s	Second bubble diameter (mm)
E-E	Euler-Euler
E_O	Eotvos number ($= \frac{g(\rho_L - \rho_G){d_B}^2}{\sigma}$) (dimensionless)
F	Volume fraction function
FAD	Favre-averaged-drag
FCT	Flux-Corrected Transport
G	Generation term (kg/m s^2)
g	Gravitational constant (m/s^2)
H	Height (m)
I	Iteration
k	Turbulent kinetic energy per unit mass (m^2/s^2)
LDA	Laser Doppler anemometry
LES	Large Eddy Simulation
M_D	Drag force (N/m^3)
MF	Membership function
M_I	Total interfacial force acting between two phases (N/m^3)
NR	Number of rules
P	Percentage of training data
PBM	Population balance model
PIV	Particle image velocimetry
R	Column radius (m)
r	Radial distance (m)
Re_b	Reynolds number ($= d_B V_S/v$) (dimensionless)
RNG	Re-Normalisation Group
RSM	Reynolds Stress Model
SVR	Support Vector Regression
S_v	Sparge hole velocity (orifice velocity)
t	Time (s)
t_c	Bubble coalescence time
t_d	Bubble detachment time
TDF	Turbulent dispersion force

TVD	Total variation diminishing
UASBR	Up flow anaerobic sludge bed reactor
V_G	Superficial gas velocity (m/s)
VOF	Volume of fluid
V_s	Axial slip velocity between gas and liquid (m^2/s)
V_T	Terminal velocity (m^2/s)

Greek Symbols

ε	Turbulent energy dissipation rate per unit mass (m^2/s^3)
$\in$	Fractional phase hold-up (dimensionless)
$\overline{\in}$	Average fractional phase hold-up (dimensionless)
μ	Molecular viscosity (Pa s)
μ_{BI}	Bubble induced viscosity (Pa s)
μ_{eff}	Effective viscosity (Pa s)
ρ	Density (kg/m^3)
μ_t	Turbulent viscosity (Pa s)
σ	Surface tension (N/m)
σ_ε	Prandtl number for turbulent energy dissipation rate (dimensionless)
σ_k	Prandtl number for turbulent kinetic energy (dimensionless)
τ_k	Shear stress of phase k (Pa)
α	The ratio of coalescence time to detachment time

Subscripts

b	Bubble
c	Coalescence
g	Gas phase
l	Liquid phase
o	Orifice
rel	Relative velocity

LIST OF APPENDICES

CHAPTER 1: INTRODUCTION

1.1 Research Motivation

Industries such as chemical, petrochemical, biochemical, wastewater treatment and metallurgical, extensively require reaction processes between gas and liquid in their plants. To assist the process, a bubble column reactor (BCR) which is a suitable multiphase reactor/contactor, is used. BCRs have many advantages such as high heat and mass transfer coefficients, low maintenance, low operating costs, and high durability of catalysts or other packing materials in comparison to other types of reactors, e.g., trickle bed reactors (fixed or packed beds), fluidized bed reactors, etc. (Pfleger & Becker, 2001; Pfleger, Gomes, Gilbert, & Wagner, 1999; Pourtousi, Sahu, & Ganesan, 2014; Pourtousi, Sahu, Ganesan, Shamshirband, & Redzwan, 2015; Tabib, Roy, & Joshi, 2008; Thorat & Joshi, 2004). The sparger distributes bubbles into the BCR containing either a liquid phase (water, etc.,) or a liquid–solid suspension (Kantarci, Borak, & Ulgen, 2005; Pfleger & Becker, 2001; Pfleger et al., 1999; Pourtousi et al., 2014; Tabib et al., 2008).

A detailed understanding of BCR hydrodynamics such as bubble size and shape, the distribution of gas (hold-up) and the liquid flow patterns can assist in improving the design and optimization of BCRs for industrial usage (Bothe & Fleckenstein, 2013; Buwa, Gerlach, Durst, & Schlücker, 2007; Chakraborty, Biswas, & Ghoshdastidar, 2011; Chakraborty et al., 2009; Ruzicka, Bunganic, & Drahoš, 2009; Vafaei, Borca-Tasciuc, & Wen, 2010). Different BCR geometry and operation conditions change the characteristics of bubbles and bubble coalescence. Coalescence decreases the gas liquid superficial area, which is not helpful for efficient mass and heat transfer, resulting in reduction of reaction process and BCR efficiency. Depending on the BCR diameter and operational conditions (change in property and velocities), the bubble flow pattern

changes from homogeneous (i.e., bubbles have almost same and small diameters and low velocity) to heterogeneous (bubbles have various sizes and velocities). In general, a homogeneous regime occurs in low inlet flow rate where the bubble diameter size and shape depends on the orifice size. For instance, as flow rate increases, bubble collision and coalescence are more likely to appear inside the BCR and the homogeneous regime gradually loses its stability and changes into heterogeneous (Buwa et al., 2007; Hur, Yang, Jung, & Park, 2013; Joshi, 2001; Ma, Liu, Zu, & Tang, 2012; Mathpati, Tabib, Deshpande, & Joshi, 2009; Pourtousi et al., 2014).

One of the key factors to change the BCR hydrodynamics is sparger design parameters (e.g., sparger geometry, types and arrangement). Alteration of these parameters inside the BCR completely changes the liquid circulation and bubble size and rise velocity. Changing the sparger hole diameters produces less/more bubble coalescence and changes the BCR regime (particularly towards the sparger region). A detailed understanding of the effect of sparger parameters on bubble formation and rise characteristics (i.e., bubble size, shape and velocity, bubble detachment time, coalescence and break up process and etc.) and liquid flow patterns, in a BCR, will greatly assist in designs of reactors for various types of industrial applications (Kantarci et al., 2005).

During the past two decades, Computational Fluid Dynamics (CFD) has been found to be very useful in simulating multiphase flows in the BCR, especially due to the significant advancements in numerical techniques and computing power. CFD can be helpful to carry out parametric studies after the model has been validated to reduce experimental costs. The main drawback of CFD methods is the need to select a proper numerical method and, models which require a relatively larger computational effort and for some cases, it is prone to numerical instability. Recently soft computing methods (e.g., Adaptive Neuro-Fuzzy Inference System (ANFIS)) have been adopted

for predictions of complex physical problems without issues of computational power and numerical instability. ANFIS can be used together with CFD models as an alternative means to predict hydrodynamic characteristics of chemical and biochemical reactors under various operational conditions.

1.2 Objectives

The specific objectives of this study are:

- To investigate the liquid and gas flow patterns in an industrial BCR. Specifically, the effect of sparger geometry (i.e., ring diameters, superficial gas velocity and number of sparger holes) is investigated using CFD (Eulerian-Eulerian method).
- To investigate the formation and rise characteristics of a single bubble from BCR sparger (a microscopic study). Specifically, the effect of the size of orifice diameter, inlet velocity and the distance between two orifices are investigated experimentally as well as using the CFD method (i.e., VOF numerical method).
- To develop 'Adaptive neuro fuzzy inference system' in order to predict BCR hydrodynamic parameters. Specifically, the flow patterns and gas dynamics (e.g., gas hold up, turbulence kinetic energy (TKE), velocity) at various BCR heights for different ring sparger diameters, as well as a single bubble formation and rising characteristics (bubble size, shape, position and interface) will be predicted.

1.3 Thesis layout

This thesis consists of seven chapters. After the introduction, the second chapter critically reviews the influence of operational conditions on BCR hydrodynamics. In addition, various CFD and soft computing methods in predicting BCR from the literature are presented. The third section will discuss the effect of ring sparger design

parameters (i.e., ring sparger diameter, superficial gas velocity and number of sparger hole) on the BCR hydrodynamics parameters. In chapter four, single bubble formation, rising and the interaction between bubbles through single and multi-orifices are studied. In the fifth chapter a new ANFIS model in predicting macroscopic parameters of BCR (i.e., liquid flow pattern, gas hold-up and turbulent kinetic energy) is presented. In the sixth chapter, the ANFIS development is used in estimating single bubble formation and rising. Finally, the seventh chapter provides the conclusions and suggestions for future works of the present thesis.

CHAPTER 2: LITERATURE REVIEW

In this chapter the BCR and its hydrodynamics, as well as bubble formation, rising and the interaction between bubbles are presented. The effects of operational conditions, particularly sparger design parameters (sparger types, velocity and size) on the hydrodynamics in BCR are discussed. Various numerical techniques, namely VOF, Eluerian and soft computing techniques (i.e., Support Vector Regression (SVR), Artificial Neural Network (ANN) and Adaptive Neuro Fuzzy Inference System (ANFIS)) to predict the BCR hydrodynamics are presented. Furthermore, a comprehensive comparison of turbulence models and interfacial forces models used in prior CFD studies for study of flow patterns and gas dynamics in BCRs, has been carried out.

2.1 Single bubble formation and rise characteristics

The study of bubble formation, rising and the interaction between bubbles (i.e., coalescence and break-up) assist in improving the design and optimization of BCR in industrial settings (A. A. Kulkarni & Joshi, 2005; Tabib et al., 2008). The bubble development changes with the alteration of bubble terminal velocity, coalescence and break-up of bubbles. The air bubble dynamics i.e., bubble shapes, bubble terminal velocity, the wake structure of bubbles and coalescence of two and three bubbles in BCRs filled with different quiescent liquids e.g., water, glycerol–water solution, have been extensively studied (Chakraborty et al., 2011; Hasan & Zakaria, 2011; A. A. Kulkarni & Joshi, 2005; Lesage, Cotton, & Robinson, 2013; H. Z. Li, Mouline, & Midoux, 2002; Ruzicka et al., 2009; Zahedi, Saleh, Moreno-Atanasio, & Yousefi, 2014). Inlet gas flow rates change the dynamics of bubbles such as the increase/decrease of coalescence process in BCRs (A. A. Kulkarni & Joshi, 2005). The increase in flow rates enlarges the bubble diameter size, and speeds up the bubble detachment from the

tip of an orifice and decreases coalescence time (A. A. Kulkarni & Joshi, 2005; Ma et al., 2012). In addition, the increase of flow rate develops a strong vortex behind the leading bubble (i.e., the first bubble) that affects the size and shape of the trailing bubble generated (Buwa et al., 2007; A. A. Kulkarni & Joshi, 2005; Ma et al., 2012). The large leading bubble changes the bubble formation characteristics adjacent to the orifice from small and uniform bubbles without coalescence (type 1) to large and non-uniform bubbles with coalescence (type 2) near the orifice (Buwa et al., 2007).

The dynamics of bubbles is also affected by different liquids and feeding gas as its properties change (A. A. Kulkarni & Joshi, 2005). Many investigations are focused on studying the effect of liquid properties (i.e., viscosity, density and surface tension) on bubble formation and its dynamics (A. A. Kulkarni & Joshi, 2005; Ma et al., 2012; Zahedi et al., 2014). The bubble formation from an orifice is delayed in high viscous liquids (i.e., increment of necking process time) and results in a large size bubble. In comparison to low surface tension liquids, high surface tension liquids generate a larger bubble diameter and requires a longer period for necking process (A. A. Kulkarni & Joshi, 2005; Ma et al., 2012; Zahedi et al., 2014). The increase of surface tension also delays bubble coalescence process and forms a larger bubble after coalescence. Alterations in gas properties result in similar bubble formation and detachment, while the initial bubble diameter increase/decrease (A. A. Kulkarni & Joshi, 2005; Ma et al., 2012; Zahedi et al., 2014).

2.2 Bubble column reactor

2.2.1 General background and applications

BCR is often equipped with the gas sparger (orifice/nozzle) at the bottom (Kantarci et al., 2005; A. A. Kulkarni & Joshi, 2005; Pfleger & Becker, 2001; Pourtousi et al., 2014; Pourtousi, Sahu, et al., 2015). The gas phase (bubbles) is set to rise in a liquid phase or a liquid–solid suspension (Kantarci et al., 2005; A. A. Kulkarni & Joshi, 2005). Figure 2.1 shows the schematic diagram of BCR experimental setup, including a sample image from bubbles and experimental equipment (i.e., high speed camera, pressure transducer, air supply, gas sparger and etc.). BCRs are widely used in several industrial processes such as oxidation, hydrogenation, fermentation, biological waste water treatment, flue gas desulphurization, coal liquefaction, polymerization (production of polyolefins), biomedical engineering (blood oxygenator), production of foods, pharmaceuticals and biodiesel (Chen, Duduković, & Sanyal, 2005; Díaz et al., 2008; Kantarci et al., 2005; Pourtousi et al., 2014; Pourtousi, Sahu, et al., 2015). Table 2.1 and Table 2.2 show the summary of the operational and design parameters of cylindrical and rectangular BCRs, respectively, investigated in prior studies. According to the Table, in previous investigations, mostly air as a dispersed gas with superficial gas velocities ranged from 0.00133-0.3 m/s have been used for both cylindrical and rectangular BCRs filled with water. However, in few cases, Tellus oil, alcohol, CMC, glycerol solution are used for the study of sensitivity of liquid properties. Various BCR dimensions have been reported in the literature. For example, BCR diameters ranging from 0.078-1 mm with column heights in the range of 0.45-4.6 m have been usually used in prior studies. They are equipped with multi-point, porous plate, ring and perforated plate spargers.

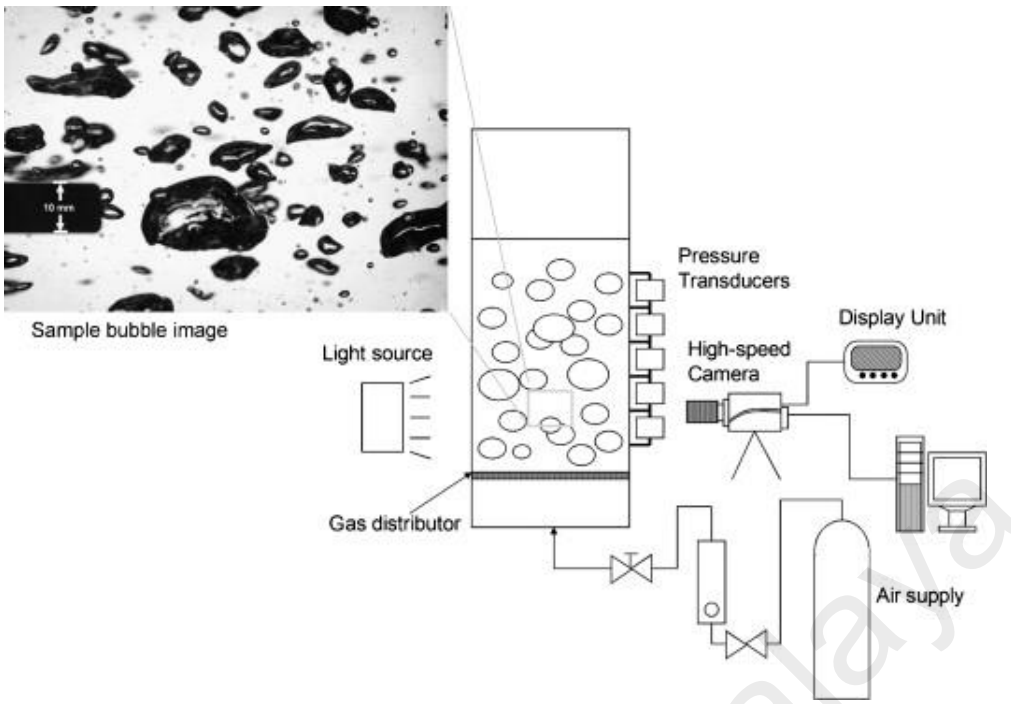

Figure 2.1: Schematic diagram of the BCR experimental setup (Lau, Mo, & Sim, 2010)

Table 2.1: Summary of the operational and design parameters of cylindrical BCRs investigated in the literature

System	Sparger	V_g(m/s)	Regime	BCR		Ref.
				D (m)	H (m)	
Air-water	perforated plate, sintered plate and single hole	0.012-0.096	Homogeneous-Heterogeneous	0.15- 0.60	1-5.44	(Tabib et al., 2008)
Air-water	-	0.01-0.08	Homogeneous-Heterogeneous	0.1, 1	1.6, 7	(Krishna & Van Baten, 2003)
Air-water	perforated plate and single hole	0.1	Heterogeneous	0.4	2	(G. Li, Yang, & Dai, 2009)
Air-water	perforated plate	0.02-0.08	Homogeneous-Heterogeneous	0.162	2.5	(Silva, d'Ávila, & Mori, 2012)
Air-water, Tellus oil	-	0.02-0.3	Homogeneous-Heterogeneous	0.174 - 0.63	2 - 3	(Van Baten & Krishna, 2001)
Air-water	perforated plate	0.02	Homogeneous	0.15	0.9	(Bhole, Joshi, & Ramkrishna, 2008)
Air-water	perforated plate	0.02-0.12	Heterogeneous	0.14 - 0.44	0.96 - 1.76	(Chen, Sanyal, & Duduković, 2005)

Air-water	perforated plate	0.02-0.12	Homogeneous-Heterogeneous	0.19	1.045 - 0.95	(Jayanta Sanyal, Vásquez, Roy, & Dudukovic, 1999)
Air-water	-	0.02-0.1	Homogeneous-Heterogeneous	0.145	4.3	(J Sanyal, Marchisio, Fox, & Dhanasekharan, 2005)
Air-water	a porous plate multiple-orifice nozzle	0.005-0.096	Homogeneous-Heterogeneous	0.1	1.35	(Olmos, Gentric, Vial, Wild, & Midoux, 2001)
Air-water	a porous plate multiple, orifice nozzle, single orifce	0.005-0.1	Homogeneous-Heterogeneous	0.1	1.35	(Olmos, Gentric, & Midoux, 2003)
Air–Therminol, Water	perforated plate	0.08-0.3	Heterogeneous	0.162 - 0.44	-	(Chen, Duduković, et al., 2005)
Air–Therminol, Water	perforated plate	0.08-0.1	Heterogeneous	0.162-0.44	-	(Chen, Sanyal, & Dudukovic, 2004)
Air-water	perforated plate	0.1	Heterogeneous	0.44	2.43	(Laborde-Boutet, Larachi, Dromard, Delsart, & Schweich, 2009)
Air-water	perforated plate sparger	0.095	Heterogeneous	0.138	1.38	(N. Yang, Wu, Chen, Wang, & Li, 2011)
Air-water	Double and single sparger	0.01-0.03	Homogeneous	1	2	(Ranade & Tayalia, 2001)
Air-water, alcohol, CMC	Multipoint spargers single point sparger	0.01-0.324	Homogeneous-Heterogeneous	0.138 - 0.6	1.37 - 4.5	(Dhotre, Ekambara, & Joshi, 2004)
water, organic kerosene	Multi point spargers	0.02	Heterogeneous	0.15	1	(Tabib & Schwarz, 2011)
Air-water	Ring Sparger perforated plate	0.0015-0.02	Homogeneous	0.288	2.6	(Pfleger & Becker, 2001)
Helium-Pb–17Li	Multi point spargers	-	Heterogeneous	0.15	0.45-0.75	(Ni, Li, Jiang, Wang, & Wu, 2014)
Air-water, glycerol solution	perforated plate	0.02-0.3	Heterogeneous	0.19	2.5	(Xing, Wang, & Wang, 2013)
Air-water	porous plate	0.01-0.06	Heterogeneous	0.078	4.6	(Sattar, Naser, & Brooks, 2013)

Table 2.2: Summary of the system properties of several studies from the literature reviewed for rectangular BCRs

System	Sparger	V_g(m/s)	Regime	BCR dimensions(m)	Ref.
Air-water	8 holes of 0.8 mm	0.00133 - 0.00238	Homogeneous	0.20×0.05×1.2	(Gupta & Roy, 2013)
Air-water	-	0.0014 - 0.0073	Homogeneous-Heterogeneous	0.2×0.05×1.2	(Selma, Bannari, & Proulx, 2010)
Air-water	perforated plate	0.0049	Homogeneous	0.15×0.15×(0.45 or 0.90)	(D. Zhang, Deen, & Kuipers, 2006)
Air-water	Distributor plate (49 holes of 1 mm)	0.0049	Homogeneous	0.15×0.15×0.45	(Dhotre, Niceno, & Smith, 2008)
Air-water	perforated plate	0.0049	Homogeneous	0.15×0.15×0.45	(Deen, Solberg, & Hjertager, 2001)
Air-water	perforated plate	0.0049	Homogeneous	0.15×0.15×0.45	(Ničeno, Boucker, & Smith, 2008)
Air-water	Multiple orifice nozzel	0.0024 - 0.0213	Homogeneous Heterogeneous	0.2×0.04×0.45	(Díaz et al., 2008)
Air-water	Multiple orifice nozzel	0.0014- 0.0073	Homogeneous	0.2×0.05×1.2	(Bannari, Kerdouss, Selma, Bannari, & Proulx, 2008)
Air-water	Multiple orifice nozzel	0.005-0.085	Homogeneous Heterogeneous	0.2×0.04×1.2	(Simonnet, Gentric, Olmos, & Midoux, 2008)
Air-water	Multiple orifice nozzel	-	Homogeneous	0.2×0.05×0.45	(Pfleger et al., 1999)
Air-water %0.25BuOH in water	Multiple orifice nozzle- Sintered disc	0.0016- 0.0083	Homogeneous	0.2×1.2×0.05	(Buwa & Ranade, 2002)

2.2.2 Operational and design parameters

The flow patterns and gas dynamics in a BCR are dependent on its operational and design parameters (i.e., BCR dimensions and sparger types, size, velocity and arrangement) (Chen, 2004; Chen, Duduković, et al., 2005; Chen, Sanyal, et al., 2005; Kantarci et al., 2005; Krishna & Van Baten, 2001; Krishna, Van Baten, & Urseanu,

2000; A. A. Kulkarni, 2008; A. A. Kulkarni, Ekambara, & Joshi, 2007; A. A. Kulkarni & Joshi, 2005; Laborde-Boutet et al., 2009; Pfleger & Becker, 2001; Pfleger et al., 1999; Pourtousi et al., 2014; Pourtousi, Sahu, et al., 2015; Tabib et al., 2008; D. Zhang, 2007). The variation in fluid motion enhances the mixing time, heat and mass transfer and this improves the performance of the BCR. The production of small and uniform bubbles with similar size, shape and velocity is required to enhance the gas and liquid interfacial area. Small bubbles produce flatter and uniform gas hold-up distribution and symmetric liquid velocity profile, resulting in higher heat and mass transfer rates. The occurrence of bubble coalescence towards the sparger region usually results in non-uniformity in size and shape of bubbles. In this case, large bubbles are more likely produced, resulting non-uniform gas hold-up distribution, in particular, near the sparger region. This undesirable process usually occurs, when the superficial gas velocity is high (V_G>0.04 m/s) or the spargers are improperly mounted at the bottom of the column.

Several studies have reported that sparger design parameters (i.e., sparger types, dimension, velocity and position) have significant effects on the BCR hydrodynamics parameters (Dhotre & Joshi, 2007; George, Shollenberger, & Torczynski, 2000; G. Li et al., 2009; Ma et al., 2012; Vial, Laine, Poncin, Midoux, & Wild, 2001). Alterations to these parameters change the distribution of the dispersed gas (gas hold-up), bubble size, bubble shape and the distribution of liquid velocity (or profile) (Dhotre & Joshi, 2007; G. Li et al., 2009). Various types of spargers have been commonly used in prior studies which can be classified into two categories: plate and pipe type spargers. Under the category of plate type spargers, sieve plate (perforated) sparger (A. V. Kulkarni, Roy, & Joshi, 2007) and porous plate (G. Li et al., 2009) sparger are usually used, while in pipe type spargers, single pipe (orifice/needle) (A. V. Kulkarni, Badgandi, & Joshi, 2009), spider (A. V. Kulkarni et al., 2009), wheel (A. V. Kulkarni & Joshi, 2011a, 2011b),

single ring (Pfleger & Becker, 2001; Pourtousi, Sahu, et al., 2015) and multiple ring spargers (A. V. Kulkarni et al., 2007) are used as shown in Figure 2.2. Note that, plate type spargers are used for small diameter BCRs and pipe type spargers are used for large diameter BCRs (A. V. Kulkarni et al., 2009).

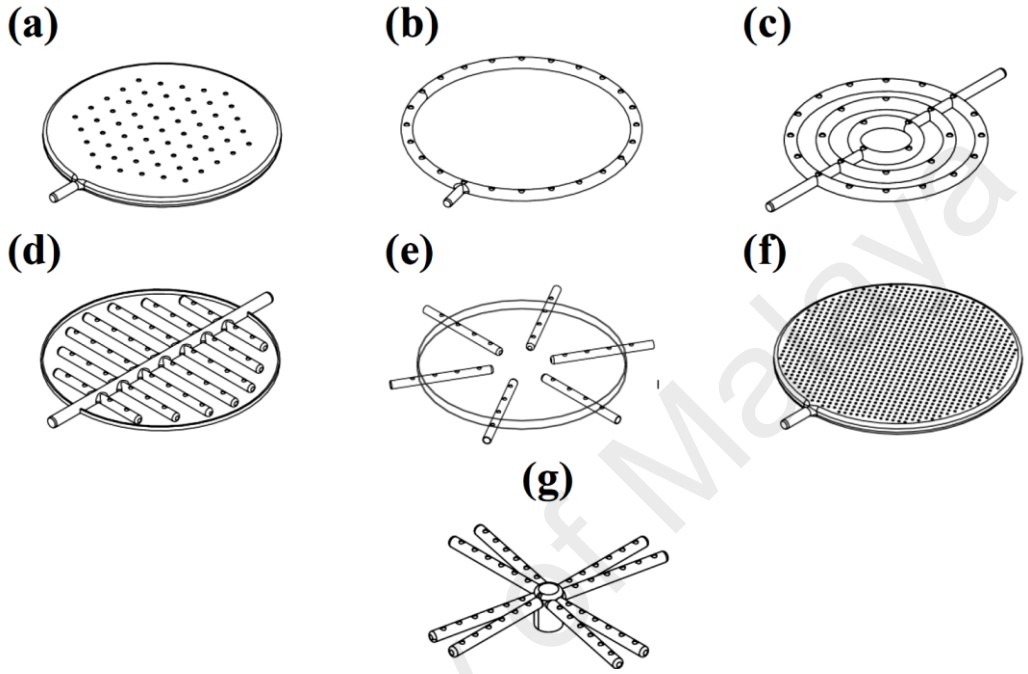

Figure 2.2:Different types of spargers: (a) sieve plate sparger (A. V. Kulkarni et al., 2007); (b) ring sparger (Pfleger & Becker, 2001; Pourtousi, Sahu, et al., 2015); (c) multiple ring sparger (A. V. Kulkarni et al., 2007); (d) spider (A. V. Kulkarni et al., 2007); (e) pipe (A. V. Kulkarni et al., 2007); (f) porous plate sparger (G. Li et al., 2009); (g) wheel (A. V. Kulkarni & Joshi, 2011b)

A. V. Kulkarni and Joshi (2011a) studied various sparger geometry parameters for different types of spargers, i.e., wheel, spider and multiple ring spargers. They reported that, the spider and multiple ring spargers provide non-uniformity in the BCR, while the wheel type is suitable for the range of operating parameters with lower manufacturing costs. Han and Al-Dahhan (2007) used three types of spargers (i.e., perforated plate having 163 holes with 0.50 mm diameter and open area of 0.156 %, perforated plate having 163 holes with 1.32 mm diameter and open area of 1.09 % and sparger with four holes and open area of 0.1 %) to study the effect of sparger types on

the mass transfer in a BCR. They reported that, the sparger has significant influence on the mass transfer for V_G<0.15 m/s, while it is vice versa for V_G>0.20 m/s. Under low superficial gas velocity, the perforated plate sparger provides higher mass transfer. When $V_G \geq 0.30$ m/s, the sparger types and sizes of sparger holes have insignificant influence on the mass transfer rate due to the high rate of bubble interaction (such as coalescence and break-up). Lau, Sim, and Mo (2009) used three types of spargers, i.e., single, perforated (sieve) plate and porous plate, to study the effect of sparger design parameters on the BCR hydrodynamics. A single sparger is not appropriate due to the production of large bubbles and the occupation of dead zone for a majority of the bed sections. It was found that was no significant difference between the perforated and porous plate spargers for a shallow BCR. Dhotre et al. (2004) studied the effect of using a single point and multipoint spargers on the distribution of the gas hold-up in the BCR of different heights. For multipoint spargers, the profile of the gas hold-up is relatively flat near the sparger region (at the bottom). In contrast, the single point sparger produces a steep profile of gas hold up adjacent to the sparger region but this profile becomes flatter with the increase of the vertical distance from the bottom. The sparger diameter and position has an effect on the bubble distribution and size in the BCR (Buwa & Ranade, 2002). Şal, Gül, and Özdemir (2013) investigated the effects of the orifice diameter of perforated plate spargers on gas holdup and regime transition in the BCR. Orifice diameter is found to have a significant effect on the total gas hold-up in the homogeneous flow regime but not in the heterogeneous regime. Bhole, Roy, and Joshi (2006) compared the gas distribution from a porous plate sparger and from a perforated plate sparger. The former is found to produce smaller bubbles, higher gas holdup and small liquid circulation in the column. Ma et al. (2012) numerically studied the influence of sparger diameter and velocity on the bubble size and occurrence of coalescence inside a rectangular BCR. They reported that, larger sparger size and

velocity result in the production of large and non-uniform bubbles. In addition, the coalescence process is more likely to occur near the sparger.

In industrial BCRs, instead of a single sparger, multi-point spargers, e.g., perforated plate, porous plate and ring spargers are usually used. Among all multipoint spargers, the ring type is preferred in the wastewater treatment, mining, biochemical and chemical industries due to its adjustable geometry, simple construction and low maintenance costs. In addition, for the academic applications, several investigations have used this type of spargers to study the effect of sparger parameters on the flow patterns and gas dynamics due to its simple structure. Haque, Nigam, and Joshi (1986) have experimentally investigated the effect of sparger design on mixing in shallow BCRs. They have measured the mixing time for single and double ring spargers. They reported a larger mixing time for the double-ring spargers than for the case of single-ring spargers. Ranade and Tayalia (2001) also studied the influence of single and double ring spargers on the BCR hydrodynamics. They showed that single-ring spargers create steeper gradients of gas volume fractions and therefore generate a much stronger liquid flow field. For the double-ring sparger, gas is distributed more uniformly and therefore leads to several local circulation cells rather than two large circulation cells. G. Li et al. (2009) studied the effect of the number of hole spargers and positions at the bottom of a cylindrical BCR on gas distribution, amount of gas, bubble size distribution, liquid flow pattern and mixing characteristics. They found that, the configuration of spargers have significant influence on the BCR hydrodynamics. The gas holdup increases with the increase of the number of the sparger holes. The position of the ring sparger, effects the liquid flow field, mixing and bubble size distribution. The asymmetrical position of spargers results in larger bubble size, non-uniform gas distribution and asymmetric axial liquid velocity. As a result of this non-uniformity in the hydrodynamics parameters, the overall amount of gas decreases, while the mixing time reduces.

In summary, the distribution of bubble size and shape, gas holdup and liquid flow patterns inside the BCR depend highly on the column geometry, operating conditions, gas and liquid properties and particularly on sparger design parameters, i.e., types, position and diameter.

2.3 CFD methods

To date, mathematical and numerical approaches have been used for predicting BCR hydrodynamics for the design and scaling-up BCRs (Kantarci et al., 2005; Ma et al., 2012; Pfleger & Becker, 2001; Pourtousi et al., 2014; Pourtousi, Sahu, et al., 2015; Tabib et al., 2008). In recent years, Computational Fluid Dynamics (CFD) has been found to be very useful in simulating multiphase flows in BCRs especially due to the significant advancements in numerical techniques and computing power. In some cases, CFD has the advantage of being more economically feasible than the truth scale of experimental methods. CFD also improves our knowledge on the complex hydrodynamic processes in BCRs. Figure 2.3 shows the CFD simulation of the bubble swarm in a square BCR.

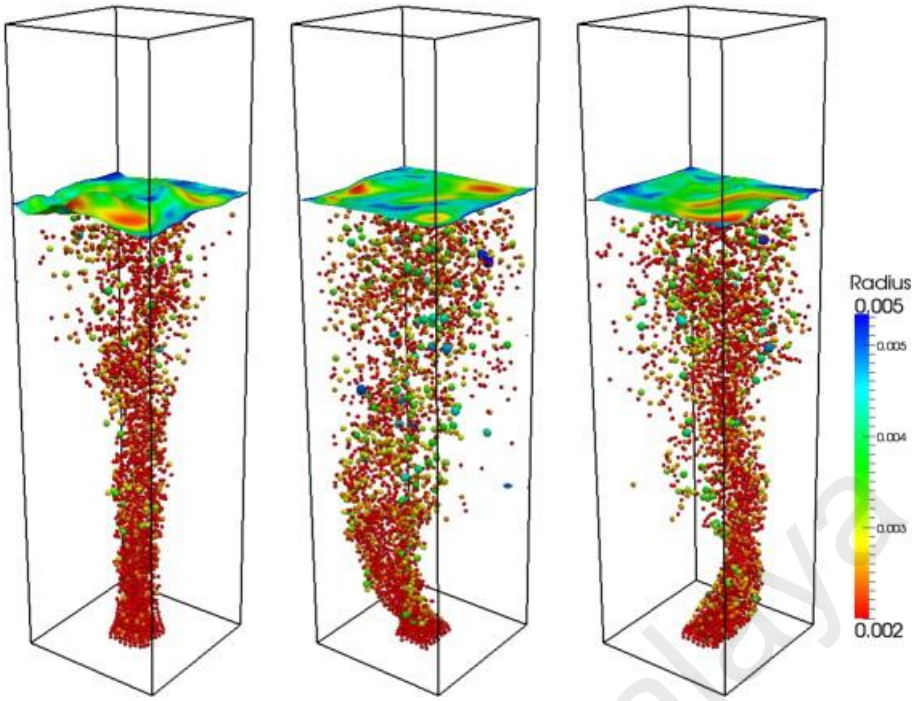

Figure 2.3: Snapshot of column showing the bubble swarm and evolution of gas–liquid interface at different time instants for the square BCR (Jain, Kuipers, & Deen, 2014)

2.3.1 Volume of fluid (VOF)

In the context of the present study, the Volume of Fluid (VOF) method is adopted for modeling a single bubble formation and rise (see Figure 2.4 and Figure 2.5) and to investigate the interaction between bubbles in the process of bubble merging (coalescence) and bubble break-up into smaller bubbles (Buwa et al., 2007; Hasan & Zakaria, 2011; Ma et al., 2012; Pourtousi, Ganesan, Kazemzadeh, Sandaran, & Sahu, 2015; Zahedi et al., 2014). VOF has been used to investigate the dynamics of single bubbles in BCRs filled with a quiescent liquid (Albadawi, Donoghue, Robinson, Murray, & Delauré, 2013; Hasan & Zakaria, 2011; Krishna & Van Baten, 1999; Rabha & Buwa, 2010; X. Wang et al., 2010; Zahedi et al., 2014). For example, X. Wang et al. (2010) used the VOF method to study the dynamics of a single bubble in ionic liquids. They reported the influence of various ionic liquids (i.e., $bmimBF_4$, $bmimPF_6$ and $omimBF_4$) on bubble deformation, velocity and diameter, when the bubbles form and

rise in the column. The results of the velocity and pressure fields around the bubbles were consistent with that of their experimental study. Chakraborty et al. (2009) examined and validated the effect of different gravity and buoyancy forces on bubble volume, formation frequency, bubble detachment rate and diameter for various gas flow rates, i.e., 0.167×10^{-6} – 3.33×10^{-6} m^3/s, using VOF. In another study, Zahedi et al. (2014) used this method with their experimental observation to study the effect of orifice diameter, surface tension (0.364-0.1456 N/m), liquid density (998.2-3000 kg/m^3) and viscosity (1.003×10^{-3}- 5×10^{-2} kg/m.s) on bubble size, shape and detachment and bubble collapsing at free surface. They again reported a good agreement in results between VOF method and their experimental investigations. Albadawi et al. (2013) demonstrated the capability of VOF to predict the bubble center of gravity, aspect ratio, and contact angle for various flow rates (i.e., 50, 100, 150, and 200 mlph) to investigate bubble formation at low capillary and Bond numbers.

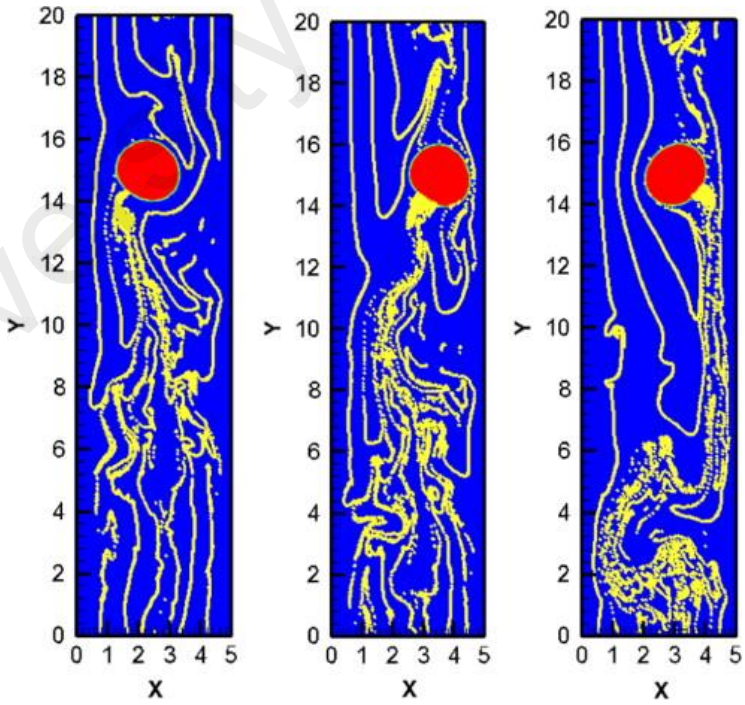

Figure 2.4: Snapshots of predicted shape of large bubbles and trajectories of small bubbles for Ar=5.66, Eo=0.2, . FrB=0.146, αb=24.5 % (Hua, 2015)

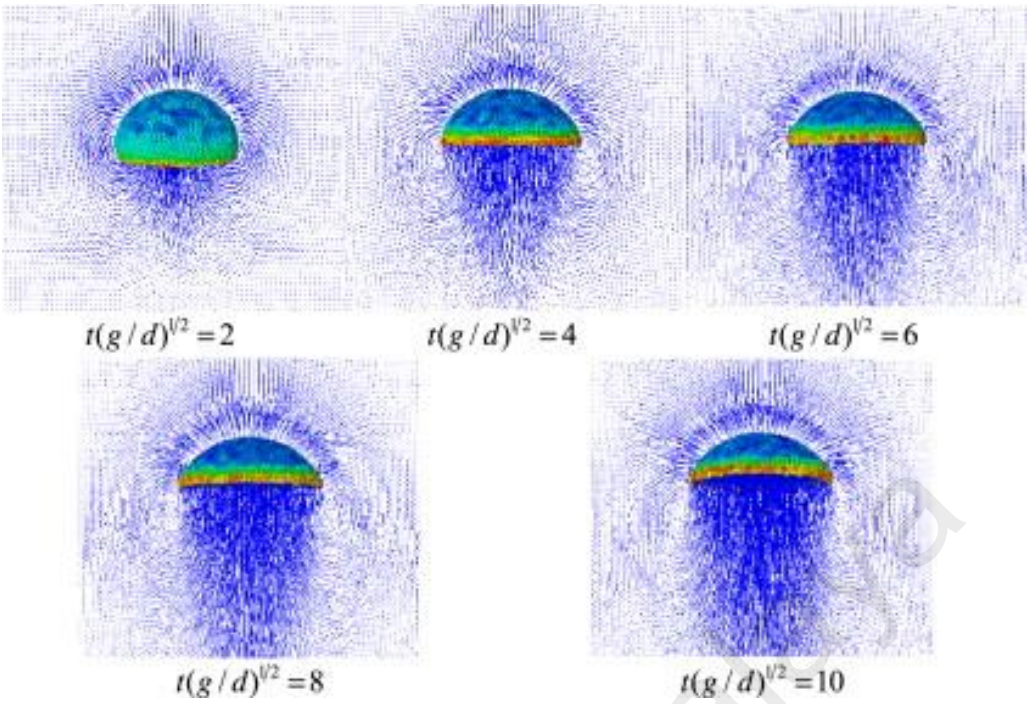

Figure 2.5: The velocity distribution around the bubble at different time instants (A. Zhang, Sun, & Ming, 2015)

Notwithstanding the above mentioned capability of VOF, coalescence (merging bubbles) or break-up (splitting into small bubbles) can also be predicted by VOF. For example, Hasan and Zakaria (2011) studied the coalescence of two co-axial bubbles in a cylindrical BCR for various Reynolds numbers (8.50-10), Bond numbers (4.25-50) and Morton numbers (0.0125–14.7). They reported that, the VOF method accurately predicts the bubble shape, size and coalescence time when two bubbles merge. The deformation of bubble after collision and coalescence is presented in that study.

In summary, the VOF method can predict bubble position, interface and size, when it forms from the tip of the orifice, rises inside the column and collapses at the BCR surface for various operational conditions. It can also predict bubble position, interface and size when the coalescence or break up occurs inside the BCR.

2.3.2 Eulerian-Eulerian method

Two main approaches have been recommended for the modeling of multiphase flows in BCRs ; they are Eulerian–Eulerian (Gupta & Roy, 2013; Krishna, Urseanu, Van Baten, & Ellenberger, 2000; Pfleger & Becker, 2001; Pfleger et al., 1999; Pourtousi et al., 2014; Tabib et al., 2008; D. Zhang et al., 2006) and the Eulerian–Lagrangian approaches (Buwa, Deo, & Ranade, 2006; Hu & Celik, 2008; Laın, Bröder, Sommerfeld, & Göz, 2002; X. Zhang & Ahmadi, 2005). The former approach is a popular and suitable option for an industrial BCR since the volume fraction of the dispersed phase is often not small and distributed by a sparger rather than a single nozzle. In addition, the former approach requires a relatively lesser computational effort than that for Eulerian-Lagrangian approach (Pourtousi, Sahu, et al., 2015). However, correct selections of interphase forces (e.g., drag, lift, turbulent dispersion and virtual mass) and its models and turbulence models (e.g., k–ε model, Reynolds Stress Model (RSM), Large Eddy Simulation (LES)) are required for an accurate flow prediction in the Eulerian-Eulerian model (Frank, Zwart, Krepper, Prasser, & Lucas, 2008; Gupta & Roy, 2013; Tabib et al., 2008). The interaction between the liquid and gas phase is determined by solving the momentum equation which includes interfacial forces i.e., drag, lift, turbulent dispersion, virtual mass and wall lubrication; either some or all of the interfacial forces are investigated in these references. However, the drag force is often considered as the predominant interfacial force in the E-E approach to predict flow patterns inside the BCR (Chen, Sanyal, et al., 2005; Gupta & Roy, 2013; Krishna & Van Baten, 2003; Laborde-Boutet et al., 2009; Olmos et al., 2003; Olmos et al., 2001; Pfleger & Becker, 2001; D. Zhang et al., 2006).

2.3.2.1 Drag force

In the gas-liquid BCR, the effect of the drag force on the flow pattern is significantly higher than added mass, lift and turbulent dispersion forces (Chen, 2004; Chen, Duduković, et al., 2005; Laborde-Boutet et al., 2009; Larachi, Desvigne, Donnat, & Schweich, 2006; Oey, Mudde, & Van den Akker, 2003; Pfleger & Becker, 2001; Pfleger et al., 1999). Laborde-Boutet et al. (2009) have reported that the drag force is a predominate interfacial force in a gas-liquid interaction compared to other forces. They found that the magnitude of drag force is 100 times larger than for other forces. The drag force determines the gas phase residence time and velocity of the bubbles and it has a great effect on the macroscopic flow patterns in BCRs (Ahmadi & Ma, 1990; Ishii & Zuber, 1979; Schiller & Naumann, 1935; Tomiyama, Tamai, Zun, & Hosokawa, 2002; D. Z. Zhang & Vanderheyden, 2002). Some numerical studies have used a constant drag coefficient model instead of using drag models when the bubble diameters, shapes and velocities are approximately the same in order to reduce the computational time (Monahan & Fox, 2007; Pfleger & Becker, 2001; Smith, 1998). D. Zhang et al. (2006) reported on the changes of the time-averaged vertical liquid velocity profiles, and gas hold-up with respect to the drag coefficient; the gas phase (bubble) velocity was found to decrease but the gas hold-up increased as the drag force increased. Pfleger and Becker (2001) used the constant drag coefficient of 0.44 for simulation of cylindrical BCR, when superficial gas velocity is 0.005 m/s. They found about 6 % (underestimation) near the walls and 1 % (overestimation) at the column centre for the gas hold-up result. Zhang et al. (2006) studied the effect of different constant drag coefficients (i.e., 0.98 and 1.52) on the accuracy of numerical results for rectangular BCR. In comparison to 1.52 drag coefficient, using 0.98, results in better prediction for gas and liquid velocity. For example, as a result of using the drag coefficients of 0.98 and 1.52 in the numerical method, both drag coefficients of 0.98

and 1.52 overestimates the liquid velocity about 5 % and 43 %, respectively at the column centre, while these values produce better results (about 1 % error) towards the wall region. Drag models such as 'Schiller-Naumann' (Schiller & Naumann, 1935), 'Ishii-Zuber' (Ishii & Zuber, 1979), 'Tomiyama' (Tomiyama et al., 2002), 'Zhang-Vanderhyden' (D. Z. Zhang & Vanderheyden, 2002), 'Grace et al.' (Grace, Wairegi, & Nguyen, 1976) and 'Ahmadi-Ma' (Ahmadi & Ma, 1990) have been extensively used to calculate the drag force in BCR cases (Chen, Duduković, et al., 2005; Gupta & Roy, 2013; Olmos et al., 2003; Olmos et al., 2001; D. Zhang et al., 2006). For small spherical bubbles (e.g., 2.5-4 mm), the 'Schiller-Naumann' model is found to be very suitable, while for larger bubble size, a model proposed by 'Ishii-Zuber' is suitable for various bubble shapes such as sphere, ellipse and cap shape (Ishii & Zuber, 1979; Miao, Lucas, Ren, Eckert, & Gerbeth, 2013; Xu, Yuan, Ni, & Chen, 2013).

Gupta and Roy (2013) investigated different drag models e.g., 'Schiller-Naumann', 'Ishii-Zuber', 'Tomiyama', and 'Zhang-Vanderhyden' to study a gas- liquid BCR with a superficial gas velocity (i.e., 0.00133 m/s). They have also included the population balance method (PBM) which considers bubble coalescence, break-up and different bubble sizes in two phase flows. No difference was found between the different drag models under the low superficial velocity. However, the 'Schiller-Naumann' model demonstrates slightly better results compared to the other drag models and this is expected due to the spherical or spherical-like bubble shapes in the multiphase flow. D. Zhang et al. (2006) used the 'Ishii-Zuber' and 'Tomiyama' correlations to predict the velocity profiles and gas hold-up distribution in a two square cross-sectioned BCR. In comparison to the 'Tomiyama' model, the 'Ishii-Zuber' model results are more accurate in a shorter BCR (H/D=3), but it is vice versa in a taller BCR (H/D=6).

Silva et al. (2012) used the 'Ishi-Zuber' and 'Zhang-Vanderheyden' models to study the gas liquid in a cylindrical BCR for 0.02 and 0.08 m/s superficial gas velocities. Both drag models are not able to accurately predict the local gas hold-up where the results are over-predicted or under-predicted in comparison to that of experimental data. For example, the 'Ishii-Zuber' overestimates the gas hold-up especially at the area adjacent to the column wall (33 %) while the 'Zhang-Vanderheyden' model underestimates it at about 36 %. The discrepancy found between the models prediction and experimental data in the center of the BCR is 15 % (overestimate) and 12 % (underestimate) for the 'Ishii-Zuber' and 'Zhang-Vanderheyden', respectively. However, in terms of computing the gas velocity, both models are able to produce accurate results when compared to experiments. Tabib et al. (2008) studied the sensitivity of drag models such as the 'Schiller-Naumann', Ishii-Zuber', 'Zhang-Vanderhyden', 'Grace et al.' and 'Ahmadi-Ma' to predict the gas liquid flow patterns in a cylindrical BCR. The results from the 'Ishi-Zuber', 'Zhang-Vanderhyden' and 'Ahmadi-Ma' models are closer to the experimental data especially for a superficial gas velocity of 0.012 m/s. The Zhang and Vanderheyden model is also suitable for predicting the flow pattern at a high superficial gas velocity of 0.096 m/s. For a higher superficial gas velocity, the use of drag law alone as the only interfacial force in some cases delivers inaccurate results (Bhole et al., 2008; Gupta & Roy, 2013; A. A. Kulkarni et al., 2007; Pourtousi et al., 2014). This is reported in Refs (Bhole et al., 2008; Frank et al., 2008; Gupta & Roy, 2013; A. A. Kulkarni, 2008) in which the drag force itself fails to predict accurate plume oscillations, particularly when the flow regime is heterogeneous (superficial gas velocity more than 0.04 m/s).

2.3.2.2 Lift force

In addition to the drag force, the lift force which is in a perpendicular direction and relative to the flow direction, has a significant effect on defining the flow patterns in BCRs. Bubbles traveling through a fluid in shearing motion will experience a lift force transverse to the direction of motion. The lift force takes into account the effect of the shearing motion on the movement of the gas phase (Drew & Lahey Jr, 1987; Žun, 1990). Some studies show that it is possible to neglect the lift force in modelling, in order to reduce the computational costs (Chen, Duduković, et al., 2005; Pfleger & Becker, 2001; Pourtousi et al., 2014). However, A. A. Kulkarni et al. (2007), Frank et al. (2008), Gupta and Roy (2013) and Bhole et al. (2008) have shown that modelling of the lift force for bubble movement in the BCR improves the flow field prediction by capturing the transient flow. Some lift models such as the 'Magnaudet-Legendre' (Magnaudet & Legendre, 1998), 'Tomiyama et al.' and 'Auton' (Auton, 1987) have been frequently used to estimate the lift force in BCR related problems (Bhole et al., 2008; Dhotre, Niceno, Smith, & Simiano, 2009; Gupta & Roy, 2013; A. A. Kulkarni, 2008; Silva et al., 2012; Tabib et al., 2008). In general, the lift model is defined as a function of the bubble Eötvös number and bubble Reynolds number. Ervin and Tryggvason (1997) and Tomiyama, Sou, Žun, Kanami, and Sakaguchi (1995) reported that if there is a substantial deformation of the bubble, the non-dimensional lift coefficient (C_L) is calculated as the function of the non-dimensional variable of Eötvös number and bubble Reynolds numbers (Bhole et al., 2008; Gupta & Roy, 2013; Silva et al., 2012; D. Zhang et al., 2006). Silva et al. (2012) and Bhole et al. (2008) used the 'Tomiyama et al.' model together with PBM to study the effect of the lift force on the flow patterns and gas hold-up for 0.02 m/s and 0.08 m/s superficial gas velocities. They reported that, using the lift model results in a uniform profile of gas hold-up. This is due

to the fact that the gas bubbles not only move towards the column centre but also near the wall region and make the gas hold-up profile flatter.

In some studies, a constant value was used for C_L, for instance, Lopez de Bertodano (M. A. L. de Bertodano, 1992), Takagi and Matsumoto (S. Takagi & Matsumoto, 1998) suggested C_L = 0.1 and Drew and Lahey Jr (1987) suggested C_L= 0.5. Dhotre et al. (2009) have recommended the use of the lift force coefficient of 0.1–0.5 for a homogeneous flow regime with 2.5 mm small spherical bubbles. Tabib et al. (2008) studied the effect of $C_L = 0, 0.06,$ and 0.2 on the flow pattern using different gas superficial velocities (0.012-0.096 m/s) in the BCR; at the low superficial gas velocity, no significant effect was found on the flow patterns but this is not the case at high superficial velocities.

D. Zhang et al. (2006) used Tomiyama's lift model and lift coefficient to simulate two types of rectangular BCRs i.e., a short column (H/D=3) and a tall column (H/D=6). The gas hold-up predicted by Tomiyama et al.'s lift model is found to be more accurate for the taller column especially when adjacent to the walls while for the short column, a constant value of $C_L = 0.5$ gives better results. Gupta and Roy (2013) studied various lift models (i.e., 'Auton', 'Tomiyama et al.' and 'Magnaudet-Legendre') and $C_L = 0.5$ for simulations of a rectangular BCR by incorporating PBM. The authors reported that the bubble plume oscillations and instantaneous bubble velocity can only be predicted by incorporating the lift force together with the drag force.

2.3.2.3 Turbulent dispersion force (TDF)

The turbulent dispersion force (TDF) is defined when the liquid velocity continuously and randomly fluctuates and acts on the gas volume fraction (Krepper, Beyer, Frank, Lucas, & Prasser, 2009). TDF takes into account the effect of the turbulent eddies in the liquid on the dispersed bubbles (Miao et al., 2013). Several

studies have emphasized on the importance of using the TDF model in the prediction of BCRs (G. Li et al., 2009; Lu, Qi, Zhang, Jin, & Zhang, 2009; Pourtousi et al., 2014; Pourtousi, Sahu, et al., 2015; Silva et al., 2012; Tabib et al., 2008). TDF model of Lopez de Bertodano (M. L. de Bertodano, 1991) has been frequently used in BCR cases (Miao et al., 2013; Silva et al., 2012). The use of the turbulent dispersion coefficient (C_{TD}) of 0.1–0.5 in the TDF model of Lopez de Bertodano has improved the observations of bubbly flow where the bubble diameters were of the order of a few millimetres (M. A. Lopez de Bertodano, 1998; Moraga, Larreteguy, Drew, & Lahey Jr, 2003). Tabib et al. (2008) used C_{TD} of 0, 0.2 and 0.5 to predict the flow patterns for different superficial velocities (i.e., 0.012 and 0.096 m/s) in the BCR. TDF model and its C_{TD} have an insignificant effect at a low superficial gas velocity (V_g =0.012 m/s). However, it is not the case for a higher V_g and the prediction of the gas hold-up improves by including C_{TD} (Sato & Sekoguchi, 1975; Tabib et al., 2008). Similarly, Pourtousi, Sahu, et al. (2015) examined the effect of a C_{TD} of 0.1-0.5 on the liquid velocity and gas hold-up results for 0.005 m/s superficial gas velocity; All C_{TD} values are reported to improve the prediction of the flow pattern and in particular, a C_{TD} of 0.3 estimates slightly better results of the axial liquid velocity and gas hold-up near the wall region. Silva et al. (2012) used a C_{TD} value of 0.1 and 0.2 to predict the flow patterns in the BCR for superficial gas velocities ranging 0.02-0.08 m/s. In that study, the PBM is incorporated to include various bubble sizes. They reported that these TCDs underestimate the gas velocity profile. In general, most commonly used C_{TD} s are 0.2 and 0.3 as these give better results in comparison to other values (Pourtousi et al., 2014; Pourtousi, Sahu, et al., 2015; Silva et al., 2012; Tabib et al., 2008).

2.3.2.4 Added mass force

The virtual mass can be defined as a work of bubbles which perform from the acceleration of the liquid surrounding the bubbles. The liquid acceleration is

automatically computed through the calculation of the virtual mass force (Dhotre et al., 2009). In general, numerical studies use a constant virtual mass coefficient (i.e., 0-0.5). The use of an appropriate mass coefficient in particular conditions may assist in obtaining a clearer vision of the flow patterns in the BCRs which matches the experimental data (Gupta & Roy, 2013) especially in the sparger region (Dhotre, Deen, Niceno, Khan, & Joshi, 2013). A recent study by Gupta and Roy (Gupta & Roy, 2013) shows that the combined use of the mass coefficient and the lift in the homogeneous flow regime slightly improves the gas hold up results especially near the wall and centre region. However, for particular conditions (e.g., a column diameter of greater than 0.15 m) contributing the mass coefficient into the numerical studies can be neglected to save computational costs (Deen et al., 2001; Díaz et al., 2008; Tabib et al., 2008; D. Zhang et al., 2006). Tabib et al. (2008) studied the effect of different virtual mass coefficients (i.e., 0 and 0.5) for various superficial gas velocities (0.012-0.096 m/s) in a cylindrical BCR. It was shown that there is no significant contribution of the virtual mass coefficient in axial liquid velocity and gas hold-up results. A study by D. Zhang et al. (2006) shows the contribution of the mass coefficient into the simulation of the homogeneous regime in short (H/D=3) and tall (H/D=6) BCRs. They reported that the simulation results are insusceptible to the mass coefficient for various BCR dimensions.

In summary, 'Schiller-Naumann' proposed the best drag model for the homogeneous flow regime with small spherical bubbles (2.5 mm). However, in this regime, the constant drag coefficient can also predict the flow patterns and gas hold-up with less computational time. For higher superficial gas velocities (<0.096 m/s) the 'Zhang- Vanderheyden' model is more suitable, especially for various bubble sizes ranging from 6 to 9 mm. When larger bubble sizes are created in the column, the 'Ishii-Zuber' model delivers results that are more accurate. This model is unsusceptible to the bubble shapes and has been verified for various shapes such as sphere, ellipse and cap

shape. The model especially predicts a more accurate velocity profile and gas hold-up in shorter BCRs (H/D = 3).

The Lift models improve the accuracy in the prediction of the axial liquid velocity, turbulent kinetic energy and radial gas hold-up when the superficial gas velocity is about 0,096 m/s. The 'Tomiyama et al.' lift model is often used to investigate the flow in the BCRs due to its flexibility in different operational conditions.

Various turbulent dispersion coefficients (i.e., 0.1-0.5) have improved the flow pattern and gas hold-up inside the BCR where the bubble diameters were of the order of few millimeters. However, several studies suggested the turbulent dispersion coefficients of 0.2 and 0.3.There is no significant contribution of virtual mass model for different BCR types, e.g., short and tall BCRs and column diameter of greater than 0.15 m. However, when PBM model is incorporated with the CFD method, there is a slight improvement near the wall and center region. Table 2.3 shows various interfacial force models which have been used in prior studies. Among all interfacial force, drag is a predominate force in Eulerian approach due to higher magnitude of this force (about 100 times) than other forces. In contrast, the turbulent dispersion force has been rarely incorporated into the numerical algorithm.

Table 2.3: Summary of the adopted t turbulence models and interfacial force models in the Eulerian-Eulerian model from the literature on BCRs

Turbulence models	Interfacial force models	Models	Ref.
k–ε	Drag	Euler- Euler	(Van Baten & Krishna, 2001)
k–ε	Drag	Euler- Euler	(Krishna & Van Baten, 2003)
k–ε, Laminar	Drag	Euler- Euler	(Pfleger et al., 1999)
k–ε	Drag	Euler- Euler, PBM	(Chen, Duduković, et al., 2005)

k–ε	Drag	Euler- Euler, PBM	(J Sanyal et al., 2005)
k–ε	Drag	Euler- Euler, PBM	(Olmos et al., 2001)
k–ε	Drag	Euler- Euler, PBM	(Olmos et al., 2003)
k–ε	Drag	Euler- Euler, PBM, ASM	(Chen, Sanyal, et al., 2005)
k–ε	Drag	Euler- Euler, PBM, ASM	(Chen et al., 2004)
RNG *k–ε*, standard *k-ε* and Realizable *k–ε*,	Drag	Euler- Euler, PBM	(Laborde-Boutet et al., 2009)
standard *k–ε*	Drag	Euler- Euler	(Pfleger & Becker, 2001)
k–ε	Drag, Lift	Euler- Euler, PBM	(Bhole et al., 2008)
LES	Drag, Lift, Turbulent Dispersion	Euler- Euler	(Tabib & Schwarz, 2011)
k–ε, RSM	Drag, Lift, Turbulent Dispersion	Euler- Euler	(Silva et al., 2012)
RNG *k–ε,* standard *k-ε,* Laminar and RSM	Drag, Lift, Virtual Mass	Euler- Euler, PBM	(Gupta & Roy, 2013)
standard *k-ε* model	Drag, Lift, Virtual Mass	Euler- Euler, PBM	(Selma et al., 2010)
k–ε and RSM	Drag, Lift, Virtual Mass	Euler- Euler	(D. Zhang et al., 2006)
standard *k–ε*, LES	Drag, Lift, Virtual Mass, Turbulent Dispersion	Euler- Euler	(Dhotre et al., 2008)
k–ε, LES	Drag, Lift, Virtual Mass	Euler- Euler	(Deen et al., 2001)
k–ε, LES	Drag, Lift, Virtual Mass	Euler- Euler	(Ničeno et al., 2008)
k–ε	Drag, Lift, Virtual Mass	Euler- Euler, MUSIG	(Díaz et al., 2008)
k–ε	Drag, Lift, Virtual Mass	Euler- Euler, PBM	(Bannari et al., 2008)
standard *k-ε*	-	Euler- Euler	(Ranade & Tayalia, 2001)
k–ε	Drag, Lift, Virtual Mass	Euler- Euler	(Dhotre et al., 2004)
k–ε	Drag, Lift, Virtual Mass	Euler- Euler, Euler-Lagrange	(Simonnet et al., 2008)
standard *k-ε*	Drag, Lift, Virtual Mass	Euler- Euler, PBM	(Buwa & Ranade, 2002)
k–ε	Drag, Virtual Mass	Euler- Euler, PBM	(Ni et al., 2014)
standard *k-ε*	Drag	Euler- Euler, PBM	(Sattar et al., 2013)

2.4 Turbulence models

Besides the interfacial forces, the turbulence model is one of the key factors to capture the hydrodynamic properties of the BCR. In this section, various turbulence models such as the standard *k–ε* model RSM and LES are studied.

2.4.1 k–ε

Over the past 20 years, the *k–ε* model has been intensively used to describe the flow pattern in BCRs. This model is inexpensive and adequately reliable due to its simplicity and low computational requirements (Pfleger & Becker, 2001; Pfleger et al., 1999; Pourtousi et al., 2014; Pourtousi, Sahu, et al., 2015; Tabib et al., 2008). In comparison with the modified *k–ε* model, the standard *k–ε* shows a finer agreement with the averaged experimental result. However, when there is a radial or axial distribution of a fluctuating liquid velocity and the same distribution of turbulent kinetic energy near the wall region, the modified *k–ε* model delivers more accurate results. Pfleger and Becker (2001) used the standard *k–ε* model to study the bubbly flow and compared the results with the experimentally measured data using the laser Doppler anemometry (LDA) and particle image velocimetry (PIV) methods. These experimental techniques are commonly used to measure liquid velocity profiles, bubble rise velocity, bubble plume oscillation frequency, bubble size and turbulence structure in the BCRs. The standard *k–ε* model can accurately predict the flow properties in the column, especially for the liquid velocity and the turbulent kinetic energy profiles. Gupta and Roy used various turbulence models namely Re-Normalisation Group (RNG) *k-ε*, simple *k-ε* and RSM. In general, there was not a substantial difference between the results of the different turbulence models especially at low superficial velocity. The (RNG) *k–ε* model beside the PBM significantly improves the results compared to other models. They suggested the RNG *k–ε* turbulence model with the ‘Schiller-Naumann’ drag model and

Constant lift coefficient (C_L) or 'Legendre-Magnaduet' lift model as the adequate model for modeling bubbly flows.

Silva et al. (2012) used the *k–ε* turbulence model for both low and high superficial gas velocities in a cylindrical BCR. The standard *k–ε* model has improved the results of gas hold-up and velocity profile in the fully developed region. In general, the standard *k–ε* model is the preferable model due to its simplicity over other turbulence models when the flow in the BCR is fully developed. For this regime the model can successfully predict the hydrodynamic properties of the flow e.g., gas hold up and velocity profile. Other *k–ε* models can also be used in a fully developed flow however, in heterogeneous regimes e.g., churn-turbulent flows only the RNG *k–ε* gives the premium results.

2.4.2 Large eddy simulation (LES)

In this model, in the governing equation of each phase, the large scale motions are segregated from the smallest motions e.g., the bubble motion in a turbulence flow by using a filtering operation. This model has been used in several investigations to predict the flow patterns inside BCRs (Dhotre et al., 2013; Dhotre et al., 2009; Tabib et al., 2008). In comparison with the *k–ε* models, the LES model predicts more accurately the gas hold-up, velocity and its fluctuations. This model has been developed for complex systems such as buoyancy driven flow operating at higher void fractions (Dhotre et al., 2013; Dhotre et al., 2009; Tabib et al., 2008).

Bove et al. used the LES model to investigate the flow in a BCR and reported that among different schemes that can be used to solve governing equations high order schemes e.g., the second order Flux-Corrected Transport (FCT) delivers more accurate results especially for tracking the interaction of gas and liquid. However, to obtain such results adequately fine grids and proper initial boundary conditions must be used. This

model is useful to study irregular motions of bubble plumes. In fact, in comparison with *k–ε* models, the LES model clearly captures the instable nature of a bubble plume. Additionally, among turbulence models, the LES model has a specific ability to capture transient bubble movements. This model has been used to study the instantaneous flow profiles and coherent structures. In general, two types of LES (sub-grid scale models) models have been used in BCR simulation, which are the 'Smagorinsky' model and the dynamic SGS model proposed by Germano.

Dhotre et al. (2009) used the 'Smagorinsky' and the dynamic procedure of Germano to study the gas-liquid flow in a square cross-sectioned BCR. The 'Smagorinsky' model and the dynamic model of Germano can produce a good solution for the axial liquid and gas velocity. Dhotre et al. (2013) reviewed the use of the LES method in predicting gas and liquid flow inside the BCR. They suggested that in the simulation of LES, the central difference scheme should be used for the discretization of advection terms and the high-order schemes (MUSCL, QUICK, or Second-Order) are adequate for scalar variables. It was recommended to undertake more investigations on the influence of the discretization method, boundary condition, wall models and numerical parameters to obtain minimum computational costs in the Large Eddy Simulation model.

2.4.3 Reynolds stress model (RSM)

Several studies used the RSM model to predict the flow pattern inside the BCR (Silva et al., 2012; Tabib et al., 2008). In comparison with the *k–ε* model, the RSM model can predict more accurately the swirling flow inside the BCR. This model can show all of the characteristics of BCRs where bubble induced turbulence and anisotropy of turbulence are significant. Tabib et al. (2008) compared various turbulence models such as the RSM, *k–ε* and LES model to study the flow pattern inside the cylindrical

BCR. In that study, the RSM model has a good performance to show anisotropic flows, involving swirls, acceleration, deceleration and buoyancy in the BCR. Furthermore, in comparison with the *k–ε* model, the RSM model can predict better, the average liquid flow field inside the column.

In summary, with RSM and LES simulations, there is very little gain in information related to hydrodynamics and clear observation of coherent structures and instantaneous flow profiles at the cost of higher computational resources. Hence, the k–ε model is commonly used over the RSM and LES models for simulating 3D industrial BCRs for getting average information at lower computational efforts. Table 2.3 shows various turbulence models which have been used in previous studies. The *k–ε* model is used predominantly for turbulence modeling due to its simplest algorithm and lower computational resources. In a few cases, the LES and RSM models have been incorporated in the Eulerian approach. In addition, some studies used PBM in their numerical method to evaluate various bubble sizes and shapes, as well as rate of bubble interaction.

2.5 Adaptive neuro-fuzzy inference system (ANFIS)

In addition to the CFD approach, recently soft computing methods have been used to predict the multiphase processes in industrial applications (i.e., chemical, biochemical, wastewater treatment) (Aminossadati, Kargar, & Ghasemi, 2012; Azwadi, Zeinali, Safdari, & Kazemi, 2013; Ben-Nakhi, Mahmoud, & Mahmoud, 2008; Mahmoud & Ben-Nakhi, 2007; Pashaie, Jafari, Baseri, & Farhadi, 2012). These methods provide smart tools to show nonlinear input-output mapping data and simultaneously solve a number of nonlinear and complex problems. Because these prediction methods are nonlinear computing tools, they are preferred over other prediction methods for solving complex problems. In comparison to the empirical

curve-fitted and numerical methods, these methods can estimate complicated problems containing incomplete sets of data with small computational time. There are several soft computing methods (e.g., Support Vector Regression (SVR), Artificial Neural Network (ANN), Adaptive Neuro Fuzzy Inference System (ANFIS)) that have been used in the prediction of multiphase flows inside chemical and biochemical reactors. For instance, Gandhi, Joshi, Jayaraman, and Kulkarni (2007) used the SVR method to develop a mathematical correlation for estimation of overall gas hold-up inside the BCR. This mathematical correlation was established as a function of gas and liquid properties (i.e., density, viscosity, molecular weight of gas and liquid surface tension) and BCR operation conditions (operating temperature, operating pressure, gas and liquid superficial velocity, sparger parameters and column dimension). The developed SVR model showed a prediction accuracy of 97 % with relative error of 12.11 %. In comparison to previous correlations, the SVR correlation showed significant enhancement in estimating the amount of gas. In another investigation, Gandhi and Joshi (2010) used the SVR method to study heat transfer coefficient inside the BCR for different operation conditions. It was found that, this prediction method provided an estimation accuracy of 98.56 % and an average absolute relative error of 7.05 %. In addition, their mathematical correlation (obtained from SVR method) improved the prediction of heat and mass transfer rate in comparison to existing empirical correlations.

Few studies used ANN method to predict the BCR hydrodynamics. For instance, Shaikh and Al-Dahhan (2003) used a combination of Dimensional Analysis and ANN modelling to develop a gas hold-up correlation. They investigated the effect of different dimensionless parameters such as Re, Fr, Eo and Mo on gas hold-up. It was found that, the obtained correlation had an average absolute relative error (AARE) of 15 % and a standard deviation of 14 %. The predicted results showed the significant improvement

in the estimation of gas hold-up. Lin, Chen, and Tsutsumi (2003) studied the long term behavior of BCR hydrodynamics using the ANN model for three column diameters (i.e., 200, 400 and 800 mm). They reported that, the ANN model has a high ability for the long-term prediction of BCR hydrodynamics, when experimental time series and gas velocity are used as training data in learning algorithm.

Recently, the adaptive neuro-fuzzy inference system (ANFIS) have been used in several chemical, biochemical and wastewater industrial applications. Table 2.4 shows the application of this method in different industries. The ANFIS is part the ANN family, which estimates different multiphase problems, particularly in chemical, biochemical wastewater treatment processes. This method can be considered as a hybrid intelligent system, which combines techniques of artificial neural networks (ANNs) and representation of fuzzy logic. The ANFIS method provides a transparent computing framework with reliable results for uncertain systems. In comparison with other soft computing methods, it accurately predicts the nonlinear correlations between the input and output data using a hybrid learning method. This method is preferred over other methods due to several advantages such as no required knowledge of internal system parameters (initial boundary conditions), compact solution for multi-variable problems and its numerical stability (Aminossadati et al., 2012; Azwadi et al., 2013; Ben-Nakhi et al., 2008; Mahmoud & Ben-Nakhi, 2007; Pashaie et al., 2012). Due to the combination of the advantages of the learning process in ANN and decision process and linguistic transparency of the fuzzy logic method, the ANFIS method is preferred over other soft computing methods. It contains a set of fuzzy if–then rules with proper membership functions to create input–output pairs with a high degree of accuracy (Sarkheyli, Zain, & Sharif, 2015). The ANFIS method solves the limitations of the ANN and fuzzy logic methods, providing especially a robust framework identification method when the

connection between input and output variables is not trivial (Vasileva-Stojanovska, Vasileva, Malinovski, & Trajkovik, 2015).

Shahbazi, Rezai, Chelgani, Koleini, and Noaparast (2013) used the ANFIS method to estimate the Sauter mean bubble size and surface area flux of the bubble in a flotation process. In their prediction procedures, the operational conditions of flotation, impeller peripheral speed, and superficial gas velocity and weight percent solids are used as inputs. They reported that this method can accurately predict output parameters without implementation of new experimental set-up. Erdirencelebi and Yalpir (2011) studied the hydrodynamics behavior of a up flow anaerobic sludge bed reactor (UASBR) system which generates nonlinear behavior between output and input variables using three different ANFIS models. They showed that, the ANFIS method can predict nonlinear functions between multiple inputs and outputs for a complex wastewater treatment process at different loading rates. To the best of the author's knowledge, among all soft computing methods, the adaptive neuro-fuzzy inference system (ANFIS) has not been used in the prediction of BCR hydrodynamic parameters using either experimental or CFD results. However, this method has been incorporated with CFD results to predict various multiphase processes (Aminossadati et al., 2012; Azwadi et al., 2013; Ben-Nakhi et al., 2008; Mahmoud & Ben-Nakhi, 2007; Pashaie et al., 2012).

In summary, soft computing methods particularly support vector machines and neural networks have been recently developed to predict the BCR hydrodynamics. These methods have shown a high ability to predict the physical process in a very short time. In comparison to other soft computing methods, the ANFIS method provides higher predictive accuracy in less computational time due to the combination of artificial neural networks (ANNs) and fuzzy logic methods. Although this method is a

capable algorithm to learn and predict the multiphase process in industries, it has not been used in predicting the multiphase flow inside BCRs.

Table 2.4: Use of the ANFIS method in different industrial applications

Num	Area of research	Ref
1	Pilot scale LSCFB system	(Razzak, 2012)
2	Hybrid microgeneration system	(L. Yang & Entchev, 2014)
3	Helicoidal double-pipe heat exchangers	(Mehrabi & Pesteei, 2011)
4	Developing circular duct flow	(Hasiloglu, Yilmaz, Comakli, & Ekmekci, 2004)
5	Refrigeration system	(Hosoz, Ertunc, & Bulgurcu, 2011)
6	Wind turbine	(Nikolić, Petković, Shamshirband, & Ćojbašić, 2015) (Al-Shammari et al., 2015)
7	Biodiesel reactor	(Wali, Al-Shamma'a, Hassan, & Cullen, 2012)
8	Wastewater treatment	(Mullai, Arulselvi, Ngo, & Sabarathinam, 2011) (Mingzhi, Ma, Jinquan, & Yan, 2009) (Waewsak, Nopharatana, & Chaiprasert, 2010)

2.6 Research Gap

Ring sparger

Previous studies have showed that, the BCR operation highly affects liquid flow patterns, gas hold-up, dynamics of gas bubbles and BCR regime. For example, several publications have widely studied the effect of gas and liquid properties, bubble column dimensions and gas flow rates on the BCR hydrodynamics, while there are fewer studies on the influence of sparger design, particularly ring sparger parameters on the BCR hydrodynamics. In addition, in the literature, mostly, the uniform inlet gas velocity has been considered as the sparger and there is a need to implement the exact location and truthful inlet condition of the sparger.

Single bubble formation and rising

From a microscopic viewpoint, the influence of distance between spargers, and number of spargers on the bubble coalescence and detachment time has not been completely studied.

ANFIS model development

There is a lack of studies about using soft computing methods (particularly ANFIS) in predicting macroscopic (e.g., gas hold-up and liquid flow pattern) and microscopic (bubble formation and rising) characteristics in BCRs. Furthermore, there is a need to develop soft computing methods (e.g., ANFIS) besides CFD simulations to predict BCR hydrodynamics, when the CFD study is necessary to implement for any small changes in operational conditions due to minimizing of the computational effort.

CHAPTER 3: CFD STUDY OF GAS FLOW FROM RING TYPE SPARGER

3.1 Introduction

In the design of ring type spargers, an appropriate selection of sparger design parameters (i.e., sparger arrangement, position and velocity as well as the number of sparger holes) results in higher gas hold-up, heat and mass transfer rate and generation of bubbles without coalescence towards the sparger region. As mentioned in Chap 2, the BCR with a low rate of coalescence produces a uniform bubble size, shape and velocity and gas distribution. For instance, as the sparger velocity (corresponding superficial gas velocity) or sparger diameter increases, the bubble collision, coalescence and break-up is more likely to occur in the BCR, resulting in a heterogeneous regime. The increment in sparger size and velocity also results in production of non-uniform shapes and various sizes of bubbles. In contrast, using a small sparger hole (orifice) results in the production of very small bubbles with almost identical size, shape and velocity, resulting in a uniform gas distribution as well as homogeneous flow regime. Note that, in comparison with the heterogeneous flow regime, the homogeneous one with the same operational conditions, contains a higher gas and liquid interfacial area and heat and mass transfer rate.

Notwithstanding all investigations about spargers, there are still many aspects on sparger position, velocity and dimension, as well as number of spargers that requires further studies. There is a need to study the influence of the ring sparger diameter, number of sparger holes and superficial gas velocity on the uniformity of gas, distribution of turbulent kinetic energy and liquid circulation. This chapter studies the effect of the diameters of the ring sparger, number of sparger holes and sparger velocity on the BCR hydrodynamics parameters using the Euler-Euler method. Sensitivity studies using different types of drag force models, different values of turbulent

dispersion coefficient and different bubble diameters are also carried out. Furthermore, the prior experimental and numerical results, as well as mathematical correlations in the literature are used for validation of the CFD study.

3.2 Methodology

3.2.1 Governing equations

The two-phase model based on the Eulerian–Eulerian approach is used to simulate dispersed gas-liquid flows in BCRs. In this approach each fluid (or phase) is treated as a continuum in the domain under consideration. The phases share this domain and interpenetrate as they move within it. The Eulerian modelling framework is based on the ensemble-averaged mass and momentum transport equations for each phase and it is described as follows:

Continuity equation:

$$\frac{\partial}{\partial t}(\rho_k \varepsilon_k) + \nabla(\rho_k \varepsilon_k u_k) = 0 \tag{1}$$

Momentum transfer equation:

$$\frac{\partial}{\partial t}(\rho_k \varepsilon_k u_k) + \nabla(\rho_k \varepsilon_k u_k u_k) = -\nabla(\varepsilon_k \tau_k) - \varepsilon_k \nabla p + \varepsilon_k \rho_k g + M_{I,K} \tag{2}$$

The terms on the right hand side of Eq. (2) represent the stress, the pressure gradient, the gravity and the ensemble-averaged momentum exchange between the phases due to the interface forces. The pressure is shared by both phases. The stress term of the phase *k* is described as follows:

$$\tau_K = -\mu_{eff,k}(\nabla u_k + (\nabla u_k)^T - \frac{2}{3} I(\nabla u_k) \tag{3}$$

where $\mu_{\text{eff},k}$ is the effective viscosity. The effective viscosity of the liquid phase is composed of three contributions: the molecular viscosity, the turbulent viscosity and an extra term due to the bubble induced turbulence as given below:

$$\mu_{eff,l} = \mu_L + \mu_{T,L} + \mu_{\mathrm{BI},L} \tag{4}$$

The model proposed by Sato and Sekoguchi (1975) was used to take account of the turbulence due to the movement of bubbles, which can be written as

$$\mu_{BI,L} = \rho_L C_{\mu,\mathrm{BI}} \varepsilon_G d_B \left| u_G - u_L \right| \tag{5}$$

with the model constant of $C_{\mu,\mathrm{BI}}$ is set to 0.6 as recommended in Sato and Sekoguchi (1975). The calculation of the effective gas viscosity is based on the effective liquid viscosity which is:

$$\mu_{eff,G} = \frac{\rho_G}{\rho_L} \mu_{eff,\mathrm{L}} \tag{6}$$

The total interfacial force acting between the two phases are based on the interphase drag force and turbulent dispersion force, which can be written as follows:

$$\boldsymbol{M}_{I,L} = \boldsymbol{M}_{I,\mathrm{G}} = \boldsymbol{M}_{\mathrm{D},L} + \boldsymbol{M}_{\mathrm{TD},L} \tag{7}$$

The effect of the drag force is significantly higher than that of the added mass, lift and turbulent dispersion effects when it comes to predicting the flow pattern inside BCRs (Chen, Duduković, et al., 2005; Chen, Sanyal, et al., 2005; Laborde-Boutet et al., 2009; Pourtousi et al., 2014). In addition, in the homogeneous regime, both the lift force and virtual mass have insignificant effect on the gas hold-up and liquid velocity distribution (Dhotre et al., 2013; Gerlach, Tomar, Biswas, & Durst, 2006; Krepper et al., 2009; Laborde-Boutet et al., 2009; Pfleger & Becker, 2001; Tabib et al., 2008; D. Zhang et al., 2006). Therefore, the lift force and virtual mass are neglected in the current study. The drag force resulted from the resistance on gas bubbles moving in the liquid. Viscous stress creates skin drag and the pressure distribution around the moving body creates form drag. The later becomes significant as the Reynolds number for the bubble becomes larger. The interphase momentum transfer between the gas and liquid due to the drag force is given by:

$$M_{D,L} = -\frac{3}{4} \epsilon_G \, \rho_L \, \frac{C_D}{d_B} |u_G - u_L| (u_G - u_L) \tag{8}$$

where C_D is the drag coefficient taking into account the characteristics of the flow around the bubble, and d_B is the bubble diameter. In the homogeneous regime, bubbles approximately have the same shapes (usually a spherical shape), size and terminal velocities in the BCR (Kazakis, Mouza, & Paras, 2008; Lemoine et al., 2008; Monahan, Vitankar, & Fox, 2005; Olmos et al., 2001; Ruzicka, Vecer, Orvalho, & Drahoš, 2008; Sathe, Joshi, & Evans, 2013; Thorat & Joshi, 2004). Therefore, a constant drag coefficient can be used instead of the drag models such as the 'Schiller-Naumann', 'Ishii-Zuber', etc. (Pourtousi et al., 2014). In the present numerical study a constant drag coefficient of 0.44 is used which is suggested in the other references (Dhotre & Smith, 2007; Pfleger & Becker, 2001; Smith, 1998). In addition, the sensitivity of the use of the 'Schiller-Naumann' (Schiller & Naumann, 1935), 'Ishii-Zuber' (Ishii & Zuber, 1979), 'Grace et al'. (Grace et al., 1976) drag models are investigated and C_D of the respective models is given in Table 3.1.

Table 3.1: Drag models used in the present numerical study

Author	Model
Schiller and Naumann	$C_D = \frac{24}{Re_B}\left(1+0.15Re_B^{0.687}\right),\ if\ Re_B < 1000$ $C_D = 0.44, if\ Re_B > 1000$
Grace et al.	$C_D = \frac{4}{3}\frac{gd_B}{V_T^{\,2}}\frac{\rho_L - \rho_G}{\rho_L}$
Ishii and Zuber	$C_D = \frac{2}{3}E_O^{\,0.5}$
Constant drag coefficient	$C_D = 0.44$

The turbulent dispersion force derived by M. Lopez de Bertodano, Lahey Jr, and Jones (1994) is used, which is

$$M_{TD,L} = -M_{TD,G} = -C_{TD}\rho_L K \nabla \in_L \tag{9}$$

where k and C_{TD} are the liquid turbulent kinetic energy per unit of mass and turbulent dispersion coefficient, respectively. The turbulent dispersion force is defined when the liquid velocity continuously and randomly fluctuates and acts on the gas volume fraction (Krepper et al., 2009). The turbulent dispersion force takes into account the effect of the turbulent eddies in the liquid on the dispersed bubbles (Miao et al., 2013). In the current simulations, values of 0.2 to 0.5 are used as the turbulent dispersion coefficients, as suggested in the literature (M. Lopez de Bertodano et al., 1994; Silva et al., 2012; Tabib et al., 2008).

3.2.2 Turbulence modelling

In addition to interfacial forces models, incorporating a turbulence model leads to better estimation of the bubble column hydrodynamics parameters. For the disperse

bubbly phase a zero equation turbulence model is used, while the standard k–ε model is applied for the continuous phase which have been recommended in prior studies. Among all turbulence models, the standard k–ε model is usually preferred to predict the liquid flow pattern and gas hold-up under low superficial gas velocity due to simplest algorithm and lower computational cost (Frank et al., 2008; Pfleger & Becker, 2001; Pourtousi, Ganesan, & Sahu, 2015; Silva et al., 2012; Tabib et al., 2008). In general, with RSM and LES simulations, there is very little gain in hydrodynamics information and clear observation of coherent structures and instantaneous flow profile at the cost of higher computational resources (Tabib et al., 2008). These two turbulence methods have better performance when the coalescence and break-up occur under higher superficial gas velocity. Hence, the k–ε model is commonly used over the RSM and LES models for simulating 3D industrial bubble column reactors for getting average information at lower computational efforts (Tabib et al., 2008). The turbulent eddy viscosity, the turbulent kinetic energy (k) and its energy dissipation rate (ε) are formulated as follows:

$$\mu_{T,L} = \rho_L C_\mu \frac{K^2}{\varepsilon} \tag{10}$$

$$\frac{\partial}{\partial t}(\rho_L \in_L K) + \nabla(\rho_L \in_L u_L K) = -\nabla(\in_L \frac{\mu_{eff,L}}{\sigma_K} \nabla_K) + \in_L (G - \rho_L \varepsilon) \tag{11}$$

$$\frac{\partial}{\partial t}(\rho_L \in_L \varepsilon) + \nabla(\rho_L \in_L u_L \varepsilon) = -\nabla(\in_L \frac{\mu_{eff,L}}{\sigma_\varepsilon} \nabla_\varepsilon) + \in_L \frac{\varepsilon}{K}(C_{\varepsilon 1} G - C_{\varepsilon 2} \rho_L \varepsilon) \tag{12}$$

The model constants are C_μ = 0.09; σ_k = 1.00; σ_ε = 1.00; $C_{\varepsilon 1}$ = 1.44, $C_{\varepsilon 2}$ = 1.92. The term G in the above equation is the production of turbulent kinetic energy and described by:

$$G = \tau_L : \nabla u_L \tag{13}$$

3.2.3 Geometrical structure and Simulation cases

A three-dimensional (3D) domain of a BCR as that referred to in Pfleger and Becker (2001) with a height and diameter of 2.6 m and 0.288 m, respectively is used. Air bubbles are sparged throughout the ring sparger with a 0.07 mm sparger hole diameter in the quiescent water. A total of 31 simulation cases are carried out and the details are given in Table 3.2. Note that, the selection of these parameters is based on industrial applications and prior studies. A summary of the simulation cases are:

a. Mesh sensitivity and validation of CFD method

Cases 1-3 show the simulation cases for sensitivity study of various number of elements (i.e., Grid 1=40500, Grid 2=59000 and Grid 3=82320) for mesh independency. In these cases, bubble diameter, C_{TD} and C_D are 4 mm, 0.3 and 4, respectively. For benchmarking, Case 1 containing 40500 number of elements, which is same as that used in Pfleger and Becker (2001), is compared with prior experimental and numerical results and mathematical correlations. However, the inlet boundary condition for the sparger in the present study is not the same as that used in Pfleger and Becker (2001). In this study, for simulation of ring sparger, the exact position of each sparger holes are simulated with source terms as an inlet boundary condition, while the study of Pfleger and Becker used the uniform inlet boundary condition at the bottom of BCR. The present modeling of inlet BCR is much closer to the experimental condition of Pfleger and Becker. Note that, for comparison, the superficial gas velocity and BCR dimensions for both present CFD and numerical study of Pfleger and Becker are similar with experimental study of Pfleger and Becker.

b. Sensitivity of drag laws

The sensitivity study of various drag laws (i.e., 'Schiller-Naumann', 'Ishii-Zuber', 'Grace et al.') and constant drag coefficient of 0.44 on BCR hydrodynamics results are studied in Cases 4-7, where the ring sparger diameter, number of sparger holes and superficial gas velocity are 0.14 m, 20 and 0.005 m/s, respectively. In these cases, bubble diameter and C_{TD} are 4 mm and 0.3, respectively.

c. Sensitivity of bubble diameter

The sensitivity study of various bubble diameters (i.e., 4, 4.5, 5, 5.5 mm) on the flow pattern and gas hold-up results are studied in Cases 8-11, where the ring sparger diameter, number of sparger holes and superficial gas velocity are 0.14 m, 20 and 0.005 m/s, respectively. In these cases, C_{TD} and C_D are 0.3 and 4, respectively.

d. Sensitivity of Turbulent dispersion coefficient

The sensitivity study of various turbulent dispersion coefficients (ranging 0.2-0.5) on the flow pattern and gas hold-up results are studied in Cases 12-15, where the ring sparger diameter, number of sparger holes and superficial gas velocity are 0.14 m, 20 and 0.005 m/s, respectively. In these cases, bubble diameter and C_D are 4 mm and 4, respectively.

e. Effect of ring sparger diameter

Cases 16-18 represent the effect of various ring sparger diameters (i.e., 0.07, 0.14 and 0.20 m) on the flow pattern and gas hold-up, where the number of sparger holes and superficial gas velocity are 20 and 0.005 m/s, respectively. In these cases, bubble diameter, C_{TD} and C_D are 4 mm, 0.3 and 4, respectively.

f. Effect of superficial gas velocities

Cases 19-21 show the effect of various superficial gas velocities (i.e., 0.0025, 0.005 and 0.01 m/s) on the BCR hydrodynamics parameters, where the number of sparger holes and ring sparger diameter are 10 and 0.14 m, respectively. In these cases, bubble diameter, C_{TD} and C_D are 4 mm, 0.3 and 4, respectively.

g. Effect of number of sparger holes

Cases 22-25 show the effect of the number of sparger holes (i.e., 5, 10, 20 and 30) on the BCR hydrodynamics parameters. The BCR has the superficial gas velocity of 0.01 m/s with 0.14 m sparger diameter. In these cases, bubble diameter, C_{TD} and C_D are 4 mm, 0.3 and 4, respectively.

h. Further simulation cases for prediction

Cases 26-31 will be used in Chap 5 in the training and development of the ANFIS model for prediction of the influence of different ring sparger diameters on the BCR hydrodynamics. In these cases, bubble diameter, C_{TD} and C_D are 4 mm, 0.3 and 4, respectively.

Note that, Cases 4, 8, 12 and 17 are same as Case 1 in terms of operational conditions and CFD setting.

Table 3.2: Simulation cases

Cases	V_G (m/s)	N.S	S_d (mm)	Drag law	B_d (mm)	C_{TD}	Num elements	Remarks
1-3	0.005	20	140	CD=0.44	4	0.3	40500, 59000, 82320	Mesh independency study and validation of CFD method
4-7	0.005	20	140	CD=0.44 Grace et al. Ishii and Zuber Schiller Naumann	4	0.3	40500	Sensitivity study of drag laws on the BCR hydrodynamics
8-11	0.005	20	140	CD=0.4	4, 4.5, 5, 5.5	0.3	40500	Sensitivity study of bubble diameter on the BCR hydrodynamics
12-15	0.005	20	140	CD=0.4	4	0.3, 0.4, 0.5	40500	Sensitivity study of turbulent dispersion force on the BCR hydrodynamics
16-18	0.005	20	70, 140 and 200	CD=0.4	4	0.3	40500	Effect of ring sparger diameters on the BCR hydrodynamics at various column heights
19-21	0.0025, 0.005, 0.01	10	140	CD=0.4	4	0.3	40500	Effect of superficial gas velocity on the BCR hydrodynamics at various column heights
22-25	0.01	5, 10, 20, 30	140	CD=0.4	4	0.3	40500	Effect of number of sparger holes on the BCR hydrodynamics at various column heights
26-31	0.005	20	50, 90, 110, 130, 150, and 170	CD=0.4	4	0.3	40500	These cases will be used in Chap 5 for prediction process using ANFIS method

3.2.4 Boundary conditions and numerical methods

The gas velocity from each nozzle of the ring sparger is calculated based on a superficial gas velocity. The ring nozzles are not directly modelled but instead a mass source was applied at the exact location of the nozzle to reduce the total number of mesh elements (G. Li et al., 2009; Tabib et al., 2008). Hence, the 'mass sources' are used as the inlet condition at the bottom of the domain. The top surface of the BCR is treated as the 'degassing' boundary condition which permits only the dispersed air bubbles to escape but not the liquid phase (Díaz et al., 2008; G. Li et al., 2009; Silva et al., 2012; Simonnet et al., 2008). On the side walls, a no-slip boundary condition is used for the liquid phase and a free-slip condition for the gas phase (Díaz et al., 2008; Frank et al., 2008; Monahan et al., 2005; Rzehak & Krepper, 2013; H. Wang et al., 2014; Zarei, Hosseini, & Rahimi, 2013).

Simulations were carried out using the commercial CFD software package of the ANSYS-CFX 14.0. The conservation equations were discretized using the control volume technique. The equation system was solved using the SIMPLEC procedure. In comparison to SIMPLE, the SIMPLEC method requires low computational time (Van Doormaal & Raithby, 1984). This method has been preferred over SIMPLE method in prediction of BCR in several studies (Joshi, 2001; Krishna, Van Baten, et al., 2000; Jayanta Sanyal et al., 1999; Van Baten & Krishna, 2001). The high order differencing schemes of the total variation diminishing (TVD) is used, which is suggested for the Eulerian-Eulerian multiphase models to reduce numerical diffusion (Deen, Solberg, & Hjertager, 2000; Pfleger & Becker, 2001; Pfleger et al., 1999). Using this scheme results in accuracy of numerical solution for the simple and complicated fluid flow cases with existence of discontinuities in flow filed, particularly multiphase interaction due to robust calculation procedure. This scheme is usually implemented to improve the liquid flow pattern and gas hold-up results in prediction of bubble columns (Deen et al.,

2000; Pfleger & Becker, 2001; Pfleger et al., 1999; Pourtousi, Ganesan, & Sahu, 2015). The flow was simulated for a total of 1400 s and most of the results presented in the following section are time averaged over the last 1300 s. The time step of 0.1 s is used in the present simulation and the sensitivity of a much lower time step, i.e., 0.01 s is investigated, and no significant difference was found on the prediction of the flow pattern. The choice of the time step is also determined by the criterion that the maximum Courant–Friedrichs–Levy (CFL) number must be less than one. Several studies reported that when the CFL is smaller than 1, the numerical method can accurately predict the multiphase characteristics and further refining of the time step does not lead to remarkable changes on the flow pattern results, while using CFL above 1 results in inaccurate prediction finding (Dhotre et al., 2013; Dhotre et al., 2008; Pourtousi, Ganesan, & Sahu, 2015; Pourtousi, Zeinali, Ganesan, & Sahu, 2015).

3.2.5 Mesh sensitivity and validation of CFD method

A structured grid based on the hexahedral grid as shown in Figure 3.1 is used throughout the domain. The type of grid adopted herein is almost similar to that used in Laborde-Boutet et al. (2009). Several investigations used hexahedral meshes for their numerical studies to predict the liquid flow pattern and gas hold-up in multiphase reactors (Chen, Duduković, et al., 2005; Pfleger & Becker, 2001; Pourtousi, Ganesan, & Sahu, 2015; Pourtousi, Sahu, et al., 2015; Pourtousi, Zeinali, et al., 2015; Tabib et al., 2008). These types of meshes can accurately estimate the complicated geometry and resulting in fewer elements, lower computational cost and better numerical convergence for the flow cases having stress analysis, compared to tetrahedral or triangle meshes (Díaz et al., 2008; Pourtousi, Ganesan, & Sahu, 2015). For prediction of the bubble column hydrodynamics this type of mesh has been used, especially for the bubble column with circular cross section. The axial length of the domain is divided into 60 grid elements. The grid, namely, Grid 1, typically has about 40500 elements. On

average, the grid has an aspect ratio of 3.1, skewness of 0.62 and orthogonal quality of 0.67 and these values are within the acceptable range (Kerdouss, Bannari, & Proulx, 2006). In addition, two denser girds namely Grid 2 and 3, were created and has a total of 59000 and 82320 elements, respectively for a grid dependency study. The grid study was limited by the processing capability of the computer and for selection of number of grids, the mesh sensitivity study was implemented.

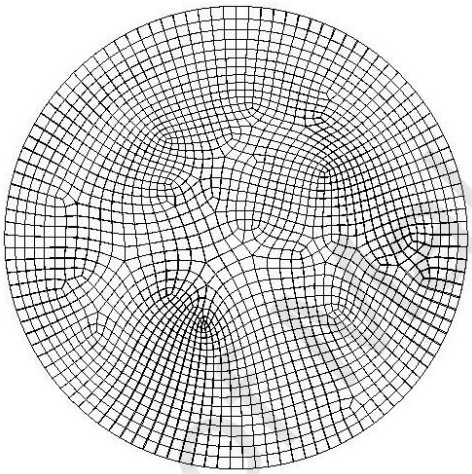

Figure 3.1: Grid intensity of the computational model consisting of 40500 structural elements

The CFD results based on the three types of grids are benchmarked against that from Pfleger and Becker (2001). Figure 3.2 and Figure 3.3 show the time averaged axial liquid velocity and gas hold-up respectively, versus the normalized radial coordinate for Grids 1, 2 and 3 at a column height of 1.6 m. Referring to Figure 3.2, in general, the liquid has an up-flow near the column centre and a down-flow near the column wall for all the Grids. The radial profile of the axial liquid velocity of Grid 1 is symmetric at the centre. However, this is not the case for Grids 2 and 3 where the peak velocity is skewed to the right and to the left, respectively, having asymmetric velocity profiles. Among the three grids, the distribution of the liquid velocity of Grid 1 is very close to the numerical results of Pfleger and Becker with slight differences near the column of the axis.

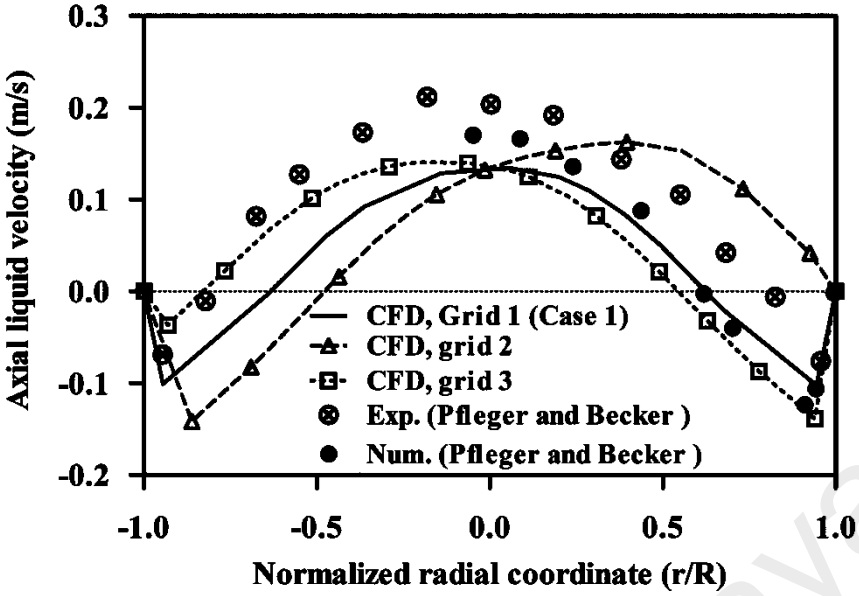

Figure 3.2: Comparison between the average of the axial liquid velocity from CFD (Grids 1,2 and 3) and that from the experimental and numerical studies of Pfleger and Becker at height 1.6 m

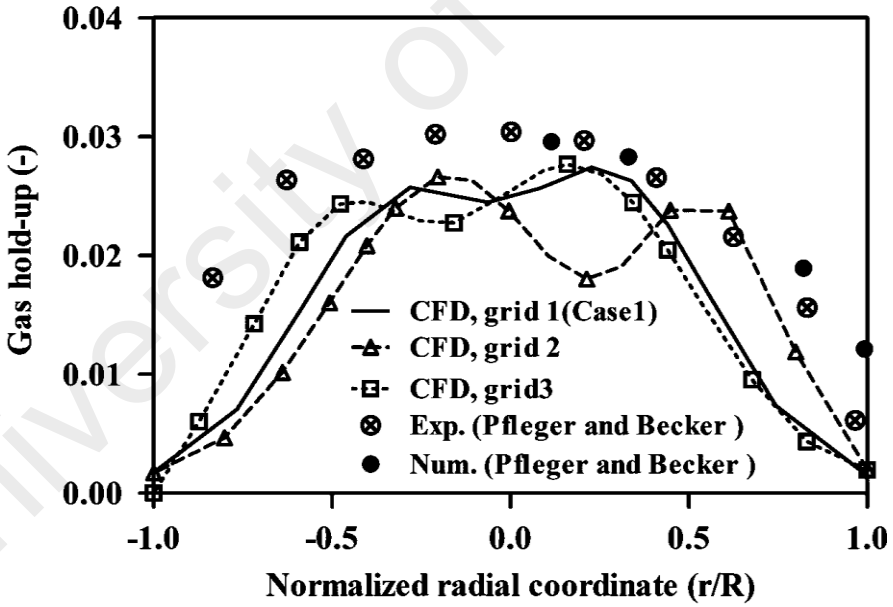

Figure 3.3: Comparison between the average of gas hold-up from CFD (Grids 1,2 and 3) and that from the experimental and numerical studies of Pfleger and Becker at height 1.6 m

Now refer to Figure 3.3, which shows the average gas hold-up at 1.6 m in height of Grids 1, 2 and 3. The profiles of the grids are quite non-uniform near the core of the flow (column centre). Clearly, profiles of two peaks can be seen, which is quite obvious

for Grid 2. The formation of the two peaks is suspected to be due to the effect of a ring sparger, which is spatially modelled using the inlet source term. For a similar case setup, such a result from the numerical investigations of Pfleger and Becker has a symmetric profile and of a slightly higher value. However, it should be noted that in Pfleger and Becker, a simplified model of the gas inlet boundary conditions is used and this has been identified to be one of the reasons for an over prediction of the gas hold-up. Therefore, a direct comparison may not possible and instead the planar average gas hold-ups at various column heights and the overall amount of gas were studied and presented in Figures 3.4 and 3.5 which include the numerical and experimental results from Pfleger and Becker and prior studies. The CFD results using Grids 1 and 3, on overall, from the bottom to the top of the column have a much closer prediction to Pfleger and Becker's experimental results in comparison to Pfleger and Becker's numerical results. The maximum difference of the CFD results is less than 15 % everywhere in the column. In particular, the current CFD results are in good agreement with the experimental data of Pfleger and Becker towards the sparger region as compared to their numerical study which over predicts the gas hold-up. Grid 1, which is less dense than Grids 2 and 3, has been selected for various investigations in the current study based on the reasonable predictions of the axial liquid velocity and gas hold-up in the column, as presented above.

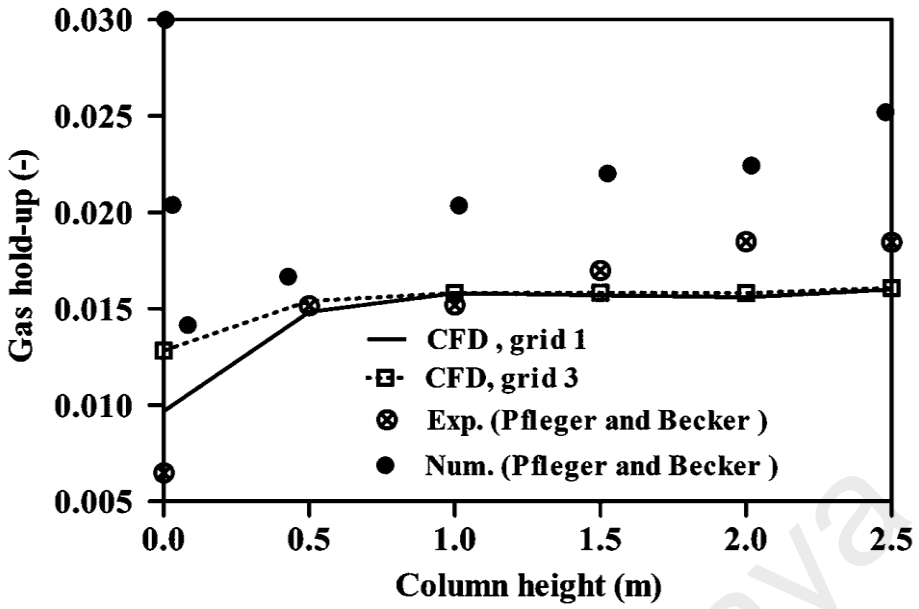

Figure 3.4: Comparison of the averaged planer gas hold-up obtained from the present CFD results (Grids 1 and 3) with the experimental and numerical data from Pfleger and Becker at various heights

For further validation a comparison is made with the previous experimental and numerical data (i.e., Pfleger and Becker (2001) and Elena Díaz, Montes, and Galán (2009)) and existing mathematical correlations (i.e., Joshi and Sharma (1979), Kumar, Degaleesan, Laddha, and Hoelscher (1976) and Hughmark (1967)) for an overall gas hold-up inside the BCR. Figure 3.5 shows the overall gas hold-up, versus the superficial gas velocities for the present CFD simulation (Case 1, Grid 1) and prior studies. The overall gas hold-up inside the BCR linearly rises when the superficial gas velocity increases. The figure shows that the present CFD results is in satisfactory agreement with the experimental and numerical studies of Pfleger and Becker (especially the experimental finding) and Diaz et al., and the mathematical correlations (i.e., Joshi and Sharma and Hughmark) for the overall amount of gas, when the superficial gas velocity varies from 0.0015 m/s to 0.01 m/s. However, the numerical study of Pfleger and Becker over predicts the gas hold-up for almost all of the superficial gas velocities. In the present study, as the superficial gas velocity is less than 0.01 m/s (homogeneous

flow regime) and the size of BCR is large (2.6 m height and 0.288 m diameter), the production of overall gas hold-up is less than 3 % in the BCR.

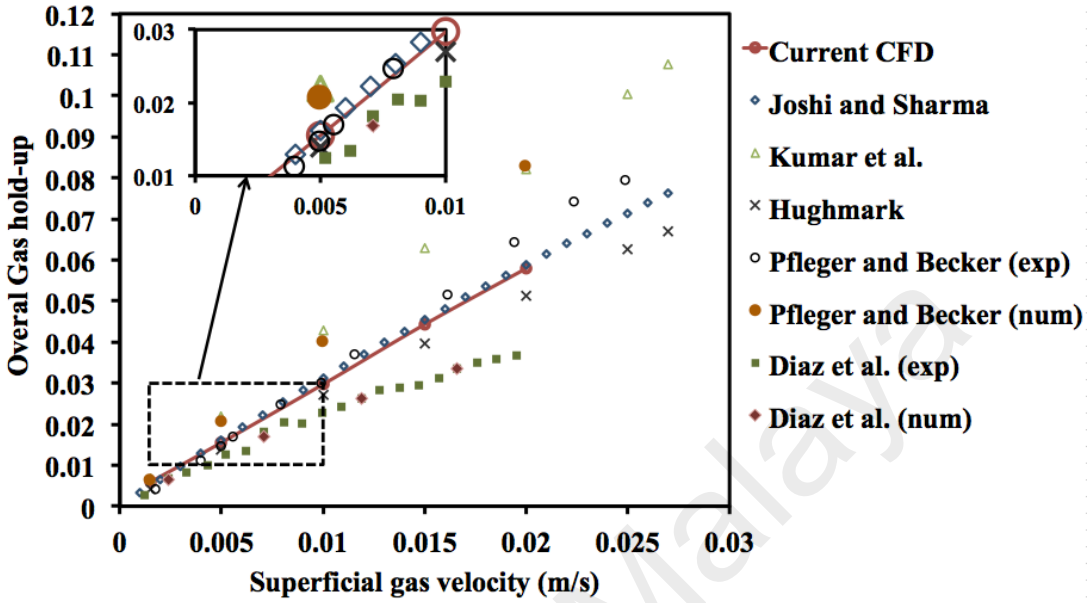

Figure 3.5: Comparison of the overall gas hold-up inside the BCR obtained from the present CFD results with existing experimental, numerical and mathematical correlations

3.2.6 Limitations

To improve the error between present CFD study and experimental data of Pfleger and Becker, there are some limitations in the present study. First, the grid used is a compromise between the availability of computational resources and the numerical accuracy. Despite that, the type of grid in the simulations is almost similar to that reported in the literature (Laborde-Boutet et al., 2009). The sensitivity study of using a much denser grid requires further investigations. However, it should be noted that it is not always the case that a denser grid increases the accuracy of a numerical prediction in a BCR as discussed in Buwa et al. (2002), Pfleger and Becker (2001) and Diaz et al. (2008) in which the use of a coarser grid have resulted in more accurate results. They reported that, as the grid size decreases, the agreement between the numerical results of the time averaged flow pattern and experimental finding deteriorates. Furthermore,

Bech (2005) showed that the transient turbulence models produce new modes of instability in the plume oscillation when the grid size decreases. This instability affects the results of the BCR hydrodynamics and requires a longer computational time to produce the mean velocity and gas hold-up results. Secondly, the use of the k–ε turbulent model is based on an isotropic assumption whereby the turbulent kinetic energy (k) formulation is constructed with a limitation that all of the normal components of the stresses are equal to each other. This may lead to an inaccuracy in the prediction of the kinetic energy. Note that various studies in the literature on BCR are based on the k–ε turbulent model due to its simple algorithm and shorter computational time. This was the main benchmark for selecting this model for the current study. In addition, as far as this study is concerned, the focus herein is to demonstrate the possible hydrodynamic differences that resulted from the use of different sizes of the ring diameters, superficial gas velocities and number of sparger holes and not to present an absolute value of any of the parameters. The present justification is that similar results as that from this study will be repeated by adopting either a denser grid or different turbulence models. Incorporation of the PBM in the Eulerian method and using the LES method as a turbulence model in CFD modelling of BCR results in better prediction of liquid and gas flow pattern and gas hold-up at different BCR heights, particularly near the sparger region ($h<0.8$ m) and bulk region ($0.8\ \text{m}<h<1.6$ m). However, using PBM and LES model requires very high computational efforts.

3.3 Results and discussion

3.3.1 Sensitivity study of drag laws

In this section, the sensitivity of the use of different types of drag laws in the predictions of axial liquid velocity and gas hold-up in the BCR have been investigated. Simulations

were carried out using the same settings as Case 1, CFD model except for drag forces. The radial distribution of the time-averaged axial liquid velocity and the gas hold-up at column height 1.6 m is shown in Figures 3.6 and 3.7, respectively, based on the drag models of 'Grace et al', 'Ishii-Zuber' and 'Schiller-Naumann'. Such results from the constant drag coefficient (CD=0.44) and that from experimental and numerical investigations of Pfleger and Becker are included in the figures for a comparison. Referring to Figure 3.6, all of the axial liquid velocity profiles from the drag models are similar to that of the constant drag coefficient (CD=0.44) and the differences between them are marginal. Near the central region of the column, the 'Grace et al.' and 'Ishii-Zuber' models have a slightly better prediction than the constant drag coefficient (CD=0.44) when compared to Pfleger and Becker's numerical data. Referring to Figure 3.7, both the 'Grace et al' and 'Ishii-Zuber' models over predict the average gas hold-up everywhere in the column in comparison to that of the constant drag coefficient (CD=0.44). In addition, these models also over predict this value at the central region of the column in comparison to the Pfleger and Becker's results. However, there is no significant difference in the gas hold-up between the 'Schiller-Naumann' model and constant drag coefficient (CD=0.44). Figure 3.8 shows the planar averaged gas hold-up at various column heights. The 'Schiller-Naumann' and constant drag coefficient (CD=0.44) results are almost identical. However, the 'Grace et al' and 'Ishii-Zuber' drag models over predict the gas hold-up at all heights in comparison with the constant drag coefficient (CD=0.44) and Pfleger and Becker's experimental results. In general, the Grace et al. and Ishii-Zuber models are appropriate for the BCR containing different shape of bubbles (i.e., cap, spherical, semi-spherical and etc.) and larger bubble sizes, while the Schiller-Naumann model and constant drag coefficient indicate the BCR with small bubble sizes and uniform shapes (approximately spherical) (Pourtousi et al., 2014). Therefore, the Grace et al. and Ishii-Zuber models produce higher overall gas

hold-up for the BCR containing larger bubbles and different shapes, as compared to Schiller-Naumann model and constant drag coefficient. As reported by Tabib et al. (2008) and D. Zhang et al. (2006), when the BCR produces larger bubble sizes with different shapes and higher rate of coalescence (merging bubbles), the bubble drag force increases due to increasing the drag coefficient. As the bubble drag force increases the overall gas phase (bubble) velocity decreases and bubbles tend to remain longer time in the BCR. The existence of higher number of bubbles in the BCR results in increasing the residence time of gas phase, as well as the overall gas hold-up.

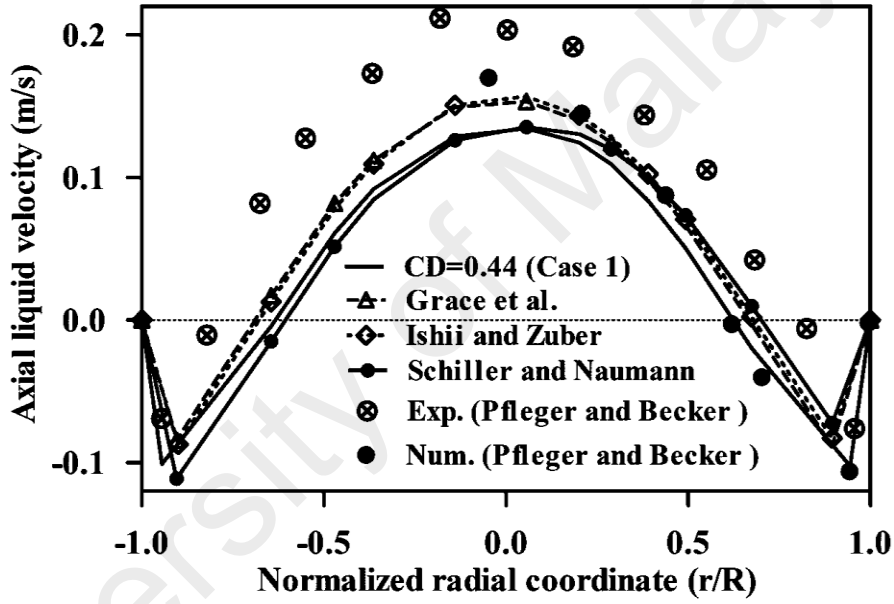

Figure 3.6: Comparison between the average of axial liquid velocity from the drag coefficient=0.44, 'Grace et al.', 'Ishii-Zuber' and 'Schiller-Naumann' and that from the experimental and numerical results of Pfleger and Becker at height 1.6 m

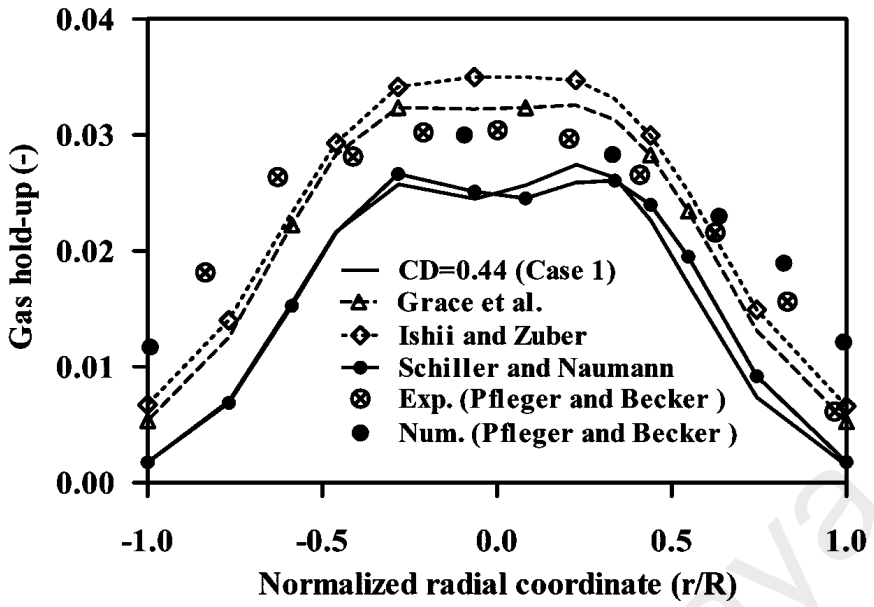

Figure 3.7: Comparison between the average of gas hold-up from the drag coefficient=0.44 , 'Grace et al.', 'Ishii-Zuber' and 'Schiller-Naumann' and that from the experimental and numerical results of Pfleger and Becker at height 1.6 m

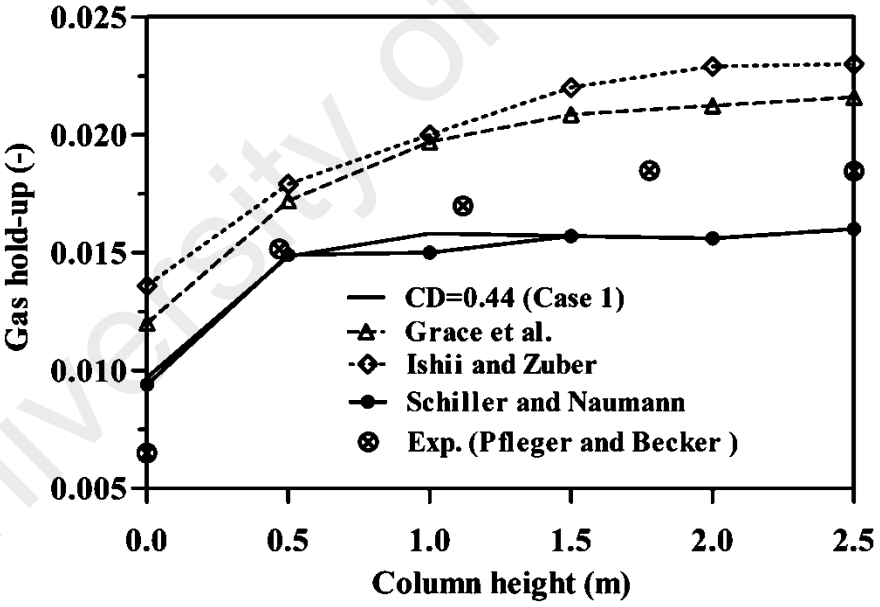

Figure 3.8: Local averaged gas hold-up for the drag coefficient=0.44, 'Grace et al.', 'Ishii-Zuber' and 'Schiller-Naumann' at various column heights

3.3.2 Sensitivity study of bubble diameters

The sensitivity of the use of different diameters of gas bubble in the predictions of axial liquid velocity and gas hold-up in the BCR have been investigated. Simulations were carried out using the same settings as that of Case 1 CFD model except for the size of the bubble diameter. The radial distribution of the time-averaged axial liquid velocity and the gas hold-up at a column height of 1.6 m is shown in Figures 3.9 and 3.10, respectively, based on bubble diameters ranging 4-5.5 mm. Figure 3.11 shows the planar averaged gas hold-up at various column heights. Such results from $d_{b=}$4 mm and that from the experimental investigation of Pfleger and Becker, both using a bubble diameter of 4 mm, are included in the figures for a comparison. The use of a bubble diameter of 4.5 mm, an increase about 0.5 mm from that of 4 mm bubble size, only results in small differences (about 4.5 %) in the radial direction of the axial liquid velocity (Figure 3.9), the gas hold-up (Figure 3.10) and the planar gas hold-up (Figure 3.11) in the column. However, this is not the case for the bubble diameter of 5 mm (or 5.5 mm) with an increase of 1 mm (or 1.5 mm) from that of 4 mm bubble size. The differences are significant. For example, the radial profile of the axial liquid is asymmetric with more positive velocity at the right side of the column. Consequently, the radial profile of the gas rises asymmetrically in the column (Figure 3.10) and has a two-peak profile. The amount of gas for the case of bubble diameters 5 and 5.5 mm at different heights of BCR is lesser than the smaller bubbles (i.e., 4 and 4.5 mm). For example, at a 2 m height, the planar average gas hold-up for the 4 and 5 mm bubbles are 0.0156 and 0.0138 respectively (see Figure 3.11). The existence of small bubble sizes inside the BCR results in a higher amount of gas and gas liquid interfacial area.

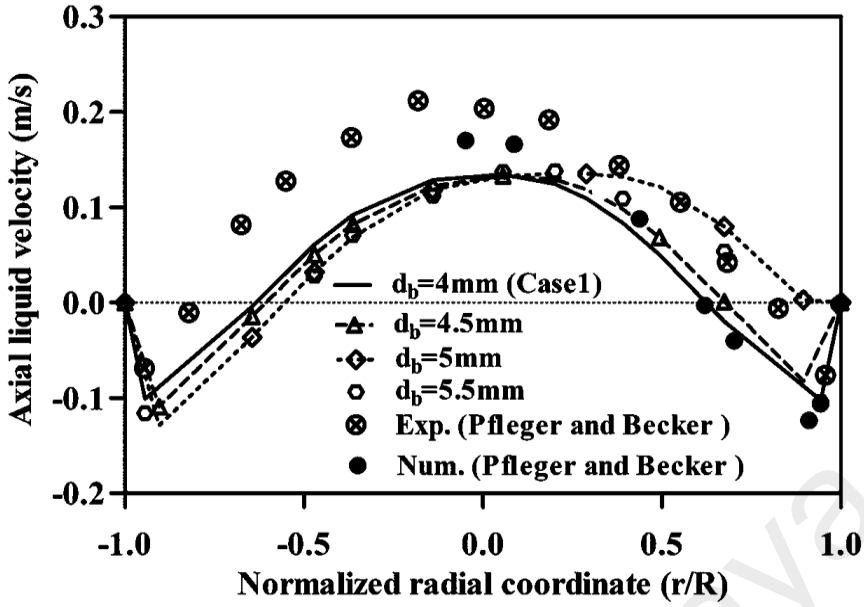

Figure 3.9: Comparison between the average of axial liquid velocity from various bubble diameter sizes and that from the experimental and numerical results of Pfleger and Becker at height 1.6 m

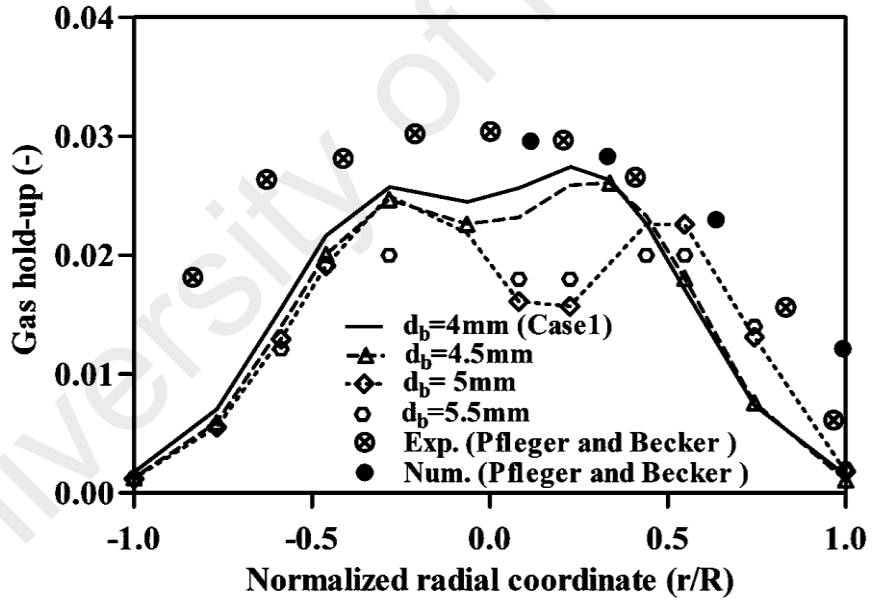

Figure 3.10: Comparison between the average of gas hold-up from various bubble diameter sizes and that from experimental and numerical results of Pfleger and Becker at height 1.6 m

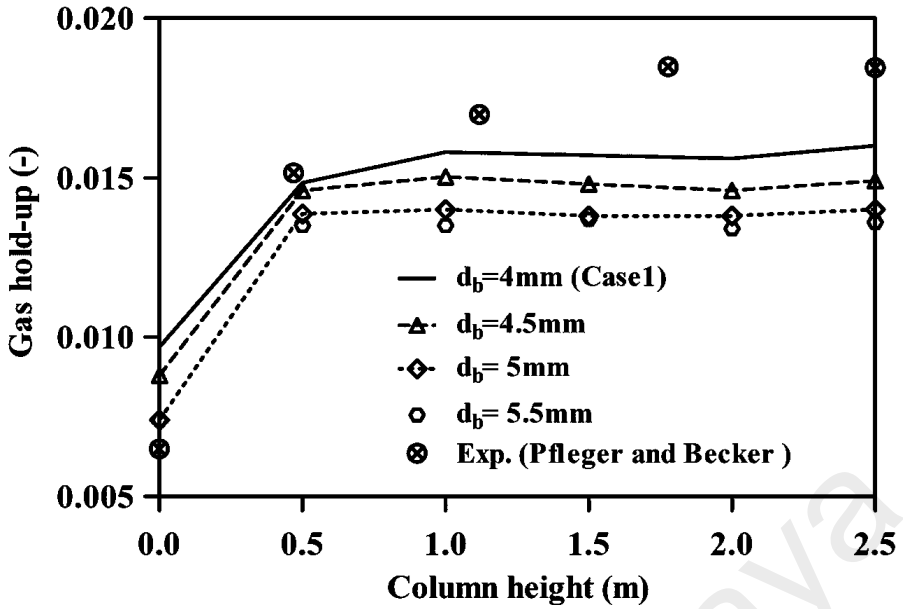

Figure 3.11: Local averaged gas hold-up for various bubble diameters at different column heights

3.3.3 Sensitivity study of turbulent dispersion force model (TDF)

In this section, the sensitivity of the coefficient value of the turbulent dispersion (C_{TD}) in range of 0.2 to 0.5 is investigated based on the results predicted. Figures 3.12 and 3.13 show the radial distribution of the time-averaged axial liquid velocity and the gas hold-up at a column height of 1.6 m for various turbulent dispersion coefficients (i.e., 0.2-0.5) with results from both the experimental and numerical investigations of Pfleger and Becker. According to the figures, the predicted results of the axial liquid velocity and gas hold-up for different values of C_{TD} are almost identical near the walls and central region, while the value of 0.3 results in a slightly better prediction for the axial liquid velocity and gas hold-up towards the wall and central regions (see Figure 3.12 and Figure 3.13). In general, the turbulent dispersion force indicates the local bubble concentration gradient (gas hold-up), random influence of turbulence eddies on the bubble motion and the effect of the interaction between fluctuating velocity and the fluctuating gas hold-up (A. A. Kulkarni, 2008; Silva et al., 2012; Tabib et al., 2008). As far as in the homogeneous flow regime, bubble column produces small and uniform

bubbles and smooth variation of the gas fraction over the column cross section with low rate of bubble interaction and turbulent eddies, using turbulent dispersion force model can only produce almost parabolic gas hold-up profile and different TDF models slightly change the results. For example, the turbulent dispersion coefficient of 0.3 slightly improves the results near the walls and column centre. This is due to the fact that, this value can better indicate effect of turbulence eddies on the liquid flow pattern and gas hold-up in homogeneous flow regime (VG<0.04 m/s), particularly at the wall and centre regions which is also consistent with prior investigations (Pourtousi, Ganesan, & Sahu, 2015; Pourtousi et al., 2014; Pourtousi, Sahu, et al., 2015; Silva et al., 2012; Tabib et al., 2008), while the value of 0.2 has been suggested for higher superficial gas velocity (VG>0.04 m/s). In general the sensitivity study of turbulent dispersion coefficients should be implemented for different operational conditions to match numerical results with experimental data. As far as in this study, the superficial gas velocity is not more than 0.01 m/s, all simulation cases are implemented with value of 0.3 based on sensitivity study, as well as previous recommendations (Pourtousi et al., 2014; Silva et al., 2012; Tabib et al., 2008).

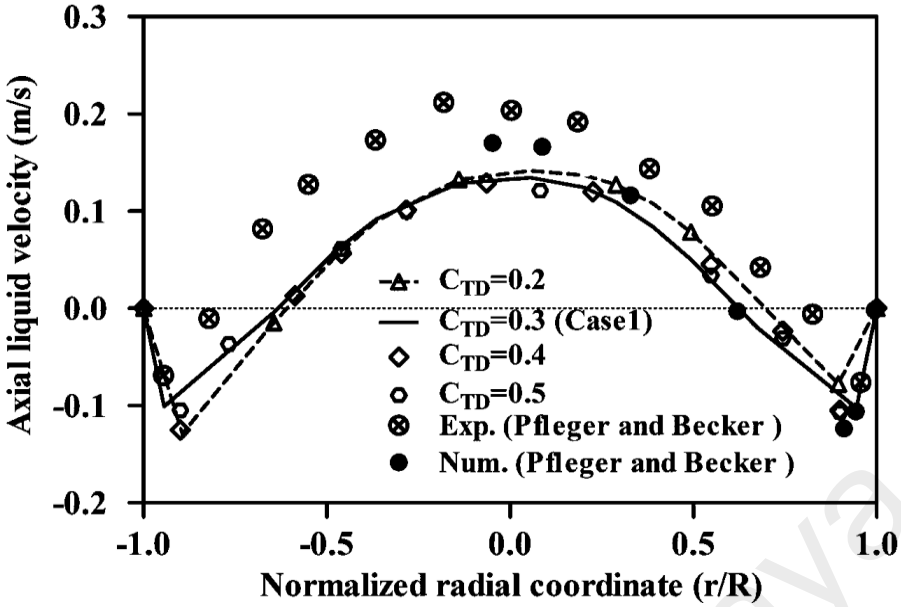

Figure 3.12: Comparison between the average of the axial liquid velocity from various turbulent dispersions and that from experimental and numerical results of Pfleger and Becker at height 1.6 m

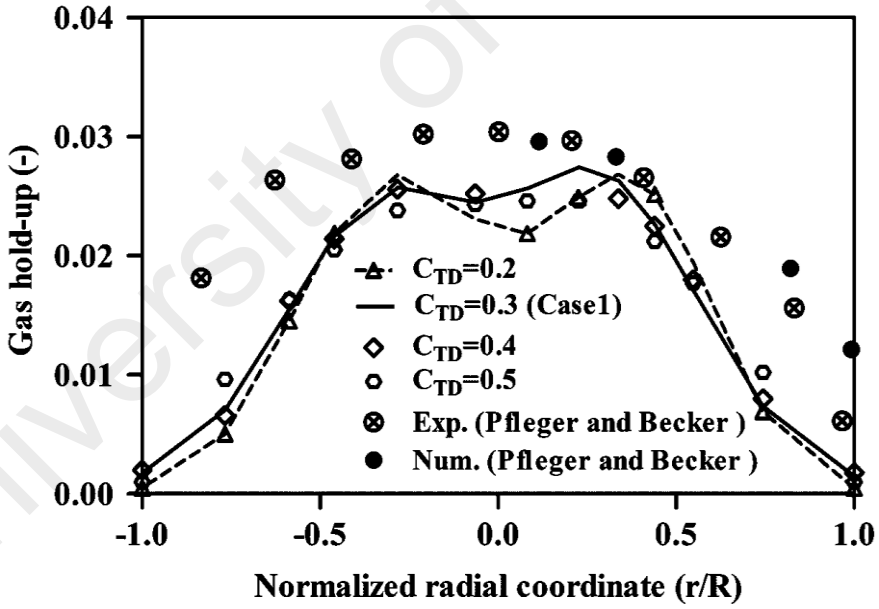

Figure 3.13: Comparison between the average of gas hold-up from various turbulent dispersions and that from the experimental and numerical results of Pfleger and Becker at height 1.6 m

3.3.4 Effect of ring sparger diameter

Figure 3.14 (a, b and c) shows the average profile of the axial liquid velocity as a function of the radial position in the column at axial heights of 1 m, 1.6 m and 2.4 m for various ring sparger diameters (i.e., 0.07, 0.14 and 0.2 m). The velocity profile of the benchmark case is the result of the use of the ring sparger with a diameter of 0.14 m. The maximum axial liquid velocity is about 0.13 m/s near the column centre. The velocity profile of the 0.07 m sparger diameter is steeper at the column centre in comparison to that of 0.14 m sparger diameter with the maximum axial liquid velocity of about 0.18 m/s, resulting in a high flow at this location. This is understandable due to the concentrated type of the ring sparger used in the 0.07 m sparger diameter which is located very close to the column axis. Unlike the 0.07 m and 0.14 m, the velocity profile of the 0.20 m sparger diameter has a downward flow at the column of the central region, whereas the upwards flow only occurs at a small circumferential region, i.e., near r/R= ±0.75. The downward flow have the downward peak axial velocity of about 0.1 m/s as a result of using a ring sparger with a diameter that is close to the column diameter. However, the use of this type of sparger increases the axial velocity near the wall.

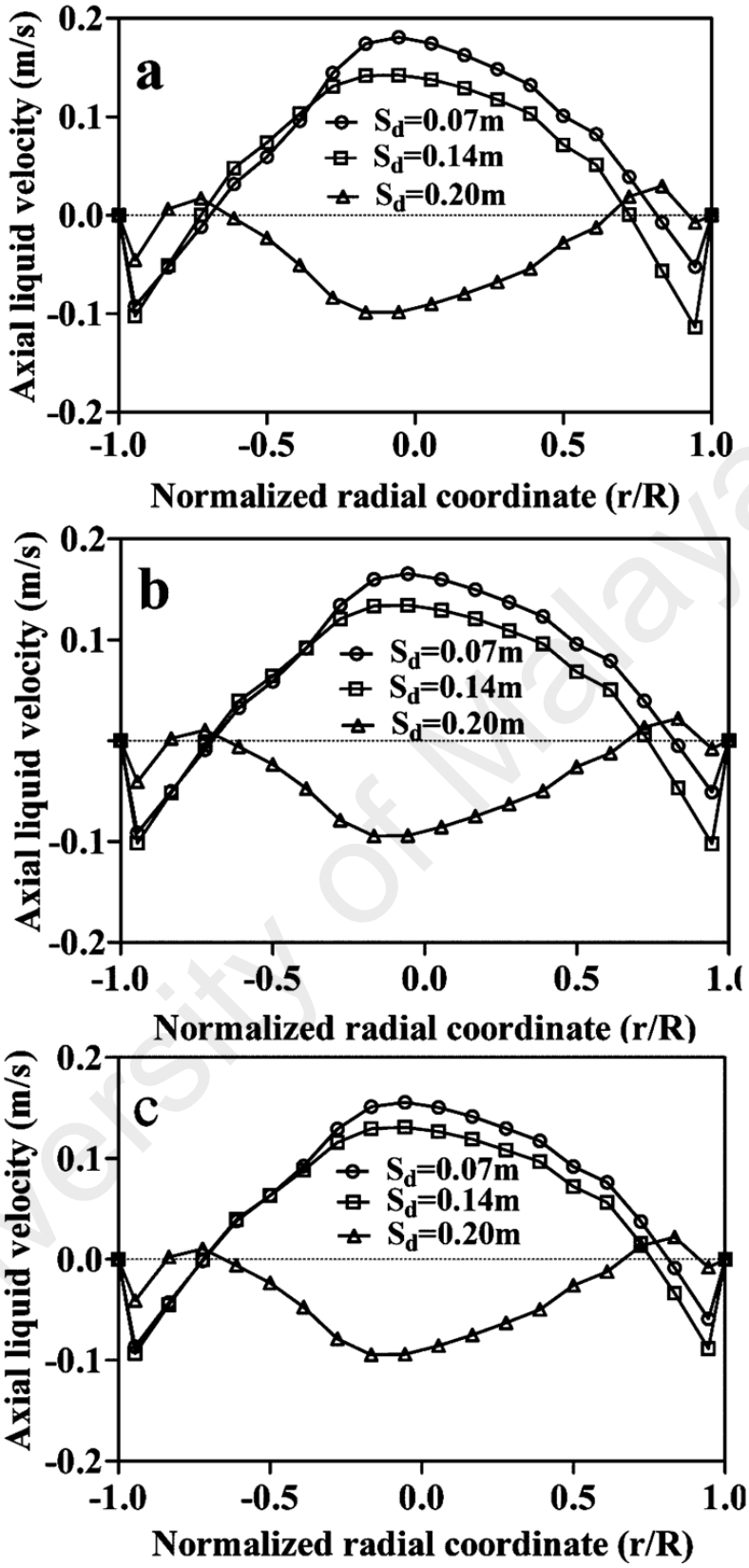

Figure 3.14: The averaged axial liquid velocity versus normalized radial coordinate for 0.07, 0.14 and 0.20 m sparger diameters at height: (a) 1 m; (b) 1.6 m; (c) 2.4 m

Figure 3.15 (a, b and c) shows the comparison of the time average profiles of the gas holdup as a function of the column radial position at axial heights of 1 m, 1.6 m and 2.4 m for the different ring sparger diameters (i.e., 0.07, 0.14 and 0.2 m). The Figure shows a significant profile difference between these three spargers. The peaks of the gas hold-up move from the column centre towards the column wall with the increase of the diameter of the ring sparger (i.e., from 0.07 to 0.20 m). The results of the gas hold-up for the 0.07 m sparger diameter has a steep profile with a peak near the column centre. Due to the concentrated sparger type, the gas flow is maximum at the column axis and minimum at the wall. The profile is steeper near the sparger, i.e., 1 m axial height, due to a strong sparger effect and less steep as the gas flow up and away from the sparger. This is quite clear as the peak of the gas hold-up decreases with the increase of the axial height, e.g., the peak value is about 0.048, 0.41 and 0.0351 at 1 m, 1.6 m and 2.4 m column heights, respectively for 0.07 m sparger diameter. However, as the profile becomes less steep at a higher column height, the gas hold-up near the wall increases, e.g., the value near the column wall is the highest at 2.4 m axial height for 0.07 m sparger diameter (see Figure 3.15 (c)).

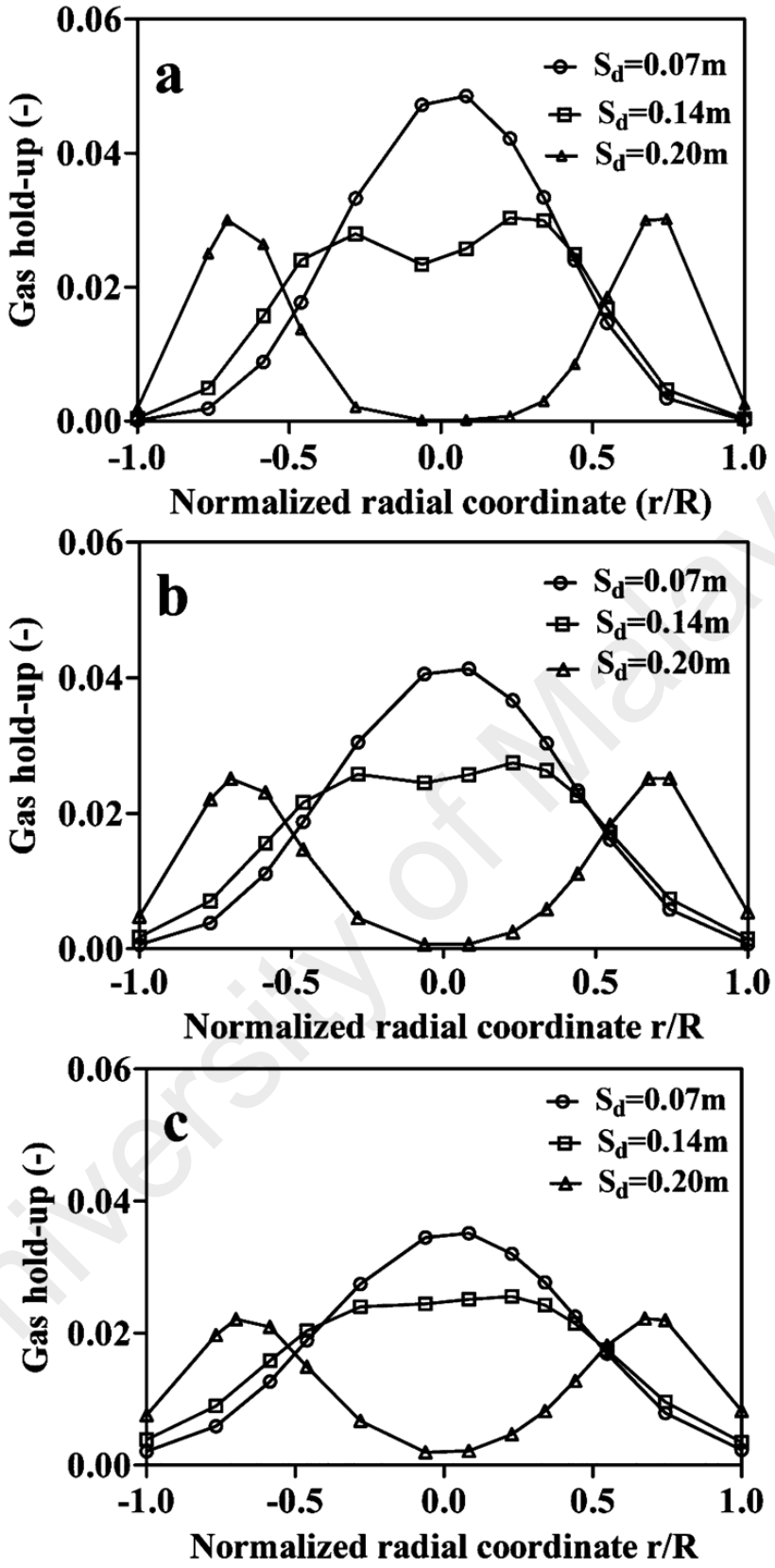

Figure 3.15: The averaged gas hold-up versus normalized radial coordinate for 0.07, 0.14 and 0.20 m sparger diameters at height: (a) 1 m; (b) 1.6 m; (c) 2.4 m

The results of the gas hold-up for the 0.14 m sparger diameter has a blunter profile in comparison with that of the 0.07 m sparger diameter at all axial heights. Most of the gas flows in the central column region of r/R= ±0.5. In addition, the profile seems to have two weakly developed peaks, see near r/R= ±0.3-0.5 due the effect of the use of the ring sparger of 0.14 m diameter in the 0.288 m column diameter, which is located in between the axis and the wall. The value of the gas hold-up near the wall is higher in the 0.14 m than in 0.07 m sparger diameter, e.g., see r/R<-0.4 for clear differences. This is expected due to the blunter profile which often increases the value near the wall because of the mass conservation. As described for the 0.07 m sparger diameter, the value of the maximum gas hold-up of the 0.14 m sparger diameter is higher at the axial height of 1 m, i.e., near the sparger, but lower at a higher axial height. The result of the gas hold-up for the 0.2 m sparger diameter has a similar profile as its axial liquid velocity (Figure 3.14) where the gas holdup has two peaks near the wall region. The gas hold-up is almost zero near the column centre.

The cross-section plane average of the gas holdup at various column heights is presented in Figure 3.16 for various sparger diameters (i.e., 0.07, 0.14 and 0.2 m). Note that the 0.14 m sparger diameter is the benchmark case and the results from this case have been validated and discussed in Sec. 3.2.5. The results of the 0.14 and 0.20 m sparger diameters are lower by about 5 % and 21 % maximum, respectively, than that of the 0.14 m sparger diameter at most of the heights except at the inlet. Given the same superficial gas velocity, a ring sparger located near the wall as that in the 0.02 m sparger diameter will result in a lower value of a planar averaged gas holdup as well as the total overall gas hold-up in the column. It is also clear that the 0.14 m sparger diameter is able to produce the highest average gas hold-up everywhere in the column in comparison to other cases.

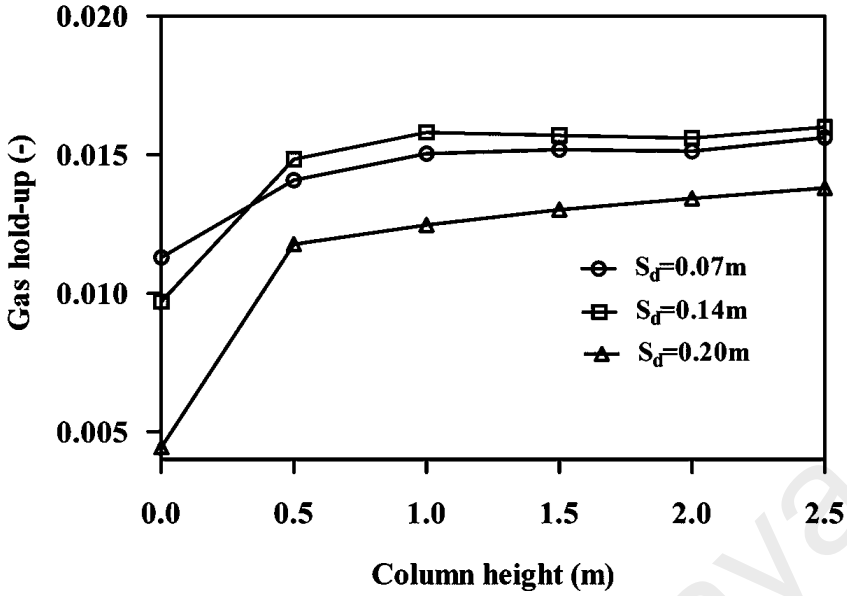

Figure 3.16: Average gas hold-up for 0.07, 0.14 and 0.20 m sparger diameters at various column heights

The comparison of the profiles of the time-averaged turbulent kinetic energy (*k*) versus the normalized radial coordinate are illustrated in Figure 3.17 (a, b and c) for the sparger diameters of 0.07 to 0.20 m at axial heights of 1 m, 1.6 m and 2.4 m. The radial profiles of *k* are significantly influenced by the use of the different types of gas spargers. The distribution of *k*, in general, is higher at the column's central region and it reduces to a zero value moving toward the column wall in all cases. The sparger diameter of 0.07 m has the highest *k* value in the central region followed by the ring sparger diameter of 0.14 m and then 0.20 m which has the least *k* value. The higher liquid velocity produces the larger liquid fluctuating components resulting in bigger values of k. The liquid velocity components and the probability of turbulence eddies colliding with bubbles are higher towards the column centre rather than wall region, due to the centralized movements of the bubbles. In addition, for smaller ring sparger diameters the liquid fluctuating components increases resulting in higher turbulence intensity. For example, at r/R=0, *k* is about 0.0251, 0.0141 and 0.0076 m^2/s^2 for sparger diameters of 0.07, 0.14 and 0.20 m respectively at 1 m axial height (see Figure 3.17 (a)). For each case, *k* at the central region reduces the increase of the axial height. The reduction is

greater for the 0.07 m diameter and least reduction occurs for the largest ring based on differences of the absolute *k* value at different heights. However, in percentage, the reduction is constant for all cases, e.g., *k* value at 1.6 m and 2.4 m heights is a reduction of about 20 % and 40 %, respectively from that at a 1 m height. The effect of the different types of spargers is again reflected in the *k* radial profile, i.e., the steep profile for the 0.07 m sparger diameter especially at a 1 m axial height and two weakly developed peaks near r/R= ±0.3-0.5 for 0.14 m diameter. However, this is different for the 0.20 m sparger diameter where its *k* profile seems not affected by the use of a larger ring size. This is despite the significant differences seen in the radial profiles of the axial liquid velocity (Figure 3.14) and gas hold-up (Figure 3.15) of the ring sparger diameter of 0.20 m. The low values of the axial liquid velocity and the effect of the column wall can be the possible causes that have damped down the *k* in the largest ring.

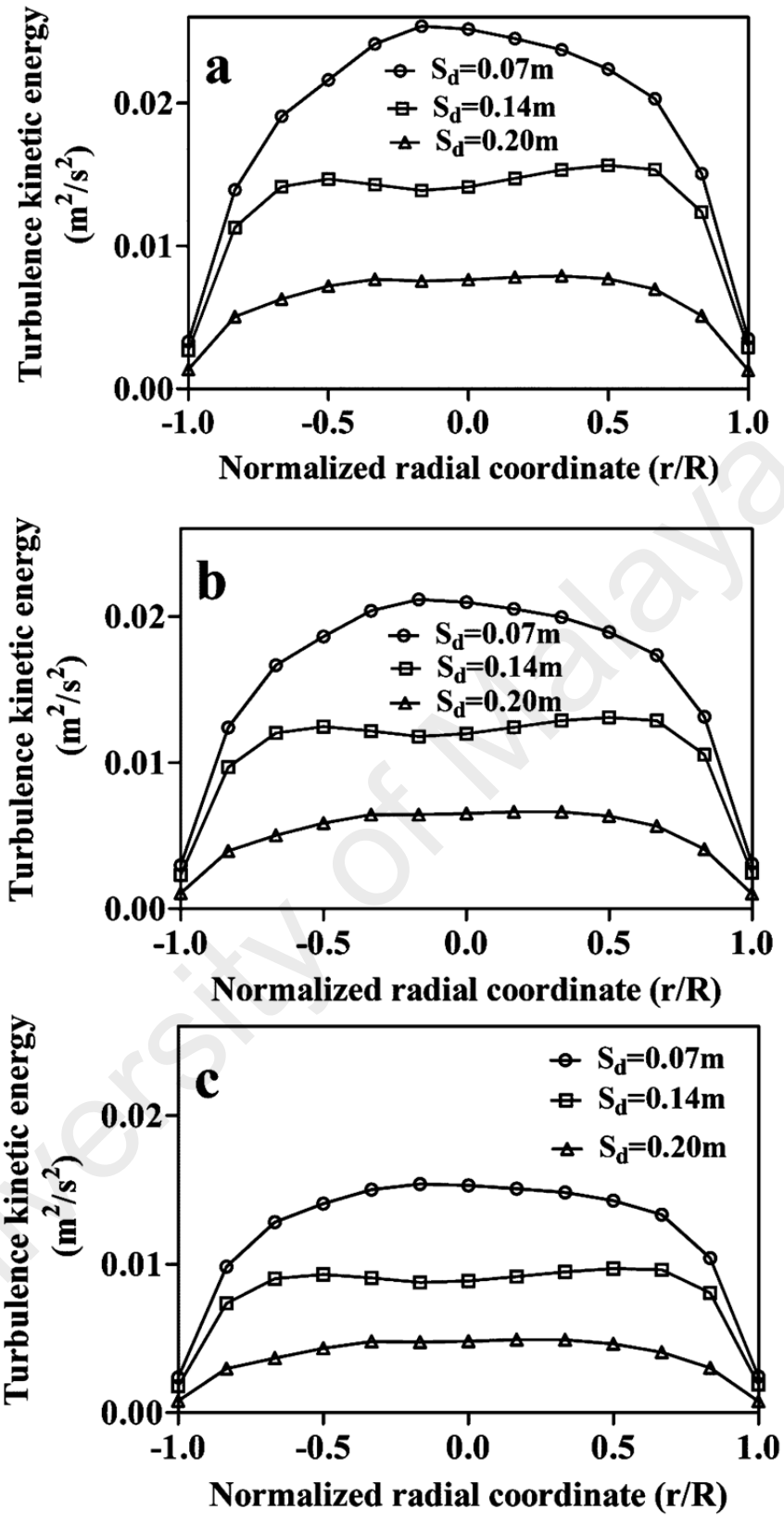

Figure 3.17: The averaged turbulence kinetic energy (TKE) versus normalized radial coordinate for 0.07, 0.14 and 0.20 m sparger diameters at height: (a) 1 m; (b) 1.6 m; (c) 2.4 m

3.3.5 Effect of superficial gas velocity

The superficial gas velocity can also change the flow pattern and gas dynamics. In this section the influence of various superficial gas velocities (i.e., 0.0025, 0.005 and 0.01 m/s) on the BCR hydrodynamics for a 0.14 m ring sparger diameter having 10 holes is studied and shown in Figures 3.18-3.22.

Figure 3.18 (a, b and c) shows an average profile of the axial liquid velocity as a function of the radial position in the column for the superficial gas velocities of 0.0025, 0.005 and 0.01 m/s at axial heights of 0.8 m, 1.6 m and 2.4 m, respectively. According to the figure, in comparison to the 0.0025 and 0.005 m/s superficial gas velocities, 0.01 m/s has a higher centre line velocity (steeper profile) at 0.8, 1 and 2.4 m in BCR heights with the maximum axial liquid velocity of about 0.176 m/s. This is due to the fact that, when the superficial gas velocity increases up to 0.01 m/s, bubbles tends to move at the centre region and the interaction between gas and liquid rises and results in increasing centre line velocity up to 43 % at the centre region of BCR (R/r=0). In addition, unlike the 0.0025 m/s and 0.01 m/s, the velocity profile of 0.005 m/s has a higher downward flow (about 0.15 m/s) near the wall regions (i.e., r/R= ±0.75) at 0.8 m BCR height. However, the superficial gas velocity of the 0.0025 and 0.01 m/s have an almost identical downward flow (0.9 m/s) at 0.8 m column height. The downward flow reduces with increase in the height of the column, e.g., in the case of the 0.005 m/s superficial gas velocity, the liquid velocity near the left and right walls are about 0.15, 0.13 and 0.10 m/s for 0.8 m, 1.6 m and 2.4 m column heights, respectively. This reduction at a higher level of the column is because of the decrease in the gas holdup gradient between the BCR centre and wall. Note that, the higher downward liquid flow produces the stronger liquid recirculation area towards the wall region and results in a higher heat and mass transfer rate inside the BCR (Alvare & Al-Dahhan, 2006).

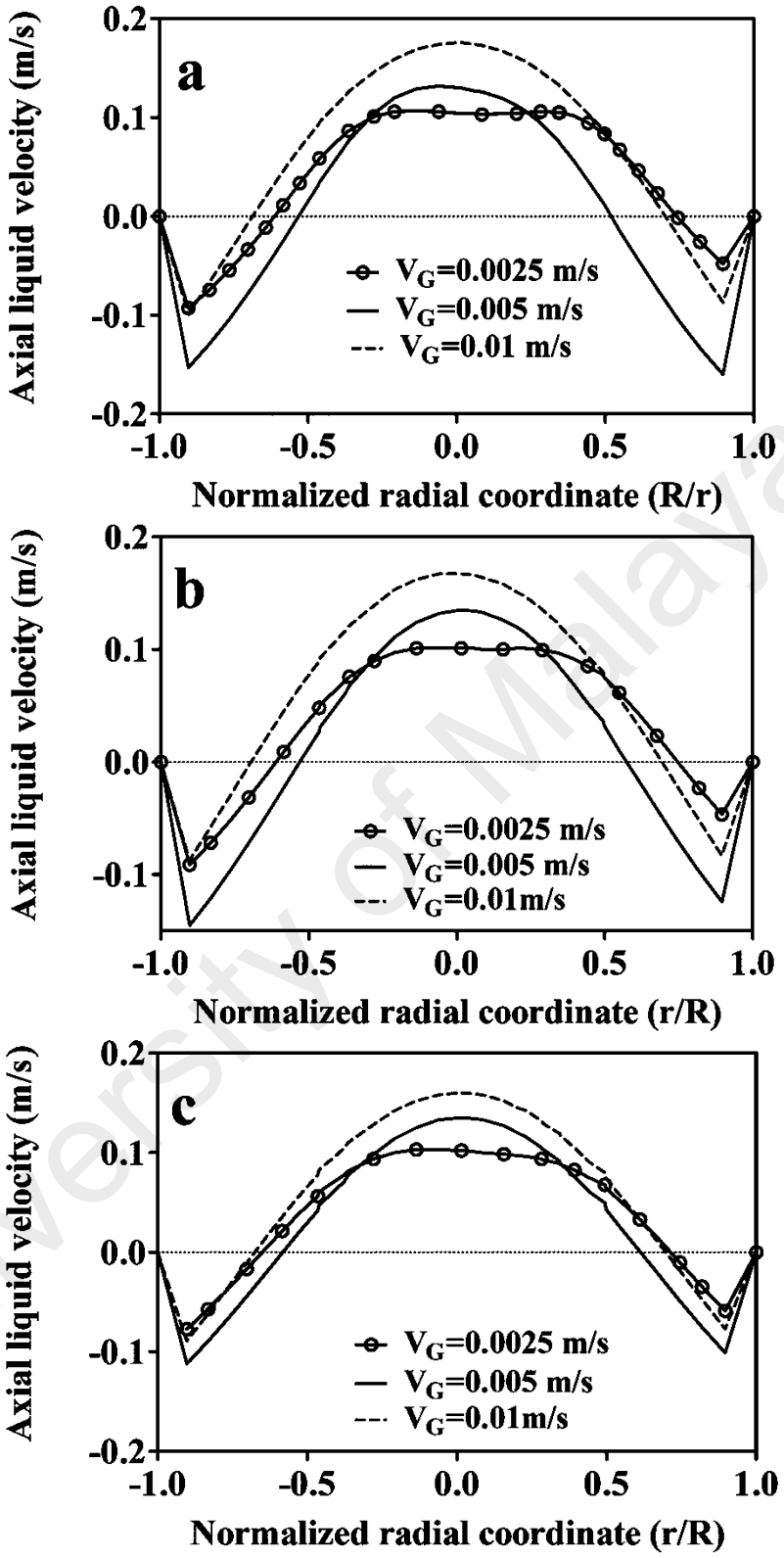

Figure 3.18: The averaged axial liquid velocity versus normalized radial coordinate for the 0.14 m ring sparger diameter with 10 holes and superficial gas velocities, 0.0025, 0.005 and 0.01 m/s at height: (a) 0.8 m; (b) 1.6 m; (c) 2.4 m

Figure 3.19 (a, b and c) shows the comparison of the time average profiles of the gas holdup as a function of the column radial position for the superficial gas velocities of 0.0025, 0.005 and 0.01 m/s at different BCR heights i.e., 0.8 m, 1.6 m and 2.4 m, respectively. The figure shows that, with an increase in superficial gas velocity from 0.0025 to 0.01 m, a remarkable increase in the magnitude of gas hold-up at the center region occurs, i.e., the peak value of gas hold-up at 0.8 m BCR height is about 0.0208, 0.0275 and 0.0487 for 0.0025, 0.005 and 0.01 m/s superficial gas velocities, respectively. However, all of the superficial gas velocities, particularly 0.0025 and 0.005 m/s contain two clear peak values due to the influence of the sparger. The gas hold-up profiles with two peaks show the non-uniform distribution over the cross section of the column, which represent the direct influence of the spargers. This influence increases the gas hold-up results, as the superficial gas velocity decreases. In contrast, the superficial gas velocity of 0.01 m/s gives a relatively flatter gas hold-up profile at almost all column heights in comparison to the 0.0025 and 0.005 m/s. This velocity provides a uniform distribution of gas, particularly at the surface region. Furthermore, for all superficial gas velocities, excluding 0.0025 m/s, the influence of the sparger on the gas hold-up profile disappears at a 2.4 m column height (see. Figure 3.19 (c)). This result shows that, the smaller superficial gas velocity produces a non-uniform gas hold-up profile for almost all of the column heights. The gas hold-up near the walls also rises as the superficial gas velocity and BCR height increase. This is due to the fact that, at a higher level of the column (h> 1.6 m), gas bubbles are trapped inside the recirculation area and tend to travel near the walls. This transvers movement of bubbles results in uniform distribution of gas over the cross section of the column (G. Li et al., 2009; Tabib et al., 2008). For case of superficial gas velocity 0.01 m/s, the gas phase almost cover all cross section area of BCR. This distribution is more likely to

appear at 2.4 m BCR height. In contrast, in case of superficial gas velocity of 0.0025 m/s, the mal-distribution is appeared at all BCR heights (see Figure 3.19).

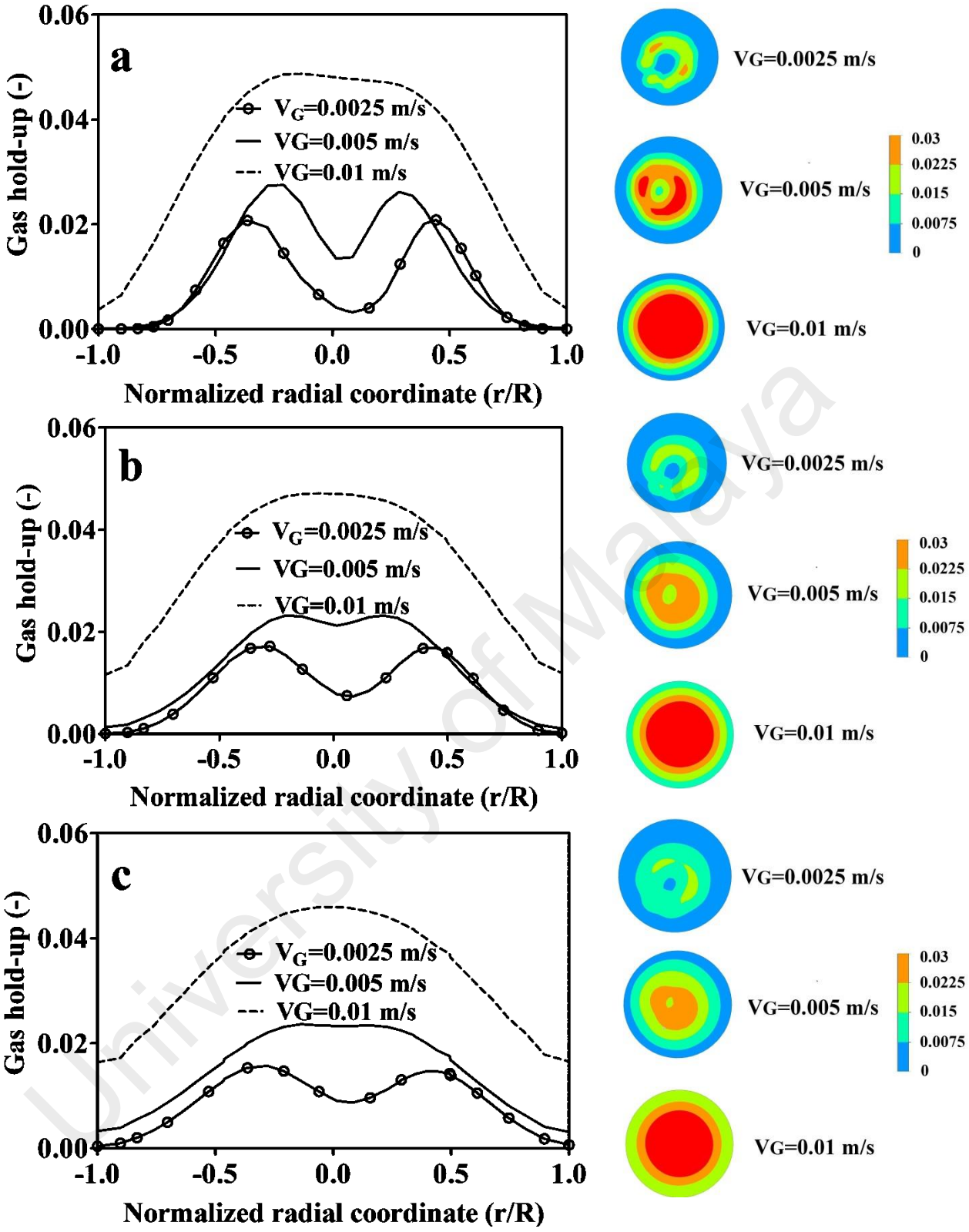

Figure 3.19: The averaged gas hold-up versus normalized radial coordinate for the 0.14 m ring sparger diameter with 10 holes and superficial gas velocities, 0.0025, 0.005 and 0.01 m/s at height: (a) 0.8 m; (b) 1.6 m; (c) 2.4 m

The cross-section planar average of the gas holdup at various column heights is shown in Figure 3.20 for the various superficial gas velocities, i.e., 0.0025, 0.005 and 0.01 m/s. According to the figure, with a decrease in superficial gas velocity from 0.01 to 0.0025 m/s, a significant decrease occurs in the magnitude of gas hold-up at all BCR heights. For example, the results of the 0.0025 m/s and 0.005 m/s superficial gas velocities are lower by about 72 % and 49 % maximum respectively, than that of the 0.01 m/s superficial gas velocity at most of the heights except at the inlet. Given the same ring sparger diameter, a superficial gas velocity of 0.0025 m/s results in the lower value of a planar averaged gas holdup, as well as a total overall gas hold-up in the column. It is also clear that, as expected, the superficial gas velocity of 0.01 m/s results in the highest average gas hold-up everywhere in the column, especially at the surface region.

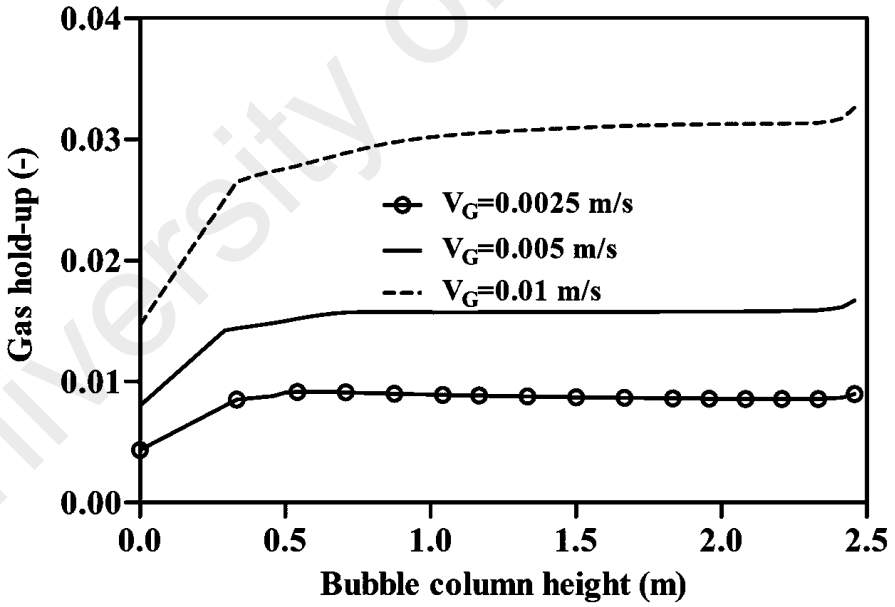

Figure 3.20: The planar averaged gas hold-up versus BCR heights for the 0.14 m ring sparger diameter with 10 holes and superficial gas velocities, 0.0025, 0.005 and 0.01 m/s

A comparison of the profiles of the time-averaged turbulent kinetic energy versus the normalized radial coordinates is illustrated in Figure 3.21 (a, b and c) for superficial gas velocities of 0.0025, 0.005 and 0.01 m/s and various BCR heights (0.8, 1.6 and 2.4 m),

respectively. The superficial gas velocity 0.01 m/s has a higher value of TKE as compared to 0.0025 and 0.005 m/s. For all of the superficial gas velocities, as the BCR height increases, the turbulent kinetic energy decreases due to the reduction in fluctuations of the turbulent fluid velocities. Like the results of the gas hold-up, the sparger also has an influence on the profile of the TKE. This influence is more likely to appear for the superficial gas velocity of 0.0025 and 0.005 m/s. As the superficial gas velocity of 0.0025 m/s and 0.005 m/s produces low number of bubbles and amount of gas (gas hold-up<1.5 %) in the BCR, bubbles cannot uniformly distribute over the BCR cross section and the gas pattern is affected by each sparger flow (jet flow) from ring sparger.

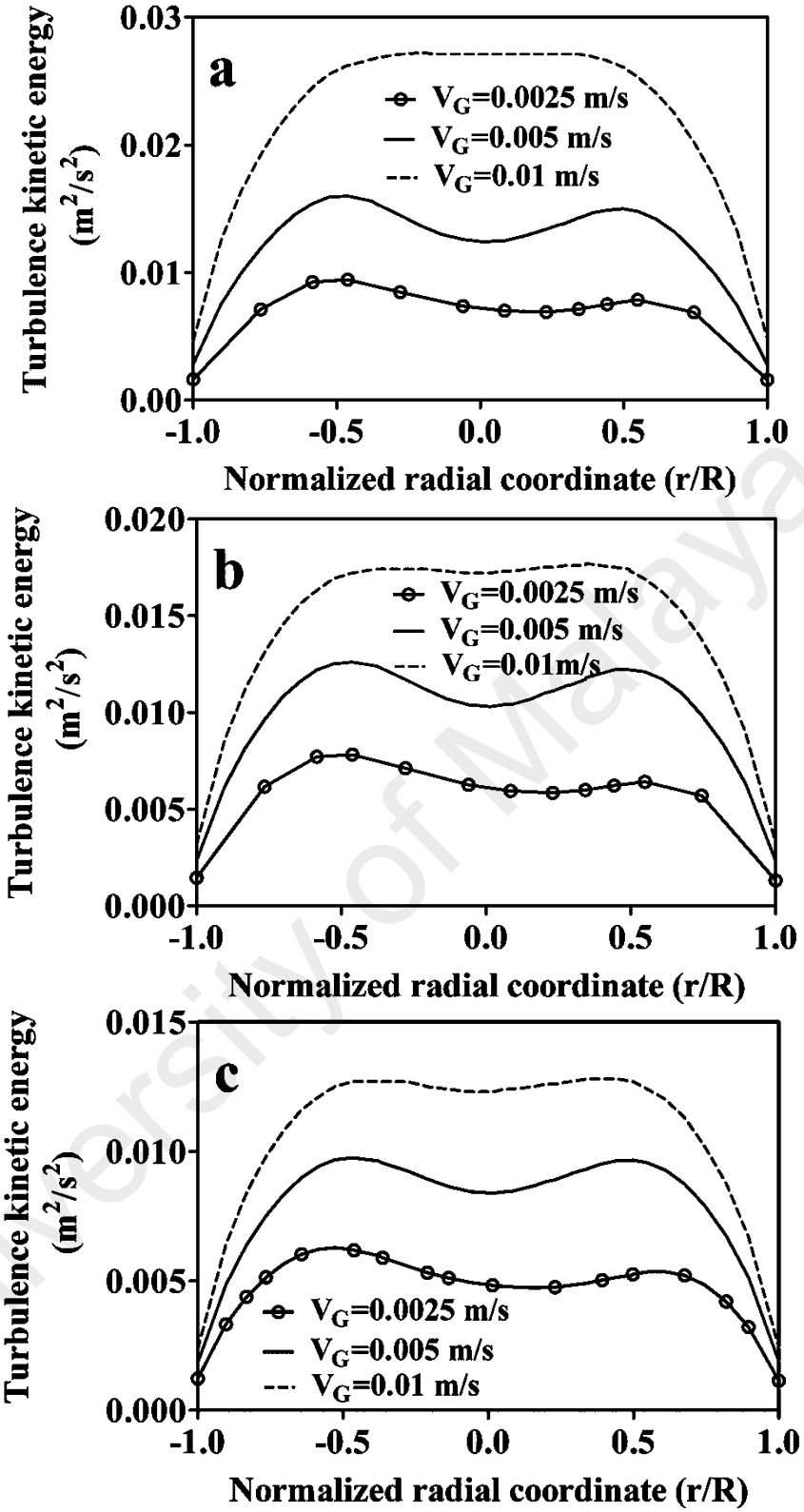

Figure 3.21: The averaged turbulent kinetic energy (TKE) versus normalized radial coordinate for the 0.14 m ring sparger diameter with 10 holes and superficial gas velocities, 0.0025, 0.005 and 0.01 m/s at height: (a) 0.8 m; (b) 1.6 m; (c) 2.4 m

The cross-section planar average of the TKE for the various superficial gas velocities, 0.0025, 0.005 and 0.01 m/s, at different column heights is shown in Figure 3.22. The figure shows that the planar average TKE for 0.01 m/s is significantly higher than other velocities. The results of the 0.0025 m/s and 0.005 m/s are lower by about 71 % and 45 % maximum, respectively than that of the 0.01 m/s superficial gas velocity at most of the heights. For all superficial gas velocities, the planner TKE decreases as the column height increases. For example, in comparison to the 0.5 m column height, near the surface region (i.e., 2.4 m), the amount of TKE decreases by 45 %, 62 % and 85 % for superficial gas velocities of 0.0025, 0.005 and 0.01 m/s, respectively.

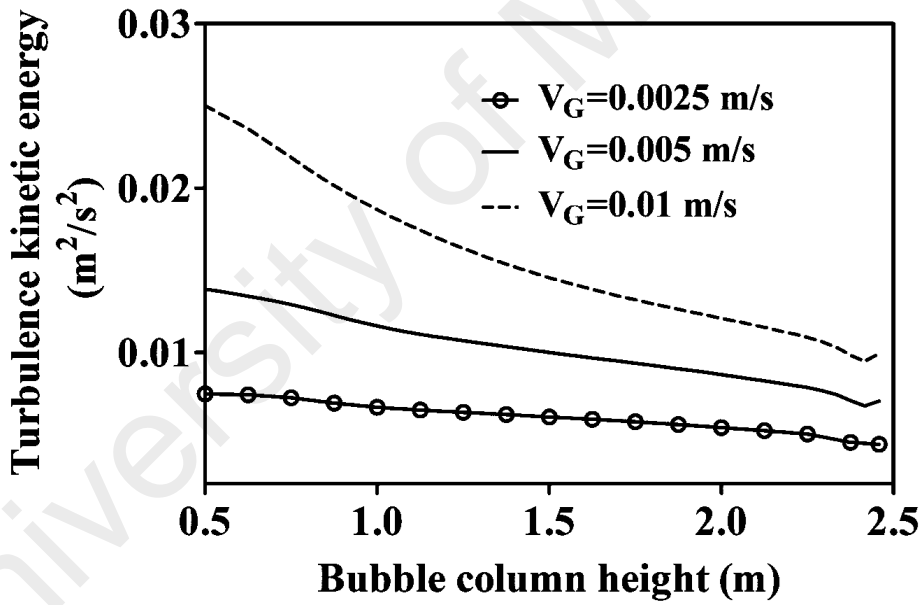

Figure 3.22: The planar averaged turbulent kinetic energy (TKE) versus BCR heights for the 0.14 m ring sparger diameter with 10 holes and superficial gas velocities, 0.0025, 0.005 and 0.01 m/s

3.3.6 Effect of the number of sparger holes

The number of sparger holes will affect the BCR hydrodynamics, herein, the effect of various ring spargers having 5, 10, 20 and 30 holes with 0.01 m/s superficial gas velocity and constant ring diameter (i.e., 0.14 m) on the BCR hydrodynamics is

studied and shown in Figures 3.23-3.30. For these cases, the superficial gas velocity of 0.01 m/s is selected as its gas hold-up and TKE profiles is quite uniform in comparison to Vg=0.0025 and 0.005 m/s. Figure 3.23 (a, b and c) shows an average profile of the axial liquid velocity as a function of the radial position in the column for the various number of sparger holes at axial heights of 0.8 m, 1.6 m and 2.4 m, respectively. As shown in the figure, with an increase in the number of sparger holes from 5 to 30, an insignificant change in the magnitude of the axial liquid velocity at the center and wall region occurs. However, when the number of holes is five, the centerline velocity is slightly higher and lower (about 10 %) than other cases (i.e., 10, 20 and 30) for the 0.8 m and 2.4 m column heights, respectively. This increment and reduction in the centerline velocity at various column heights is due to the fact that, the small number of sparger holes (i.e., N_s=5) contains a higher gas bubble velocity, resulting in a higher centerline liquid velocity near the spargers (i.e., 0.8 m). However, as the column height increases (up to 2.4 m), the bubbles are more likely to distribute over the cross section of the column and the gas hold-up gradient between the wall and central region decreases as well as the centerline liquid velocity.

Figure 3.24 (a, b and c) shows an average profile of gas hold-up as a function of the radial position in the column for various number of holes (5,10, 20, 30) at axial heights of 0.8 m, 1.6 m and 2.4 m, respectively. Figure shows that, the effect of different ring spargers having 10, 20 and 40 holes is marginal on the gas hold-up results, while the ring sparger with 5 holes affects the gas hold-up profile towards the central region, particularly at 0.8 and 1.6 m column heights, and resulting in non-uniform gas distribution (see Figure 3.24 (a and b)). Similar to that in the previous sections (3.3.4 and 3.3.5), this influence diminishes as the column height increases (see Figure 3.24 (c)). In addition, the effect of the various number of sparger holes is insignificant on the gas hold-up towards the wall region due to the use of the constant ring sparger diameter.

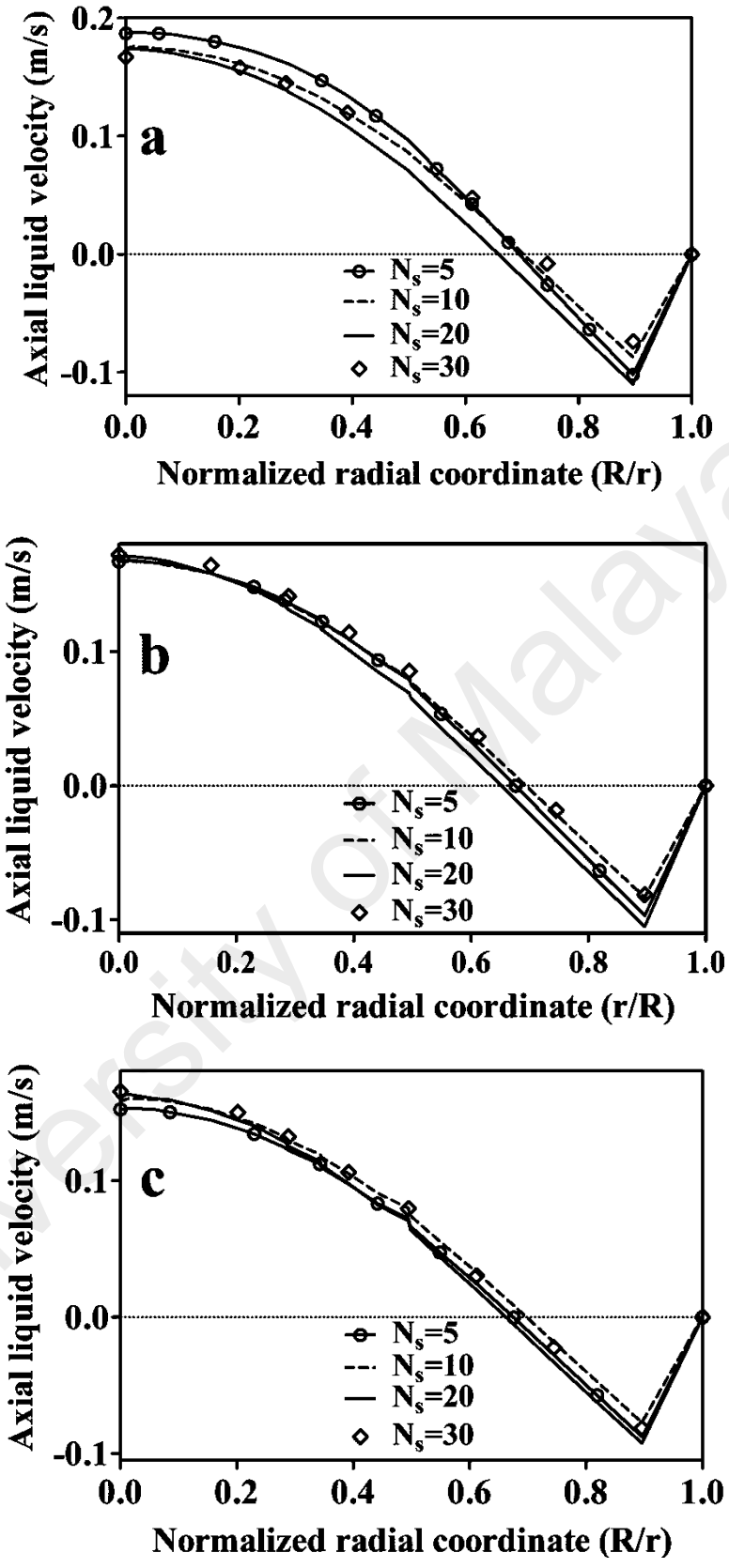

Figure 3.23: The averaged axial liquid velocity versus normalized radial coordinate for the superficial gas velocity 0.01 m/s and number of sparger holes, 5, 10, 20 and 30 at height: (a) 0.8 m; (b) 1.6 m; (c) 2.4 m

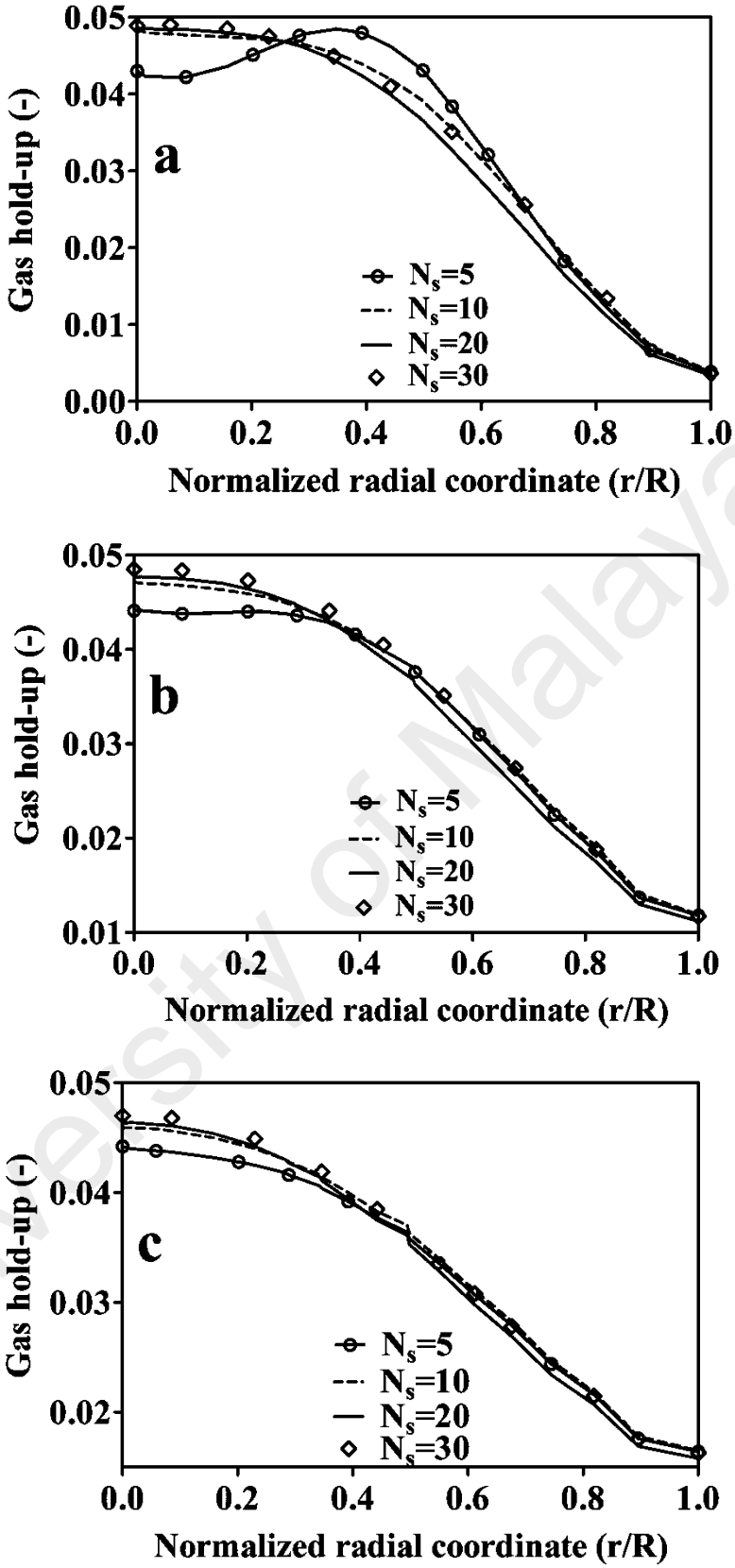

Figure 3.24: The averaged gas hold-up versus normalized radial coordinate for the superficial gas velocity 0.01 m/s and number of sparger holes, 5, 10, 20 and 30 at height: (a) 0.8 m; (b) 1.6 m; (c) 2.4 m

The cross-section planar average of the gas hold-up for various number of sparger holes ranging between 5 and 30 at different column heights, is presented in Figure 3.25. As shown in the figure, when the number of holes decreases, the amount of gas rises, particularly at the BCR with heights ranging between 0.5 and 1.5 m. However, the average gas hold-up for the BCR height varying between 1.5 to 2.5 m is almost identical for all of the sparger holes. It is because, when the effect of the sparger on the gas hold-up profile disappears, the amount of gas for different number of sparger holes insignificantly changes.

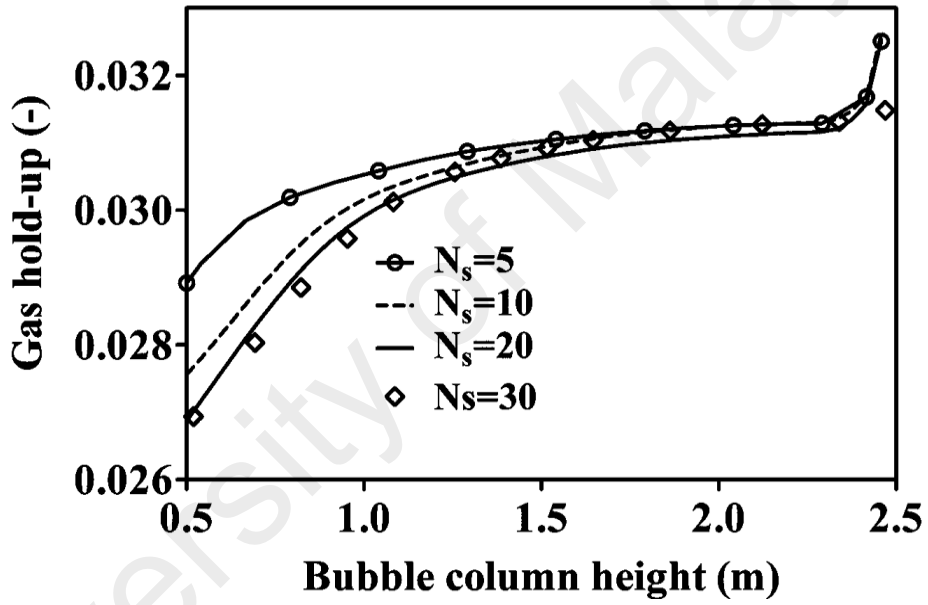

Figure 3.25: The planar averaged gas hold-up versus BCR heights for the superficial gas velocity 0.01 m/s and number of sparger holes, 5, 10, 20 and 30

Figure 3.26 (a, b and c) shows an average profile of TKE as a function of the radial position in the column for various number of sparger holes (5,10, 20, 30) at axial heights of 0.8 m, 1.6 m and 2.4 m, respectively. The figure shows that, the spargers containing 10, 20 and 30 holes have insignificant influence on the TKE results, while the sparger with 5 holes has a lower TKE towards the central region of the column at all BCR heights. However, as the column height increases, this difference in results reduces. Towards the wall region, all cases have almost similar TKE values (-

0.8>r/R>0.8). The cross-section planar average of the TKE for various number of holes and column heights is illustrated in Figure 3.27. The figure shows that the planer average TKE for the sparger containing 5 holes is lesser than the other spargers. However, the use of different ring spargers with 10, 20 and 30 sparger holes results in an almost similar average of TKE, at all BCR heights.

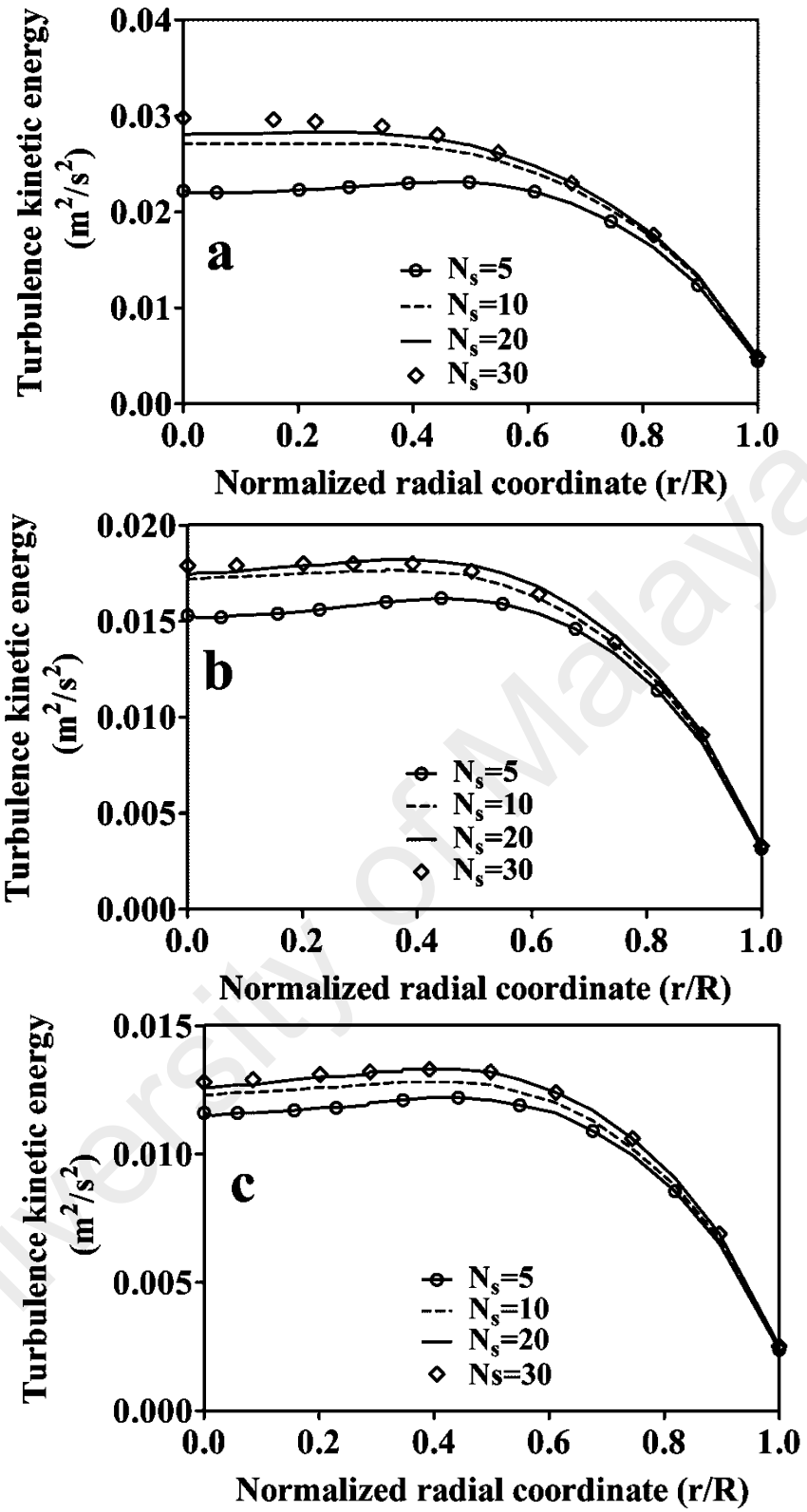

Figure 3.26: The averaged turbulent kinetic energy (TKE) versus normalized radial coordinate for the superficial gas velocity 0.01 m/s and number of sparger holes, 5, 10, 20 and 30 at height: (a) 0.8 m; (b) 1.6 m; (c) 2.4 m

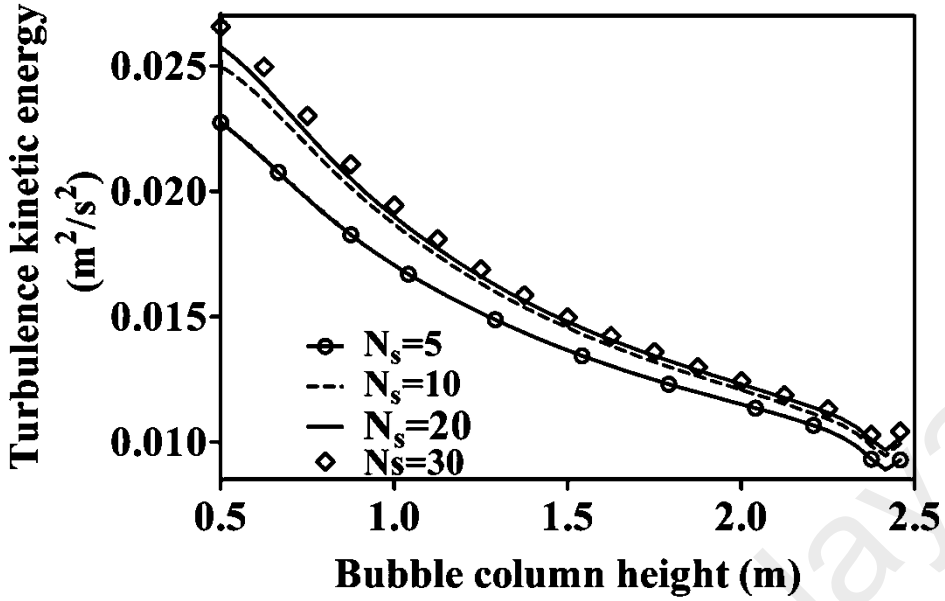

Figure 3.27: The planner averaged turbulent kinetic energy (TKE) versus BCR heights for the superficial gas velocity 0.01 m/s and number of sparger holes, 5, 10, 20 and 30

Figures 3.28, 3.29 and 3.30 show the histogram and contour plots of the distribution of gas hold-up at column heights of 0.21667, 0.65, 1.08333, 1.57167, 1.95 and 2.3833 m for the 5, 10 and 30 sparger holes, respectively. The figures show that the gas hold-up uniformly distributes, particularly near the sparger region, when the number of holes increases. For example, for a ring sparger having five holes, the star shape gas hold up distribution (Figure 3.28) occurs near the sparger region, while the sparger containing 20 and 30 holes produce almost circular gas distribution at the sparger region (Figure 3.29 and Figure 3.30).

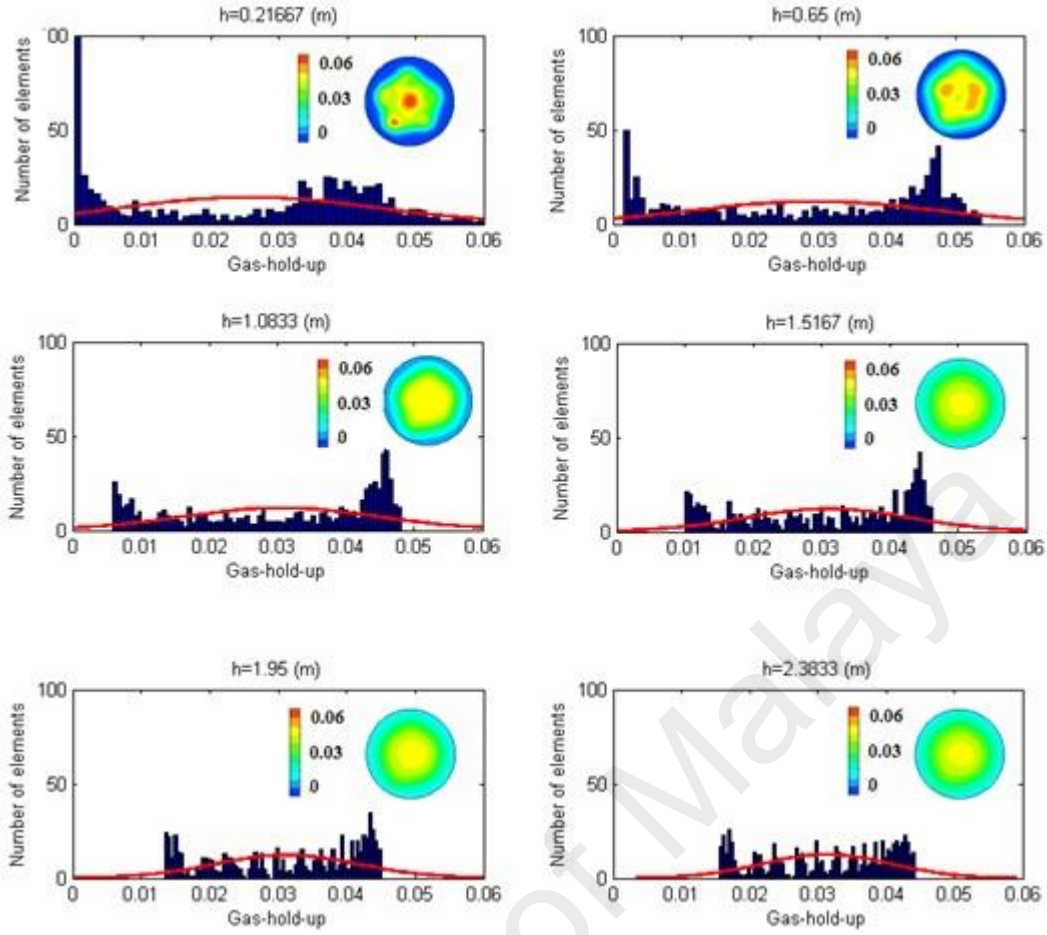

Figure 3.28: The averaged gas hold-up distribution for the superficial gas velocity 0.01 m/s and number of sparger hole 5 at various BCR heights (i.e., 0.21667, 0.65, 1.08333, 1.57167, 1.95 and 2.3833 m)

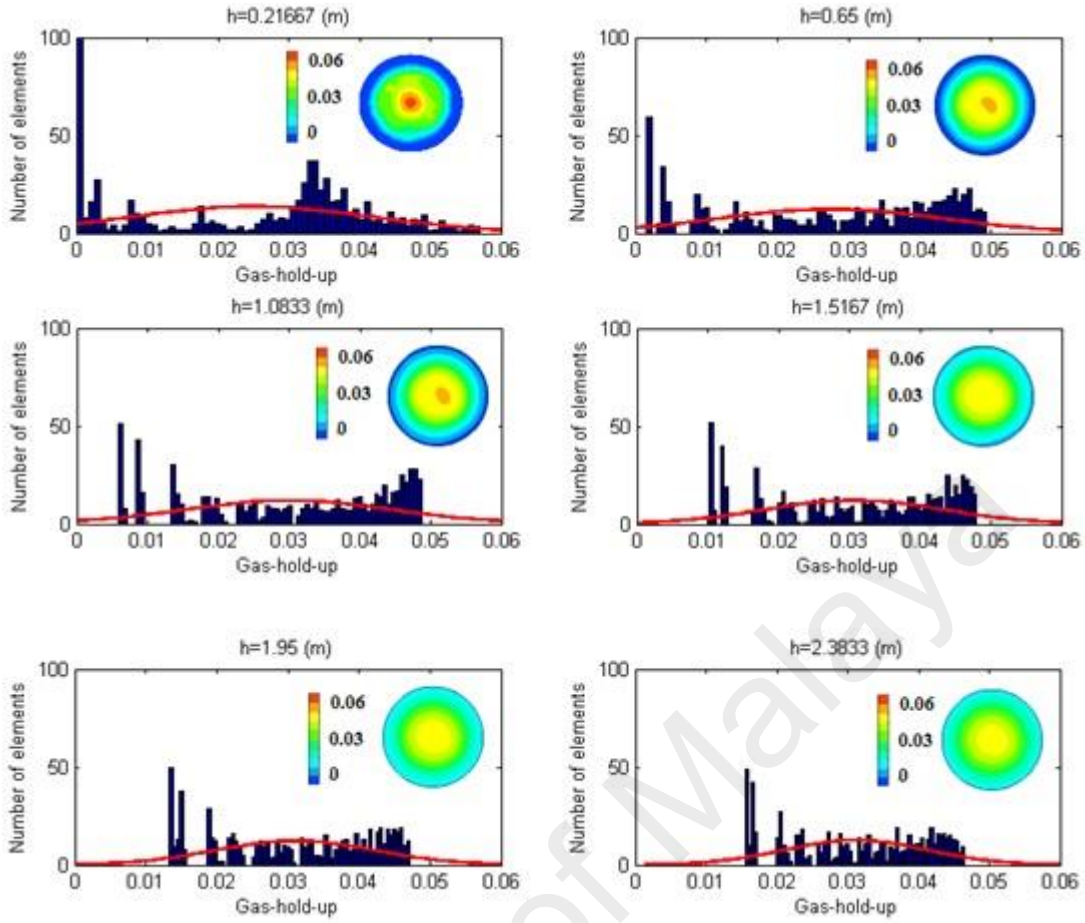

Figure 3.29: The averaged gas hold-up distribution for the superficial gas velocity 0.01 m/s and number of sparger hole 10 at various BCR heights (i.e., 0.21667, 0.65, 1.08333, 1.57167, 1.95 and 2.3833 m)

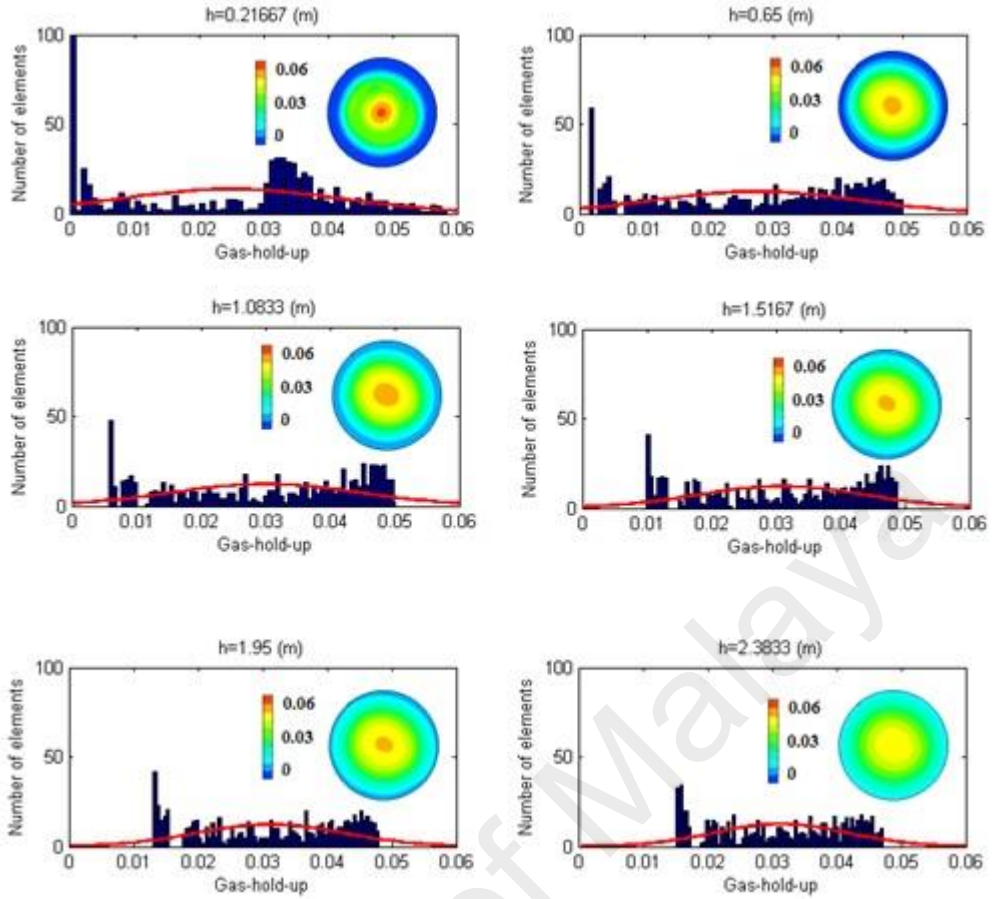

Figure 3.30: The averaged gas hold-up distribution for the superficial gas velocity 0.01 m/s and number of sparger hole 30 at various BCR heights (i.e., 0.21667, 0.65, 1.08333, 1.57167, 1.95 and 2.3833 m)

3.4 Conclusions

In the present chapter, the effects of the ring sparger diameters (0.07-0.20 m), superficial gas velocities (0.0025-0.01 m/s) and number of sparger holes (5-30) on the macroscopic hydrodynamics parameters of the BCR (i.e., liquid flow pattern, gas hold-up and turbulent kinetic energy) have been studied using the Eulerian-Eulerian method within the commercial package of ANSYS-CFX, Version 14. The prior numerical and experimental results and mathematical correlations are used for the validation of the present numerical study. The sensitivity studies of the different drag law models, turbulent dispersion coefficients and bubble diameters on the accuracy of CFD results are also carried out. The conclusions of this study are as follows:

- The ring sparger when located relatively nearer the column centre (0.07 m ring sparger diameter) results in a steeper profile of the axial liquid velocity and the gas hold-up near the column centre due to a high flow at this location from the bottom to the top of the column. The peak of the profiles is maximum at the lower column height (or near the sparger region).
- The ring sparger when located relatively nearer the column wall (0.2 m ring sparger diameter) results in a much different profile of the axial liquid velocity and the gas hold-up in comparison to that of the 0.07 m ring sparger diameter. A downward flow occurs at the column central region and an upwards flow only occurs at a small circumferential region. This type of sparger increases the axial liquid velocity near the column wall and changes the liquid circulation direction. This feature may be further explored to improve the liquid agitation near the column wall. In addition, this large recirculation area that occurred near the left and right walls is advantageous in processes that require good mass and heat transfer capabilities.

- The ring sparger when located in between the column centre and wall (0.20 m ring sparger diameter) produces a higher planar averaged gas hold-up in the column. This may have resulted due to a lower bubble flow resistance by using such a sparger.
- The superficial gas velocity of 0.01 m/s has a higher liquid centerline velocity, gas hold-up and TKE. The gas bubbles uniformly distribute over the cross section of the column at almost all column heights. In contrast, the smaller velocity (0.0025 m/s) results in a lower liquid centerline velocity, gas hold-up and TKE and the influence of the ring sparger significantly appears on the gas hold-up and TKE profiles resulting in a mal-distribution of gas. Furthermore, in comparison to all velocities, the 0.005 m/s produces the higher downward liquid flow (stronger recirculation) towards the wall regions, and providing a higher heat and mass transfer coefficient.
- The effect of using different number of sparger holes (more than 5) is marginal on the liquid flow pattern and gas dynamics, particularly towards the wall region and various BCR heights. However, using the sparger having 5 holes, results in a non-uniform gas hold-up profile almost at all column heights (especially near the sparger region). This shows that a larger number of sparger holes (more than 5) results in better distribution of gas (uniform distribution) at different heights and unpleasant influence of the sparger on the profile of liquid velocity, gas hold-up and TKE is diminished.

CHAPTER 4: SINGLE BUBBLE FORMATION AND RISE CHARACTERISTICS

4.1 Introduction

Since the Euler-Euler method is unable to predict the dynamics of the individual bubble (including the transparent interface between gas bubbles and liquid), the microscopic numerical method (i.e., VOF) has been commonly used to show the single bubble formation, detachment, rising and the interaction between bubbles (i.e., coalescence, collision and beck-up). This method also shows the detailed information of each bubble when they move and deform after a coalescence/break-up process inside the BCR.

The present chapter describes the bubble formation, rising and the interaction between bubbles through a single and multi-orifice using the VOF method. In addition, the effect of different bubble diameters on the coalescence process is studied. The experimental observation is used to show the effect of various orifice diameters and velocities on the bubble volume and detachment time, as well as the validation of the numerical method. Furthermore, the prior numerical and experimental results and mathematical correlations in the literature are also compared with the present numerical method.

4.2 Experimental set-up

For the experimental study, two different experimental set-ups are used to study the bubble formation. The first one shows the bubble formation at very small flow rates (quasi static regime), while the second one provides the faster formation at a higher velocity. The difference between these set-ups is in the controlling inlet flow rate (see Figure 4.1). In order to observe the bubble formation, a Poly (methyl methacrylate)

BCR with 395 mm in height and 254 × 220 mm^2 cross section is used. The orifice is mounted at the bottom of the column so that the walls have insignificant influence on the formation of the bubble during the experiment.

4.2.1 Experimental conditions

The experimental study is implemented in the isolated laboratory, which the temperature is adjusted about 25±1 ◦C. The atmospheric air moves in the form of dispersed bubbles through the orifice inside the BCR filled with ultra-pure water. The ultra-pure water having a 18.2 megohm/cm specific resistance is purified with a Millipore purification system (Aquinity Ultra-Pure Water System) from the municipal tap water at 25^{o}C. The purification process removes the dissolved gas. The liquid has 0.072 N/s surface tension which is measured with a video-based optical contact angle measurement system OCA 15EC. In order to remove the effect of the water movement on the bubble dynamics, the experimental study is carried out after 20 minutes. The stainless steel hypodermic needle (medical needle) with various sizes (i.e., 0.4-2 mm) are installed as orifices at the bottom of the column. The bevel part of the needles are cut using a CNC EDM wire cut machine and polished to make blunt end needles, with 90^o. The diameter of needles are measured by USB digital microscope. The property values of the fluids are given in Table 4.1.

Table 4.1: Physical properties of fluids

Parameters	symbols	Values	Units
Liquid density	ρ_L	998.2	kg/m^3
Liquid viscosity	μ_L	0.001	kg/ms
Gas density	ρ_g	1.225	kg/m^3
Gas viscosity	μ_g	1.79×10^{-5}	kg/ms
Surface tension	σ	0.073	n/s
Gravity	g	9.81	m/s^2

4.2.2 Equipment for measurement

As mentioned above, the difference in these two set-ups is about controlling the air flow inside the orifice. In the first set-up, a single direct dosing system SD-DM (infusion pump) is used to regulate the air flow rate inside the orifice (see Figure 4.1 (a)). This system provides a constant volumetric flow rate ranged 1×10^{-9} m^3/s -6×10^{-9} m^3/s using electronic dosing control unit ES. The flow rate ranged from 1×10^{-9} to 6×10^{-9} m^3/s produces quasi static flow regime where a single bubble forms from 5 to 180 s. In this regime, the influence of flow rate is insignificant on the bubble dynamics. Therefore, different flow rates have insignificant effect on the accuracy of experimental study. A high-speed digital video camera capturing 87 frames per second is used to observe the bubble formation. This camera contains a high performance 6x parfocal zoom lens integrated with a continuous fine focus, adjustable observation and camera tilt angle, to focus at every location of BCR, particularly at the tip of the orifice. Note that, the parfocal zoom lens stays in focus and provides sharp images when the magnification is altered or the bubbles move very fast. The camera is installed on an adjustable base very close to the area of observation in such a way that the test section is located between the camera and an appropriate lighting system. The intensity of the lighting source along the optical path is adjustable and without hysteresis.

In the second set-up, the value of flow rate is adjusted by the manual and digital air flow meters manufactured by Dwyer Company (see Figure 4.1 (b)). Both flow meters provide a constant flow rate ranging 1.6×10^{-6} m^3/s-8.3×10^{-5} m^3/s. A Fujifilm X-S1 camera is used to observe the bubble formation. The camera is set on the camera tripod (called “Cullmann Magnesit 532”) very close to the area of observation in such a way that the BCR is installed between the camera and a proper lighting system. To take sharp images, showing the exact interface between gas and liquid, the lighting system and the distance between camera and BCR are adjusted by 10 initial images. In this

case, the distance between camera and BCR and lighting system and BCR are found by the sharp image which shows the correct location of camera, as well as lighting source. For image processing of experimental images, ImageJ software is used to calculate bubble size and volume. The experimental observations are repeated for 7 times.

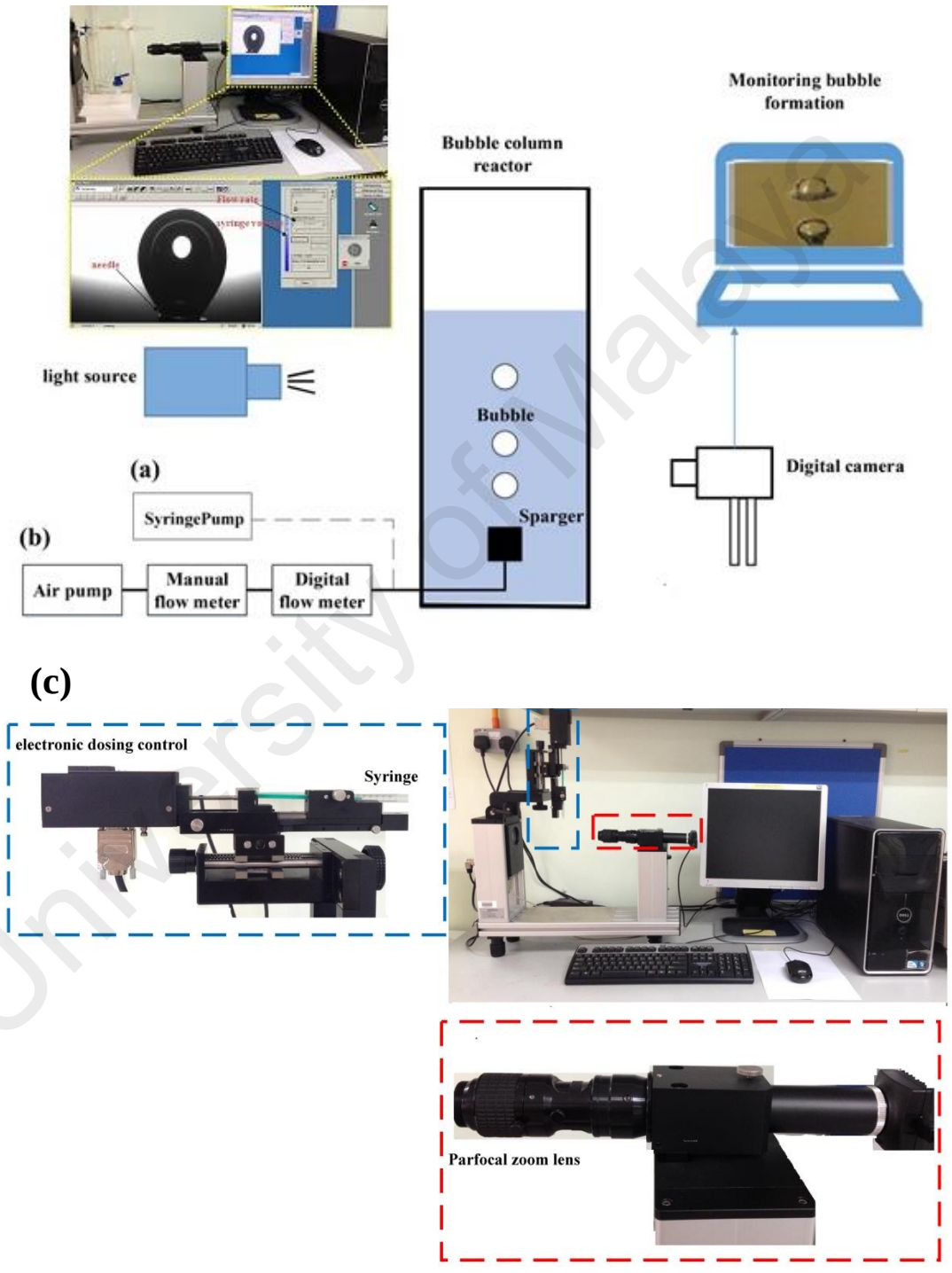

Figure 4.1: Schematic diagram of the experimental set-up: (a) First set-up; (b) Second set-up; (c) Measurement equipment.

4.3 Modeling single bubble formation (CFD technique)

The volume of fluid (VOF) method within ANSYS, FLUENT, V14 is used to simulate the single bubble in the BCR. Rectangular 2D simulation is used to avoid complex geometry and unnecessary large number of cells. The present experimental observation and existing experimental and numerical results and empirical correlation in the literature have been used for the air bubble formation and rising to validate the implementation of the numerical method.

4.3.1 Governing equations

The simulation of the single bubble formation and rising in the BCR has been studied using the VOF method (Hirt & Nichols, 1981). This method has been used in several studies to investigate the gas and liquid interface, in particular in single bubble formations and rising in the column. In this method, a volume fraction transport equation is used in addition to the continuity and momentum equations and two phases i.e., gas and liquid are treated as a homogeneous gas-liquid mixture. The flow in the BCR studied is laminar, incompressible, Newtonian, and isothermal and governed by the Navier-Stokes and continuity equations as shown here:

$$\nabla.\vec{v} = 0 \tag{1}$$

$$\frac{\partial(\rho\vec{v})}{\partial t} + \nabla(\rho\vec{v}\vec{v}) = -\nabla p + \nabla\left[\mu\left(\nabla\vec{v} + \nabla\vec{v}^{T}\right)\right] + F_s + \rho\vec{g} \tag{2}$$

where,ν, ρ, t, F_s, p, g and μ are the velocity of the mixture, pressure, time, volumetric forces, density, gravity and viscosity, respectively. The motion of the bubbles and changes in the liquid are tracked using a single set of momentum equations. Each fluid is tracked independently and the fraction of fluid volume in the grid is indicated by the indicator function F. The indicator F can be qualified by 0 for a cell containing only gas, by 1 for a liquid-filled cell and by 0-1 for a cell containing both gas and liquid.

The transport equation is used to compute the liquid volume fraction distribution (Hirt & Nichols, 1981):

$$\frac{DF}{Dt} = \frac{\partial F}{\partial t} + \left(\vec{v}.\nabla\right)F = 0 \tag{3}$$

The values of density and viscosity of the mixed fluid are calculated according to the value of the volume fraction F (Hirt & Nichols, 1981).

$$\rho\left(\vec{x},t\right) = F\left(\vec{x},t\right)\rho_l + \left[1 - F\left(\vec{x},t\right)\right]\rho_g \tag{4}$$

$$\mu\left(\vec{x},t\right) = F\left(\vec{x},t\right)\mu_l + \left[1 - F\left(\vec{x},t\right)\right]\mu_g \tag{5}$$

where, ρ_l, ρ_g ,μ_l and μ_g are the liquid density, gas density, liquid viscosity and gas viscosity, respectively. In order to take the surface tension forces into account, the CSF model is used which converts the surface tension into the body force, thereby acting on the interface according to the divergence theorem (Brackbill, Kothe, & Zemach, 1992). The surface tension when converted to a body force is added to the momentum equation.

$$F_s = \sigma\frac{\rho k \nabla F_l}{0.5\left(\rho_g + \rho_l\right)} \tag{6}$$

where $k = \nabla.\hat{n},\ \hat{n} = \left(\frac{n}{|n|}\right), n = \nabla F_q.$

4.3.2 Geometrical structure and simulation cases

A small rectangular BCR with 50 mm wide and 100 mm height is used to numerically study the bubble formation, rising and the interaction between the bubbles. Table 4.2 and Table 4.3 show the simulation and experimental cases for mesh independency, validation and result section. A total of 68 simulation and experimental cases are implemented in this chapter such as follows:

a. Mesh sensitivity

Cases 1-3 show 3 different number of grids (i.e., 2.2×10^5, 8×10^4 and 4.08×10^4), which are used in the mesh independency part, when the flow rate and the orifice size are 2.36×10^{-7} m^3/s and 1 mm, respectively, for 0.4 s.

b. Validation of CFD method

In this section; firstly: two different bubble sizes (4-5 mm) are used for the validation of bubble rise velocity (Cases 4-5); secondly: the simulation results are compared with experimental observations for bubble formation, when the flow rate and the orifice size are 7.85×10^{-8} m^3/s and 1 mm, respectively (Cases 6-7); thirdly: the experimental study is implemented for the comparison of bubble volume at detachment time with prior experimental studies. In these cases, the orifice sizes are 0.35, 0.56, 1, 1.2 mm, when the flow rate is 1×10^{-9} m^3/s (Cases 8-11).

c. Single bubble formation, rising and the interaction between bubbles

Cases 12-68 show the simulation cases for bubble formation and rising and the interaction between bubbles as shown in Table 4.3. Cases 12-17 show the effect of orifice gas velocity on bubble formation and rising, when the orifice size is 1 mm and the orifice velocity varies from 7.85×10^{-8} to 4.17×10^{-7} m^3/s, for 0.4 s. Cases 18-20 describe the influence of the different bubble sizes (i.e., 4-6 mm) on the coalescence process, when there is no orifice in the column. Cases 21-40 show the effect of different orifice arrangement on the bubble detachment and coalescence process for 2 orifices with 1.57×10^{-7} m^3/s velocity and various distances between orifices (i.e., 0.25-4 mm). In cases 41-68, the experimental study is implemented to

study the effect of various orifice sizes (i.e., 0.3, 0.6, 1 and 1.2 mm) and velocities, ranging between 1×10^{-9} and6×10^{-9} on the bubble detachment time and volume.

Table 4.2: Simulation cases for mesh independency and validation

Cases	Flow rate (m/s^3)	Bubble size (mm)	Num of orifices	Orifice size (mm)	Exp/Num	Sim time (s)	Num Grids	Remarks
1-3	2.36×10^{-7}	——	1	____	Num	0.4	2.2×10^5, 8×10^4, 4.08×10^4	Grid independency
4-5	——	4-5	____	____	Num	0.4	8×10^4	Validation of bubble rise velocity
6-7	7.85×10^{-8}	____	1	1	Num/ Exp	0.15	8×10^4	Validation of bubble formation
8-11	1×10^{-9}	____	1	0.35, 0.56, 1, 1.2	Exp	____	____	Validation of bubble volume at detachment

Table 4.3: Simulation cases for bubble formation and rising

Cases	Flow rate (m/s^3)	Num of orifices	Distance between orifices (mm)	Left orifice size (mm)	Right orifice size (mm)	Upper bubble size (mm)	Lower bubble size (mm)	Exp/Num	Sim time (s)	Remarks
12-17	7.85×10^{-8},1.57×10^{-7}, 2.36×10^{-7}, 3.14×10^{-7} ,$3.93\times10^{-}7$, 4.17×10^{-7}	1	____	1 mm	____	____	____	Num	0.4	Effect of orifice velocity on bubble formation and rising
18	——	____	____	____	____	6	4	Num	0.4	Effect of bubble size on coalescence process
19	——	____	____	____	____	4	4	Num	0.4	
20	——	____	____	____	____	4	6	Num	0.4	
21-29	1.57×10^{-7}	2	1-4.5	1	1	____	____	Num	0.2	Effect of distance between orifices on the coalescence and detachment
30-40	1.57×10^{-7}	2	1	0.25-4	1	____	____	Num	0.2	
41-44	1×10^{-10}, 5×10^{-10}, 1×10^{-9}, 2×10^{-9}	1	____	1	____	____	____	Exp	____	Effect of flow rate on detachment time and bubble volume
45-68	1×10^{-9} -6×10^{-9}	1	____	0.3, 0.6, 1 and 1.2	____	____	____	Exp	____	

4.3.3 Boundary conditions and numerical methods

The transient model based on an explicit scheme (Ratkovich, Chan, Berube, & Nopens, 2009) with a time step of 0.0001 s and the Courant number 0.25 is used. The inlet and outlet boundary conditions are defined as velocity inlet and pressure outlet, respectively. All the solid walls are considered to have no slip boundary conditions. The operating pressure and the initial conditions of the BCR such as pressure, gas and liquid velocity and volume fraction of gas phase are specified zero. The governing equations are numerically solved using the QUICK (quadratic upwind interpolation) (Ratkovich et al., 2009) and the velocity and pressure are coupled using the Pressure Implicit Split Operators (PISO) method (Ma et al., 2012; Ratkovich et al., 2009; Taha & Cui, 2002). The piecewise linear interface calculation (PLIC) algorithm is used to reconstruct the interface (Gerlach et al., 2006; Ma et al., 2012; van Sint Annaland, Deen, & Kuipers, 2005; Youngs, 1982). The rate at which the solution changes during the iteration is controlled by defining the under-relaxation factors of 0.3 and 0.7 for pressure and momentum respectively. The solution is converged when the sum of relative errors does not exceed 10^{-9}.

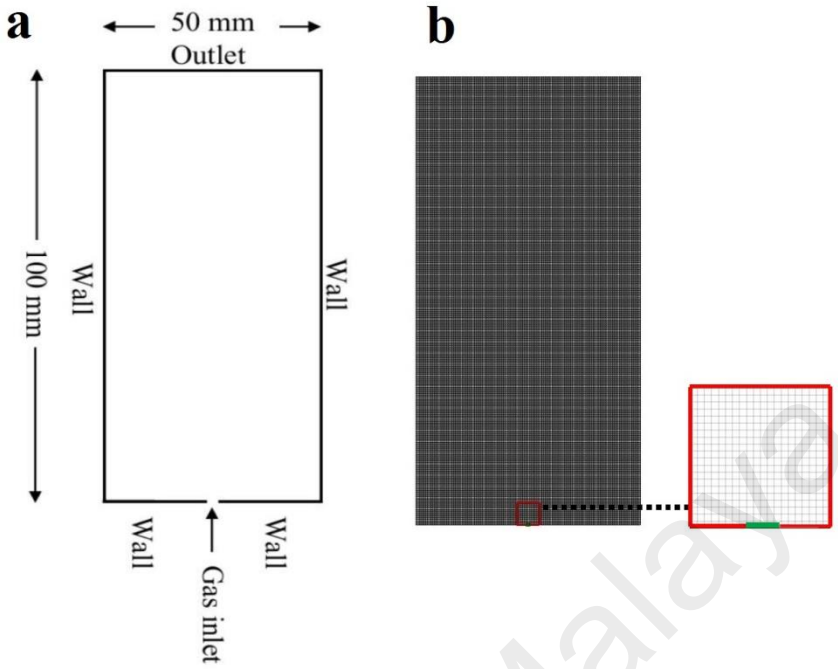

Figure 4.2: (a) Schematic of the gas-liquid BCR and boundary conditions; (b): computational mesh containing 80000 elements

4.3.4 Mesh sensitivity

Figure 4.2 shows the schematic diagram of the BCR and boundary conditions, as well as computational mesh structure. Various element sizes for the 2D BCR are used (i.e., 0.15 mm ×0.15 mm, 0.25 mm ×0.25 mm, 0.35 mm ×0.35 mm and the corresponding numbers of grid points are 2.2×10^5, 8×10^4, 4.08×10^4, respectively). Mesh independency tests are carried out for the leading bubble distance and equivalent diameter for different period of times. Figure 4.3 shows the leading bubble distance and the equivalent diameters against time for different grid densities. According to the figure, for different grid sizes there is a small difference in the values of bubble heights i.e., measured from the bottom of the column (see Figure 4.3 (a)). In contrast, the bubble equivalent diameter shows more dependency on the grid size, especially for grid size of 0.35 mm ×0.35 mm to 0.25 mm ×0.25 mm. Increasing the grid intensity to 0.15 mm×0.15 mm shows little change in the value of bubble equivalent diameter (see

Figure 4.3 (b)). The percentage of deviation between the element sizes 0.25 mm ×0.25 mm and 0.15 mm×0.15 mm in the equivalent diameter for 0.1 s, 0.15 s and 0.2 s are 1.5 %, 1.1 % and 1.1 %, respectively. Therefore, the grid size of 0.25 mm×0.25 mm is adopted in this chapter to simulate the bubble formation and rising inside the BCR.

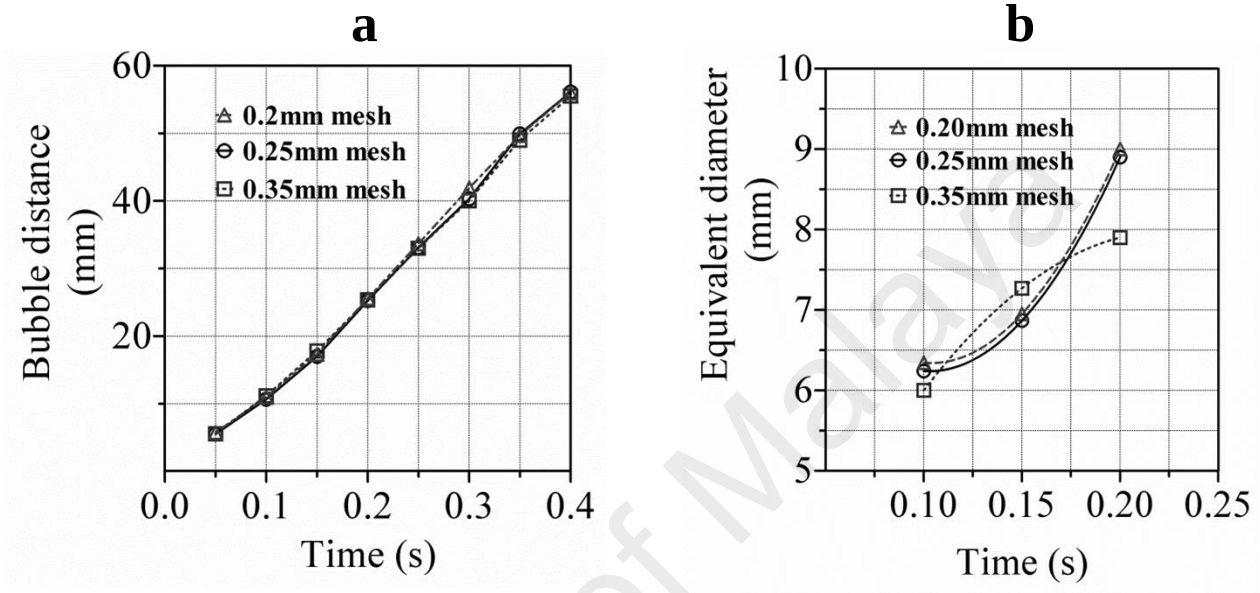

Figure 4.3: Grid independency study of the single bubble dynamics for the orifice gas velocity 0.3 m/s: (a) bubble distance against time; (b) bubble equivalent diameter against time

4.3.5 Validation of CFD method

As a first step, it is important to establish the validity of the VOF method for simulation of bubble size, shape and velocity. Therefore, a comparison has been made with the present experimental observation and existing experimental (Krishna & Van Baten, 1999), numerical (Ma et al., 2012) and mathematical correlation (Krishna & Van Baten, 1999) in the literature. Ma et al. (2012) simulated a 4 mm air bubble in the 50×100 mm 2D BCR filled with quiescent water. The sizes of the BCR and air bubble used in the present numerical method for validation are set to be equal to those used in the investigation of Ma et al.. Figure 4.4 shows the rising velocity of air bubble with a diameter of 4 mm in the quiescent water, versus simulation time for the present and

numerical study of Ma et al. (2012). An excellent comparison was obtained between the present numerical results and Ma et al.'s study for bubble rising velocity at all simulation times, particularly from 0.1-0.3 s. In addition, Table 4.4 compares the terminal velocity obtained from the present numerical study and the experimental data and the empirical correlation of Krishna and Van Baten (1999). Krishna and Van Baten (1999) studied terminal velocity for various air bubble diameters (ranging 0.002-0.014 m) in the BCR diameter, 0.03 and 0.051 m filled with quiescent water. For validation, the bubble diameter of 0.004 and 0.005 are simulated in a similar BCR geometry and compared with their data. The error for terminal velocity obtained from the present numerical study for bubble diameter sizes, 4 and 5 mm are 5.8 % and 6.4 %, respectively. In addition, the terminal velocity obtained from the present numerical study is compared with the empirical correlation of Krishna and Van Baten (1999) and the error for bubble diameter sizes, 4 and 5 mm are 3.4 % and 4.8 %, respectively.

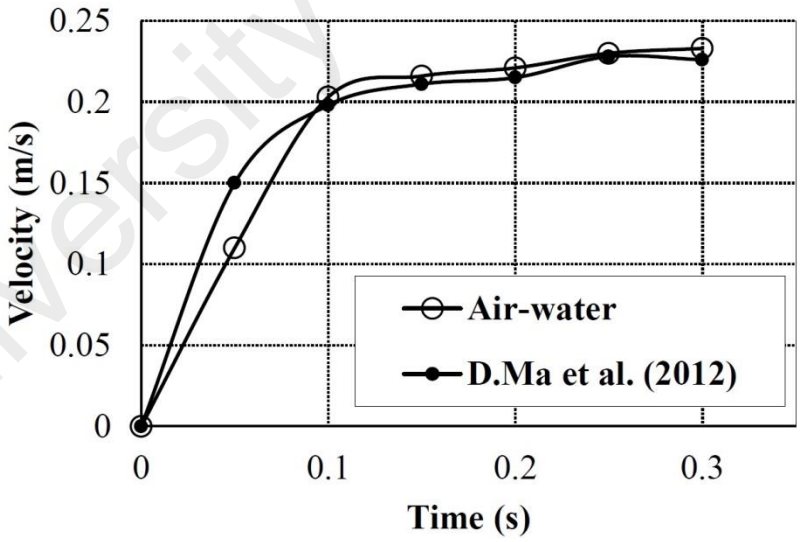

Figure 4.4: Bubble rise velocity versus time for the present numerical study and Ma et al. investigation for 4 mm bubble size

Table 4.4: Terminal bubble velocity of the current numerical simulations, empirical correlations and experimental data of Krishna and Van Baten (1999)

Primary phase	d_b (mm)	Simulation result (m/s)	Correlation result (m/s)	Experimental result (m/s)
Air- water	4	0.225	0.233	0.239
	5	0.216	0.227	0.231

The validity of the present numerical method is also studied by comparing the numerical results with the present experimental observation for the shape of bubble and formation and expansion time when the orifice diameter is 1 mm, as shown in Figure 4.5. According to the figure, as the bubble grows from 0 to 0.063 s, the surface tension force is significantly higher than the buoyancy force, thus resulting in a slow formation of bubble. By increasing the bubble size, the buoyancy force rises and gradually overcomes the surface tension force at 0.11 s. At this moment, the bubble detaches itself from the tip of the orifice. The agreement between the present numerical results and that of the experimental observations can be seen to be excellent for the shape of bubble and formation and expansion time. This result is also consistent with prior studies (Ma et al., 2012).

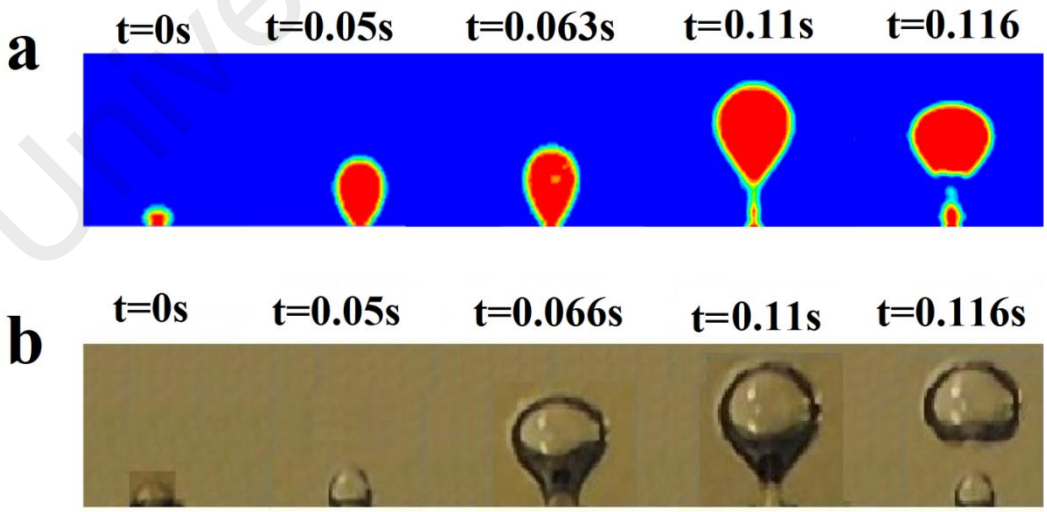

Figure 4.5: Comparison between VOF and experimental observation for the bubble formation at 1 mm diameter orifice size

A comparison between the present experimental and the prior experimental study of Di Marco and Grassi (2009), Di Bari, Lakehal, and Robinson (2013), Albadawi et al. (2013) and Vafaei et al. (2010) and the correlations developed by Tate (1864) for detachment volume, when the flow rate is small (1×10^{-9} m^3/s) is also given in Figure 4.6. The results show that, the present experimental finding is in good agreement with previous experimental observations, particularly for the 0.35 and 0.56 mm orifice diameters. As the shape of the detached bubble is almost spherical for small orifice diameters (i.e., 0.35-0.56 mm), the present experimental results for orifice size 0.35 and 0.56 mm is in good agreement with the Tate correlation formulating the spherical bubble diameter.

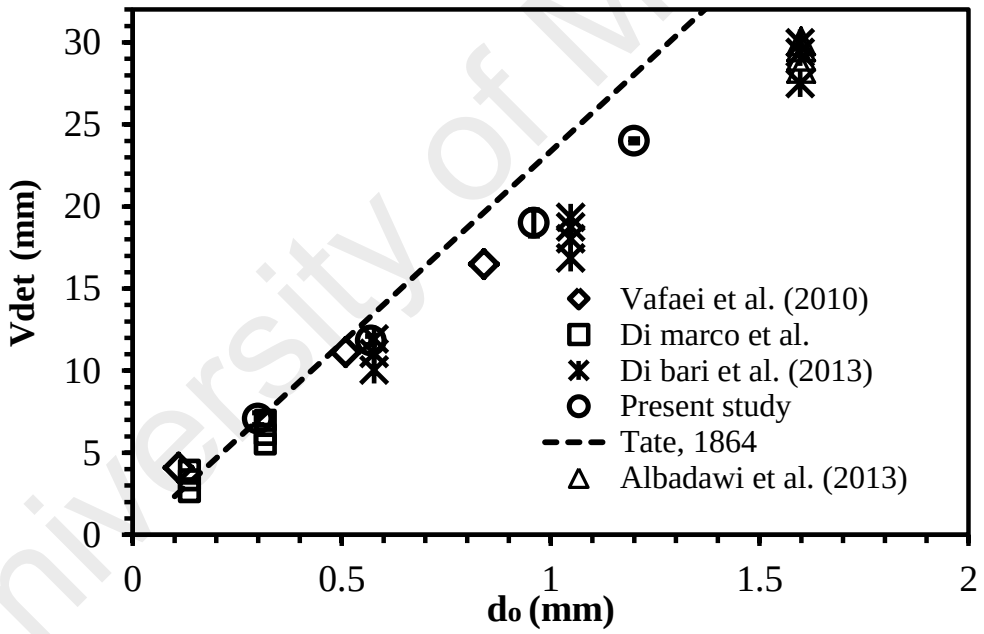

Figure 4.6: Detachment volume versus orifice diameter for the present experimental study and existing experimental studies in the literature at 1×10^{-9} m^3/s flow rate

4.4 Results and discussion

4.4.1 Effect of orifice velocity

Figures 4.7, 4.8 and 4.9 show the bubble formation and rising through a 1 mm orifice for various inlet gas velocities (ranged 0.1-0.6 m/s) and timeframes (0.05-0.4 s). The figures show that the bubble shape, size and number of existing bubbles are highly affected by gas flow rates. The small flow rates, i.e., 0.1-0.2 m/s produce almost identical bubble shapes, sizes and velocities (see Figure 4.7), while by increasing the flow rate, the rate of bubble interactions (coalescence and break-up) rises, resulting in non-uniform bubble sizes, shapes and velocities. In this case, the size of the bubble changes from 0.25 mm to 10 mm due to the occurrence of coalescence and break-up.

For small flow rates (i.e., 0.1-0.2 m/s), the bubble shapes are almost spherical, spherical cap and ellipse. In contrast, by increasing the flow rate up to 0.4 m/s, the bubble size increases and the shapes of bubbles are elongated in a horizontal direction (see Figure 4.8). This is due to the fact that the first bubble produces a large wake area and attracts the next generated bubble (second bubble). When the second bubble reaches the first one, it deforms the shape of the bubble. However, the shape of the second bubble is changed to a bullet at the moment of collision. As the flow rate exceeds 0.4 m/s, the bubble coalescence and break-up are more likely to appear in the BCR. In this case, the bubble shapes are almost non-uniform due to the high rate of coalescence and break-up. In general, large bubbles produce large wake areas and result in fast detachment of the next bubbles. The influence of these wake areas change the next generated bubble size, shape and velocity (see Figure 4.9).

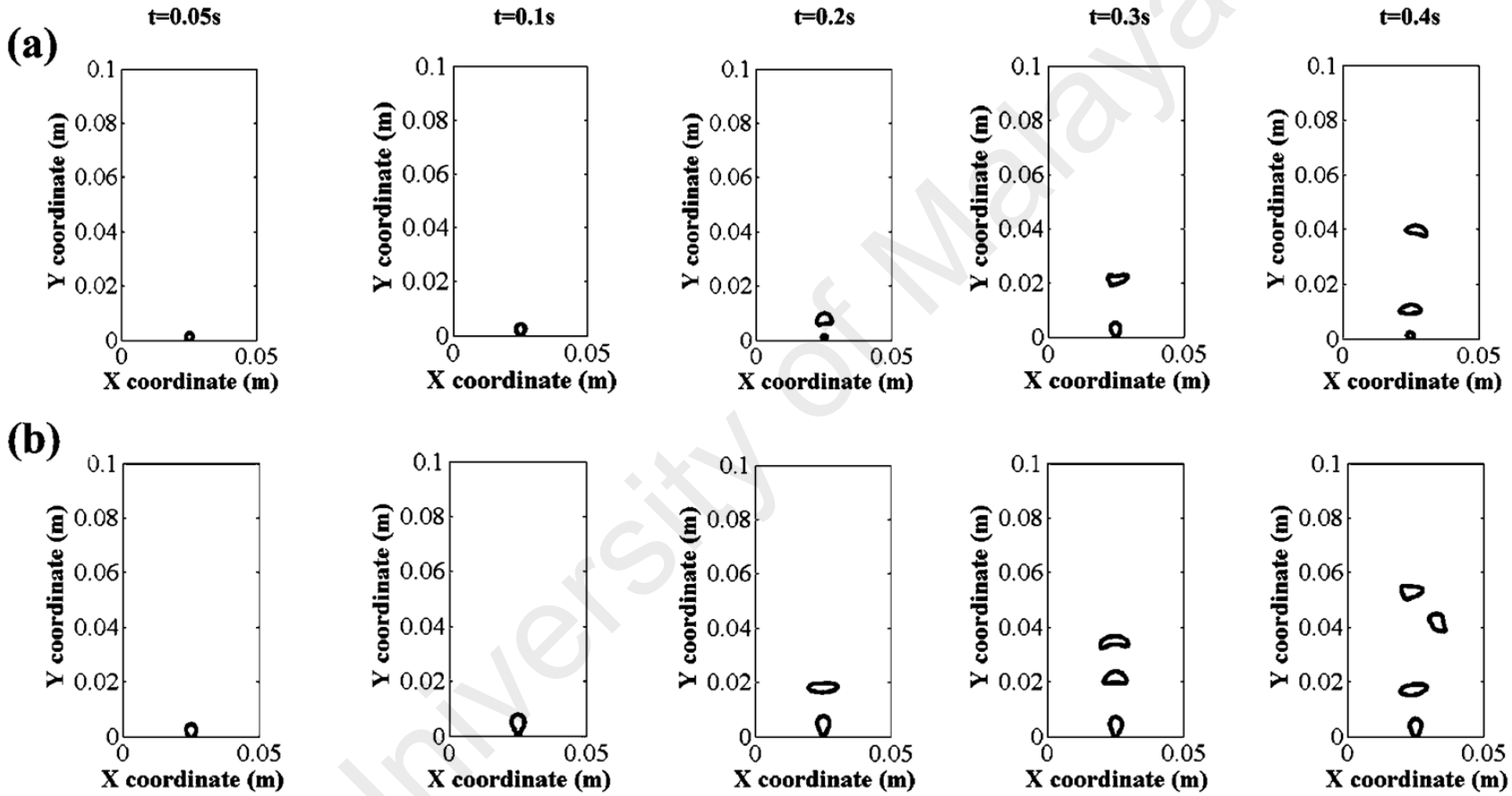

Figure 4.7: Bubble formation and rising at various time instances (i.e., 0.05, 0.1, 0.2, 0.3 and 04 s) for different orifice velocities: (a) S_V=0.1 m/s; (b) S_V=0.2 m/s

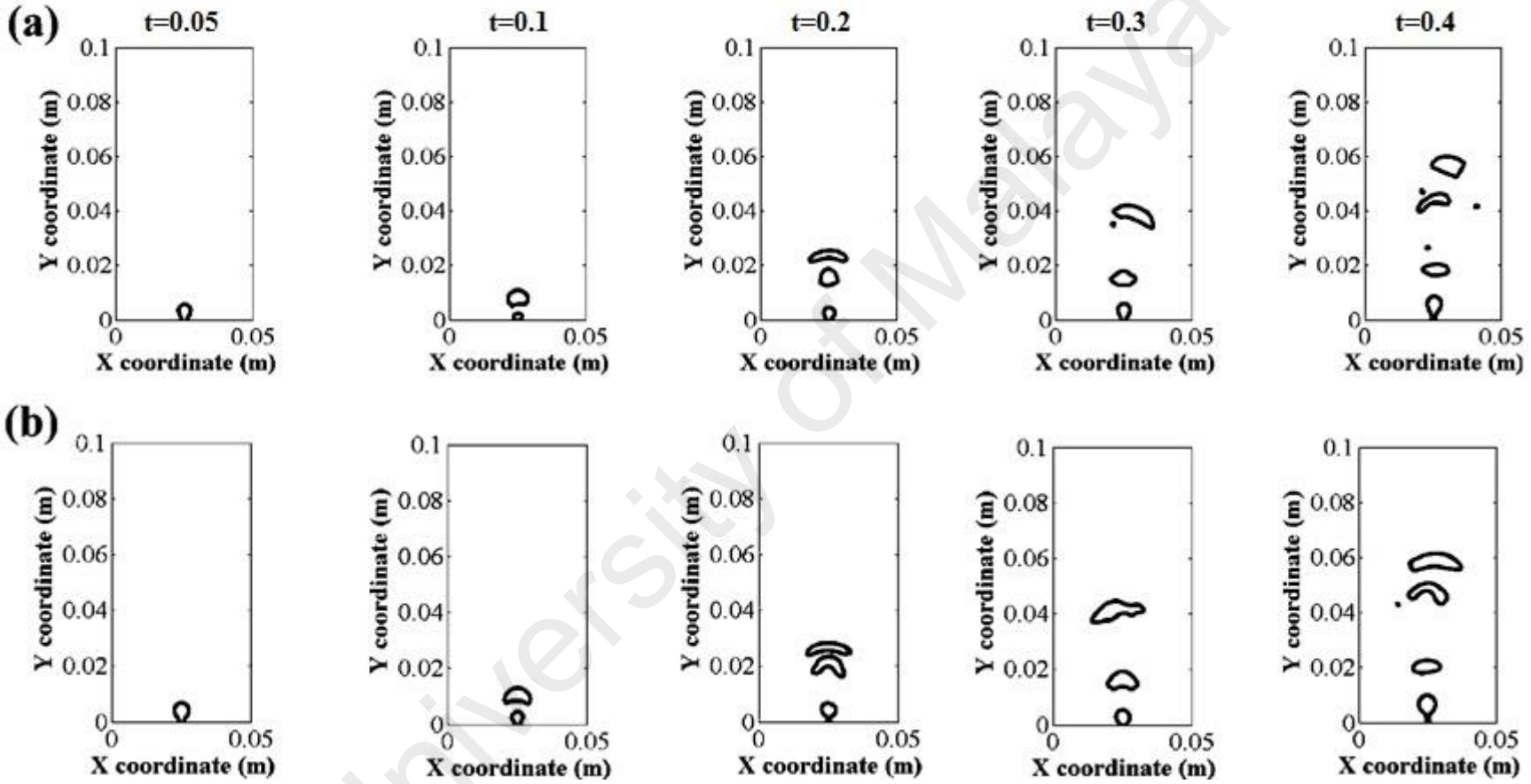

Figure 4.8: Bubble formation and rising at various time instances (i.e., 0.05, 0.1, 0.2, 0.3 and 04 s) for different orifice velocities: (a) S_V=0.3 m/s; (b) S_V=0.4 m/s

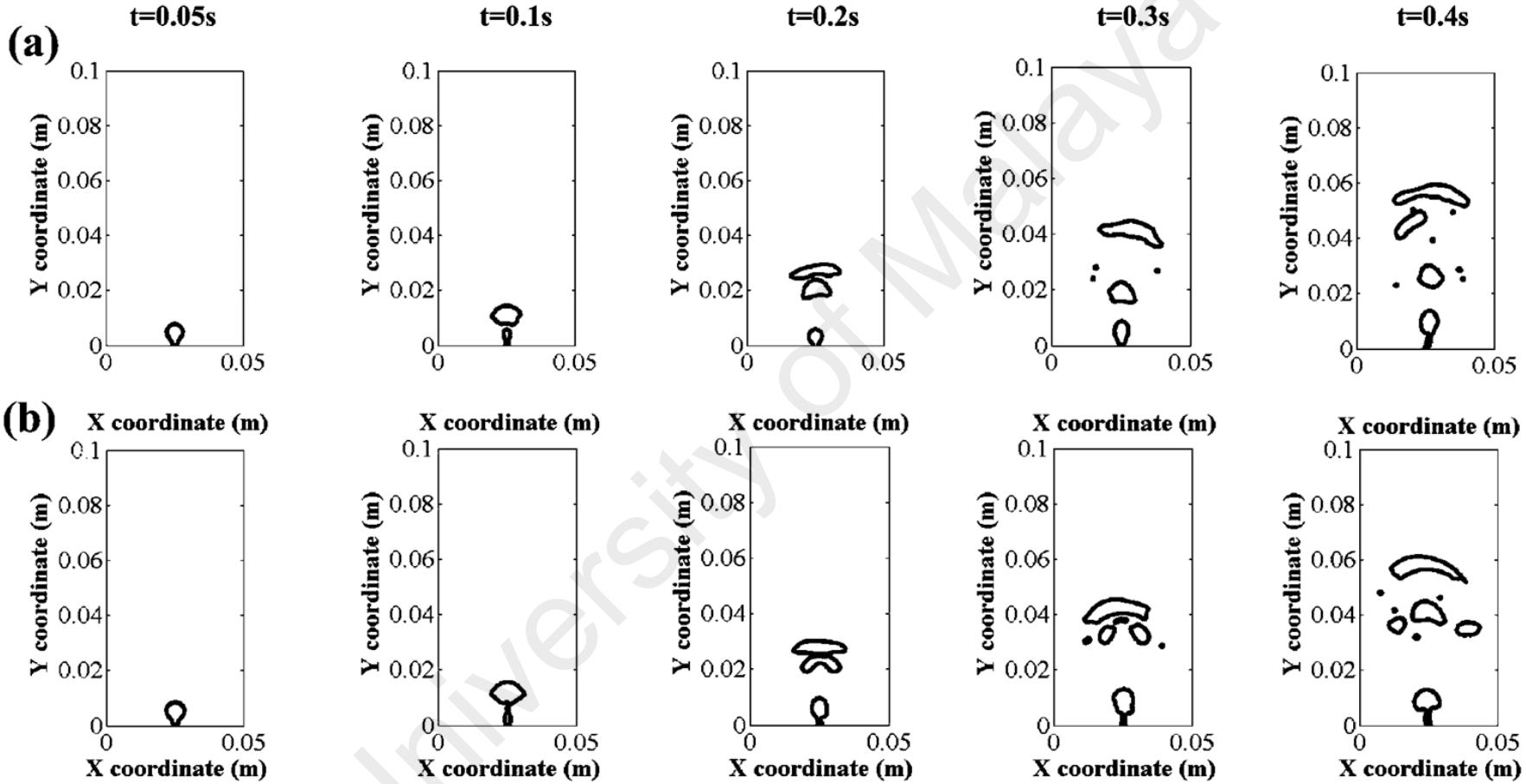

Figure 4.9: Bubble formation and rising at various time instances (i.e., 0.05, 0.1, 0.2, 0.3 and 04 s) for different orifice velocities: (a) S_V=0.5 m/s; (b) S_V=0.6 m/s

4.4.2 Bubble coalescence

As a result of the existing differences in the bubble diameter sizes, the rate of coalescence in the column increases/decreases. Generally, two possible configurations of bubbles occur which are, late and early coalescence. When the orifice velocity less than 0.2 m/s, there is no coalescence near the orifice which results in the production of bubbles of a consistent diameter (see Figure 4.10 (a-c)). In this condition, the diameters of the bubbles are predominantly dictated by the orifice size, and coalescence may happen far from the orifice (late coalescence). With the increase of flow rate, larger bubbles appear, because the coalescence of bubbles often occur with the next generated bubble or the neighbour bubble (early coalescence). The new bubble is detached from the orifice and travels in the same path of the previous bubble following the accumulated bubble (see Figure 4.10 (d-e)). In the early coalescence state, the bubbles also break into smaller sizes (bubble breakage). When breakage occurs, the bubbles separate in the column and locate other bubbles that are adjacent to them (see Figure 4.10 (f)).

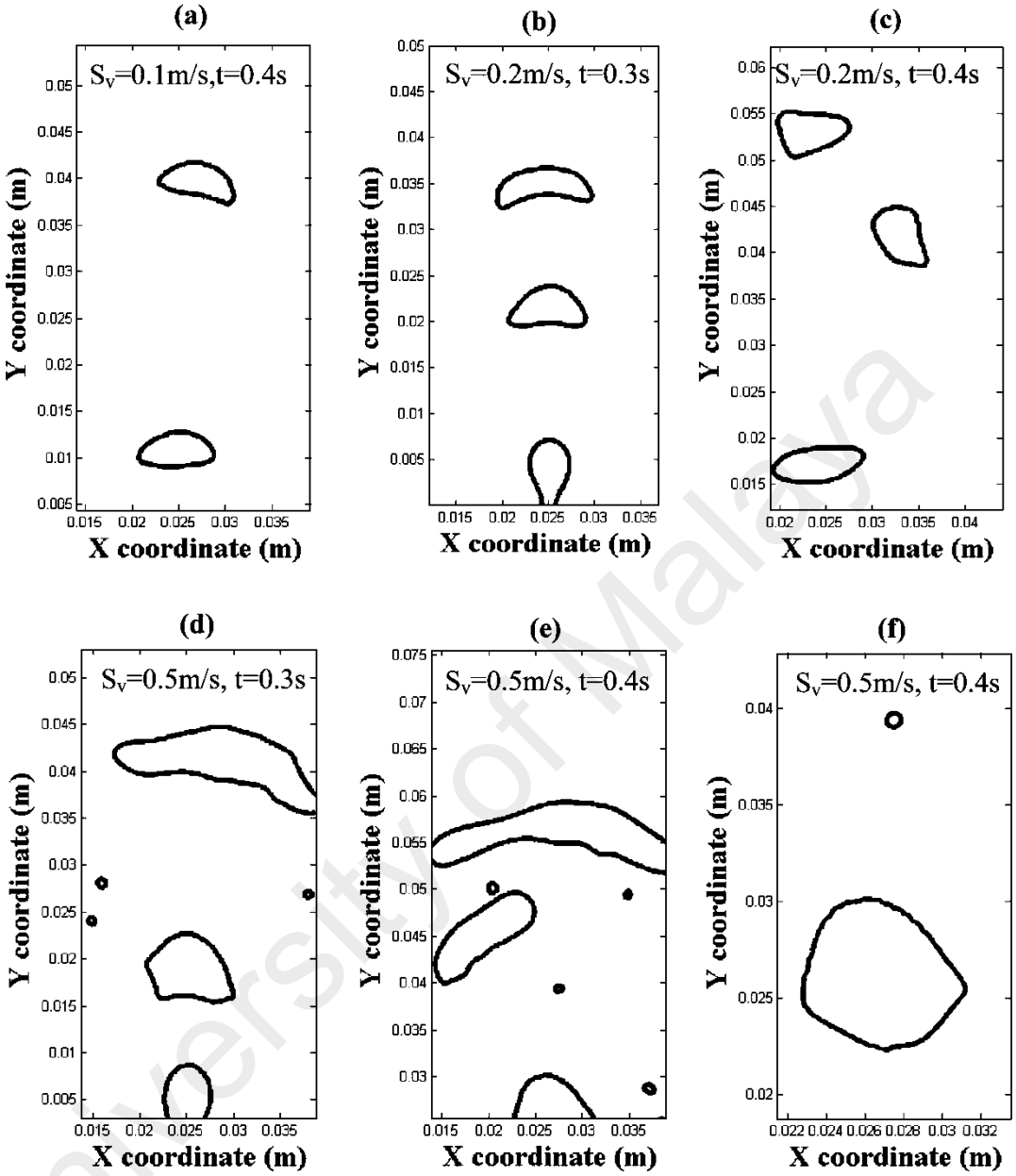

Figure 4.10: Bubble configuration in the BCR: (a, b and c) bubbles sizes are almost similar; (d and e) Upper bubble is bigger than the lower one due to the coalescence process; (f) Upper bubble is smaller than the lower one due to the break-up process

Since the existing different bubble sizes change the coalescence time, the effect of bubble sizes on the coalescence time is studied. Figure 4.11 shows the effect of the diameter of two consecutive bubbles on the possible coalescence time, while they travel vertically. When two consecutive bubbles travel in a vertical position at $t > 0$ s, both of them move towards the top surface of the column with different velocities. Owing to the wake effect of the first bubble, the second bubble experiences less drag and faster movement than the first one. The increase of the second bubble velocity results in bubble collision and the formation of a thin film at the first and second bubble interface. The water within this film is drained until it reaches a critical thickness at which molecular attractive forces dominate and cause the film to rupture and lead to coalescence. The decrease of the upper bubble diameter results in a slower collision and coalescence between bubbles due to the decrease of the weak area behind the first bubble. The Figure shows that for the 4 mm diameter of the upper bubble and 6 mm diameter of the lower bubble, the time almost doubles in comparison with the case, when the upper and lower bubble size are 6 and 4 mm, respectively (see Figure 4.11 (c)). The present results show that decreasing the coalescence time (early coalescence) is caused by existing of large bubbles inside the BCR which are generated by the coalescence process. Therefore, considering an appropriate operation condition to produce a very small bubble (e.g., using a porous plate sparger) or break larger bubbles into smaller ones (e.g., using sieve plate at various BCR heights), changes early coalescence to a late one which improves the BCR efficiency.

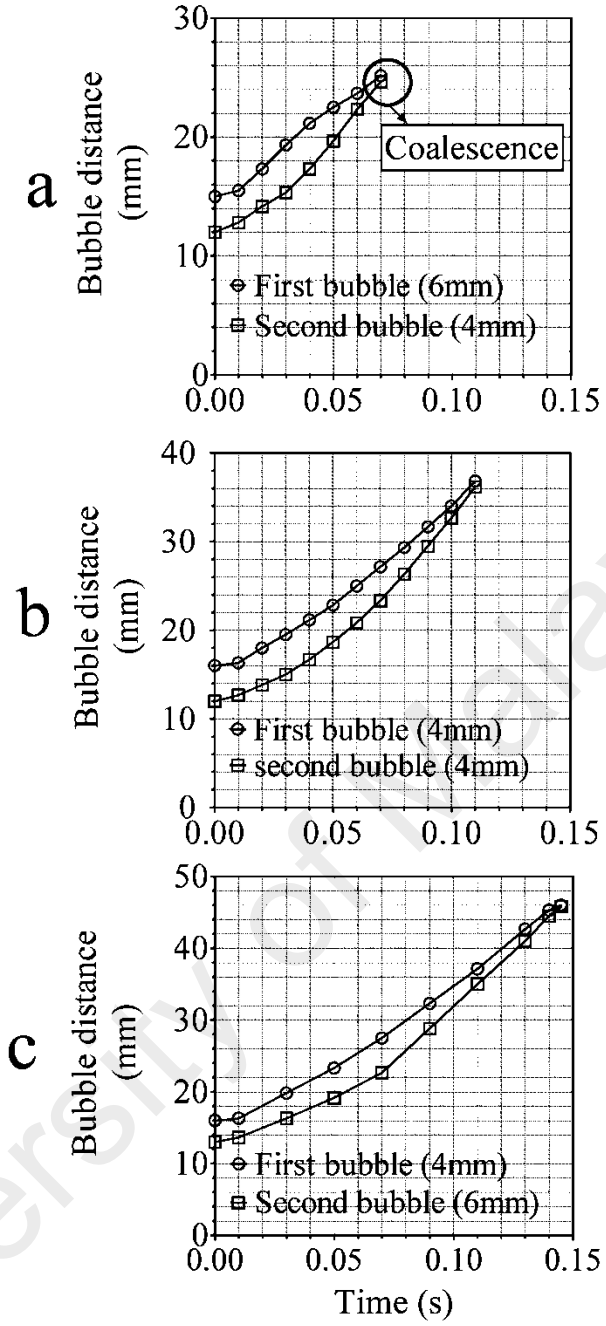

Figure 4.11: Vertical distance for the first and second bubble for various bubble diameters: (a) d_F =6 mm and d_s =4 mm; (b) d_F = d_s =4 mm; (c) d_F =4 mm and d_s =6 mm

4.4.3 Effect of distance between two orifices

In order to avoid coalescence from occurring adjacent to the orifices, determining the distance between orifices has a critical role in the BCR design and manufacturing. The coalescence may occur at different times depending on the distance between orifices. It can be categorized to: a coalescence before detachment time, at the same time as the detachment and after detachment. The ratio of the coalescence time to detachment time ($\alpha = \frac{t_c}{t_d}$) is introduced for better understanding of the effect of the distance between two orifices (D) on coalescence and detachment time. D ranges from 1 mm to 4.5 mm with a step size of 0.5 mm for 1 mm orifices with a inlet gas velocity of 0.1 m/s. Figure 4.12 shows the influence of the distance between two orifices on the bubble coalescence and detachment time. The coalescence occurs faster than bubble detachment when α is smaller than 1 as expected for the small differences between orifices (D<3 mm). In this case, unlike the bubble formation from the single orifice, the shape of bubble changes to a half ring shape during its formation and the bubble size and velocity increase. When α approaches to 1 bubble completely form from orifices and then they merge at the same time with their detachment ($3 \leq D \geq 4$). The detached bubble has an almost similar size and velocity to the bubble when α<1. When α is greater than 1, bubbles collide and accumulate after the detachment time (D>4 mm). In this case, the bubbles spherically grow and detach without interaction and their shapes and velocities are the same as a single bubble formation through one orifice. In general when the ratio of α>1, orifices produce smaller bubbles, higher gas hold-up and interfacial bubble area which improve the BCR efficiency.

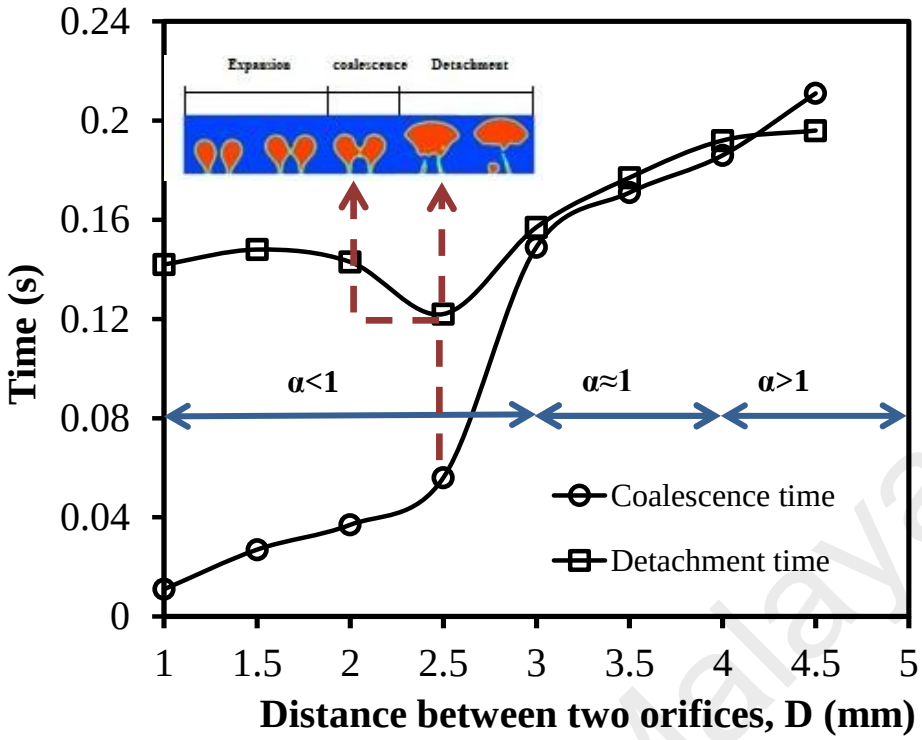

Figure 4.12: Influence of distance between two orifices on coalescence time and detachment time for orifice gas velocity 0.1 m/s and orifices diameter 1 mm

Number of orifices can be another factor to change bubble coalescence and detachment time. The influence of the number of orifices on bubble detachment and coalescence time is studied, when the D is constant (1 mm). The increase in the number of orifices (more than two orifices) has an almost insignificant effect on the bubble coalescence time but results in faster detachment time and larger bubble sizes. Since the increase in the number of orifices results in larger bubbles and a less interfacial area, determining the optimum distance between them can improve the BCR efficiency.

The detachment time is also investigated by fixing one orifice diameter (1 mm) and changing the size of a neighbouring one. Figure 4.13 shows the effect of various orifice diameter sizes (0.25 mm-4 mm) on the bubble detachment time, when both orifices have 0.1 m/s inlet velocity. The Figure shows that in the case of double orifices, when one orifice is smaller than the neighbouring one, there is no difference for bubble detachment (0.25 mm≤orifice size≤0.5 mm). As the orifice diameter increases, the

detachment time gradually decreases due to the increase in the accumulated bubble volume. Because of the occurring of the coalescence adjacent to orifices, the bubble detaches itself faster in contrast to the single orifice (especially single orifice diameter e.g., 0.25 and 0.5 mm). As the altered orifice diameter size increases to more than 2 mm, the bubble detaches itself at almost the same time as the single orifice. In addition, in the case of double orifices, the alteration of one of the orifice diameter size has an insignificant effect on coalescence time.

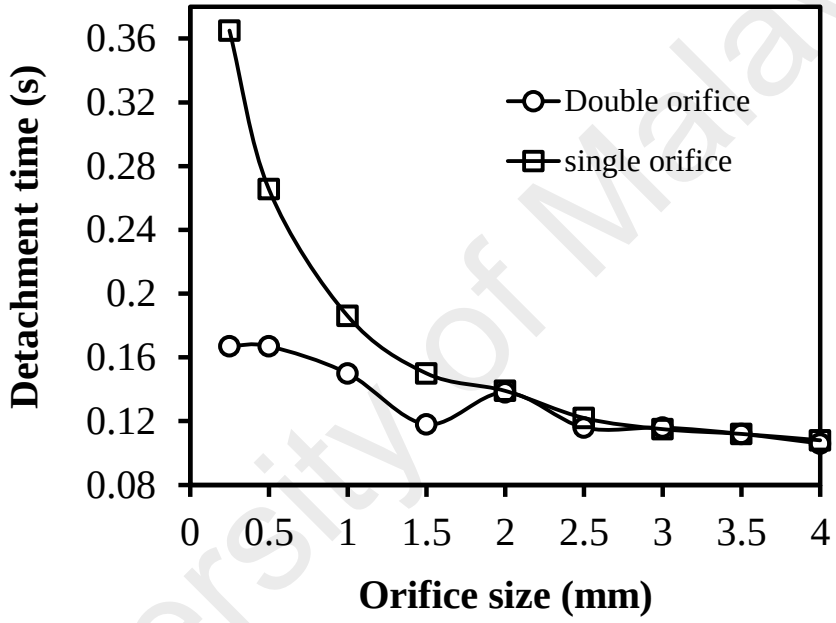

Figure 4.13: Effect of various orifice diameter sizes which are in the vicinity of the orifice with fix diameter 1 mm when orifice gas velocity is 0.1 m/s for both orifices on bubble detachment time and in comparison with single orifice sizes with orifice gas velocity 0.1 m/s

4.4.4 Effect of orifice size and velocity on the bubble volume

The effect of various orifice diameters (i.e., 0.35, 0.56, 1 and 1.20 mm) and flow rates (i.e., 1×10^{-9}-6×10^{-9} m^3/s) on bubble detachment volume is shown in Figure 4.14. As shown in the figure, as the orifice diameter increases, the volume of detachment increases. This is due to the fact that, the bubble requires more volume (corresponding buoyance force) to overcome the surface tension. For instance, the bubble volume for 1

mm orifice diameter is 1.6 times more than 0.56 mm orifice diameter. In contrast, various flow rates have insignificant influence on the bubble detachment time. This is due to the fact that, in very low flow rates (quasi static regime), due to slow formation of bubbles (5-170 s), as shown in Figure 4.14, the detachment volume only depends on the size of the orifice. The size and shape of the bubble in this regime is dictated from the orifice and the influence of the former detached bubble is insignificant. This finding is also consistent with the prior studies (Albadawi et al., 2013; Di Bari et al., 2013; Vafaei & Borca-Tasciuc, 2014).

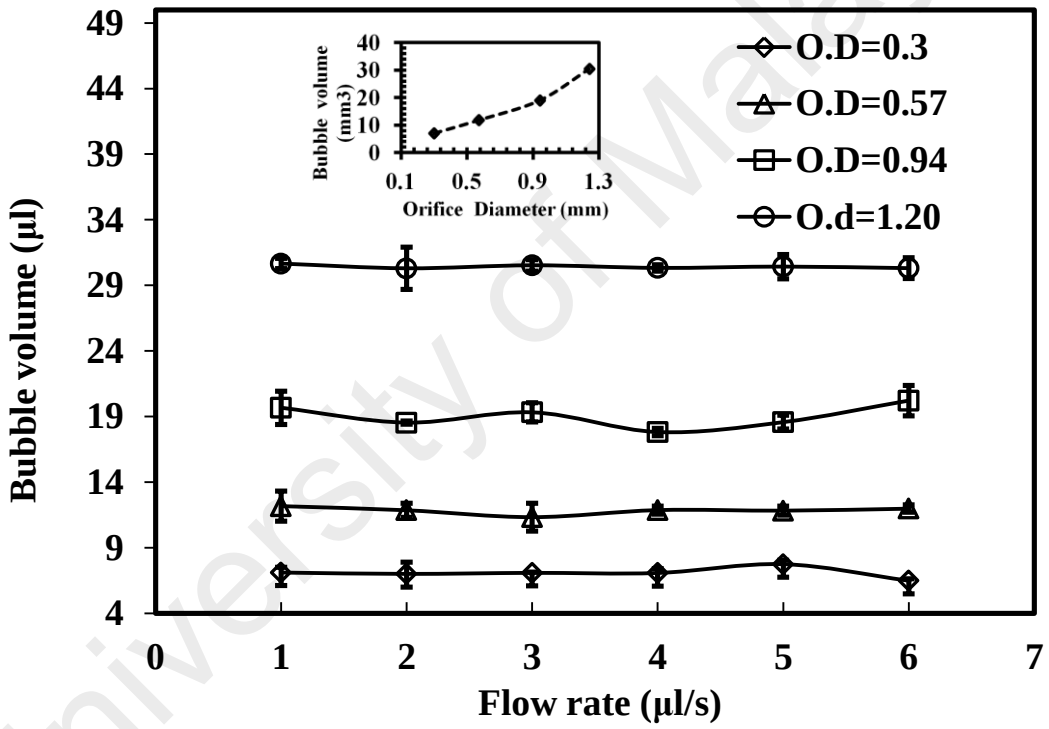

Figure 4.14: Effect of various orifice diameters i.e., 0.35, 0.56, 1 and 1.20 mm on bubble volume detachment for flow rates 1, 2, 3, 4, 5, and 6 μ l /s

4.5 Conclusion

In the present chapter, the effect of orifice velocity and size on bubble formation and rising characteristics has been studied using the numerical method (i.e., VOF) and experimental study. In addition, the effect of the bubble diameter on the coalescence process and influence of distance between orifices on the coalescence and detachment time have been studied. The present experimental results and prior experimental and numerical results as well as empirical correlation in the literature have been used for the validation of the numerical method. Conclusions of this study are as follows:

- As a result of the existing large bubbles (accumulated bubbles), coalescence occurs faster inside the BCR. Therefore selecting the BCR, producing very small bubble sizes (e.g., using porous plate orifice) or breaks in large bubbles into small ones (e.g., using sieve plate at various BCR heights) changes early coalescence to a late one and enhances the BCR efficiency.
- The increase in the number of orifices (more than two orifices) has almost insignificant effect on the bubble coalescence time but results in faster detachment. The increment of this parameter results also in the production of large bubbles with a non-uniform shape. To avoid this unpleasant production inside the column, particularly near the orifice region, optimizing the distance between orifices is critical. This distance must be greater than 4 mm (when the ratio of α >1) which results in a homogeneous regime towards the orifices, smaller bubbles with a uniform shape and higher bubble interfacial area.
- For small flow rates (i.e., $q<6\times10^{-9}$ m^3/s), the increase of orifice size (with constant orifice velocity) enlarges the bubble size and volume and reduces bubble detachment time, while the increment in orifice velocity (with constant orifice size) only decreases the bubble detachment time. For flow rates larger

than 7.85×10^{-8} m^3/s, the increase of both orifice size and velocity results in larger bubble size and volume with faster bubble detachment.

- When the flow rate is small ($q\leq6\times10^{-9}$ m^3/s), bubble shape is predominantly dictated from the orifice. For example, when the orifice size is smaller than 0.56 mm, it produces a spherical bubble shape at the detachment time. However, by increasing the flow rate, the shape of the bubble is not only affected by the orifice parameters but this is also altered by the influence of the former detached bubble size, shape and its wake area.

CHAPTER 5: DEVELOPMENT OF ADAPTIVE NEURO FUZZY INFERENCE SYSTEM (ANFIS) FOR BCR PREDICTION

5.1. Introduction

Although many experimental and numerical techniques (e.g., Euler-Euler and VOF) have been developed to measure and predict BCR hydrodynamics (Dhotre et al., 2013; Dhotre et al., 2004; Dhotre & Joshi, 2007; Kantarci et al., 2005; Pfleger & Becker, 2001; Pfleger et al., 1999; Pourtousi et al., 2014; Tabib et al., 2008), it is not easy to obtain the details of hydrodynamics at all spatial locations for a continuous process in the BCR for all types of operating conditions. For instance, measuring the BCR hydrodynamics experimentally everywhere in a column is extremely expensive since this requires a number of measuring equipments. In addition, the measuring probe placement in the BCR sometimes causes flow disturbances. Although the CFD method solves these problems, it requires a huge computational effort especially for a large BCR domain and various operation conditions (Dhotre et al., 2013; Dhotre et al., 2004; Dhotre & Joshi, 2007; Díaz et al., 2008; Kantarci et al., 2005; G. Li et al., 2009; Pfleger & Becker, 2001; Pfleger et al., 1999; Pourtousi et al., 2014; Tabib et al., 2008). Soft computing methods, e.g., the ANFIS method can be used as an alternative to predict the multiphase flow in BCRs for different operation conditions.

The present chapter describes the development of the ANFIS method for the prediction of the liquid flow pattern and gas dynamics for the BCR case described in Sec. 3.2.3. In addition, the effect of various ANFIS setting parameters (i.e., membership function (*M.F*) and percentage of training data (*P*)) on the prediction accuracy will be discussed.

5.2. Methodology

5.2.1 Adaptive-Network-based Fuzzy Inference System (ANFIS)

ANFIS is an inference fuzzy system to accurately predict the behavior of complex and nonlinear systems. Figure 5.1 shows the structure of the employed ANFIS method for predicting the hydrodynamic characteristics in the 3D BCR. Various inputs i.e., sparger diameter, X,Y and Z coordinate of mesh are taken to obtain the gas hold-up, TKE and liquid velocity components as output. The inputs are divided into various numbers of membership functions (*MF*s) in the first layer. The incoming signals from the first layer are multiplied according to the AND rule as the node function for the second layer. For instance, the function of the ith rule for three inputs (i.e., ring sparger diameters, X and Y coordinate of mesh) is described as:

$$w_i = \mu_{A_i}\left(D_s\right) \times \mu_{B_i}\left(x\right) \times \mu_{C_i}\left(H\right) \tag{1}$$

where w_i is the out coming signal of the second layer's node and μ_{A_i}, μ_{B_i} and μ_{C_i} are incoming signals from the implemented *MF*s on the inputs, sparger diameter (D_s), Y coordinate of mesh (H) and X coordinate of mesh (x), to the second layer's node.

In layer three, the relative value of the firing strength of each rule is calculated. This value is equal to the weight of each layer over the total amount of the firing strengths of all rules:

$$\bar{w}_i = \frac{w_i}{\sum_{i=1}^{n}\left(w_i\right)} \tag{2}$$

where $\bar{w}_i$ is called normalized firing strengths. The fourth layer applies the function of the consequence if-then rule proposed by Takagi and Sugeno (T. Takagi & Sugeno, 1985). Thus, the node function can be described as:

$$\bar{w}_i f_i = \bar{w}_i\left(p_i D_s + q_i x + r_i H + s_i\right) \tag{3}$$

where p_i, q_i, r_i and s_i are the if-then rules' parameters and called consequent parameters. All incoming signals from layer four are aggregated to obtain the model output, which represent the estimation result.

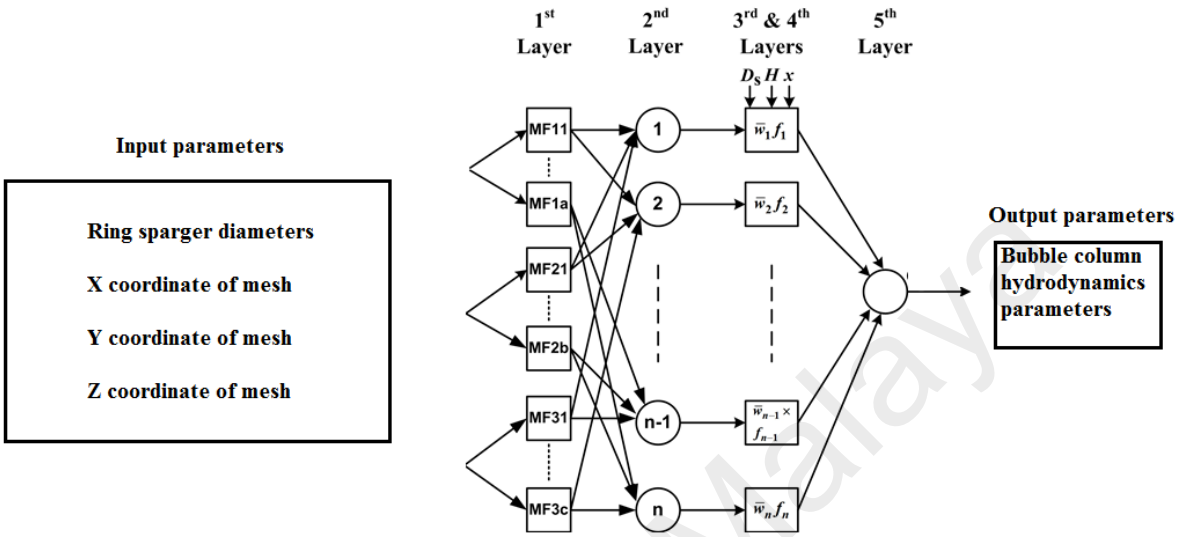

Figure 5.1: Schematic diagram of the ANFIS architecture structure

A hybrid-learning algorithm is used to update the parameters in which the *MF* parameters are updated using the gradient descent method and consequent parameters are updated using the Least Squares Estimate (LSE) method. In other words, this algorithm trains and adjusts the premise and consequent parameters. In this study, six different membership functions, i.e., Gaussian-shaped ('*gauss'* and *'gauss2'*), Triangular-shaped ('*tri'*), Trapezoidal-shaped ('*tra*'), Bell-shaped ('*gbell*') and p-shaped (*'pi'*) are examined. *P* is used to set the percentage of training data (input data) which describes the ability of method to train and predict the parameters and *I* is defined as a iteration of overall code to compute and train data.

5.2.2 Accuracy of ANFIS model

The performance and accuracy of the ANFIS method is calculated based on the statistic parameters as follows:

- Root Mean Square Error (RMSE):

  RMSE is used to calculate the difference between the ANFIS prediction values and actual data, which is

$$RMSE = \sqrt{\frac{\sum_{i=1}^{n}(P_i - O_i)^2}{n}} \tag{4}$$

- Pearson correlation coefficient (r)

  The coefficient is used to represent a linear correlation between the ANFIS values and CFD results, showing a value between +1 and −1 and is represented as follows:

$$r = \frac{n\left(\sum_{i=1}^{n} O_i \cdot P_i\right) - \left(\sum_{i=1}^{n} O_i\right) \cdot \left(\sum_{i=1}^{n} P_i\right)}{\sqrt{\left(n\sum_{i=1}^{n} O_i^2 - \left(\sum_{i=1}^{n} O_i\right)^2\right) \cdot \left(n\sum_{i=1}^{n} P_i^2 - \left(\sum_{i=1}^{n} P_i\right)^2\right)}} \tag{5}$$

- Coefficient of determination (R^2),

  R^2 is a criterion that illustrates how well the ANFIS data fits a statistical model and is given as follows:

$$R^2 = \frac{\left[\sum_{i=1}^{n}\left(O_i - \overline{O_i}\right) \cdot \left(P_i - \overline{P_i}\right)\right]^2}{\sum_{i=1}^{n}\left(O_i - \overline{O_i}\right) \cdot \sum_{i=1}^{n}\left(P_i - \overline{P_i}\right)} \tag{6}$$

  where O_i, P_i, and n are the ANFIS (predicted) values, actual data and overall number of test data, respectively.

5.2.3 Development of the ANFIS model for predictions

Matlab software (version 2014) has been used to develop the ANFIS model. The flowchart of the ANFIS code development in Matlab is shown in Figure 5.2. Please refer to Appendix A for the code details. At first, 70 % of the CFD results data from Chap. 3 is given as an input for the training process of ANFIS. In ANFIS, the parameters such as the Membership Function (*M.F*), Number of Iteration (*I*) and Percentage of training data (*P*) have be to set to a reasonable value for an accurate prediction. These values are iteratively corrected until the convergence criteria are reached which are based on R^2>0.9, MSE<0.01 and RMSE<0.01. According to the previous studies, the R^2 should be more than 0.80 and the error between the predicted data and actual value should be less than 5 % for accurate prediction (Mayer & Butler, 1993). Therefore, an ANFIS model for a selected case has been developed using 70 % of the CFD data. The capability of the developed ANFIS model is then tested by comparing with the remaining 30 % of the CFD data. Please take note, the process is referred to as ANFIS testing in the flowchart (Fig. 5.2a). A good ANFIS model can be used for a completely new prediction in which none of data has used in the training process. Figure 5.2 (b) shows the prediction steps. Firstly, a new ANFIS mesh domain is generated and then the developed ANFIS model is used to predict the required results. For validation, the ANFIS results are compared against the CFD results.

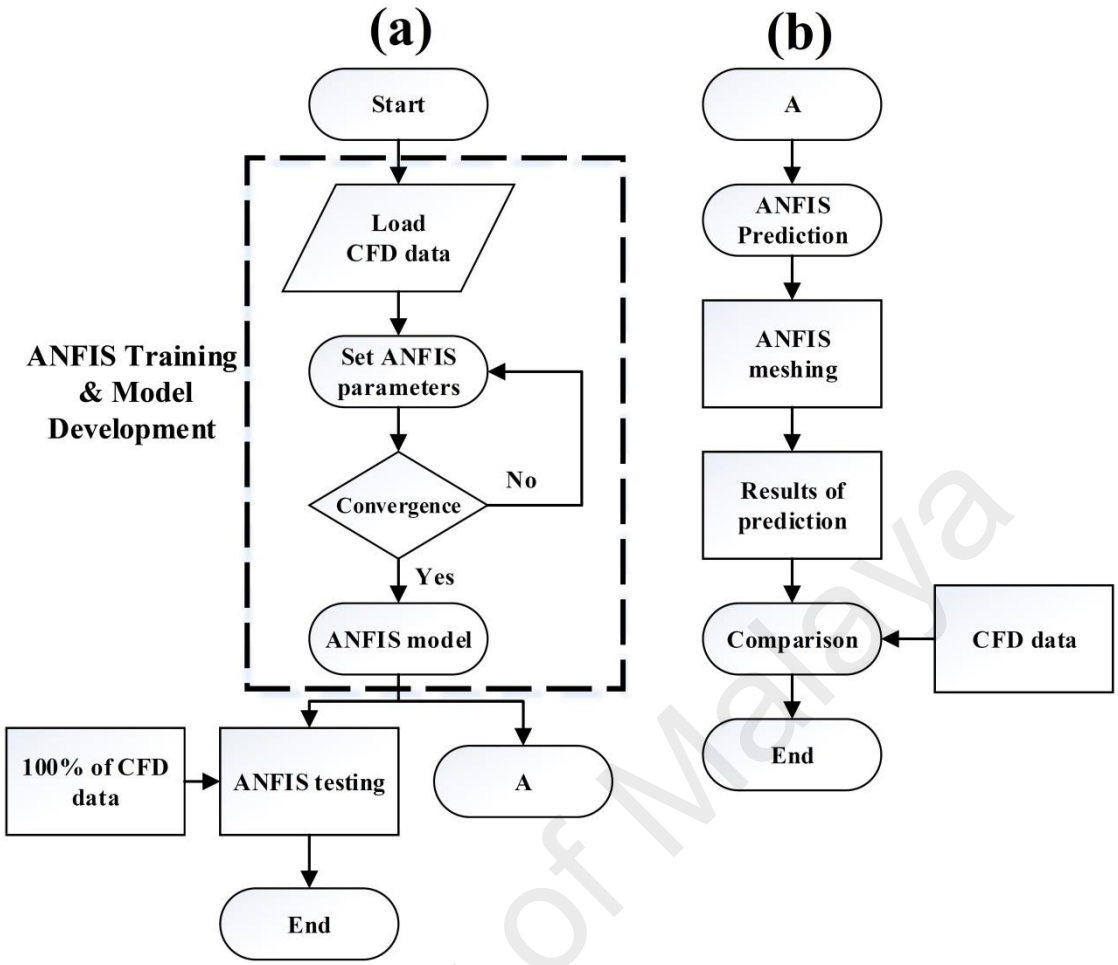

Figure 5.2: Flow-chart of ANFIS code development; (a) Training, Model development and Testing process; (b) Prediction process

5.2.4 Simulation cases

Simulations cases are sectioned to three main categories, namely, (a) Training and testing of ANFIS; (b) Sensitivity study of ANFIS setting parameters; and (c) ANFIS model development and prediction.

a. Training and testing (T-T) of ANFIS

A total of eight cases (Cases 1-8) are used to examine the capability of the ANFIS model for the prediction of the BCR hydrodynamics, see Table 5.1. Herein, the CFD results of Case 1 (Chap. 3) are used for the training, development and testing of the developed ANFIS model. At first, five cases (Cases 1-5) are used to T-T of U_x, U_y, U_Z,

T.K.E and ϵ_g at the column heights of 1.3, 1.5, 1.6 and 1.69 m. In these cases, 70 % of the CFD results, i.e., for 494 nodes, is given as input to ANFIS for the training and model development purpose. For testing, the developed ANFIS model is used to predict for 705 nodes, which represent 100 % of the data. Under the ANFIS setting parameters, the membership function (*MF*), number of rules (*N.R*) and iteration (*I*) and percentage of training data *P* are set to : '*gbell*', 8, 1000 and 70 %, respectively. Similarly, three cases (Cases 6-8) are used to T-T the gas hold-up (ϵ_g) near the sparger (h=0.0001 m), at the middle (h=0.823 m) and near the top surface (h=2.56 m). The ANFIS results from the training (494 nodes) and testing (705 nodes) will be presented in the section on Results and Discussion.

b. Sensitivity study of ANFIS setting parameters

A total of 9 (Cases 9-17) simulation cases were used to study the sensitivity of the ANFIS setting parameters and its value on the prediction accuracy. This will allow for an appropriate selection of the parameters and values.

Table 5.2 shows the sensitivity study of the ANFIS setting parameters (i.e., *P* and *M.F*), which are:

Percentage of training data (*P*)

The effect of different percentages of the input data (*P*), namely 70 %, 30 %, 10 % and 5 %, on the results of the gas hold-up at a 1.6 m column height is tested using Cases 9-12. Parameter *I*, *M.F* and *N.R* are set to 1000, '*gbell*' and 8, respectively. The purpose of this test is to evaluate an appropriate percentage of the input data (actual data) for the ANFIS model development.

Membership function (*M.F)*

Cases 13-17 are used to study the effect of six different membership functions (*M.F*), i.e., Gaussian-shaped (‘*gauss’* and *‘gauss2’*), Triangular-shaped (‘*tri’*), Trapezoidal-shaped (‘*tra*’), Bell-shaped (‘*gbell*’) and p-shaped (*‘pi’*) on the prediction of U_x, U_y , U_Z, T.K.E and ϵ_g at column heights of 1.3, 1.5, 1.6 and 1.69 m. Parameter *I*, *P* and *N.R* are set to 1000, 70 % and 8, respectively.

c. ANFIS model Development & Prediction

Some cases will be carried out in this section to test the ability of the ANFIS model for a new prediction. For example, Case 18 is used to predict the results of ϵ_g at column heights (Y mesh coordinate) of 0.43, 0.86, 1.3, 1.73, 2.16 and 2.56 m, see Table 5.3 for details. The number of prediction data in X and Z mesh coordinate is now increased to 4800 nodes. For the ANFIS training and model development, 70 % of the actual data, which is the CFD results from Chap. 3, at column heights of 0.217, 0.47, 0.73, 0.997, 1.3, 1.56, 1.8, 2.08, 2.3 and 2.6 m is given as an input. In addition, the number of data in X and Z mesh coordinate for the input is reduced to three quarters or to only 490 nodes. Please take note, the prediction is for the column heights that are not given as input data to the ANFIS model and hence the ability of the model is tested. The ANFIS model setting parameters *P*, *M.F*, *I* and *N.R* are set to 70 %, ‘*gbell*’, 1000 and 8, respectively.

Cases 19-21 are used to predict U_y, T.K.E and ϵ_g for different ring sparger diameters, see Table 5.3 for details. However, for these cases, the prediction is limited to the X-Y plane (2-D rectangular domain) for simplicity. U_y, T.K.E and ϵ_g input data, which is CFD results from Chap. 3 (Cases 16, 17, 18 and 26-31), for the ANFIS training and model development are for:

(i) sparger diameters ranging from 0.05 to 0.17 m with a step size of 0.02;

(ii) bubble column height or Y mesh coordinate ranging from 0 to 2.6 m with a step size of 0.0433;

(iii) 50 nodes X mesh coordinates

U_y, T.K.E and ϵ_g for ring sparger diameters from 0.08 to 0.14 m with step size of 0.02 are predicted using the ANFIS model for the same X and Y mesh. Parameter *P, M.F, I* and *N.R* are set to 70 %, '*gbell*', 1000 and 8, respectively.

5.2.5 ANFIS mesh

In the prediction section, the new mesh domain is generated to represent the cylindrical bubble column. This domain contains 288000 nodes, see Figure 5.3. The cross section has 4800 nodes and the height of the column is divided into 60 sections.

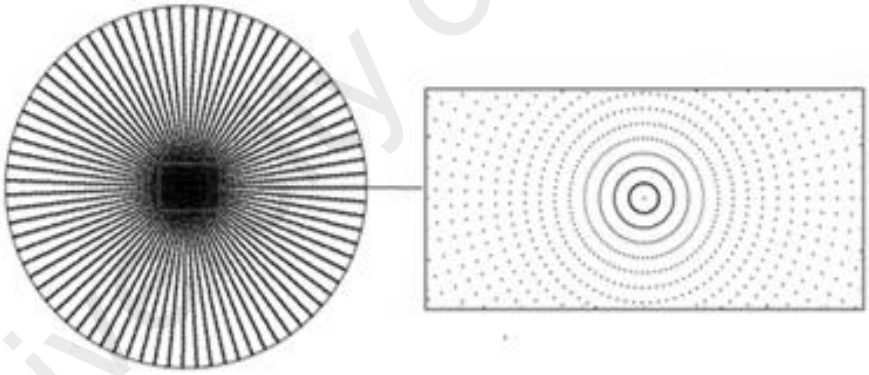

Figure 5.3: Grid intensity of ANFIS study containing 288000 nodes

Table 5.1: Simulation cases for the training and testing of ANFIS

Case study	Training/Model development		Testing		ANFIS setting Parameters	Remarks	CFD Simulation cases Chap.3
	Input		Output				
1-5	X-coordinate of mesh	494 nodes	X-coordinate of mesh	705 nodes	*N.R* =8 *P*=70 % *M.F*='*gbell*' *I*=1000	Validation of ANFIS method for various BCR hydrodynamics	Case 1
	Y-coordinate of mesh for selected heights	1.3, 1.5, 1.6 and 1.69 m	Y-coordinate of mesh	1.3, 1.5, 1.6 and 1.69 m			
	Z-coordinate of mesh	494 nodes	Z-coordinate of mesh	705 nodes			
	Hydrodynamics parameters	U_x U_y, U_Z T.K.E ϵ_g	Hydrodynamics parameters	U_x U_y, U_Z T.K.E ϵ_g			
6	X-coordinate of mesh	494 nodes	X-coordinate of mesh	705 nodes	*N.R* =8 *P*=70 % *M.F*='*gbell*' I=1000	Validation of gas hold-up at 0.0001 m column height	Case 1
	Y-coordinate of mesh	0.0001 m	Y-coordinate of mesh	0.0001 m			
	Z-coordinate of mesh	494 nodes	Z-coordinate of mesh	705 nodes			
	Hydrodynamics parameters	ϵ_g	Hydrodynamics parameters	ϵ_g			
7	X-coordinate of mesh	494 nodes	X-coordinate of mesh	705 nodes	*N.R* =8 *P*=70 % *M.F*='*gbell*' *I*=1000	Validation of gas hold-up at 0.823 m column height	Case 1
	Y-coordinate of mesh	0.823 m	Y-coordinate of mesh	0.823 m			
	Z-coordinate of mesh	494 nodes	Z-coordinate of mesh	705 nodes			
	Hydrodynamics parameters	ϵ_g	Hydrodynamics parameters	ϵ_g			

8	X-coordinate of mesh	494 nodes	X-coordinate of mesh	705 nodes	*N.R* =8 *P*=70 % *M.F*='*gbell*' *I*=1000	Validation of gas hold-up at 2.56 column height	Case 1
	Y-coordinate of mesh	2.56 m	Y-coordinate of mesh	2.56 m			
	Z-coordinate of mesh	494 nodes	Z-coordinate of mesh	705 nodes			
	Hydrodynamics parameters	ϵ_g	Hydrodynamics parameters	ϵ_g			

Table 5.2: Sensitivity study of ANFIS setting parameters

Case study	**Training**		**Testing**		**ANFIS setting Parameters**	**Remarks**	**CFD Simulation cases Chap.3**
	Input		**Output**				
9	X-coordinate of mesh	494 nodes	X-coordinate of mesh	705 nodes	*N.R* =8 *P*=70 % *M.F*='*gbell*' *I*=1000	Sensitivity study of percentage of training data	Case 1
	Y-coordinate of mesh	1.6 m	Y-coordinate of mesh	1.6 m			
	Z-coordinate of mesh	494 nodes	Z-coordinate of mesh	705 nodes			
	Hydrodynamics parameters	ϵ_g	Hydrodynamics parameters	ϵ_g			
10	X-coordinate of mesh	212 nodes	X-coordinate of mesh	705 nodes	*N.R* =8 *P*=30 % *M.F*='*gbell*' *I*=1000		Case 1
	Y-coordinate of mesh	1.6 m	Y-coordinate of mesh	1.6 m			
	Z-coordinate of mesh	212 nodes	Z-coordinate of mesh	705 nodes			
	Hydrodynamics parameters	ϵ_g	Hydrodynamics parameters	ϵ_g			

11	X-coordinate of mesh	50 nodes	X-coordinate of mesh	705 nodes	*N.R* =8 *P*=10 % *M.F*='*gbell*' *I*=1000	Sensitivity study of percentage of training data	Case 1
	Y-coordinate of mesh	1.6 m	Y-coordinate of mesh	1.6 m			
	Z-coordinate of mesh	50 nodes	Z-coordinate of mesh	705 nodes			
	Hydrodynamics parameters	ϵ_g	Hydrodynamics parameters	ϵ_g			
12	X-coordinate of mesh	35 nodes	X-coordinate of mesh	705 nodes	*N.R* =8 *P*=5 % *M.F*='*gbell*' *I*=1000		Case 1
	Y-coordinate of mesh	1.6 m	Y-coordinate of mesh	1.6 m			
	Z-coordinate of mesh	35 nodes	Z-coordinate of mesh	705 nodes			
	Hydrodynamics parameters	ϵ_g	Hydrodynamics parameters	ϵ_g			
13-17	X-coordinate of mesh	494 nodes	X-coordinate of mesh	705 nodes	*N.R* =8 *P*=70 % *M.F*='*gbell*' *'Gauss'* *'Gauss2'*, *'tri'*, *'trap'* *'pi'* *I*=1000	Sensitivity study of membership function	Case 1
	Y-coordinate of mesh	1.3, 1.5, 1.6 and 1.69 m	Y-coordinate of mesh	1.3, 1.5, 1.6 and 1.69 m			
	Z-coordinate of mesh	494 nodes	Z-coordinate of mesh	705 nodes			
	Hydrodynamics parameters	U_x U_y, U_Z T.K.E ϵ_g	Hydrodynamics parameters	U_x U_y, U_Z T.K.E ϵ_g			

Table 5.3: Simulation cases for model development and prediction

Case study	Training		Prediction		ANFIS Setting	Remarks	CFD Simulation cases Chap.3
	Input		Output				
18	X-coordinate of mesh	494 nodes	X-coordinate of mesh	4800 nodes	*N.R* =5 *P*=70 % *M.F*='*gbell*' *I*=1000	Prediction of ϵ_g, at X, Y and Z coordinate.	Case 1
	Y-coordinate of mesh	0.217, 0.47, 0.73, 0.997, 1.3, 1.56, 1.8, 2.08, 2.3 and 2.6 m	Y-coordinate of mesh	0.43, 0.86 1.3, 1.73, 2.16 and 2.56 m			
	Z-coordinate of mesh	494 nodes	Z-coordinate of mesh	4800 nodes			
	Hydrodynamics parameters	ϵ_g	Hydrodynamics parameters	ϵ_g			
19-21	X-coordinate of mesh	50 nodes	X-coordinate of mesh	50	*N.R* =8 *P*=70 % *M.F*='*gbell*' *I*=1000	Prediction of ϵ_g U_y, and T.K.E for various ring sparger diameters at Y coordinate	Case 16, 17, 18 and 26-31
	Y-coordinate of mesh	0-2.6 m Step size=0.0433	Y-coordinate of mesh	0-2.6 m			
	Ring sparger diameters	0.05-0.17 m size=0.02	Sparger diameter	0.08, 0.010, 0.012 and 0.014			
	Hydrodynamics parameters	ϵ_g U_y, T.K.E	Hydrodynamics parameters	ϵ_g U_y, T.K.E			

5.3. Results & Discussion

5.3.1 Training and testing (T-T) of ANFIS

Cases 1-5

Using Cases 1-5 (Sec. 5.2.4), the BCR hydrodynamics parameters of ϵ_g, T.K.E, U_x, U_y and U_Z are predicted at 1.3, 1.5, 1.6 and 1.69 m column heights using the ANFIS and the results are compared with the actual values from the CFD results from Chap. 3 at the same heights. The coefficient of determination (R^2) between the ANFIS and the CFD results of ϵ_g, T.K.E, U_x, U_y and U_Z are shown in Figure 5.4 for the training (ANFIS model development) and testing. For training, R^2 value of ϵ_g, T.K.E, U_x, U_y and U_Z is 0.9686, 0.9717, 0.9865, 0.997, 0.99, respectively. This shows that a high correlation between the predicted and actual values has been achieved and a reasonable ANFIS model has been developed. Please take note that only 70 % of the actual data has been used for the training. Testing of the ANFIS model is carried out by comparing with 100 % of the actual data and R^2 value of ϵ_g, T.K.E, U_x, U_y and U_Z is 0.961, 0.9626, 0.9724, 0.9962, 0.9779 , respectively suggesting an accurate prediction is achieved using the ANFIS model. However, there is a small drop (maximum 2 %) in the testing of R^2 values in comparison to that of the training and this is not significant.

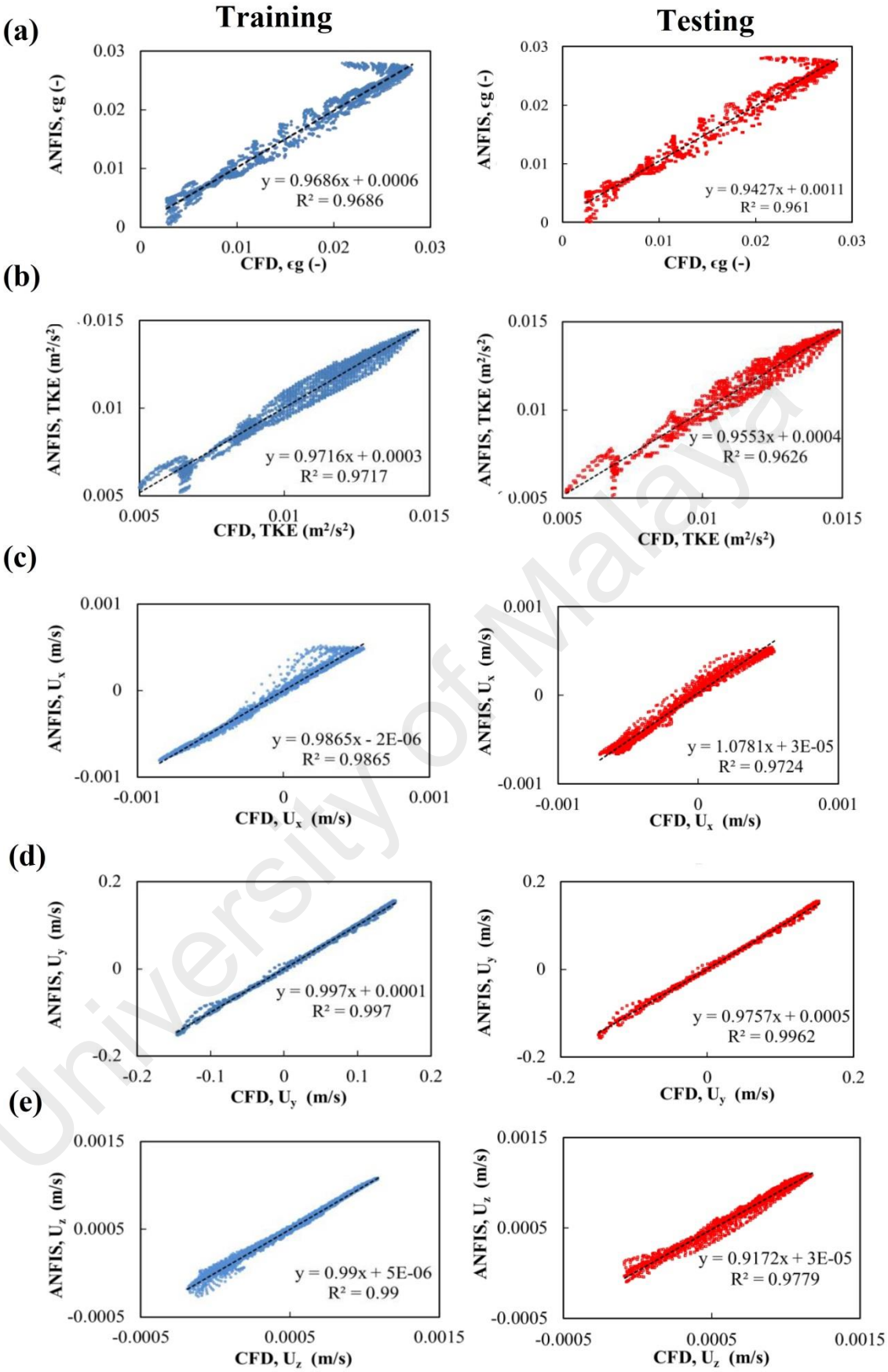

Figure 5.4: Evaluation of the coefficient of determination (R^2) for training and testing data: (a) ϵ_g; (b) T.K.E; (c) U_x; (d) U_y; (e) U_Z

For further validation, the accuracy of the ANFIS results for ϵ_g, T.K.E, U_x, U_y and U_Z at 1.3, 1.5, 1.6 and 1.69 m column heights are evaluated and compared with actual values using i.e., RMSE and r. The RMSE and r between the ANFIS and the CFD results of ϵ_g, T.K.E, U_x, U_y and U_Z are shown in Table 5.4 for the training and testing. For training, the RMSE value of ϵ_g, T.K.E, U_x, U_y and U_Z are 0.00105, 0.00032, 0.000043, 0.0032, 0.000030, respectively. This shows that the error between the predicted data and actual value is less than 0.3 % for all of the hydrodynamics parameters. Furthermore, the r value of ϵ_g, T.K.E, U_x, U_y and U_Z are 0.984, 0.985, 0.993, 0.998 and 0.995, respectively. This shows the high degree of linear dependence (r) between the ANFIS and CFD results in the training process. In the testing process of the RMSE value of ϵ_g, T.K.E, U_x, U_y and U_Z are 0.0014, 0.0004, 0.00004, 0.00414 and 0.0000418, respectively. This shows that, the ANFIS model can accurately predict the BCR hydrodynamics with an error of less than 0.4 %. This table also shows the r value of ϵ_g, T.K.E, U_x, U_y and U_Z which are 0.9803, 0.9811, 0.986, 0.998 and 0.988, respectively for the testing data.

Table 5.4: Performance statistics of the ANFIS model for BCR hydrodynamics estimation based upon different criteria

Hydrodynamics parameters		RMSE	r
ϵ_g	Training	0.001059	0.984173
	Testing	0.001424	0.980315
T.K.E	Training	0.00032	0.985726
	Testing	0.000401	0.981131
U_x	Training	4.36e-05	0.993236
	Testing	4.4e-05	0.986119
U_y	Training	0.003203	0.998482
	Testing	0.00414	0.998106
U_Z	Training	3.06e-05	0.995009
	Testing	4.18e-05	0.988907

Cases 6-8

The accuracy of ANFIS method to predict gas hold-up at various column heights are examined using Cases 6-8 (Sec. 5.2.4). The degree of difference between the ANFIS prediction and CFD results of the gas hold up (ϵ_g) at different column heights is shown in Figure 5.5 for the training and testing steps. R^2 value of Case 6 (0.001 height) is 0.92 and 0.86 for the training and testing steps, respectively. Similarly, such values of Case 7 (0.823 height) are 0.999, 0.999, respectively and Case 8 (2.5 height) are 0.999, 0.995, respectively. Unlike Cases 7 & 8, the R^2 value of Case 6 is much lower, thus suggesting a less accurate prediction by the ANFIS model for this case. For further comparisons, the XZ plane contour plot of the gas hold up at different column heights is shown in Figure 5.6 from the ANFIS and CFD models. For Case 6, some variations can be seen in the gas hold up between the ANFIS and CFD model. The CFD results show some effects of discrete jet flow due to the sparger nozzles on the gas hold-up. The ANFIS model predicts reasonably well but with a uniform jet flow due to the sparger. For Case 7 & 8, the gas hold up contour of the ANFIS and CFD is very similar, thus suggesting an accurate prediction by the ANFIS model. In order for a better prediction of gas distribution towards the sparger region, different ANFIS setting parameters (i.e., membership function, number of iteration, percentage of training data and etc.) should be selected.

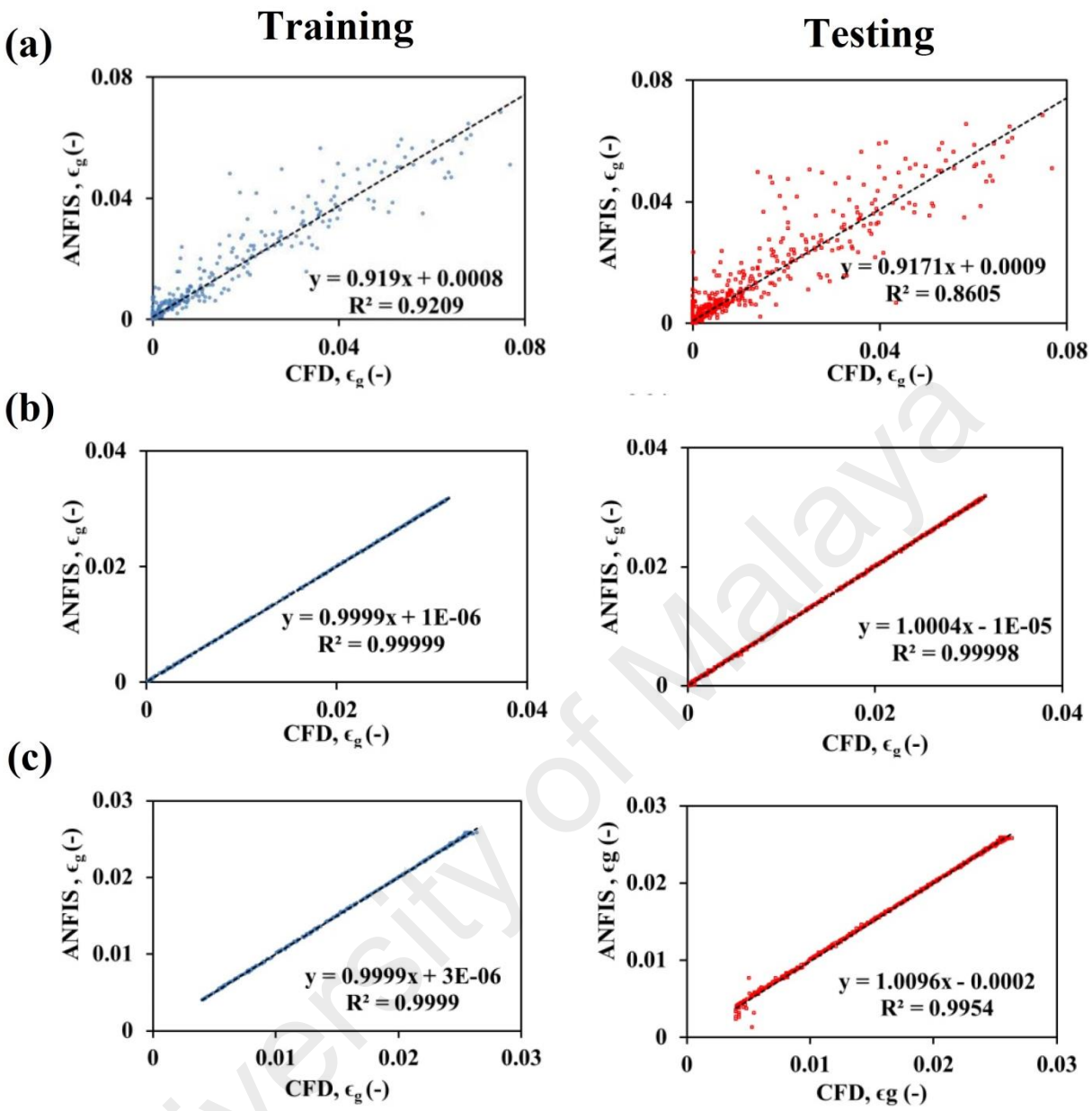

Figure 5.5: Scatter plots of ANFIS predicted values against CFD results for gas hold-up at BCR heights: (a) 0.0001 m; (b) 0.823 m; (c) 2.56 m

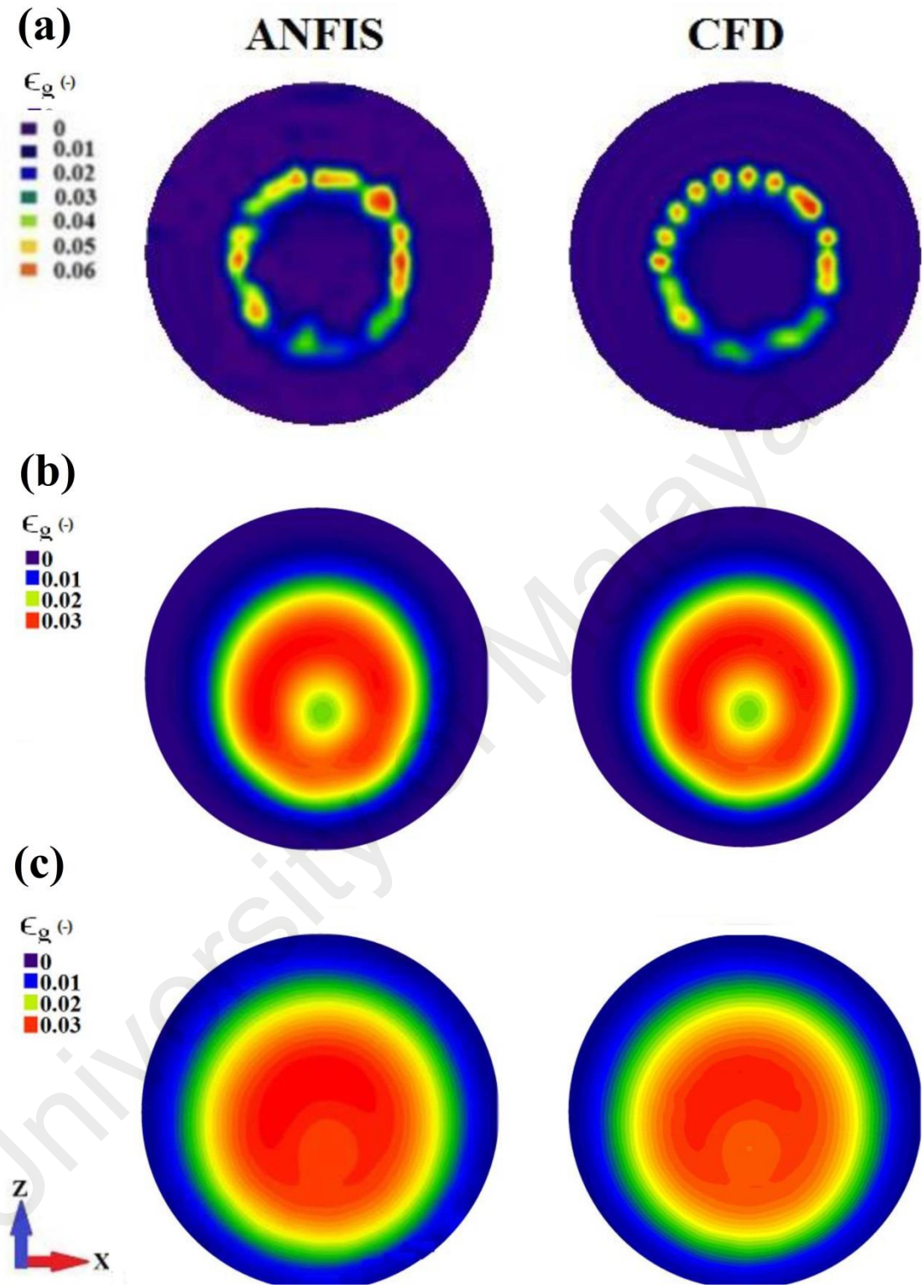

Figure 5.6: Contour plot of gas-hold-up for ANFIS and CFD methods at different BCR heights: (a) 0.001 m; (b) 0.823 m; (c) 2.56 m

The RMSE and MSE values between the ANFIS and the CFD results of ϵ_g at 0.001, 0.823 and 2.56 m are shown in Table 5.5 for the training and testing. The MSE values of Case 6 (0.001 m height) are 0.00002 and 0.000046 for the training and testing steps, respectively. Similarly, such values of Case 7 (0.8 m height) are 2.6×10^{-9}, 8.22×10^{-9}, respectively and Case 8 (2.5 m height) are 6.6×10^{-9}, 2.59×10^{-7}, respectively. Furthermore, the RMSE values of Case 6 (0.001 m height) are 0.0044 and 0.0064 for training and testing steps, respectively. Similarly, such value of Case 7 (0.8 m height) are 5.15×10^{-5}, 9.07×10^{-5}, respectively, and for Case 8 (2.5 m height) are 8.15×10^{-5}, 5.09×10^{-4}, respectively. According to the table, the predicted gas hold-up at various BCR heights have small RMSE and MSE values, particularly at the 0.832 m column height.

Table 5.5: Performance statistics of the ANFIS models for various BCR heights based upon different criteria

BCR heights (m)	Train		Test	
	MSE	RMSE	MSE	RMSE
0.001	2.01e-05	0.004481	4.68e-05	0.006843
0.823	2.6562e-09	5.1538e-05	8.2276e-09	9.0706e-05
2.56	6.6579e-09	8.1596e-05	2.591e-07	0.00050901

5.3.2 Sensitivity study of the ANFIS setting parameters

5.3.2.1 Percentage of training data (*P*)

Cases 9-12

Using Cases 9-12 (Sec. 5.2.4), the gas hold-up is predicted at 1.6 m in column height for different values of *P*, 70 %, 30 %, 10 % and 5 % in the ANFIS method and the results are compared with the actual values from the CFD results from Chap. 3 at the same height. The coefficient of determination (R^2) between the ANFIS and the CFD results of ϵ_g for different values of *P* are shown in Figure 5.7 for the training and testing steps. For the training, the R^2 value of different *P* values, are 70 %, 30 %, 10 % and 5 % is 0.999, 1, 1 and 1, respectively. However, for the testing step, the R^2 value of the different *P* values, 70 %, 30 %, 10 % and 5 % are 0.999, 0.998, 0.968, and 0.907, respectively. As expected, for small values of *P* of less than 30 % due to the reduction in the number of data in the training process, the accuracy of the ANFIS model increases in the training mode but this is not the case for the testing step. As the percentage of training data (*P*) decreases, the ability of the ANFIS model in the prediction process reduces.

For further comparisons, the XZ plane contour plot of the gas hold up at the 1.6 m column height for different *P* values, 70 %, 30 %, 10 % and 5 % is shown in Figure 5.8 from ANFIS and CFD models. According to the Figure, when *p* is 30 %, the ANFIS method predicts a circular gas distribution, resulting in a minimum and maximum value of gas towards the wall and center region, respectively. In contrast, when *P* is less than 10 percent, the ANFIS method estimates a rectangular gas distribution with an over prediction near the walls due to small value of *P*. The

sensitivity study of different values of *P* shows that the *P* value can be 70 % for an accurate prediction.

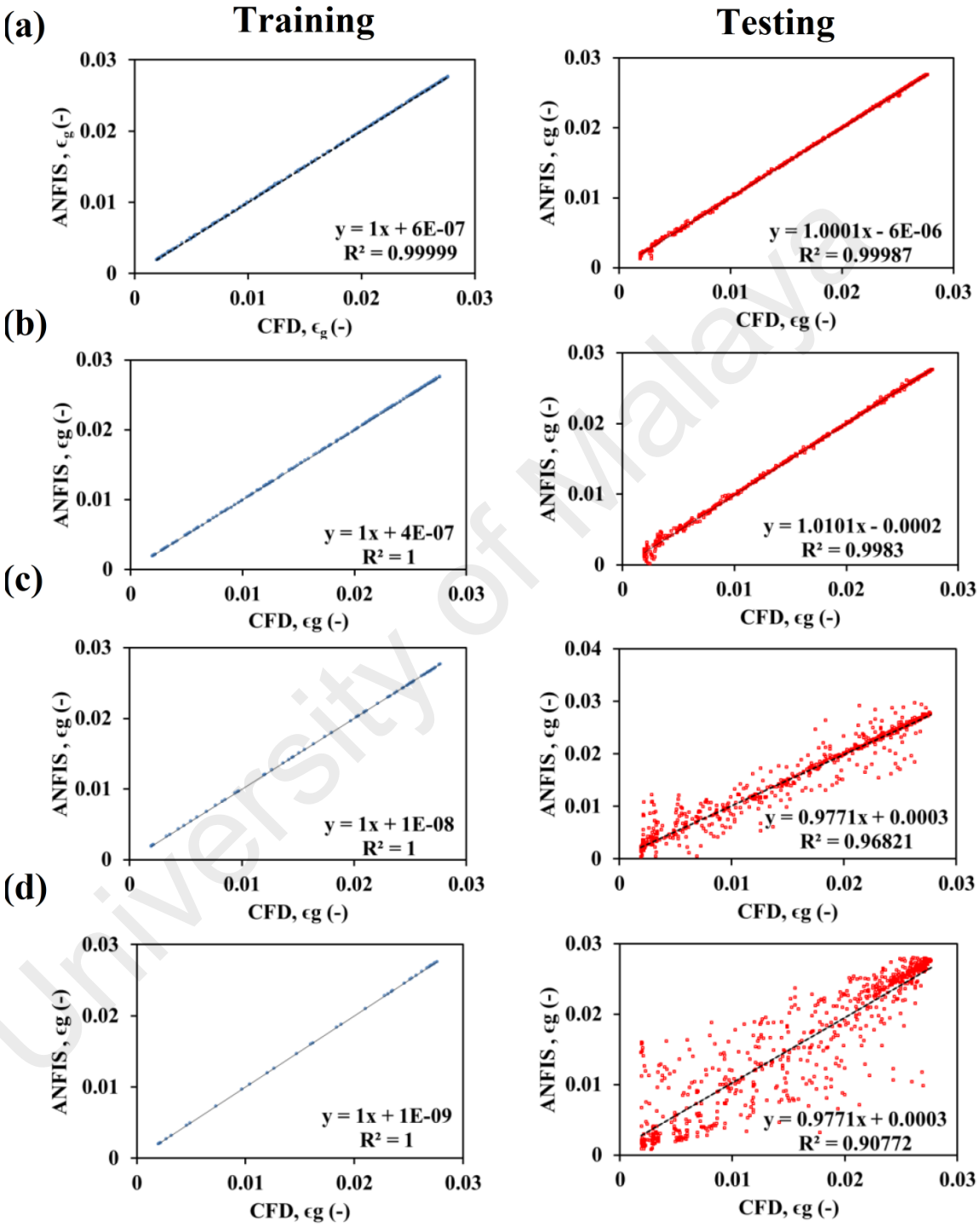

Figure 5.7: Scatter plots of ANFIS predicted values against CFD results for gas hold-up at 1.6 m BCR height for different values of *P*: (a) 70 %; (b) 30 %; (c) 10 %; (d) 5 %

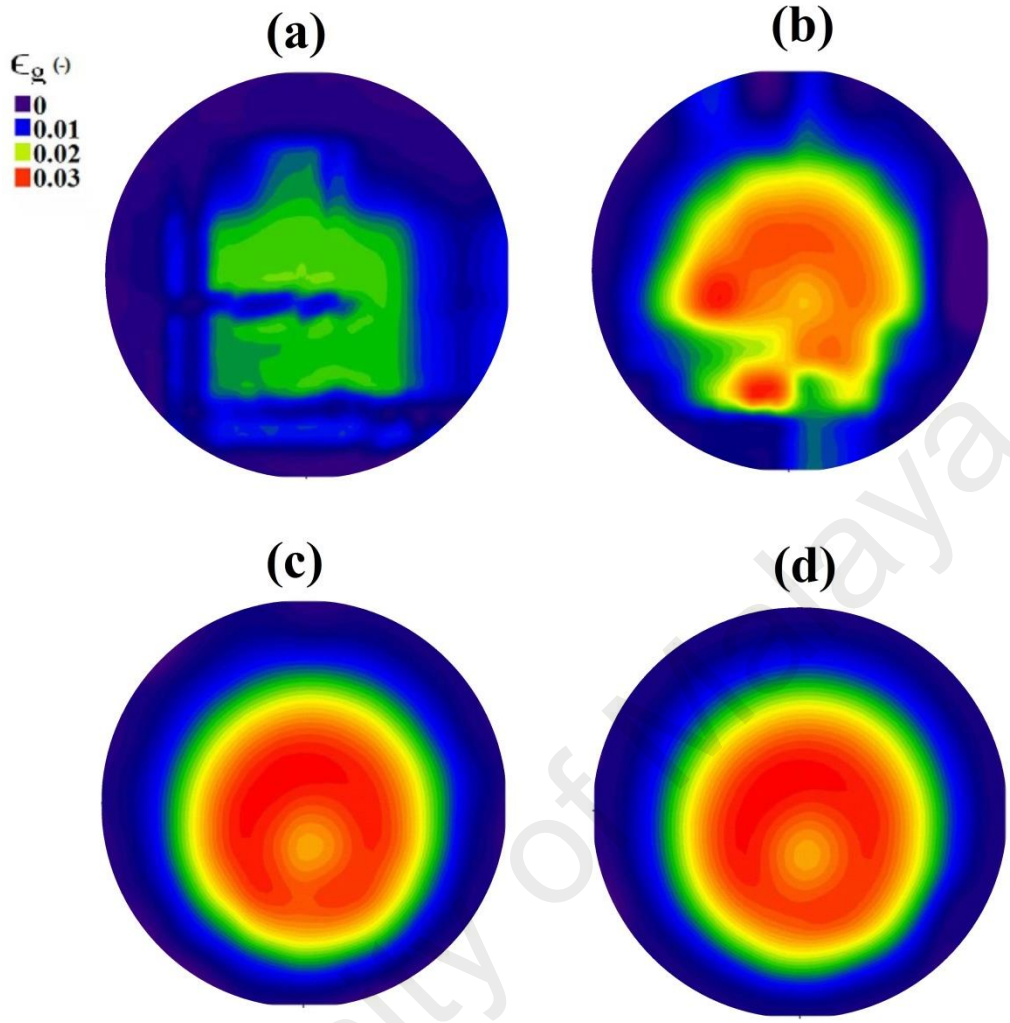

Figure 5.8: Contour plot of gas-hold-up at 1.6 m BCR height for different values of *P*: (a) 5 %; (b) 10 %; (c) 30 %; (d) 70 % using ANFIS method

5.3.2.2 Membership function (*M.F*)

Cases 13-17

Using Cases 13-17 (Sec. 5.2.4), the BCR hydrodynamics parameters of ϵ_g, T.K.E, U_x, U_y and U_Z are predicted at 1.3, 1.5, 1.6 and 1.69 m column heights using different membership functions (i.e., '*gbell*', *'Gauss'*, *'Gauss2'*, *'tri'*, *'trap'* and *'pi'*) and the results are compared with the actual values from the CFD results, at the same heights, from Chap. 3. R^2, r and RMSE between the ANFIS and CFD results of ϵ_g, T.K.E, U_x, U_y and U_Z are shown in Tables 5.6-5.10. Table 5.6 shows the values of R^2, r

and RMSE for the predicted gas hold-up (ϵ_g) using different *MFs*, as mentioned above (Case 13). According to the Table, the '*gbell*' membership function contains a higher ability to predict the gas hold-up. The values of the RMSE, r and R^2 are 0.00105, 0.98 and 0.96. However, *'pi' MF* shows the lowest ability in the prediction of gas hold-up. In this *MF*, the value of RMSE, r and R^2 are, 0.00334, 0.91 and 0.92, respectively.

The accuracy of different *MFs* for liquid velocity in X,Y, and Z directions (U_x, U_y and U_z) is shown in Table 5.7 (Case 14), Table 5.8 (Case 15) and Table 5.9 (Case 16). Similarly, to the gas hold-up, U_x, U_y and U_z are better predicted using the '*gbell'* function. For example, when the *MF* is '*gbell*', the value of R^2 for U_x, U_y and U_z are 0.972, 0.996, 0.977, respectively and the value of RMSE for U_x, U_y and U_z are 4.4×10^{-5}, 0.0032 and 4.18×10^{-5}, respectively. This shows the high accuracy of the '*gbell*' membership function in predicting liquid velocity components.

Table 5.10 shows the accuracy of different *MFs* in predicting TKE. Similar to gas hold-up and liquid velocity components TKE is better predicted with '*gbell*' membership function. In this case, the values of RMSE, r and R^2 are 0.00032, 0.981 and 0.96, respectively. However, using *'pi' MF* results in lower prediction accuracy among other types of *MF*.

Table 5.6: Statistical and deviance measurement of ANFIS model for ϵ_g

ϵ_g	***MF***					
	'gbell'	***'Gauss'***	***'Gauss2'***	***'tri'***	***'trap'***	***'pi'***
RMSE	0.001059	0.001143	0.002321	0.003423	0.029734	0.00334
r	0.980315	0.979855	0.974552	0.915352	0.924542	0.9122
R^2	0.961	0.9597	0.9453	0.9325	0.937	0.929

Table 5.7: Statistical and deviance measurement of ANFIS model for U_x

U_x	*MF*					
	'gbell'	***'Gauss'***	***'Gauss2'***	***'tri'***	***'trap'***	***'pi'***
RMSE	4.4e-05	4.45e-05	4.56e-05	4.55e-05	4.54e-05	4.7e-05
r	0.986119	0.979843	0.965534	0.964543	0.964443	0.95653
R^2	0.9724	0.9698	0.9609	0.9615	0.9611	0.9501

Table 5.8: Statistical and deviance measurement of ANFIS model for Uy

U_y	*MF*					
	'gbell'	***'Gauss'***	***'Gauss2'***	***'tri'***	***'trap'***	***'pi'***
RMSE	0.003203	0.003433	0.004255	0.004123	0.004076	0.005723
r	0.998106	0.995642	0.997864	0.997774	0.996987	0.990988
R^2	0.9962	0.9891	0.9809	0.9811	0.9856	0.9798

Table 5.9: Statistical and deviance measurement of ANFIS model for U_Z

U_Z	*MF*					
	'gbell'	***'Gauss'***	***'Gauss2'***	***'tri'***	***'trap'***	***'pi'***
RMSE	4.18e-05	4.19e-05	4.21e-05	4.22e-05	4.22e-05	4.24e-05
r	0.988907	0.987908	0.984532	0.982341	0.982341	0.980006
R^2	0.9779	0.9765	0.9709	0.9698	0.9698	0.9342

Table 5.10: Statistical and deviance measurement of ANFIS model for TKE

TKE	*MF*					
	'gbell'	***'Gauss'***	***'Gauss2'***	***'tri'***	***'trap'***	***'pi'***
RMSE	0.00032	0.00056	0.00077	0.000843	0.000902	0.001211
r	0.981131	0.981012	0.980986	0.980875	0.980798	0.980122
R^2	0.9601	0.9598	0.9512	0.9412	0.9398	0.9211

5.3.3 Prediction of ANFIS and Validation

The ANFIS method can predict the BCR hydrodynamics with different operational conditions in less computational time and provide continuous results. In order to examine the prediction ability, the BCR hydrodynamics are predicted for different column heights (case 18). Furthermore, this method is also used in predicting the BCR with different sparger diameters (cases 19-21). All predicted results are compared with the CFD results which are not used in the training process.

5.3.3.1 Prediction of gas hold-up at various column heights

Figure 5.9 shows the predicted contour plot of gas hold-up at various column heights (i.e., 0.432, 0.86, 1.3, 1.73, 2.17 and 2.56 m) for the ANFIS and CFD methods. According to the figure, the ANFIS results are in good agreement with the CFD results for almost all of the column heights. The ANFIS method predicts the circular gas hold-up distribution for almost all of the column heights, which is similar with the CFD results. Both the CFD and ANFIS show a higher gas hold-up at the center region of the columns, ranging from 0.02 to 0.03, while this parameter reaches to zero value near the walls. Towards the sparger region (h=0.432 m), the sparger has influence on the gas distribution, resulting in a ring shape gas fraction (with 0.0012 m inner and 0.09 m outer diameter). As the column height increases, this influence diminishes and results in a uniform distribution of gas. In comparison to the CFD results, the ANFIS method slightly over predicts the gas hold-up towards the walls at 2.56 m. This may attribute to the fact that, the ANFIS method cannot accurately recognize gas behavior near the BCR boundary (particularly outlet). In order to enhance this over prediction, different ANFIS setting parameters or data filtering are required.

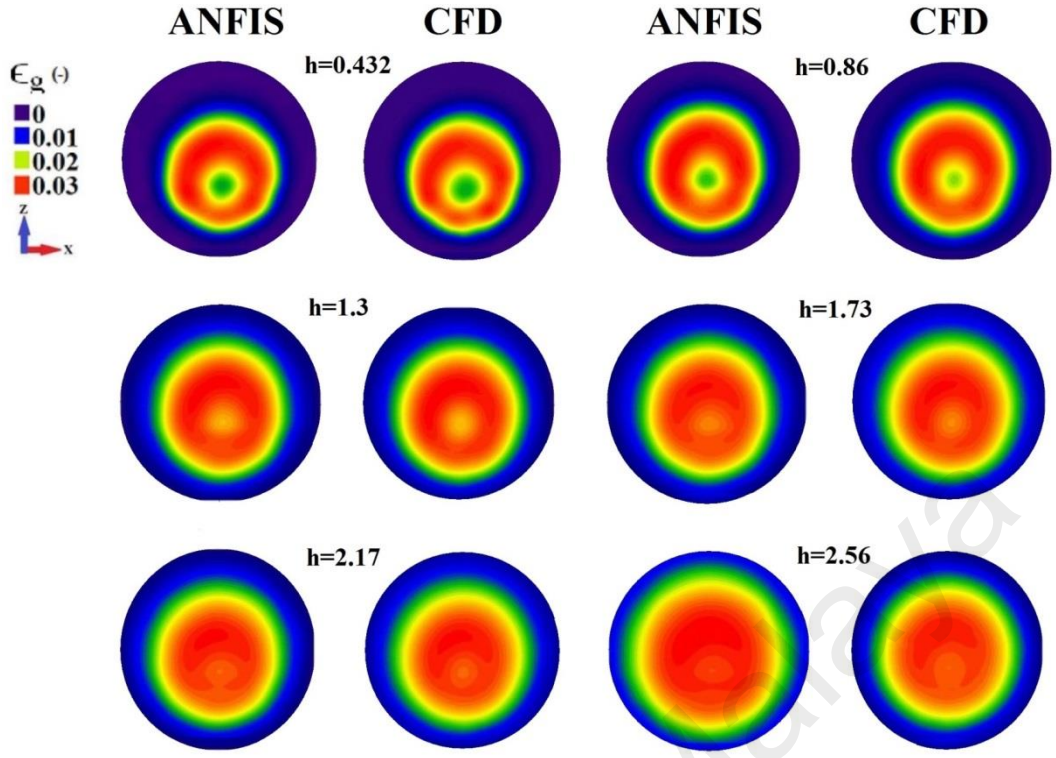

Figure 5.9: Contour of gas hold-up at various column heights for ANFIS and CFD method

5.3.3.2 Prediction of BCR hydrodynamics for ring sparger diameters

Figures 5.10, 5.11 and 5.12 show the predicted axial liquid velocity (U_Y), gas hold-up (ϵ_g) and turbulent kinetic energy (TKE) at the 1.3 m column height using the ANFIS and CFD methods for different ring sparger diameters, 0.08, 0.10, 0.12 and 0.14 m. Figure 5.10 shows that the results of the axial liquid velocity using the ANFIS method are in good agreement with the CFD results for all sizes of ring spargers at the column center (r/R=0). However, the ANFIS method slightly predicts a weaker downward flow near the wall (r/R=0.89). For example at the center region (r/R=0) the maximum difference between the ANFIS and CFD results for all ring sparger diameters is less than 3 %. However, this difference near the wall region (r/R=0.89) reaches to a maximum of 21 % for the smallest ring sparger size of 0.08 m (see Figure 5.10 (a)).

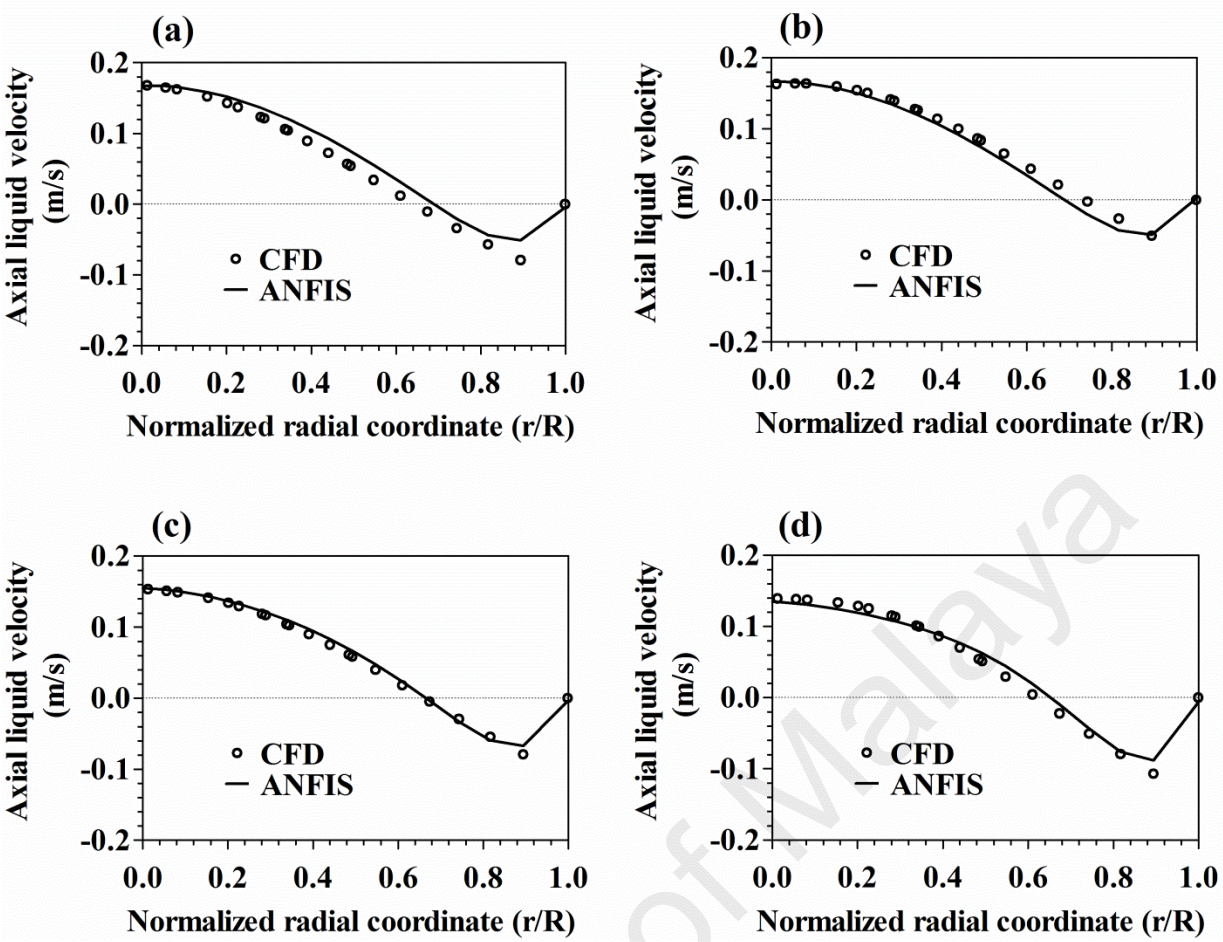

Figure 5.10: Axial liquid velocity at 1.3 m height for CFD and ANFIS methods and ring sparger diameters: (a) 0.08 m; (b) 0.10 m; (c) 0.12 m; (d) 0.14 m

Referring to Figure 5.11, the results of the predicted gas hold-up distribution ($\epsilon_{g)}$ are in good agreement with the CFD results for all sparger diameters. However, there is a small variation at the column center and wall region for sparger diameters of 0.08 and 0.010 m (see Figure 5.11 (a and b)). In general, for all sizes of the ring spargers, in comparison to the CFD method, the ANFIS method slightly over predicts the gas hold-up near the wall (-0.6>r/R>0.6), while it is vice versa at the column center.

This method is susceptible near the wall boundaries and cannot exactly predict the liquid velocity and gas hold-up at this region. In order to enhance the under estimation near the walls and over estimation at the centre, more information near the boundaries, data filtering and sensitivity study of ANFIS setting parameters at particular region (finding an appropriate models) are required. The number of percentage of data (*P*) can

be increased in the training process, particularly near the wall region, as well as BCR centre. This way improves the training process to better predict liquid velocity and gas distribution near the walls and BCR centre. The filtering algorithm can be also used in the ANFIS method to improve the over estimation and under estimation. In addition, at these particular regions, different ANFIS methods can be implemented. For example, higher number of rules, different membership functions can be used at these regions to improve the prediction results. However, using higher number of rules increases the training time.

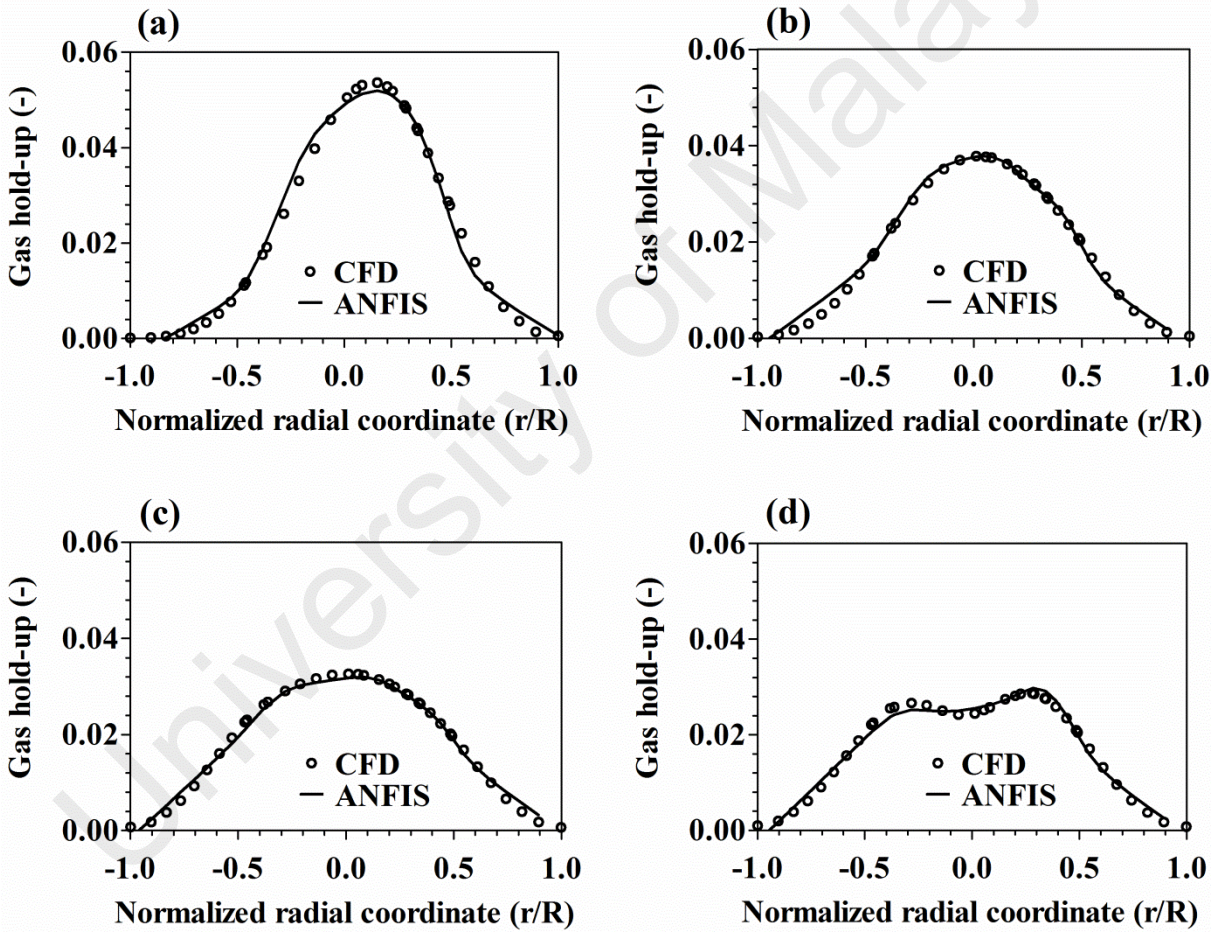

Figure 5.11: Gas hold-up at 1.3 m height for CFD and ANFIS methods and ring sparger diameters: (a) 0.08 m; (b) 0.10 m; (c) 0.12 m; (d) 0.14 m

Figure 5.12 shows that unlike the gas hold-up and axial liquid velocity, the results of the turbulent kinetic energy (TKE) for all ring sparger diameters are in good agreement near the walls (-0.6>r/R>0.6). However, the TKE at the center region is not

well predicted for sparger diameters, 0.08 and 0.012 m (see Figure 5.12 (a and c)). For example, for the ring sparger diameter, 0.08 m, the ANFIS method at -0.2<r/R<0.2 over predicts the TKE (Figure 5.12 (a)), while for the ring sparger diameter, 0.012 m this method under predicts the TKE at 0<r/R<0.2 (Figure 5.12 (c)).

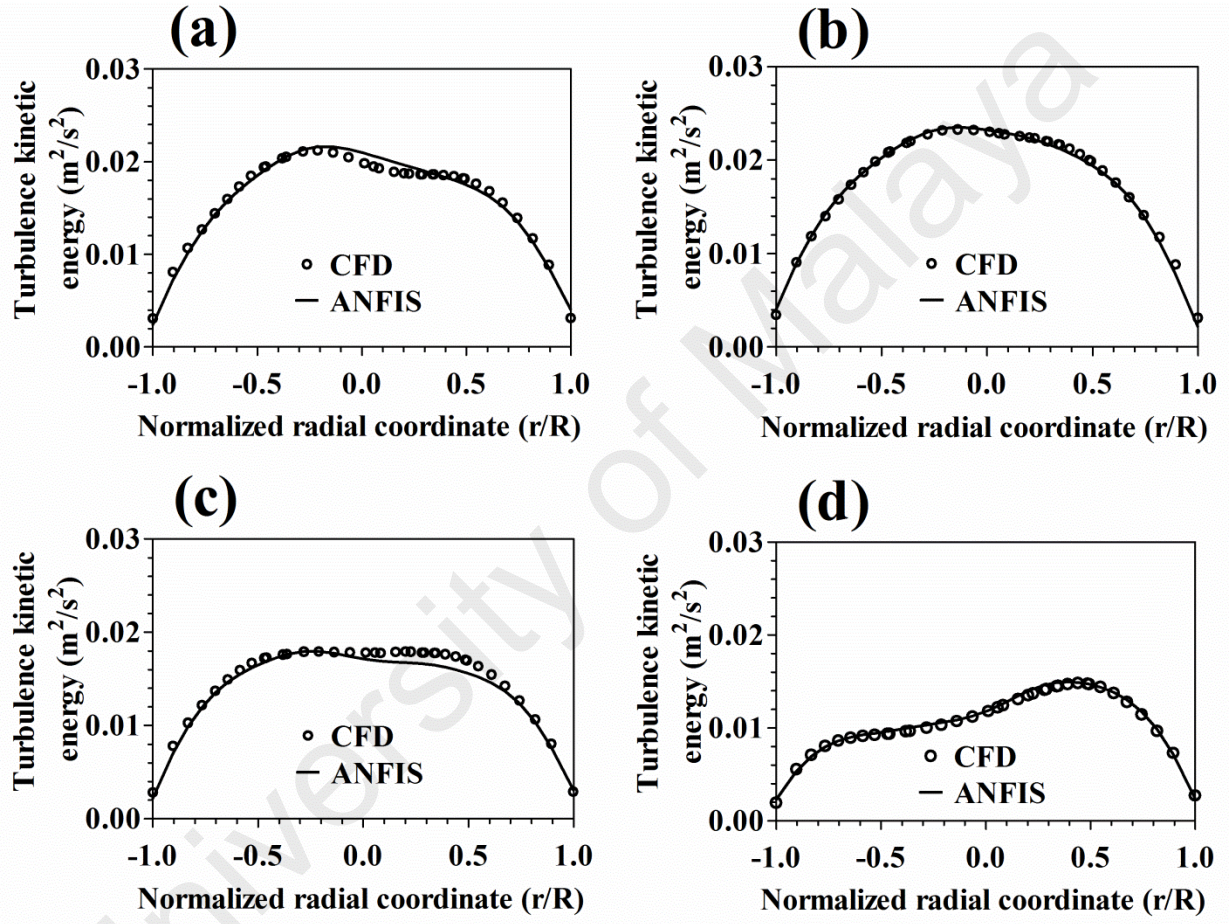

Figure 5.12: TKE at 1.3 m height for CFD and ANFIS methods and ring sparger diameters: (a) 0.08 m; (b) 0.10 m; (c) 0.12 m; (d) 0.14 m

In summary, in comparison to the CFD, the ANFIS method provides the approximated BCR hydrodynamics result in a continuous domain (see Figure 5.13). When certain results of different ring sparger diameters and column heights are trained in the ANFIS method, it can appropriately approximate the flow pattern and gas dynamics within these particular ranges. The results show that the ANFIS method can

be used as an alternative tool beside the CFD study to minimize computational efforts, when the CFD simulation is necessary to be employed for small changes in operational conditions. Since this method requires less computational efforts without computational problems (computational instability) in the modeling of industrial BCRs, it can easily find optimum values. For example, in industrial BCRs, the homogeneous flow condition, having a uniform gas hold-up distribution is required to increase the mass and heat transfer and consequently the BCR efficiency. To find the BCR with this condition, many CFD or experimental efforts are necessary. Therefore, the ANFIS method can be trained and developed with only a few CFD cases and find to the BCR with the appropriate (optimum) conditions.

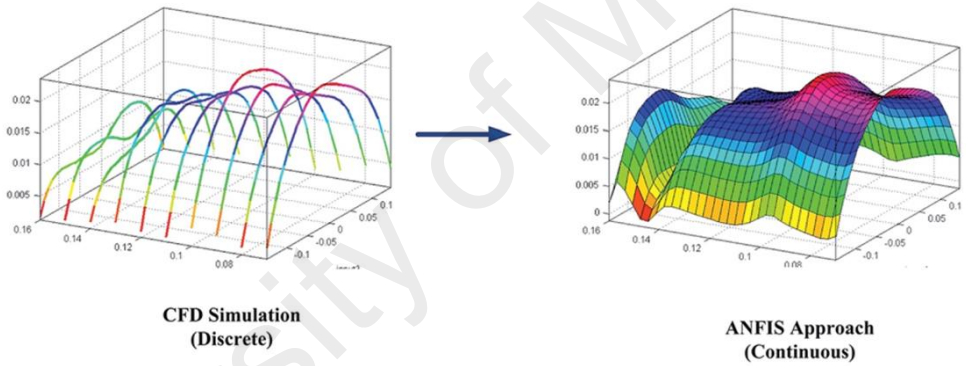

Figure 5.13: Schematic diagram of the prediction procedure of BCR using ANFIS method

The main issue in this study is the inaccurate prediction of parameters at the surface and sparger regions. In order to solve this problem, the ANFIS method should be trained with more information from those particular regions. Furthermore, for an accurate prediction of the BCR, the ANFIS method must be learned at all possible physical conditions. Another main goal of the future research should be the hybridization of the ANFIS methodology with other soft computing methods in order to improve the optimization structure of the ANFIS method.

5.4. Conclusions

In the present chapter, for the first time, the ANFIS method has been developed to predict the macroscopic BCR hydrodynamics parameters (i.e., liquid flow pattern, gas hold-up and turbulent kinetic energy) for various ring sparger diameters and heights. In addition, the sensitivity study of the ANFIS setting parameters (i.e., membership functions (*M.F*) and percentage of training data (*P*)) on the accuracy of prediction results have been carried out. The conclusions of this study are as follows:

- Both the CFD and ANFIS prediction methods show that, near the BCR center, the gas hold-up is higher than the wall regions. In addition, the liquid velocity results show the upward liquid movement towards the column center, while two-recirculation areas appear near the walls.
- Both the CFD and ANFIS prediction methods illustrate that the larger ring sparger diameter produces a flatter gas hold-up profile in the BCR cross-section. In addition, for all sparger diameters, the centerline velocity, gas hold-up and turbulent kinetic energy are higher near the sparger region.
- The ANFIS results are in excellent agreement with the CFD results, for all liquid velocity components, turbulent kinetic energy and gas hold-up which implies that the model succeeded in the prediction of a multiphase BCR hydrodynamics. The best estimation is found for the liquid velocity in X direction (i.e., RMSE=4.4e-05, R^2=0.9724, r=0.986119) and in Z direction (i.e., RMSE=4.18E-05, R^2=0.9779, r=0.988907). In addition, the ability of this method at the middle of the column is higher than that at the sparger and surface regions. For instance, near the BCR outlet, this method over predicts the gas hold-up towards the wall. In order to enhance the accuracy of this method, more information is required from the sparger and surface regions for the

training process. In addition, changing the ANFIS setting parameters or filtering data may result in better prediction of those particular regions.

- The results show that, in the case of a proper ANFIS learning process (when *P*=70 %, *M.F*='*gbell*', *I*=1000, *N.R*=8), the ANFIS method can adequately predict the BCR hydrodynamics.
- A new view point of the ANFIS development using a CFD data set can be considered as an assistance tool of the CFD implementation, when the CFD study is required to be implemented for new cases (small changes) due to the changes of operational conditions (e.g., bubble column dimension, ring sparger parameters and liquid and gas properties). In general, this code development can assist in the reduction of the CFD simulations that require small changes in the boundary conditions. Furthermore, the use of the ANFIS development using the CFD data set results in a non-discrete data set at each point of the bubble column domain and produces the prediction results with a small step size. However, the CFD methodology is unable to generate continuous results in a specific range of changes with small step sizes as this requires high computational efforts. In general, the learning procedure of the ANFIS method should be thoroughly trained by the behavior of flow pattern and gas dynamics within the domain of the CFD simulation. If in the learning process, all of the changes are considered, it means the ability of the method increases and covers more fluid flow phenomena inside the bubble column reactor.

CHAPTER 6: ADAPTIVE NEURO FUZZY INFERENCE SYSTEM (ANFIS) FOR THE PREDICTION OF THE SINGLE BUBBLE FORMATION AND RISING

6.1 Introduction

In Chapter 4, the single bubble formation from an orifice and rise characteristics of bubbles were predicted using the CFD, VOF methods. In the present chapter, an ANFIS method will be developed for some of the cases in Chapter 4. The results from ANFIS and CFD will be compared. To the best of the author's knowledge, the ANFIS method is developed for the first time to predict the bubble size, shape, position and the interface between bubble and liquid during the formation and rising from the orifice.

6.2 Methodology

A similar method as discussed in Sec. 5.2.1 is adopted for the present chapter. In addition, similar to Sect. 5.2.2, different statistical and deviance measurement formulae such as the RMSE, MSE and R^2 are used for the examination of the prediction accuracy. In the ANFIS code, the microscopic CFD results (VOF) from Chapter 4 is used in the training and development stage. The training and development, as well as the prediction algorithms of the ANFIS model for the bubble formation and rising are also similar with Chapter 5.

6.2.1 Simulation cases

Simulations cases are sectioned to three main categories, namely, (a) Training and testing (T-T) of ANFIS; (b) Sensitivity study of ANFIS setting parameters; and (c) ANFIS model development and prediction.

a. Training and testing (T-T) of ANFIS

A total of four cases (Cases 1-4) are used to examine the capability of the ANFIS model for the prediction of the single bubble formation and rising, see Table 6.1. Herein, the CFD results of Case 12 (Chap. 4) are used for the training, development and testing of the developed ANFIS model. Cases 1-4 are used to T-T of gas phase (gas fraction) at different formation and rising times, 0.05, 0.09, 0.13 and 0.17 s. In these cases, 70 % of the CFD results, i.e., for 11767 nodes, are given as input to the ANFIS for the training and model development purpose. For the testing, the developed ANFIS model is used to predict for 16810 nodes, which represent 100 % of the data. Under the ANFIS setting parameters, membership function (*MF*), number of rules (*N.R*), number of iteration (I) and percentage of training data (*P*) are set to: '*gbell*', 7, 1000 and 70 %, respectively.

b. Sensitivity study of the ANFIS setting parameters

A total of 16 (Cases 5-20) simulation cases are used to study the sensitivity of the ANFIS setting parameters and its value on the prediction accuracy. This will allow for an appropriate selection of the parameters and values. Table 6.2 shows the sensitivity study of the ANFIS setting parameters (i.e., *P, M.F* and *N.R*), which are:

Percentage of training data (*P*)

The effect of different percentages of the input data (*P*), namely 5 %, 10 % 30 %, 50 % and 70 %, on the result of the single bubble formation and rising at different simulation time ranging between 0.01 and 0.19 s with a step size of 0.02 is tested using Cases 5-9 as shown in Table 6.2. Parameter *I, M.F* and *N.R* are set to 1000, '*gbell*' and 7, respectively. The purpose of this test was to evaluate an appropriate percentage of the input data (actual data) for the ANFIS model development.

Membership function (*M.F)*

Cases 10-16 are used to study the effect of the six different membership functions (*M.F*), i.e., Gaussian-shaped (‘*gauss’* and *‘gauss2’*), Triangular-shaped (‘*tri’*), Trapezoidal-shaped (‘*tra*’), Bell-shaped (‘*gbell*’) and p-shaped (*‘pi’*) on the prediction of the single bubble formation and rising at different simulation times ranging 0.01-0.19 s with a step size of 0.02. Parameters *I*, *P* and *N.R* are set to 1000, 70 % and 7, respectively (see Table 6.2).

Number of rules (*N.R*)

Cases 17-20 are used to study the effect of different values of number of rules (2, 3, 4 and 7) on the prediction of single bubble formation and rising at different simulation time ranging 0.01-0.19 s with a step size of 0.02. Under the ANFIS setting parameters, the membership function (*MF*), number of iteration (*I*) and percentage of training data (*P*) are set to: ‘*gbell*’, 1000 and 70 %, respectively (see Table 6.2).

c. ANFIS model Development & Prediction

One simulation case (Case 21) will be carried out in this section to test the ability of the ANFIS model for a new prediction. Case 21 shows the prediction of the bubble formation and rising using the ANFIS method for simulation time ranging 0.01-0.19 with a step size of 0.001 (see Table 6.3). The number of prediction data in the X and Y mesh coordinates is now increased to 251001 nodes. For the ANFIS training and model development, 70 % of the actual data, which is the CFD results from Chapter 4 is given as the input. In addition, the number of data in the X and Z mesh coordinates for the input is reduced to three-quarters or to only 11767 nodes. Please take note, the prediction of bubble formation and rising is not given as an input data to the ANFIS

model and hence the ability of the model is tested. The ANFIS model setting parameters *P*, *M.F*, *I* and *N.R* are set to 70 %, '*gbell*', 1000 and 7, respectively.

Table 6.1: Simulation cases for the training and testing of ANFIS

Case study	Training/Model development		Testing		ANFIS setting Parameters	Remarks
	Input		Output			
1-4	X-coordinate of mesh	11767 nodes	X-coordinate of mesh	16810 nodes	*N.R*=7 *M.F*='*gbell*' *P*=70 % *I*=1000	Validation of ANFIS method
	Y-coordinate of mesh for selected heights	11767 nodes	Y-coordinate of mesh	16810 nodes		
	Hydrodynamics parameters	Gas phase	Hydrodynamics parameters	Gas phase		
	Sim Time (s)	t=0.01-0.19 step size=0.02	Sim Time (s)	t=0.05, 0.09, 0.13, 0.19		

Table 6.2: Simulation cases for the sensitivity study of ANFIS method

Case study	Training		Testing		ANFIS setting Parameters	Remarks
	Input		Output			
5-9	X-coordinate of mesh	11767 nodes	X-coordinate of mesh	16810 nodes	*N.R*=4 *M.F*='*gbell*' *P*=5 %, 10 % 30 %, 50 %, 70 % *I*=1000	Sensitivity study of *P*
	Y-coordinate of mesh for selected heights	11767 nodes	Y-coordinate of mesh	16810 nodes		
	Hydrodynamics parameters	Gas phase	Hydrodynamics parameters	Gas phase		
	Sim Time (s)	t=0.01-0.19 step size=0.02	Sim Time (s)	t=0.01-0.19 step size=0.02		
10-16	X-coordinate of mesh	11767 nodes	X-coordinate of mesh	16810 nodes	*N.R* =4 *P*=70 % *I*=1000 *M.F* ='*gbell*', *'dsig'*, *'Gauss'* *'Gauss2'* *'pi'*, *'psig'*	Sensitivity study of *MF*
	Y-coordinate of mesh for selected heights	11767 nodes	Y-coordinate of mesh	16810 nodes		
	Hydrodynamics parameters	Gas phase	Hydrodynamics parameters	Gas phase		
	Sim Time (s)	t=0.01-0.19 step size=0.02	Sim Time (s)	t=0.01-0.19 step size=0.02		
17-20	X-coordinate of mesh	11767 nodes	X-coordinate of mesh	16810 nodes	*N.R* =2,3,4,7 *P*=70 % *I*=1000 *M.F* ='*gbell*'	Sensitivity study of *NR*
	Y-coordinate of mesh for selected heights	11767 nodes	Y-coordinate of mesh	16810 nodes		
	Hydrodynamics parameters	Gas phase	Hydrodynamics parameters	Gas phase		
	Sim Time (s)	t=0.01-0.19 step size=0.02	Sim Time (s)	t=0.01-0.19 step size=0.02		

Table 6.3: Simulation cases for the prediction of single bubble formation and rising

Case study	Training		Testing		ANFIS setting Parameters	Remarks
	Input		Output			
21	X-coordinate of mesh	11767 nodes	X-coordinate of mesh	251001 nodes	*N.R* =7 *P*=70 % *M.F* ='*gbell*' *I*=1000	Prediction
	Y-coordinate of mesh for selected heights	11767 nodes	Y-coordinate of mesh	251001 nodes		
	Hydrodynamics parameters	Gas phase	Hydrodynamics parameters	Gas phase		
	Sim Time (s)	t=0.01-0.19 step size=0.02	Sim Time (s)	t=0.01-0.19 step size=0.001		

6.2.2 ANFIS mesh

In the prediction section, the new mesh domain is generated to represent the 2D rectangular BCR, similar with the BCR size in Chapter 4. This domain contains 251001 nodes which are equally adopted next to each other.

6.3 Results & Discussion

6.3.1 Training and testing (T-T) of ANFIS Mode

Cases 1-4

Using Cases 1-4 (Sec. 6.2.1), the bubble formation (through 1 mm orifice diameter with 0.1 m/s inlet velocity) and rising are predicted at different simulation times (i.e., 0.05, 0.09, 0.13 and 0.17 s) using the ANFIS and the results are compared with the actual values from the CFD results from Chapter 4 at the same time. The coefficient of determination (R^2) between the ANFIS and CFD results of the single bubble formation and rising at 0.05, 0.09, 0.13 and 0.17 s are shown in Figure 6.1 for the training (ANFIS model development) and testing. For the training, R^2 values of the single bubble formation and rising at 0.05, 0.09, 0.13 and 0.17 s are 0.9461, 0.9372, 0.9538 and 0.9268, respectively. This shows that a high correlation between the predicted and actual values has been achieved and a reasonable ANFIS model has been developed. Please take note that only 70 % of the actual data has been used for the training. The testing of the ANFIS model is carried out by comparing with 100 % of the actual data and R^2 values of different formation and rising time of 0.05, 0.09, 0.13 and 0.17 s is 0.9449, 0.9439, 0.9445 and 0.9295, respectively, and suggesting an accurate prediction is achieved using the ANFIS model.

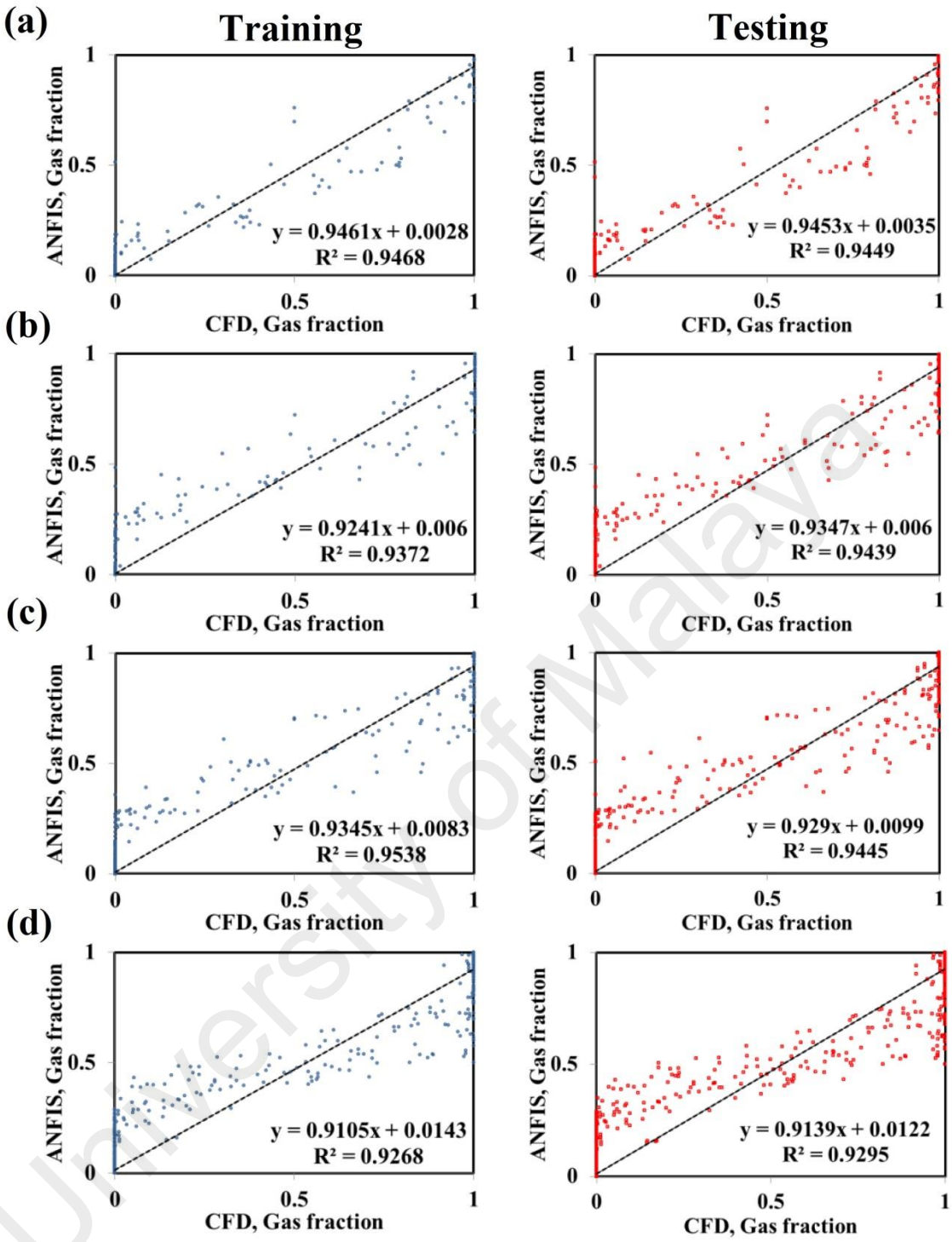

Figure 6.1: Evaluation of coefficient of determination (R^2) for training and testing data at different bubble formation and rising time: (a) 0.05 s; (b) 0.09 s; (c) 0.13 s; (d) 0.17 s

For further validation, the accuracy of the ANFIS model for formation and rising at different time periods, 0.05, 0.09, 0.13 and 0.17 s are evaluated and compared with actual values using i.e., MSE and RMSE. The RMSE and MSE between the ANFIS and the CFD results of the single bubble formation and rising are shown in Table 6.4 for the training and testing. For training, RMSE value of formation and rising times of 0.05, 0.09, 0.13 and 0.17 s is 0.0455, 0.0625, 0.0678 and 0.0920, respectively. This shows that the error between the predicted data and actual value at the beginning of formation is smaller than rising. In the testing process, the RMSE value of formation and rising times of 0.05, 0.09, 0.13 and 0.17 s is 0.0458, 0.0626, 0.0737 and 0.0926, respectively. The prediction accuracy reduces, as the bubble detaches from the orifice. In order to enhance the accuracy, the method requires more information between the formation and rising stages.

Table 6.4: Performance statistics of the ANFIS model for training and testing of bubble formation and rising at different time

Time (s)	Train MSE	Train RMSE	Test MSE	Test RMSE
0.05	0.0020	0.0455	0.0021	0.0458
0.09	0.0030	0.0625	0.0039	0.0626
0.13	0.0046	0.0678	0.0054	0.0737
0.17	0.0080	0.0920	0.0086	0.0926

6.3.2 Sensitivity study of ANFIS setting parameters

In this section, the sensitivity study of the effect of different ANFIS setting parameters on the accuracy of the ANFIS model in predicting bubble formation and rising at 0.01, 0.13, 0.15 and 0.19 s is studied.

6.3.2.1 Percentage of training data (*P*)

Cases 5-9

Using Cases 5-9 (Sec. 6.2.1), the bubble formation and rising are predicted at different time periods of 0.01, 0.13, 0.15 and 0.19 s for different values of *P*, 5 %, 10 %, 30 %, 50 % and 70 % in the ANFIS method and the results are compared with the actual values from the CFD results from Chapter. 4 at the same time. The bubble formation and rising at different times for different values of *P* are shown in Figures 6.2-6.5. Figure 6.2 shows the formation and rising of bubbles at different times for *P* value of 5 %. According to the figure, when *P* is 5 %, the ANFIS method cannot predict the bubble shape, size, position and interface between gas and liquid during the formation and rising. For example, at the beginning of the bubble formation (t=0.01 s), this method over predicts the hemispherical bubble shape. In this case, the predicted bubble size using the ANFIS method is about double, as compared to the CFD results. In addition, the exact location of the bubble formation from the tip of the orifice is not correctly predicted by the ANFIS method. As the formation time increases, the ANFIS method estimates different bubble shapes and sizes which are not similar with the CFD results and reality (t=0.13 and 0.15 s). For example, unlike the CFD results, the bubble slender neck, connecting the spherical shape of the bubble to the tip of the orifice is not predicted by the ANFIS method at 0.13 and 0.15 s. In this case, the bubble shape, size and position are not similar with the CFD results due to the less number of training data. Note that, as discussed in Chapter 5, when the percentage of training data (*P*) at boundary conditions is 10 %, the accuracy of the ANFIS model reduces. After detachment (t=0.19 s), this method predicts the break-up process of one large and smaller bubbles which is impossible for the small inlet orifice velocity of 0.1 m/s. The results show that, due to a small number of training data (*P*=5 %) at boundary conditions and the interface between bubble and liquid in the ANFIS learning process,

this method cannot predict the bubble size, position, slender neck, and particularly the interface between gas and liquid.

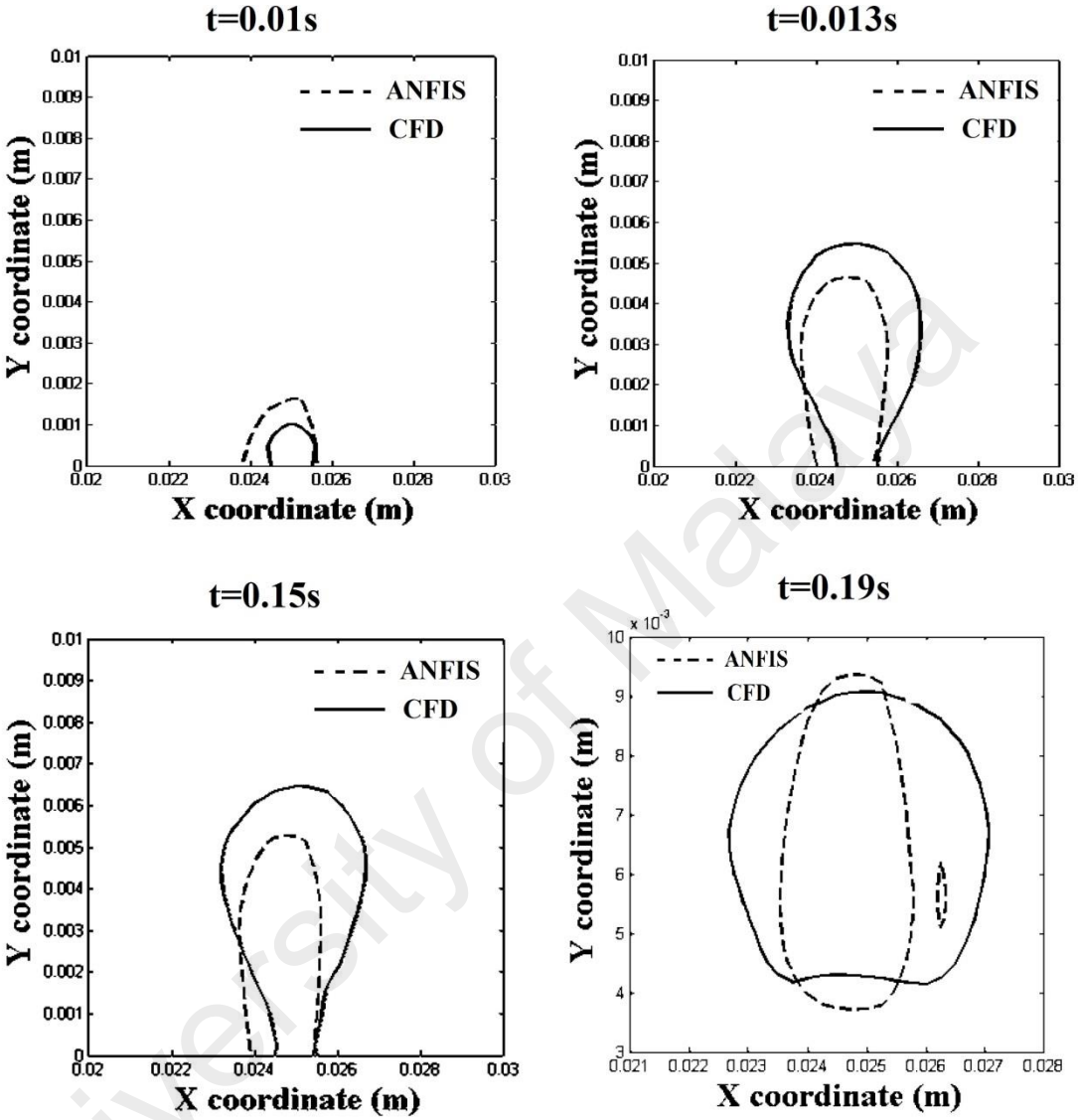

Figure 6.2: Comparison between ANFIS and CFD results for bubble formation and detachment when *P* is 5 %

Figure 6.3 shows that as the percentage of the training data increases up to 10 %, the size of bubble almost matches the CFD data, excluding at the beginning of the bubble formation (t=0.01 s). Although this method can approximately predict bubble size, it cannot accurately estimate the shape and interface of the bubble. In addition, the predicted results show that, the slender neck disappeared and only the spherical part of the bubble appeared during the formation stage (t=0.13-0.15 s). After detachment, the

result of the bubble size and position using the ANFIS method are almost similar to that of the CFD results. However, this method is still unable to show the exact shape and interface of gas and liquid (at t=0.19 s).

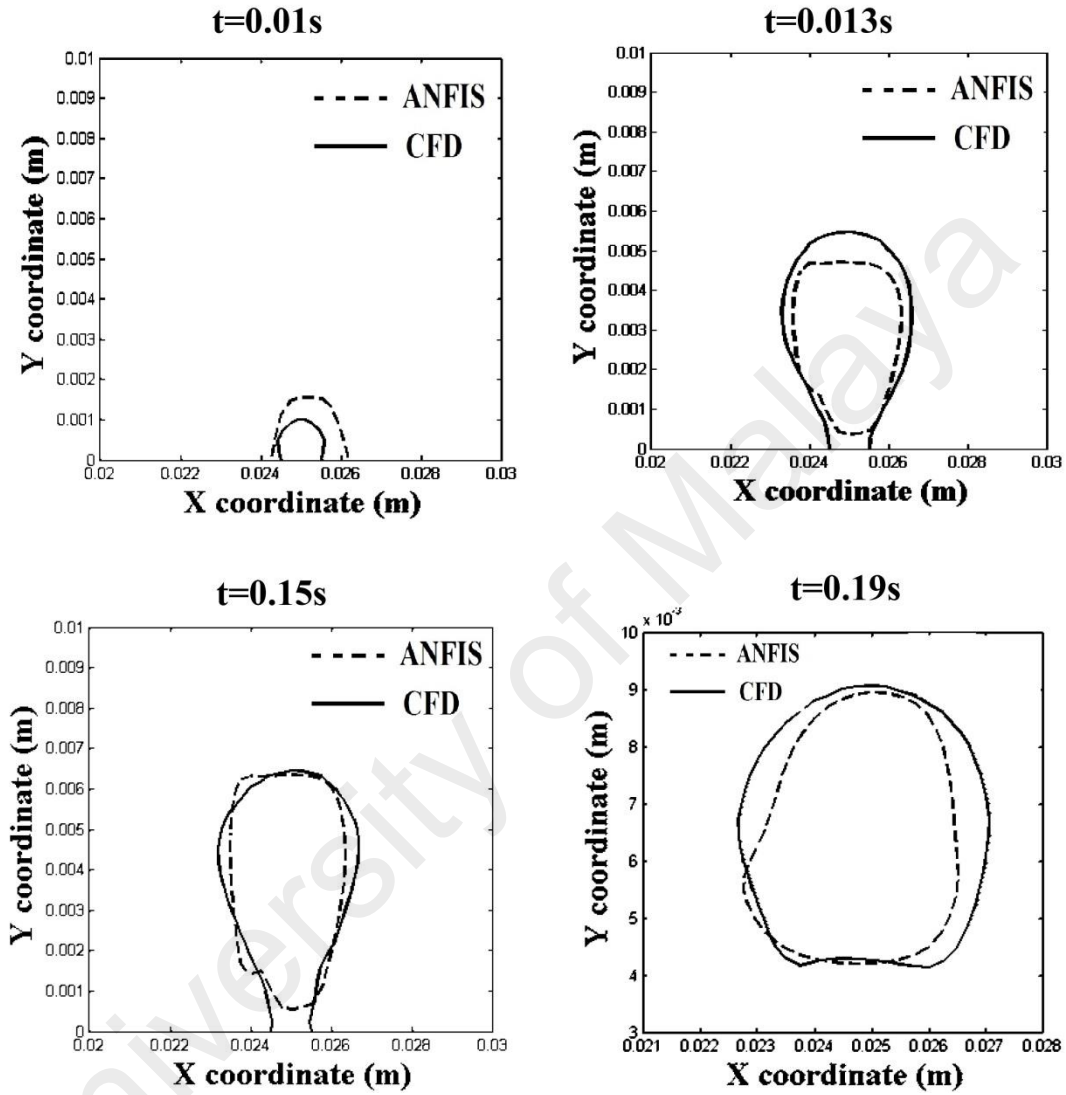

Figure 6.3: Comparison between ANFIS and CFD results for bubble formation and detachment when *P* is 10 %

Figure 6.4 shows that the ability of method in predicting bubble size and shape at the beginning of the bubble formation (t=0.01 s) does not increase and the accuracy of the method in predicting the size decreases, when *P* increases up to 30 %. However, by increasing the formation time, the ANFIS method can predict the slender neck at 0.15 s,

as well as the bubble size and shape. After detachment, the ANFIS method can only predict the bubble position.

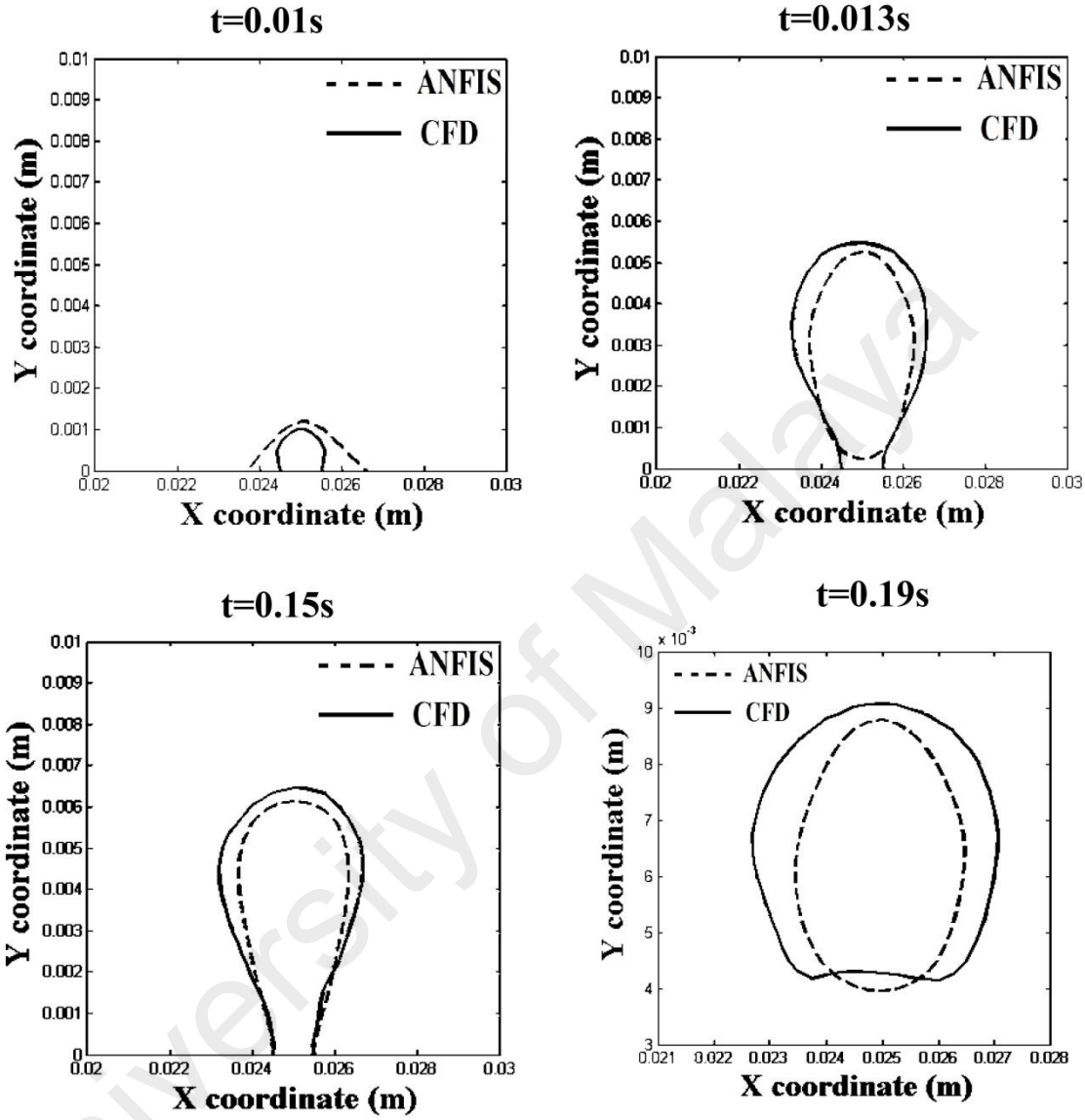

Figure 6.4: Comparison between ANFIS and CFD results for bubble formation and detachment when *P* is 30 %

When *P* reaches to 70 %, the ANFIS method can better predict the bubble size, shape, position and the interface between gas and liquid (see Figure 6.5). In this case during formation time (t=0.01-0.15 s), the bubble size, shape, position and the gas and liquid interface are well predicted. However, there is a small variation between the CFD and ANFIS results for the bubble interface. Similar to the bubble formation, the ability of this method increases, when the bubble detaches form the orifice. At 0.19 s, the size

and position of the bubble is almost similar with the CFD results, while the exact shape and interface of gas and liquid slightly different with the CFD result. The increase of *P* at the interface between gas and liquid may result in better predictions.

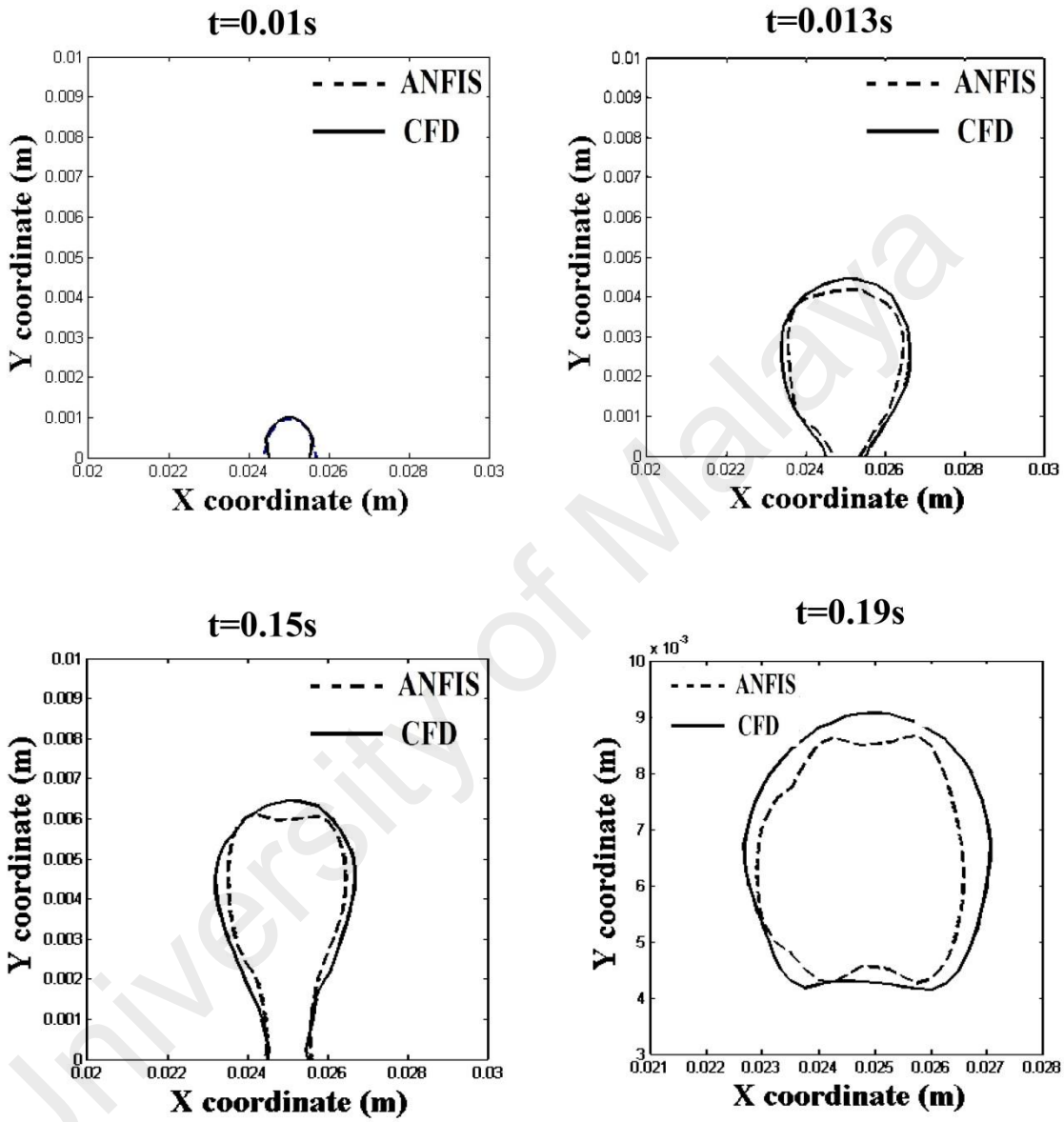

Figure 6.5: Comparison between ANFIS and CFD results for bubble formation and detachment when *P* is 70 %

For further validation, the accuracy of the ANFIS results at different formation and rising times, 0.01, 0.13, 0.15 and 0.19 s are evaluated and compared with the actual values using i.e., MSE and RMSE and R^2. The R^2, RMSE and MSE between the ANFIS

and the CFD results of different times are shown in Table 6.5 for the training and testing.

The best performance as expected is obtained when 70 % of the CFD data is used in the training process. In this case, R^2 is 0.90 and MSE and RMSE for both training and testing results is less than 0.090. However, using only 5 % of the actual results leads to the lowest value of R^2 and highest value of RMSE and MSE for both training and testing results.

Table 6.5: Performance criteria of ANFIS method for different percentage of training data.

P	Train MSE	Train RMSE	Test MSE	Test RMSE	Train R^2	Test R^2
5 %	0.0127	0.112	0.0214	0.146	0.84	0.78
10 %	0.0094468	0.097195	0.012186	0.11039	0.84	0.81
30 %	0.0135	0.1164	0.014326	0.11969	0.81	0.81
50 %	0.015413	0.12415	0.015796	0.12568	0.80	0.79
70 %	0.00823	0.090719	0.0082275	0.090705	0.90	0.90

6.3.2.2 Membership Function (*M.F*)

Cases 10-16

Using Cases 10-16 (Sec. 6.2.1), the bubble formation and rising is predicted at different times, 0.01, 0.13, 0.15 and 0.19 s for different membership functions (i.e., '*gbell*', *'Gauss'*, *'Gauss2'*, *'tri'*, *'trap'* and *'pi'*) in the ANFIS method and the results are compared with the actual values from the CFD results from Chapter 4 at the same time. The bubble formation and rising at different times for different *MF*s are shown in Table 6.6. According to the table, the '*gbell*' and '*dsi* functions are in good agreement with the CFD results. However, the '*gbell*' function has a slightly better performance in the MSE and RMSE error criteria. In this case, the R^2 for both the training and testing result is 0.90, while the MSE and RMSE are less than 0.083 and 0.091 for both the

training and testing data. In contrast, the *'pi'* contains the lowest accuracy between all membership functions.

Table 6.6: Performance criteria of ANFIS method for different membership function.

M.F	Train MSE	Train RMSE	Test MSE	Test RMSE	Train R^2	Test R^2
'dsig'	0.015413	0.12415	0.015796	0.12568	0.90	0.90
'Gauss'	0.011958	0.10935	0.011782	0.10855	0.84	0.84
'Gauss2'	0.012927	0.1137	0.012993	0.11399	0.83	0.83
'pi'	0.24024	0.49015	0.24005	0.48995	0.80	0.79
'psig'	0.013092	0.11442	0.013382	0.11568	0.83	0.82
'*gbell*'	0.00823	0.090719	0.0082275	0.090705	0.90	0.90

6.3.2.3 Number of rules (*N.R*)

Cases 17-20

Using Cases 17-20 (Sec. 6.2.1), the bubble formation and rising is predicted at different times, 0.01, 0.13, 0.15 and 0.19 s for different number of rules (i.e., 2, 3, 4 and 7) using the ANFIS method and the results are compared with the actual values from the CFD results from Chapter 4 at the same time. The bubble formation and rising at different times for the different *NR* are shown in Table 6.7. According to the Table, the number of rules has more influence on the ability of the prediction process, as compared to other setting parameters. When the number of rules is less than three, this method fails to predict, while for the number of rules ranging from 4 to 7, the accuracy of the method rises. For example, for the 7 number of rules, the R^2 is more than 0.94 and the MSE and RMSE for both the training and testing results is less than 0.066.

Table 6.7: Performance criteria of ANFIS method for number of rules

N.R	Train MSE	Train RMSE	Test MSE	Test RMSE	Train R^2	Test R^2
2	0.045939	0.21433	0.045225	0.21266	0.41	0.41
3	0.01557	0.12478	0.015164	0.12314	0.79	0.79
4	0.00823	0.090719	0.0082275	0.090705	0.90	0.90
7*****	0.0042568	0.065244	0.0044803	0.066935	0.94	0.94

The results of the sensitivity study shows that, in the selection of the setting parameters in the ANFIS algorithm, 70 % of the VOF data must be used in the learning process, while the '*gbll*' membership function with the 7 number of rules and 1000 iteration should be used in the algorithm.

6.3.3 Prediction of ANFIS and Validation

The ANFIS method can predict the microscopic hydrodynamic parameters of the BCR (i.e., bubble size, shape, position and the interface between gas and liquid) with different operational conditions and process time, in less computational time and provide continuous results. In order to examine the prediction ability, the formation and rising are predicted for different simulation time periods (case 21). All predicted results using the ANFIS method are not used in the training process.

6.3.3.1 Single bubble formation

Figure 6.6 shows the prediction of the single bubble formation using the ANFIS method at various formation time periods (i.e., 0.01, 0.025, 0.055, 0.085, 0.105, 0.125, 0.155 and 0.16 s). The method shows that the bubble expansion occurs from 0.01 s to 0.16 s. According to the figure, the hemi-spherical bubble shape at the beginning of the growing appeared at 0.01 s and 0.025 s. As the time increases, the bubble volume increases which is similar with the CFD results, but the interface between gas and liquid is not almost identical with the reality and CFD results. In order to enhance this interface, the ANFIS algorithm requires more training data from the interface of gas and liquid, as well as the increasing number of rules. The figure also shows that, the bubble neck and position of orifice are accurately predicted with the ANFIS method.

6.3.3.2 Single bubble rising

Figure 6.7 shows the prediction of single bubble dynamics after detachment with the ANFIS method. Like the formation process, in the rising stage, the bubble size and position are accurately estimated. This method is also unable to predict the interface between the gas and liquid for the rising stage. It can show the moment of detachment (i.e., 0.172 s). After detachment, the bubble rises to the top surface of the column (outlet). At 0.175 s, the next generated bubble appeared from the tip of the orifice. The ANFIS together with the VOF method provides a detailed information of the bubble formation and rising which is a non-discrete data. This continuous information assists in finding the detailed information of the bubble formation and rising. For example, to show the exact time of detachment, the CFD method must be implemented for time step smaller than 0.01 s, resulting in a longer computational time and computational instability. In contrast, the ANFIS method, due to providing non-discrete results is able to predict the formation and rising for time step of 0.001 s without computational difficulties.

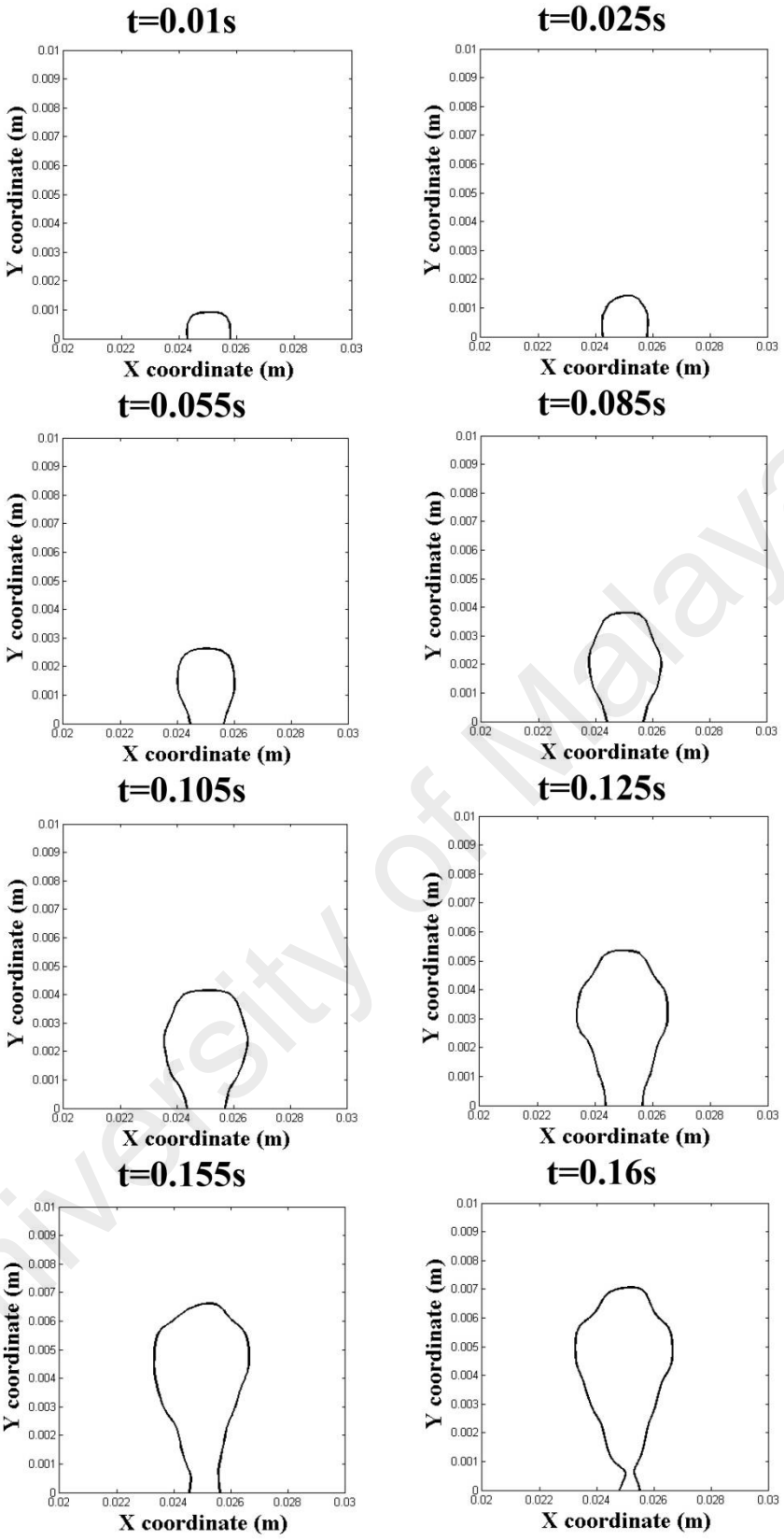

Figure 6.6: Prediction of single bubble formation at different simulation time, 0.01, 0.025, 0.055, 0.085, 0.105, 0.125, 0.155 and 0.16 s

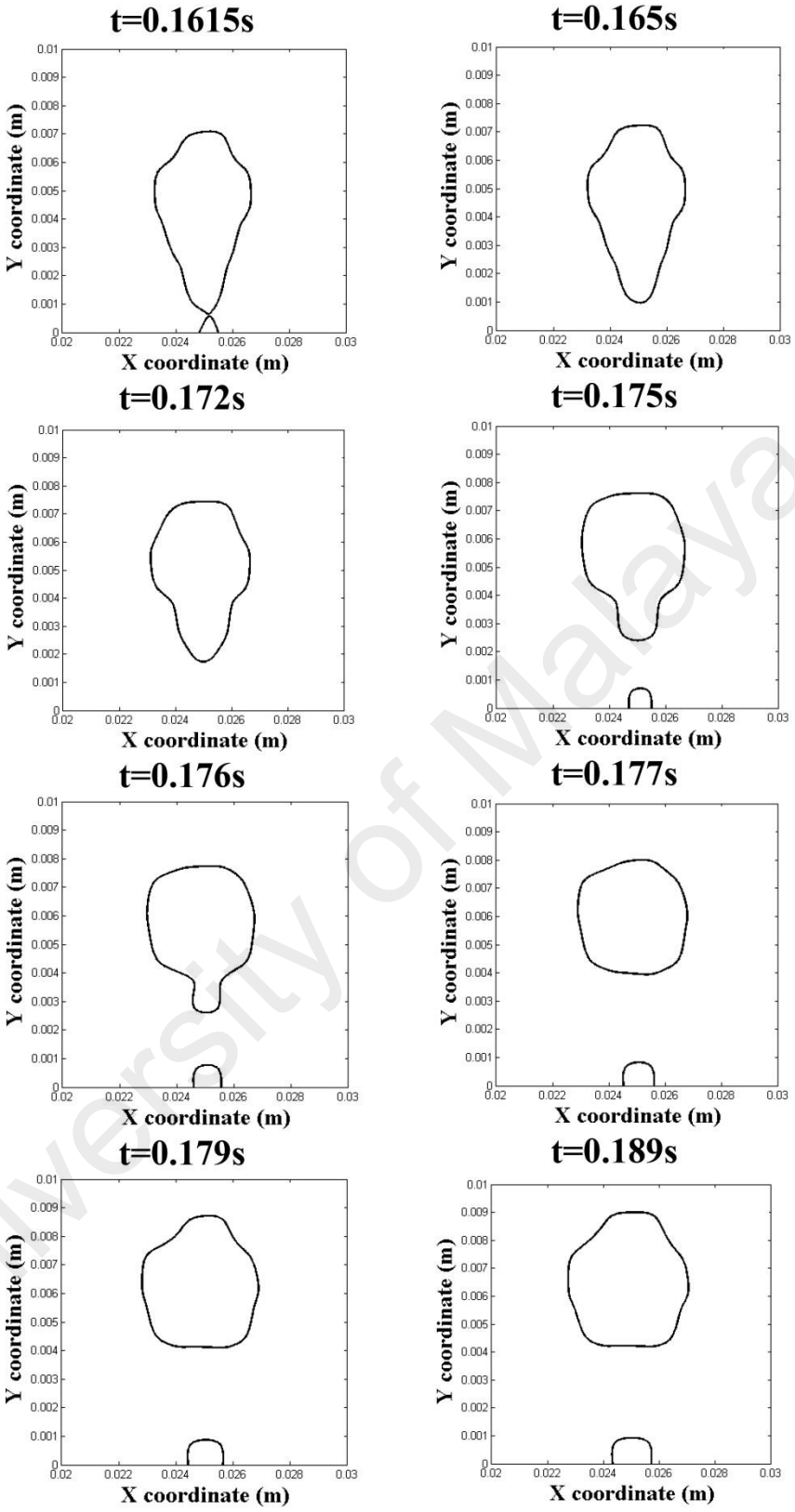

Figure 6.7: Prediction of single bubble rising at different simulation time, 0.1615, 0.165, 0.172, 0.175, 0.176, 0. 177, 0.179 and 0.198 s

Table 6.8: The predicted bubble distance from the bottom using the ANFIS and CFD methods

Time (s)	ANFIS	CFD	Error (%)
0.01	0.001	0.00105	4.7619
0.055	0.0028	0.0029	3.4483
0.105	0.0041	0.0042	2.381
0.155	0.0068	0.0069	1.4493
0.1615	0.007	0.0072	2.7778
0.172	0.0075	0.0078	3.8462
0.176	0.0079	0.008	1.25
0.179	0.0089	0.009	1.1111

Table 6.8 shows a comparison between the ANFIS and CFD method for the bubble distance from the bottom (bubble position) at various times. According to the Table, the bubble position is predicted accurately using the ANFIS for the formation and rising. For example, at the beginning of the formation the error between the CFD and ANFIS result is 4.77 % (t=0.01 s). This error decreases up to 1.44 % (t=0.155 s). Due to sudden separation of air fraction from the tip of the orifice, the error between the CFD and ANFIS increases up to 2.7 % and this increment in error continuous till 0.172 s. Like the formation process, this error reduces, as the time of rising increases.

6.4. Conclusions

In the present chapter, for the first time, the ANFIS method has been developed to predict the microscopic hydrodynamic parameters of BCR. The single bubble formation from an orifice and rise characteristics are predicted and compared with the CFD results (i.e., VOF). The sensitivity study of the ANFIS setting parameters (i.e., percentage of training data (*P*), membership functions (*MF*) and number of rules (*NR*)) on the accuracy of prediction results are carried out. The conclusions of this study are as follows:

- The ANFIS model can accurately predict bubble size and position during the formation and rising time, as well as the bubble slender neck. However, this model cannot predict accurately the exact shape of the bubble, particularly the interface between the bubble and liquid during formation and rising.
- ANFIS can be used as an assistance tool together with the VOF method to predict the bubble formation and rising for a very small time step. The developed ANFIS model can predict the bubble formation and rising with less computational efforts due to having non-discrete results.
- The accuracy of the ANFIS model in predicting the bubble formation and rising highly depends on the number of rules. When the number of rules reaches to seven, the best performance of this method is achieved. In this case the MSE and RMSE are smaller than 0.066 and the R^2 is larger than 0.94. The '*gbell*' membership function can also improve the results of the bubble shape, size, position and the interface between gas and liquid. Furthermore, the ability of this method in the learning stage increases when 70 % of the CFD data is used in the training process (MSE and RMSE<0.09 and R^2>0.90).

CHAPTER 7: CONCLUSIONS

7.1 Conclusions

In the present PhD thesis the influence of sparger design parameters on the macroscopic bubble column hydrodynamics (i.e., liquid flow pattern and gas dynamics) is studied. The single bubble formation and rise characteristics and the interaction between bubbles are numerically and experimentally investigated for various orifice sizes and velocities. The present experimental observations and prior experimental and numerical results and mathematical correlations are used for the validation of the present CFD study. For the first time, a novel development of the ANFIS method using CFD, the Euler-Euler results have been used to predict the liquid flow pattern, gas hold-up and turbulent kinetic energy for various ring sparger diameters and column heights. This method has also been developed with the CFD, VOF results to predict bubble formation and rising through a single orifice. The following provides a summary of the main conclusions of the study.

CFD study of gas flow from ring type sparger

The influence of various ring sparger design parameters i.e., ring sparger diameters (0.07-0.20 m), superficial gas velocities (0.0025-0.01 m/s) and number of sparger holes (5-30) on the liquid flow patterns and gas dynamics for the cylindrical BCR has been studied using the Euler-Euler method. For the validation of the CFD study, the existing experimental and numerical results, as well as empirical correlations are used. In addition, the effect of using different drag models, turbulent dispersion coefficients and bubble sizes on the accuracy of the numerical results has been studied.

As a result of using different ring sparger sizes, the superficial gas velocities and number of sparger holes, rate of coalescence and break up, size of downward flow towards the wall and amount of gas can be changed in the BCR. For the small ring sparger diameters, relatively nearer the column center (0.07 m ring sparger diameter), coalescence of bubbles is more likely to appear towards the column center, particularly at the sparger region, while the liquid velocity and amount of gas are larger at the column center. In this case, a steeper profile of the axial liquid velocity and the gas hold-up appeared near the column center due to a high flow at this location from the bottom to the top of the column. As the ring sparger diameter reaches 0.14 m, relatively between the column centre and wall, the axial liquid velocity and gas hold-up at the center decreases, while the overall amount of gas inside the column rises. This shows that there is an optimum ring sparger size to provide a higher gas hold-up, which enhance the BCR efficiency. In the case of using the larger ring sparger size, relatively nearer to the column wall (0.2 m ring sparger diameter), the coalescence of bubbles rarely occurs near the sparger region. However, this type of sparger can provide a strong downward flow at the column center. This type of sparger increases the axial liquid velocity and gas hold-up near the wall region and changes the liquid circulation direction. This feature in the larger sparger size may be further explored to enhance the liquid agitation and reaction process near the column wall.

Changing the superficial gas velocity can mainly alter the uniformity of the gas distribution in the column. In comparison to other superficial gas velocities, the 0.01 m/s provides the uniform gas distribution over the cross section of the column at almost all column heights, while as expected the centerline liquid velocity, gas hold-up and TKE are higher than other superficial gas velocities. In contrast, the smaller V_G (0.0025 m/s) causes a mal-distribution of the gas. Furthermore, in comparison to all velocities,

the 0.005 m/s produces the higher downward liquid flow (stronger recirculation) towards the wall regions which can provide a higher heat and mass transfer coefficient.

The effect of using different number of sparger holes (more than 5) is insignificant on the results of the liquid velocity, gas hold-up and TKE, particularly towards the wall region. However, using the sparger having 5 holes, results in a non-uniform gas hold-up profile almost at all column heights (especially near the sparger region). In this case, the sparger velocity increases and results in the production of large bubbles through each sparger and consequently the mal-distribution of gas, while the increase of number of sparger holes decreases the inlet velocity of each sparger and produces a uniform and small sized bubbles which result in the uniformity of gas distribution.

Single bubble formation and rise characteristics

The effect of the orifice velocity and size on the bubble formation and rising characteristics has been studied using the microscopic CFD method (i.e., VOF) and experimental study. In addition, the effect of the bubble diameter on the coalescence process and the influence of the distance between orifices and number of orifices on the coalescence and detachment time have been studied. The experimental observation is used to examine the volume of bubble and detachment time for different orifice sizes and velocities. The present experimental results and prior experimental and numerical results and empirical correlation in the literature have also been used for the validation of the numerical method.

Existing large and non-uniform bubbles in the BCR leads to early coalescence near the orifices and increases the coalescence rate, especially near the sparger region. This unpleasant production of large and non-uniform bubbles results in a smaller rate of the amount of gas and bubble interfacial area. To avoid this unpleasant production

inside the column, particularly near the orifice region, the optimizing distance between orifices is critical. This distance must be greater than 4 mm (when the ratio of α >1), and able to results in a homogeneous regime towards the orifices, smaller bubbles with uniform shapes and higher bubble interfacial area. Furthermore the selection of the BCR, produces very small bubble sizes or break larges bubbles into small ones (e.g., using sieve plate at various BCR heights) and changes early coalescence to a later one and leads to the formation of small bubbles with spherical shapes.

The increase in the number of orifices (more than two orifices) has an almost insignificant effect on the bubble coalescence time but results in faster detachment. The increment of this parameter results also in the production of large bubbles with a non-uniform shape.

For small flow rates (i.e., $q<6\times10^{-9}$ m^3/s), the increase of the orifice size (with constant orifice velocity) enlarges the bubble size and volume and reduces the bubble detachment time. However, the increase of the orifice velocity only decreases the bubble detachment time. In low flow rates, the bubble shape is predominantly dictated from the orifice due to an insignificant effect of the former detached bubble and liquid movement. As the flow rate rises, the bubble size, shape and detachment time are not only affected by orifice parameters but also altered by the influence of the former detached bubble size, shape and its wake area.

A novel development of the Adaptive Neuro Fuzzy Inference System (ANFIS) model

For the first time, the ANFIS method has been developed with a CFD data, the Euler-Euler to predict the macroscopic hydrodynamic parameters of the BCR (i.e., liquid flow patterns, gas hold-up and turbulent kinetic energy) for different ring sparger diameters and column heights. The multiphase flow field throughout the 3D BCR is

also illustrated using the ANFIS method. Furthermore, this method, for the first time, has been developed with a microscopic CFD data (VOF) to predict a single bubble formation and rising characteristics (i.e., bubble size, shape, position and the interface between bubble and liquid). The influence of the different ANFIS setting parameters on the accuracy of the prediction results has been studied.

The ANFIS method can accurately predict the macroscopic BCR hydrodynamic parameters (i.e., liquid flow patterns, gas hold-up and TKE) for various ring sparger diameters and column heights. This method can also predict the bubble formation and rise characteristics (i.e., bubble size and position) at various formation and rising time. However, it cannot well predict the exact interface between the bubble and liquid during formation and rising. In general, this method can predict the microscopic and macroscopic parameters in a very short time and provide a non-discrete (continuous) result, while the CFD simulation needs to be employed for any changes in the operational conditions. In this method, the implementation of a high number of grids (fine mesh) and small time step have insignificant effects on the computational time.

A new view point of the ANFIS development using the CFD data set can be considered as an assistance tool of CFD implementation, when the CFD study is necessary to be carried out for new simulation cases due to the small changes in physical conditions (e.g., bubble column dimension, ring sparger parameters and liquid and gas properties). Furthermore, the use of the ANFIS development using CFD data set results in non-discrete data set at each location of the BCR domain and produces the prediction results with a small step size. However, the CFD methodology is unable to generate continues results in a specific range of changes with the small step size as it requires high computational efforts and repetition in simulation and numerical instability. In general, the learning procedure of the ANFIS method should be thoroughly trained by the behavior of flow patterns and gas dynamics within the domain

of CFD simulation. If in the learning process, all the changes are considered, it means the ability of the method increases and covers more fluid flow phenomena inside the bubble column reactor.

7.2 Suggestion for future work

Major future developments can include the following:

- The heterogeneous flow regime (having different bubbles sizes, shapes and velocities) should be studied for different superficial gas velocities and ring sparger design parameters using the integration of population balance model (PBM) with the Euler-Euler method. Furthermore, the PBM model could evaluate the range of bubble sizes and velocities towards the sparger, bulk (middle) and surface (outlet) regions. The rate of coalescence and break-up can be calculated for different operational conditions. This work should also be done to other bubble column diameters, having different gas and liquid properties.
- Other turbulence methods (i.e., RSM and LES) should be used for the prediction of BCRs. Using the RSM and LES result in clear observations of coherent structures and instantaneous flow profiles, particularly when the superficial gas velocity is high and the rate of interaction between bubbles increases.
- The ANFIS should be integrated into the DAQ acquisition control card in order to make a control device for this type of investigation. Another main goal for future research should be the hybridization of the ANFIS methodology with other soft computing methods in order to improve the optimization structure of the ANFIS network. Additionally, in order to generate an accurate ANFIS multiphase flow model, various bubble column regimes and operational conditions should be simulated with CFD methods to introduce more detailed information about multiphase flow in the ANFIS learning process. There is a

need to develop multi-membership functions and rules for different operational conditions and column heights to improve the accuracy of the ANFIS method near the boundary conditions. Other soft computing methods (e.g., SVR, PSO, GA) could be individually trained using the CFD data to predict both microscopic and macroscopic hydrodynamics parameters.

- The experimental study should be implemented to evaluate the liquid velocity (using PIV technique), gas hold-up and bubble size, shape and velocity (using high speed camera) for homogeneous and heterogeneous flow regimes. The obtained results could be compared with the CFD methods (i.e., VOF and Euler-Euler). This result should be used in the ANFIS method in order for better development of intelligent soft computing methods in BCR applications.
- The image processing technique should be incorporated with the ANFIS method to produce new viewpoints in the modelling of microscopic parameters through experimental images. In this case, the bubble shape, position, size and interface can be predicted for different operational conditions without using CFD and conventional mathematical modelling methods.
- The formation and rising characteristics (bubble size, shape and velocity) and the interaction between bubbles should be investigated for different gas (e.g., Methane) and liquid properties through single and multi-spargers using the VOF methods.
- The sensitivity study of different bubble diameters on the accuracy of the CFD results for various operational conditions (i.e., superficial gas velocity and ring sparger diameters) could be implemented in the numerical method. Furthermore, using this sensitivity study can show the predominate range of bubble sizes at different BCR heights.

7.3 Applications of present study

Although many experimental and numerical techniques (e.g., Euler-Euler and VOF) have been used to measure and predict the microscopic and macroscopic hydrodynamic parameters in BCR industries, finding the optimum value for these parameters requires expensive equipment in experimental studies and high computational efforts in numerical techniques. This study, for the first time proposes a new view point of BCR modelling through the ANFIS development model to produce non-discrete results, helping to find optimum values within the specific range of the data. This model can be considered as an assistance tool for CFD implementations, when the CFD study is required to simulate new cases (small changes) due to the changes in operational conditions (e.g., bubble column dimension, ring sparger parameters and liquid and gas properties). For example, the ANFIS model can be used as an alternative means in BCR applications to complete data set, when there is a limitation in use of sensors in the BCRs or increasing number of meshes in the CFD study. This study also shows that, the ANFIS model can be also used in other types of chemical and biochemical reactors with different operational conditions.

REFERENCES

Ahmadi, G., & Ma, D. (1990). A thermodynamical formulation for dispersed multiphase turbulent flows—1: Basic theory. *International Journal of Multiphase Flow, 16*(2), 323-340.

Al-Shammari, E. T., Amirmojahedi, M., Shamshirband, S., Petković, D., Pavlović, N. T., & Bonakdari, H. (2015). Estimation of wind turbine wake effect by adaptive neuro-fuzzy approach. *Flow Measurement and Instrumentation, 45*, 1-6.

Albadawi, A., Donoghue, D., Robinson, A., Murray, D., & Delauré, Y. (2013). On the analysis of bubble growth and detachment at low capillary and bond numbers using volume of fluid and level set methods. *Chemical Engineering Science, 90*, 77-91.

Alvare, J., & Al-Dahhan, M. H. (2006). Liquid phase mixing in trayed bubble column reactors. *Chemical Engineering Science, 61*(6), 1819-1835.

Aminossadati, S., Kargar, A., & Ghasemi, B. (2012). Adaptive network-based fuzzy inference system analysis of mixed convection in a two-sided lid-driven cavity filled with a nanofluid. *International Journal of Thermal Sciences, 52*, 102-111.

Auton, T. (1987). The lift force on a spherical body in a rotational flow. *Journal of fluid Mechanics, 183*, 199-218.

Azwadi, C. S. N., Zeinali, M., Safdari, A., & Kazemi, A. (2013). Adaptive-network-based fuzzy inference system analysis to predict the temperature and flow fields in a lid-driven cavity. *Numerical Heat Transfer, Part A: Applications, 63*(12), 906-920.

Bannari, R., Kerdouss, F., Selma, B., Bannari, A., & Proulx, P. (2008). Three-dimensional mathematical modeling of dispersed two-phase flow using class method of population balance in bubble columns. *Computers & Chemical Engineering, 32*(12), 3224-3237.

Bech, K. (2005). Dynamic simulation of a 2D bubble column. *Chemical Engineering Science, 60*(19), 5294-5304.

Ben-Nakhi, A., Mahmoud, M. A., & Mahmoud, A. M. (2008). Inter-model comparison of CFD and neural network analysis of natural convection heat transfer in a partitioned enclosure. *Applied Mathematical Modelling, 32*(9), 1834-1847.

Bhole, M. R., Joshi, J. B., & Ramkrishna, D. (2008). CFD simulation of bubble columns incorporating population balance modeling. *Chemical Engineering Science, 63*(8), 2267-2282.

Bhole, M. R., Roy, S., & Joshi, J. B. (2006). Laser Doppler anemometer measurements in bubble column: effect of sparger. *Industrial & Engineering Chemistry Research, 45*(26), 9201-9207.

Bothe, D., & Fleckenstein, S. (2013). A volume-of-fluid-based method for mass transfer processes at fluid particles. *Chemical Engineering Science, 101*, 283-302.

Brackbill, J. U., Kothe, D. B., & Zemach, C. (1992). A continuum method for modeling surface tension. *Journal of Computational Physics, 100*(2), 335-354.

Buwa, V. V., Deo, D. S., & Ranade, V. V. (2006). Eulerian–Lagrangian simulations of unsteady gas–liquid flows in bubble columns. *International Journal of Multiphase Flow, 32*(7), 864-885.

Buwa, V. V., Gerlach, D., Durst, F., & Schlücker, E. (2007). Numerical simulations of bubble formation on submerged orifices: Period-1 and period-2 bubbling regimes. *Chemical Engineering Science, 62*(24), 7119-7132.

Buwa, V. V., & Ranade, V. V. (2002). Dynamics of gas–liquid flow in a rectangular bubble column: experiments and single/multi-group CFD simulations. *Chemical Engineering Science, 57*(22), 4715-4736.

Chakraborty, I., Biswas, G., & Ghoshdastidar, P. S. (2011). Bubble generation in quiescent and co-flowing liquids. *International Journal of Heat and Mass Transfer, 54*(21), 4673-4688.

Chakraborty, I., Ray, B., Biswas, G., Durst, F., Sharma, A., & Ghoshdastidar, P. S. (2009). Computational investigation on bubble detachment from submerged orifice in quiescent liquid under normal and reduced gravity. *Physics of Fluids, 21*(6), 1-17.

Chen, P. (2004). *Modeling the fluid dynamics of bubble column flows.* Washington University, 2004. Department of Chemical Engineering.

Chen, P., Duduković, M. P., & Sanyal, J. (2005). Three-dimensional simulation of bubble column flows with bubble coalescence and breakup. *AIChE journal, 51*(3), 696-712.

Chen, P., Sanyal, J., & Dudukovic, M. P. (2004). CFD modeling of bubble columns flows: implementation of population balance. *Chemical Engineering Science, 59*(22), 5201-5207.

Chen, P., Sanyal, J., & Duduković, M. P. (2005). Numerical simulation of bubble columns flows: effect of different breakup and coalescence closures. *Chemical Engineering Science*, *60*(4), 1085-1101.

de Bertodano, M. A. L. (1992). *Turbulent bubbly two-phase flow in a triangular duct.*

de Bertodano, M. L. (1991). *Turbulent bubbly flow in a triangular duct.* Ph. D. Thesis, Rensselaer Polytechnic Institute, Troy New York.

Deen, N. G., Solberg, T., & Hjertager, B. H. (2000). *Numerical simulation of the gas-liquid flow in a square cross-sectioned bubble column.* Paper presented at the 14th Int. Congress of Chemical and Process Engineering. , Praha-Czech Republic.

Deen, N. G., Solberg, T., & Hjertager, B. H. (2001). Large eddy simulation of the gas–liquid flow in a square cross-sectioned bubble column. *Chemical Engineering Science, 56*(21), 6341-6349.

Dhotre, M. T., Deen, N. G., Niceno, B., Khan, Z., & Joshi, J. B. (2013). Large eddy simulation for dispersed bubbly flows: a review. *International Journal of Chemical Engineering, 2013*, 1-22.

Dhotre, M. T., Ekambara, K., & Joshi, J. B. (2004). CFD simulation of sparger design and height to diameter ratio on gas hold-up profiles in bubble column reactors. *Experimental Thermal and Fluid Science, 28*(5), 407-421.

Dhotre, M. T., & Joshi, J. B. (2007). Design of a gas distributor: Three-dimensional CFD simulation of a coupled system consisting of a gas chamber and a bubble column. *Chemical Engineering Journal, 125*(3), 149-163.

Dhotre, M. T., Niceno, B., & Smith, B. L. (2008). Large eddy simulation of a bubble column using dynamic sub-grid scale model. *Chemical Engineering Journal, 136*(2), 337-348.

Dhotre, M. T., Niceno, B., Smith, B. L., & Simiano, M. (2009). Large-eddy simulation (LES) of the large scale bubble plume. *Chemical Engineering Science, 64*(11), 2692-2704.

Dhotre, M. T., & Smith, B. L. (2007). CFD simulation of large-scale bubble plumes: comparisons against experiments. *Chemical Engineering Science, 62*(23), 6615-6630.

Di Bari, S., Lakehal, D., & Robinson, A. J. (2013). A numerical study of quasi-static gas injected bubble growth: Some aspects of gravity. *International Journal of Heat and Mass Transfer, 64*, 468-482.

Di Marco, P., & Grassi, W. (2009). Effect of force fields on pool boiling flow patterns in normal and reduced gravity. *Heat and Mass Transfer, 45*(7), 959-966.

Díaz, M. E., Iranzo, A., Cuadra, D., Barbero, R., Montes, F. J., & Galán, M. A. (2008). Numerical simulation of the gas–liquid flow in a laboratory scale bubble column: influence of bubble size distribution and non-drag forces. *Chemical Engineering Journal, 139*(2), 363-379.

Drew, D. A., & Lahey Jr, R. T. (1987). The virtual mass and lift force on a sphere in rotating and straining inviscid flow. *International Journal of Multiphase Flow, 13*(1), 113-121.

Elena Díaz, M., Montes, F. J., & Galán, M. A. (2009). Influence of the lift force closures on the numerical simulation of bubble plumes in a rectangular bubble column. *Chemical Engineering Science, 64*(5), 930-944.

Erdirencelebi, D., & Yalpir, S. (2011). Adaptive network fuzzy inference system modeling for the input selection and prediction of anaerobic digestion effluent quality. *Applied Mathematical Modelling, 35*(8), 3821-3832.

Ervin, E. A., & Tryggvason, G. (1997). The rise of bubbles in a vertical shear flow. *Journal of Fluids Engineering, 119*(2), 443-449.

Frank, T., Zwart, P. J., Krepper, E., Prasser, H.-M., & Lucas, D. (2008). Validation of CFD models for mono-and polydisperse air–water two-phase flows in pipes. *Nuclear Engineering and Design, 238*(3), 647-659.

Gandhi, A. B., & Joshi, J. B. (2010). Estimation of heat transfer coefficient in bubble column reactors using support vector regression. *Chemical Engineering Journal, 160*(1), 302-310.

Gandhi, A. B., Joshi, J. B., Jayaraman, V. K., & Kulkarni, B. D. (2007). Development of support vector regression (SVR)-based correlation for prediction of overall gas hold-up in bubble column reactors for various gas–liquid systems. *Chemical Engineering Science, 62*(24), 7078-7089.

George, D. L., Shollenberger, K. A., & Torczynski, J. R. (2000). *Sparger effect on gas volume fraction distributions in vertical bubble-column flows as measured by gamma-densitometry tomography*. Paper presented at the Fluids Engineering Division Summer Meeting, Boston.

Gerlach, D., Tomar, G., Biswas, G., & Durst, F. (2006). Comparison of volume-of-fluid methods for surface tension-dominant two-phase flows. *International Journal of Heat and Mass Transfer, 49*(3), 740-754.

Grace, J. R., Wairegi, T., & Nguyen, T. H. (1976). Shapes and velocities of single drops and bubbles moving freely through immiscible liquids. *Transactions of the Institution of Chemical Engineers, 54*(3), 167-173.

Gupta, A., & Roy, S. (2013). Euler–Euler simulation of bubbly flow in a rectangular bubble column: Experimental validation with Radioactive Particle Tracking. *Chemical Engineering Journal, 225*, 818-836.

Han, L., & Al-Dahhan, M. H. (2007). Gas–liquid mass transfer in a high pressure bubble column reactor with different sparger designs. *Chemical Engineering Science, 62*(1), 131-139.

Haque, M. W., Nigam, K. D. P., & Joshi, J. B. (1986). Optimum gas sparger design for bubble columns with a low height-to-diameter ratio. *The Chemical Engineering Journal, 33*(2), 63-69.

Hasan, N., & Zakaria, Z. B. (2011). Computational approach for a pair of bubble coalescence process. *International Journal of Heat and Fluid Flow, 32*(3), 755-761.

Hasiloglu, A., Yilmaz, M., Comakli, O., & Ekmekci, İ. (2004). Adaptive neuro-fuzzy modeling of transient heat transfer in circular duct air flow. *International Journal of Thermal Sciences, 43*(11), 1075-1090.

Hirt, C. W., & Nichols, B. D. (1981). Volume of fluid (VOF) method for the dynamics of free boundaries. *Journal of Computational Physics, 39*(1), 201-225.

Hosoz, M., Ertunc, H. M., & Bulgurcu, H. (2011). An adaptive neuro-fuzzy inference system model for predicting the performance of a refrigeration system with a cooling tower. *Expert Systems with Applications, 38*(11), 14148-14155.

Hu, G., & Celik, I. (2008). Eulerian–Lagrangian based large-eddy simulation of a partially aerated flat bubble column. *Chemical Engineering Science, 63*(1), 253-271.

Hua, J. (2015). CFD simulations of the effects of small dispersed bubbles on the rising of a single large bubble in 2D vertical channels. *Chemical Engineering Science, 123*, 99-115.

Hughmark, G. A. (1967). Holdup and mass transfer in bubble columns. *Industrial & Engineering Chemistry Process Design and Development, 6*(2), 218-220.

Hur, Y. G., Yang, J. H., Jung, H., & Park, S. B. (2013). Origin of regime transition to turbulent flow in bubble column: Orifice-and column-induced transitions. *International Journal of Multiphase Flow, 50*, 89-97.

Ishii, M., & Zuber, N. (1979). Drag coefficient and relative velocity in bubbly, droplet or particulate flows. *AIChE journal, 25*(5), 843-855.

Jain, D., Kuipers, J. A. M., & Deen, N. G. (2014). Numerical study of coalescence and breakup in a bubble column using a hybrid volume of fluid and discrete bubble model approach. *Chemical Engineering Science, 119*, 134-146.

Joshi, J. B. (2001). Computational flow modelling and design of bubble column reactors. *Chemical Engineering Science, 56*(21), 5893-5933.

Joshi, J. B., & Sharma, M. M. (1979). A circulation cell model for bubble columns. *Chemical Engineering Research and Design, 57*, 244-251.

Kantarci, N., Borak, F., & Ulgen, K. O. (2005). Bubble column reactors. *Process Biochemistry, 40*(7), 2263-2283.

Kazakis, N. A., Mouza, A. A., & Paras, S. V. (2008). Experimental study of bubble formation at metal porous spargers: effect of liquid properties and sparger characteristics on the initial bubble size distribution. *Chemical Engineering Journal, 137*(2), 265-281.

Kerdouss, F., Bannari, A., & Proulx, P. (2006). CFD modeling of gas dispersion and bubble size in a double turbine stirred tank. *Chemical Engineering Science, 61*(10), 3313-3322.

Krepper, E., Beyer, M., Frank, T., Lucas, D., & Prasser, H.-M. (2009). CFD modelling of polydispersed bubbly two-phase flow around an obstacle. *Nuclear Engineering and Design, 239*(11), 2372-2381.

Krishna, R., Urseanu, M. I., Van Baten, J. M., & Ellenberger, J. (2000). Liquid phase dispersion in bubble columns operating in the churn-turbulent flow regime. *Chemical Engineering Journal, 78*(1), 43-51.

Krishna, R., & Van Baten, J. M. (1999). Rise characteristics of gas bubbles in a 2D rectangular column: VOF simulations vs experiments. *International Communications in Heat and Mass Transfer, 26*(7), 965-974.

Krishna, R., & Van Baten, J. M. (2001). Scaling up bubble column reactors with the aid of CFD. *Chemical Engineering Research and Design, 79*(3), 283-309.

Krishna, R., & Van Baten, J. M. (2003). Mass transfer in bubble columns. *Catalysis Today, 79*, 67-75.

Krishna, R., Van Baten, J. M., & Urseanu, M. I. (2000). Three-phase Eulerian simulations of bubble column reactors operating in the churn-turbulent regime: a scale up strategy. *Chemical Engineering Science, 55*(16), 3275-3286.

Kulkarni, A. A. (2008). Lift force on bubbles in a bubble column reactor: experimental analysis. *Chemical Engineering Science, 63*(6), 1710-1723.

Kulkarni, A. A., Ekambara, K., & Joshi, J. B. (2007). On the development of flow pattern in a bubble column reactor: experiments and CFD. *Chemical Engineering Science, 62*(4), 1049-1072.

Kulkarni, A. A., & Joshi, J. B. (2005). Bubble formation and bubble rise velocity in gas-liquid systems: A review. *Industrial & Engineering Chemistry Research, 44*(16), 5873-5931.

Kulkarni, A. V., Badgandi, S. V., & Joshi, J. B. (2009). Design of ring and spider type spargers for bubble column reactor: experimental measurements and CFD simulation of flow and weeping. *Chemical Engineering Research and Design, 87*(12), 1612-1630.

Kulkarni, A. V., & Joshi, J. B. (2011a). Design and selection of sparger for bubble column reactor. Part I: Performance of different spargers. *Chemical Engineering Research and Design, 89*(10), 1972-1985.

Kulkarni, A. V., & Joshi, J. B. (2011b). Design and selection of sparger for bubble column reactor. Part II: Optimum sparger type and design. *Chemical Engineering Research and Design, 89*(10), 1986-1995.

Kulkarni, A. V., Roy, S. S., & Joshi, J. B. (2007). Pressure and flow distribution in pipe and ring spargers: Experimental measurements and CFD simulation. *Chemical Engineering Journal, 133*(1), 173-186.

Kumar, A., Degaleesan, T. E., Laddha, G., & Hoelscher, H. E. (1976). Bubble swarm characteristics in bubble columns. *The Canadian Journal of Chemical Engineering, 54*(6), 503-508.

Laborde-Boutet, C., Larachi, F., Dromard, N., Delsart, O., & Schweich, D. (2009). CFD simulation of bubble column flows: Investigations on turbulence models in RANS approach. *Chemical Engineering Science, 64*(21), 4399-4413.

Laın, S., Bröder, D., Sommerfeld, M., & Göz, M. F. (2002). Modelling hydrodynamics and turbulence in a bubble column using the Euler–Lagrange procedure. *International Journal of Multiphase Flow, 28*(8), 1381-1407.

Larachi, F. ç., Desvigne, D., Donnat, L., & Schweich, D. (2006). Simulating the effects of liquid circulation in bubble columns with internals. *Chemical Engineering Science, 61*(13), 4195-4206.

Lau, R., Mo, R., & Sim, W. S. B. (2010). Bubble characteristics in shallow bubble column reactors. *Chemical Engineering Research and Design, 88*(2), 197-203.

Lau, R., Sim, W. S. B., & Mo, R. (2009). Effect of gas distributor on hydrodynamics in shallow bubble column reactors. *The Canadian Journal of Chemical Engineering, 87*(6), 847-854.

Lemoine, R., Behkish, A., Sehabiague, L., Heintz, Y. J., Oukaci, R., & Morsi, B. I. (2008). An algorithm for predicting the hydrodynamic and mass transfer parameters in bubble column and slurry bubble column reactors. *Fuel Processing Technology, 89*(4), 322-343.

Lesage, F. J., Cotton, J. S., & Robinson, A. J. (2013). Modelling of quasi-static adiabatic bubble formation, growth and detachment for low Bond numbers. *Chemical Engineering Science, 104*, 742-754.

Li, G., Yang, X., & Dai, G. (2009). CFD simulation of effects of the configuration of gas distributors on gas–liquid flow and mixing in a bubble column. *Chemical Engineering Science, 64*(24), 5104-5116.

Li, H. Z., Mouline, Y., & Midoux, N. (2002). Modelling the bubble formation dynamics in non-Newtonian fluids. *Chemical Engineering Science, 57*(3), 339-346.

Lin, H. Y., Chen, W., & Tsutsumi, A. (2003). Long-term prediction of nonlinear hydrodynamics in bubble columns by using artificial neural networks. *Chemical Engineering and Processing: Process Intensification, 42*(8), 611-620.

Lopez de Bertodano, M., Lahey Jr, R., & Jones, O. (1994). Turbulent bubbly two-phase flow data in a triangular duct. *Nuclear Engineering and Design, 146*(1), 43-52.

Lopez de Bertodano, M. A. (1998). Two fluid model for two-phase turbulent jets. *Nuclear Engineering and Design, 179*(1), 65-74.

Lu, C., Qi, N., Zhang, K., Jin, J., & Zhang, H. (2009). Experiment and CFD simulation on gas holdup characteristics in an internal loop reactor with external liquid circulation. *International Journal of Chemical Reactor Engineering, 7*(1), 1-22.

Ma, D., Liu, M., Zu, Y., & Tang, C. (2012). Two-dimensional volume of fluid simulation studies on single bubble formation and dynamics in bubble columns. *Chemical Engineering Science, 72*, 61-77.

Magnaudet, J., & Legendre, D. (1998). Some aspects of the lift force on a spherical bubble *In Fascination of Fluid Dynamics* (pp. 441-461): Springer.

Mahmoud, M. A., & Ben-Nakhi, A. E. (2007). Neural networks analysis of free laminar convection heat transfer in a partitioned enclosure. *Communications in Nonlinear Science and Numerical Simulation, 12*(7), 1265-1276.

Mathpati, C. S., Tabib, M. V., Deshpande, S. S., & Joshi, J. B. (2009). Dynamics of flow structures and transport phenomena, 2. Relationship with design objectives and design optimization. *Industrial & Engineering Chemistry Research, 48*(17), 8285-8311.

Mayer, D. G., & Butler, D. G. (1993). Statistical validation. *Ecological modelling, 61*, 21-32.

Mehrabi, M., & Pesteei, S. M. (2011). Modeling of heat transfer and fluid flow characteristics of helicoidal double-pipe heat exchangers using adaptive neuro-fuzzy inference system (ANFIS). *International Communications in Heat and Mass Transfer, 38*(4), 525-532.

Miao, X., Lucas, D., Ren, Z., Eckert, S., & Gerbeth, G. (2013). Numerical modeling of bubble-driven liquid metal flows with external static magnetic field. *International Journal of Multiphase Flow, 48*, 32-45.

Mingzhi, H., Ma, Y., Jinquan, W., & Yan, W. (2009). Simulation of a paper mill wastewater treatment using a fuzzy neural network. *Expert Systems with Applications, 36*(3), 5064-5070.

Monahan, S. M., & Fox, R. O. (2007). Linear stability analysis of a two-fluid model for air–water bubble columns. *Chemical Engineering Science, 62*(12), 3159-3177.

Monahan, S. M., Vitankar, V. S., & Fox, R. O. (2005). CFD predictions for flow-regime transitions in bubble columns. *AIChE journal, 51*(7), 1897-1923.

Moraga, F. J., Larreteguy, A. E., Drew, D. A., & Lahey Jr, R. (2003). Assessment of turbulent dispersion models for bubbly flows in the low Stokes number limit. *International Journal of Multiphase Flow, 29*(4), 655-673.

Mullai, P., Arulselvi, S., Ngo, H.-H., & Sabarathinam, P. L. (2011). Experiments and ANFIS modelling for the biodegradation of penicillin-G wastewater using anaerobic hybrid reactor. *Bioresource Technology, 102*(9), 5492-5497.

Ni, M., Li, M., Jiang, J., Wang, W., & Wu, Y. (2014). Numerical investigation on hydrodynamic performance of liquid lead lithium bubble column using population balance model. *Fusion Engineering and Design, 89*(6), 871-874.

Ničeno, B., Boucker, M., & Smith, B. L. (2008). Euler-Euler Large Eddy Simulation of a Square Cross-Sectional Bubble Column Using the Neptune_CFD Code. *Science and Technology of Nuclear Installations, 2009*.

Nikolić, V., Petković, D., Shamshirband, S., & Ćojbašić, Ž. (2015). Adaptive neuro-fuzzy estimation of diffuser effects on wind turbine performance. *Energy, 89*, 324–333.

Oey, R. S., Mudde, R. F., & Van den Akker, H. E. A. (2003). Sensitivity study on interfacial closure laws in two-fluid bubbly flow simulations. *AIChE journal, 49*(7), 1621-1636.

Olmos, E., Gentric, C., & Midoux, N. (2003). Numerical description of flow regime transitions in bubble column reactors by a multiple gas phase model. *Chemical Engineering Science, 58*(10), 2113-2121.

Olmos, E., Gentric, C., Vial, C., Wild, G., & Midoux, N. (2001). Numerical simulation of multiphase flow in bubble column reactors. Influence of bubble coalescence and break-up. *Chemical Engineering Science, 56*(21), 6359-6365.

Pashaie, P., Jafari, M., Baseri, H., & Farhadi, M. (2012). Nusselt number estimation along a wavy wall in an inclined lid-driven cavity using adaptive neuro-fuzzy inference system (anfis). *International Journal of Engineering-Transactions A: Basics, 26*(4), 383.

Pfleger, D., & Becker, S. (2001). Modelling and simulation of the dynamic flow behaviour in a bubble column. *Chemical Engineering Science, 56*(4), 1737-1747.

Pfleger, D., Gomes, S., Gilbert, N., & Wagner, H.-G. (1999). Hydrodynamic simulations of laboratory scale bubble columns fundamental studies of the Eulerian–Eulerian modelling approach. *Chemical Engineering Science, 54*(21), 5091-5099.

Pourtousi, M., Ganesan, P., Kazemzadeh, A., Sandaran, S. C., & Sahu, J. N. (2015). Methane bubble formation and dynamics in a rectangular bubble column: A CFD study. *Chemometrics and Intelligent Laboratory Systems, 147*, 111-120.

Pourtousi, M., Ganesan, P., & Sahu, J. N. (2015). Effect of bubble diameter size on prediction of flow pattern in Euler–Euler simulation of homogeneous bubble column regime. *Measurement, 76*, 255-270.

Pourtousi, M., Sahu, J. N., & Ganesan, P. (2014). Effect of interfacial forces and turbulence models on predicting flow pattern inside the bubble column. *Chemical Engineering and Processing: Process Intensification, 75*, 38-47.

Pourtousi, M., Sahu, J. N., Ganesan, P., Shamshirband, S., & Redzwan, G. (2015). A combination of computational fluid dynamics (CFD) and adaptive neuro-fuzzy system (ANFIS) for prediction of the bubble column hydrodynamics. *Powder Technology, 274*, 466-481.

Pourtousi, M., Zeinali, M., Ganesan, P., & Sahu, J. (2015). Prediction of multiphase flow pattern inside a 3D bubble column reactor using a combination of CFD and ANFIS. *RSC Advances, 5*, 85652–85672.

Rabha, S. S., & Buwa, V. V. (2010). Volume-of-fluid (VOF) simulations of rise of single/multiple bubbles in sheared liquids. *Chemical Engineering Science, 65*(1), 527-537.

Ranade, V. V., & Tayalia, Y. (2001). Modelling of fluid dynamics and mixing in shallow bubble column reactors: influence of sparger design. *Chemical Engineering Science, 56*(4), 1667-1675.

Ratkovich, N., Chan, C. C. V., Berube, P. R., & Nopens, I. (2009). Experimental study and CFD modelling of a two-phase slug flow for an airlift tubular membrane. *Chemical Engineering Science, 64*(16), 3576-3584.

Razzak, S. A. (2012). Hydrodynamics modeling of an LSCFB riser using ANFIS methodology: Effects of particle shape and size. *Chemical Engineering Journal, 195*, 49-61.

Ruzicka, M. C., Bunganic, R., & Drahoš, J. (2009). Meniscus dynamics in bubble formation. Part I: Experiment. *Chemical Engineering Research and Design, 87*(10), 1349-1356.

Ruzicka, M. C., Vecer, M. M., Orvalho, S., & Drahoš, J. (2008). Effect of surfactant on homogeneous regime stability in bubble column. *Chemical Engineering Science, 63*(4), 951-967.

Rzehak, R., & Krepper, E. (2013). CFD modeling of bubble-induced turbulence. *International Journal of Multiphase Flow, 55*, 138-155.

Şal, S., Gül, Ö. F., & Özdemir, M. (2013). The effect of sparger geometry on gas holdup and regime transition points in a bubble column equipped with perforated plate spargers. *Chemical Engineering and Processing: Process Intensification, 70*, 259-266.

Sanyal, J., Marchisio, D. L., Fox, R. O., & Dhanasekharan, K. (2005). On the comparison between population balance models for CFD simulation of bubble columns. *Industrial & Engineering Chemistry Research, 44*(14), 5063-5072.

Sanyal, J., Vásquez, S., Roy, S., & Dudukovic, M. P. (1999). Numerical simulation of gas–liquid dynamics in cylindrical bubble column reactors. *Chemical Engineering Science, 54*(21), 5071-5083.

Sarkheyli, A., Zain, A. M., & Sharif, S. (2015). Robust optimization of ANFIS based on a new modified GA. *Neurocomputing, 166*, 357–366.

Sathe, M., Joshi, J. B., & Evans, G. (2013). Characterization of turbulence in rectangular bubble column. *Chemical Engineering Science, 100*, 52-68.

Sato, Y., & Sekoguchi, K. (1975). Liquid velocity distribution in two-phase bubble flow. *International Journal of Multiphase Flow, 2*, 79-95.

Sattar, M. A., Naser, J., & Brooks, G. (2013). Numerical simulation of two-phase flow with bubble break-up and coalescence coupled with population balance modeling. *Chemical Engineering and Processing: Process Intensification, 70*, 66-76.

Schiller, L., & Naumann, Z. (1935). A drag coefficient correlation. *Vdi Zeitung, 77*, 318–320.

Selma, B., Bannari, R., & Proulx, P. (2010). Simulation of bubbly flows: Comparison between direct quadrature method of moments (DQMOM) and method of classes (CM). *Chemical Engineering Science, 65*(6), 1925-1941.

Shahbazi, B., Rezai, B., Chelgani, S. C., Koleini, S. M. J., & Noaparast, M. (2013). Estimation of diameter and surface area flux of bubbles based on operational gas

dispersion parameters by using regression and ANFIS. *International Journal of Mining Science and Technology, 23*(3), 343-348.

Shaikh, A., & Al-Dahhan, M. (2003). Development of an artificial neural network correlation for prediction of overall gas holdup in bubble column reactors. *Chemical Engineering and Processing: Process Intensification, 42*(8), 599-610.

Silva, M. K., d'Ávila, M. A., & Mori, M. (2012). Study of the interfacial forces and turbulence models in a bubble column. *Computers & Chemical Engineering, 44*, 34-44.

Simonnet, M., Gentric, C., Olmos, E., & Midoux, N. (2008). CFD simulation of the flow field in a bubble column reactor: Importance of the drag force formulation to describe regime transitions. *Chemical Engineering and Processing: Process Intensification, 47*(9), 1726-1737.

Smith, B. L. (1998). On the modelling of bubble plumes in a liquid pool. *Applied Mathematical Modelling, 22*(10), 773-797.

Tabib, M. V., Roy, S. A., & Joshi, J. B. (2008). CFD simulation of bubble column—an analysis of interphase forces and turbulence models. *Chemical Engineering Journal, 139*(3), 589-614.

Tabib, M. V., & Schwarz, P. (2011). Quantifying sub-grid scale (SGS) turbulent dispersion force and its effect using one-equation SGS large eddy simulation (LES) model in a gas–liquid and a liquid–liquid system. *Chemical Engineering Science, 66*(14), 3071-3086.

Taha, T., & Cui, Z. F. (2002). CFD modelling of gas-sparged ultrafiltration in tubular membranes. *Journal of Membrane Science, 210*(1), 13-27.

Takagi, S., & Matsumoto, Y. (1998). *Numerical study on the forces acting on a bubble and particle.* Paper presented at the Proceedings of the Third International Conference on Multiphase Flow, ICMF.

Takagi, T., & Sugeno, M. (1985). Fuzzy identification of systems and its applications to modeling and control. *Systems, Man and Cybernetics, IEEE Transactions on*(1), 116-132.

Thorat, B. N., & Joshi, J. B. (2004). Regime transition in bubble columns: experimental and predictions. *Experimental Thermal and Fluid Science, 28*(5), 423-430.

Tomiyama, A., Sou, A., Žun, I., Kanami, N., & Sakaguchi, T. (1995). *Effects of Eötvös number and dimensionless liquid volumetric flux on lateral motion of a bubble*

in a laminar duct flow. Paper presented at the Proceedings of the Second International Conference on Multiphase Flow, Kyoto, Japan.

Tomiyama, A., Tamai, H., Zun, I., & Hosokawa, S. (2002). Transverse migration of single bubbles in simple shear flows. *Chemical Engineering Science, 57*(11), 1849-1858.

Vafaei, S., & Borca-Tasciuc, T. (2014). Role of nanoparticles on nanofluid boiling phenomenon: Nanoparticle deposition. *Chemical Engineering Research and Design, 92*(5), 842-856.

Vafaei, S., Borca-Tasciuc, T., & Wen, D. (2010). Theoretical and experimental investigation of quasi-steady-state bubble growth on top of submerged stainless steel nozzles. *Colloids and Surfaces A: Physicochemical and Engineering Aspects, 369*(1), 11-19.

Van Baten, J. M., & Krishna, R. (2001). Eulerian simulations for determination of the axial dispersion of liquid and gas phases in bubble columns operating in the churn-turbulent regime. *Chemical Engineering Science, 56*(2), 503-512.

Van Doormaal, J. P., & Raithby, G. D. (1984). Enhancements of the SIMPLE method for predicting incompressible fluid flows. *Numerical Heat Transfer, 7*(2), 147-163.

van Sint Annaland, M., Deen, N. G., & Kuipers, J. A. M. (2005). Numerical simulation of gas bubbles behaviour using a three-dimensional volume of fluid method. *Chemical Engineering Science, 60*(11), 2999-3011.

Vasileva-Stojanovska, T., Vasileva, M., Malinovski, T., & Trajkovik, V. (2015). An ANFIS model of quality of experience prediction in education. *Applied Soft Computing, 34*, 129-138.

Vial, C., Laine, R., Poncin, S., Midoux, N., & Wild, G. (2001). Influence of gas distribution and regime transitions on liquid velocity and turbulence in a 3-D bubble column. *Chemical Engineering Science, 56*(3), 1085-1093.

Waewsak, C., Nopharatana, A., & Chaiprasert, P. (2010). Neural-fuzzy control system application for monitoring process response and control of anaerobic hybrid reactor in wastewater treatment and biogas production. *Journal of Environmental Sciences, 22*(12), 1883-1890.

Wali, W., Al-Shamma'a, A., Hassan, K. H., & Cullen, J. (2012). Online genetic-ANFIS temperature control for advanced microwave biodiesel reactor. *Journal of Process Control, 22*(7), 1256-1272.

Wang, H., Jia, X., Wang, X., Zhou, Z., Wen, J., & Zhang, J. (2014). CFD modeling of hydrodynamic characteristics of a gas–liquid two-phase stirred tank. *Applied Mathematical Modelling, 38*(1), 63-92.

Wang, X., Dong, H., Zhang, X., Yu, L., Zhang, S., & Xu, Y. (2010). Numerical simulation of single bubble motion in ionic liquids. *Chemical Engineering Science, 65*(22), 6036-6047.

Xing, C., Wang, T., & Wang, J. (2013). Experimental study and numerical simulation with a coupled CFD–PBM model of the effect of liquid viscosity in a bubble column. *Chemical Engineering Science, 95*, 313-322.

Xu, L., Yuan, B., Ni, H., & Chen, C. (2013). Numerical simulation of bubble column flows in churn-turbulent regime: comparison of bubble size models. *Industrial & Engineering Chemistry Research, 52*(20), 6794-6802.

Yang, L., & Entchev, E. (2014). Performance prediction of a hybrid microgeneration system using Adaptive Neuro-Fuzzy Inference System (ANFIS) technique. *Applied Energy, 134*, 197-203.

Yang, N., Wu, Z., Chen, J., Wang, Y., & Li, J. (2011). Multi-scale analysis of gas–liquid interaction and CFD simulation of gas–liquid flow in bubble columns. *Chemical Engineering Science, 66*(14), 3212-3222.

Youngs, D. L. (1982). Time-dependent multi-material flow with large fluid distortion. *Numerical Methods for Fluid Dynamics, 24*, 273-285.

Zahedi, P., Saleh, R., Moreno-Atanasio, R., & Yousefi, K. (2014). Influence of fluid properties on bubble formation, detachment, rising and collapse; Investigation using volume of fluid method. *Korean Journal of Chemical Engineering, 31*(8), 1349-1361.

Zarei, A., Hosseini, S. H., & Rahimi, R. (2013). CFD study of weeping rate in the rectangular sieve trays. *Journal of the Taiwan Institute of Chemical Engineers, 44*(1), 27-33.

Zhang, A., Sun, P., & Ming, F. (2015). An SPH modeling of bubble rising and coalescing in three dimensions. *Computer Methods in Applied Mechanics and Engineering, 294*, 189-209.

Zhang, D. (2007). *Eulerian modeling of reactive gas-liquid flow in a bubble column*: University of Twente.

Zhang, D., Deen, N. G., & Kuipers, J. A. M. (2006). Numerical simulation of the dynamic flow behavior in a bubble column: a study of closures for turbulence and interface forces. *Chemical Engineering Science*, *61*(23), 7593-7608.

Zhang, D. Z., & Vanderheyden, W. B. (2002). The effects of mesoscale structures on the disperse two-phase flows and their closures for dilute suspensions. *International Journal of Multiphase Flow*, *28*, 805-822.

Zhang, X., & Ahmadi, G. (2005). Eulerian–Lagrangian simulations of liquid–gas–solid flows in three-phase slurry reactors. *Chemical Engineering Science*, *60*(18), 5089-5104.

Žun, I. (1990). The mechanism of bubble non-homogeneous distribution in two-phase shear flow. *Nuclear Engineering and Design*, *118*(2), 155-162.

SUPPLEMENTARY

List of publications

As a result of this thesis, five ISI articles have been published and the first page of all papers are shown in Figures 7.1-7.5. Furthermore, one conference paper have been presented in the international conference.

Details of the paper and the conferences

The details of the published articles are arranged by the publishing year as following:

Articles

1. Pourtousi, M., Sahu, J. N., & Ganesan, P. (2014). Effect of interfacial forces and turbulence models on predicting flow pattern inside the bubble column. Chemical Engineering and Processing: Process Intensification, 75, 38-47. (ISI-Cited Publication)
2. Pourtousi, M., Sahu, J. N., Ganesan, P., Shamshirband, S., & Redzwan, G. (2015). A combination of computational fluid dynamics (CFD) and adaptive neuro-fuzzy system (ANFIS) for prediction of the bubble column hydrodynamics. Powder Technology, 274, 466-481. (ISI-Cited Publication)
3. Pourtousi, M., Ganesan, P., Kazemzadeh, A., Sandaran, S. C., & Sahu, J. N. (2015). Methane bubble formation and dynamics in a rectangular bubble column: A CFD study. Chemometrics and Intelligent Laboratory Systems, 147, 111-120. (ISI-Cited Publication)
4. Pourtousi, M., Ganesan, P., & Sahu, J. N. (2015). Effect of bubble diameter size on prediction of flow pattern in Euler–Euler simulation of homogeneous bubble column regime. Measurement, 76, 255-270. (ISI-Cited Publication)

5. Pourtousi, M., Zeinali, M., Ganesan, P., & Sahu, J. N. (2015). Prediction of multiphase flow pattern inside a 3D bubble column reactor using a combination of CFD and ANFIS. RSC Advances, 5(104), 85652-85672.

Conference paper

- M.Pourtousi , P. Ganesan, J .N. Sahu, Ghufran Redzwan, Sensitivity study of Bubble diameter for prediction of flow pattern in homogeneous bubble column regime, 7th international conference & exhibition on cooling & heating technologies 2014 (Indexed in Scopus).